DEVELOPMENT OF NANOSTRUCTURED SUPPORTED PHOTOCATALYSTS FOR HYDROGEN PRODUCTION AND INORGANIC POLLUTANTS REMOVAL

by

Davide Spanu

A dissertation submitted in partial fulfillment of the requirements for the degree of Doctor of Philosophy in

Chemical and Environmental Sciences

XXXI Cycle

University of Insubria

Department of Science and High Technology

Committee in charge:

Professor Paola Fermo

Professor Isabella Nova

Professor Josef Krýsa

Tutor

Professor Sandro Recchia

21st February 2019

Table of contents

Acknowledgements

Undertaking this Ph.D. has been a truly life-changing experience for me and it would not have been possible to do without the support and guidance that I received from many people.

First and foremost I want to express my sincere gratitude to my advisor Prof. Sandro Recchia for the continuous support of my Ph.D. study and related research, for his patience, motivation, and immense knowledge. His guidance helped me in all the time of research. I could not have imagined having a better advisor and mentor for my Ph.D. study. The joy and enthusiasm he has for his research were contagious and motivational for me, even during tough times in the Ph.D. pursuit.

My sincere thanks also go to all the members of the Analytical Chemistry group of the University of Insubria which have contributed immensely to my personal and professional growth. The group has been a source of friendships as well as good advice and collaboration. I am especially grateful to Prof. Damiano Monticelli and Prof. Carlo Dossi who were always helpful and collaborative whenever I needed their advice or technical support.

I would like to thank my Ph.D. colleagues Dr. Gilberto Binda and Dr. Daniele Moscheni with whom I have shared moments of deep anxiety but also of great fun and excitement. Their presence was very important in a process that is often felt as tremendously solitaire.

I greatly appreciate the opportunity that Prof. Patrik Schmuki gave me to join his research team (LKO) in Friedrich-Alexander-University of Erlangen-Nuremberg (FAU) for six months. I'm extremely grateful to him to allow me to do this experience which has completely changed in a positive way my Ph.D. and my approach to research. I would like to thank also all the members of LKO team for their collaboration during my period in Erlangen. In particular, I am deeply indebted to Dr. Marco Altomare for his fundamental role both during and after my period in LKO labs. His precious support has made easier and more fruitful my experience in Germany.

I would like to acknowledge the technical support provided by researchers of Politecnico di Milano, of the Institute of Molecular Science and Technologies of National Research Council (ISTM-CNR) of Milan and of the Regional Centre of Advanced Technologies and Materials (RCPTM) of Olomouc.

Finally, a special thanks to my family. Words cannot express how grateful I am to my mother and father for all of the sacrifices that they've made on my behalf. My entire study path would not have been possible without them. Thank you.

Davide Spanu

List of abbreviations

ABPE: Applied Bias Photon-to-current Efficiency
AM: Air Mass
APCE: Absorbed Photon-to-Current Efficiency
APCVD: Atmospheric Pressure Chemical Vapor Deposition
AQE: Apparent Quantum Efficiency
ATR: Attenuated Total Reflection
CB: Conduction Band
CSV: Cathodic Stripping Voltammetry
CV: Cyclic Voltammetry
CVD: Chemical Vapor Deposition
DC: Direct Current
EDS: Energy Dispersive X-Ray Spectrometry
E_g: Energy Gap
ESEM: Environmental Scanning Electron Microscopy
FEG: Field Emission Gun
FTO: Fluorine-doped Tin Oxide
HPLC: High-Performance Liquid Chromatography
ICP-MS: Inductively Coupled Plasma – Mass Spectrometry
ICP-OES: Inductively Coupled Plasma – Optical Emission Spectroscopy
IPCE: Incident Photon-to-Current Efficiency
KED: Kinetic Energy Discrimination
LED: Light Emitting Diode
LD50: Lethal Dose 50
NHE: Normal Hydrogen Electrode
NIR: Near-Infrared
NPs: Nanoparticles
NTs: Nanotubes
OCV: Open Circuit Voltage
OER: Oxygen Evolution Reaction
PEC: Photoelectrochemical
PVD: Physical Vapor Deposition
ROS: Reactive Oxygen Species
SEM: Scanning Electron Microscopy
SHE: Standard Hydrogen Electrode
STH: Solar-To-Hydrogen
UHV: Ultra-High Vacuum
UV-vis: Ultraviolet-Visible
VB: Valence Band
XRD: X-Ray Diffraction
XPS: X-ray Photoelectron Spectroscopy

Abstract

The sustainable progress of human society has gained much more attention in the last decades and several efforts have been directed to the development of new alternative clean energy supplies and "green" environmental remediation for pollution.

In this context, semiconductor photocatalysis has emerged as one of the most promising approach to exploit a renewable energy source (i.e. natural sunlight irradiation) to cause numerous redox reactions for a very extensive range of purposes such as the production of clean energy (e.g. photocatalytic H_2 evolution), removal of organic and inorganic pollutants in natural water, purification of air and antibacterial activity.

Several photo-active materials have been explored in the last years for these applications, however, most of the employed semiconductor photocatalysts (e.g. TiO_2, α-Fe_2O_3) are often characterized by low efficiencies due to recombination of charge carriers and trapping as well as a sluggish kinetics of electron transfer. For these reasons, the design of novel nanostructures and their decoration with a wide range of co-catalysts (i.e. metals or metal oxides) became a most important field of research.

In view of these recent trends, the focus of this thesis was directed towards the study of different supported photo(electro)catalytic materials (i.e. modified TiO_2 nanotubes and worm-like nanostructured α-Fe_2O_3) for topical environmental applications: i) the production of clean energy through hydrogen gas evolution from aqueous solutions and ii) the removal of highly toxic inorganic pollutants (i.e. arsenic and mercury) from natural water.

Firstly, the decoration of anodically grown highly ordered TiO_2 nanotubes with different co-catalysts (metals and/or metal oxides) through a sputtering/solid-state dewetting approach was used to obtain a strong improvement of performances towards the photocatalytic hydrogen evolution from ethanol-water mixture under UV irradiation (365 nm). Thanks to the extremely high morphological control provided by this strategy, TiO_2 nanotubes decorated with a well-defined stacked co-catalyst (a WO_3 layer decorated with Pt NPs) and with dewetted-alloyed NiCu nanoparticles were successfully fabricated and used for such application achieving high photocatalytic efficiencies. Detailed characterizations of these materials revealed the key reasons for the enhanced photocatalytic efficiency, such as the improved electron transport and charge carrier separation.

The same decoration method was employed also to fabricate Au-decorated TiO_2 nanotube arrays which were used for the first time for the photocatalytic reduction/scavenging of

inorganic Hg(II) from water under solar light illumination. This work revealed interesting novel mechanisms of action and strongly enhanced scavenging properties enabled by the presence of Au nanoparticles on the photocatalyst surface which lead to significantly high abatement performances both treating high and low Hg(II) concentration levels in natural water-like solutions.

A different catalytic approach, instead, was used for the oxidation/abatement of inorganic As(III) over hematite-based photoanodes under solar light irradiation. Such reaction, in fact, was carried out for the first time through a photoelectrochemical (PEC) approach (i.e. by applying a bias potential to the irradiated photo-active material). Although the obtained abatement results are not better than the ones reached in previous works using an open-circuit approach, relevant mechanistic features concerning the alteration of hematite surface terminations were discovered during this study.

1. Introduction

1.1. Brief history of photocatalysis: from ‘800 to nowadays

The birth of the term “catalysis” dates back to 1836 when Berzelius observed for the first time the oxidation of sulfur dioxide on hot platinum[1]. He summarized his idea of this new force as: “Several simple or compound bodies, soluble and insoluble, have the property of exercising on other bodies an action very different from chemical affinity. By means of this action they produce, in these bodies, decompositions of their elements and different recombination of these same elements to which they remain indifferent”[2].

At the end of ‘800, more precisely in 1894, the definition of the term “catalysis” was revised by Ostwald as the increase of the rate of a chemical reaction by a substance that does not directly participate in the reaction[3].

Afterwards, from the firsts years of 1900, a lot of efforts was put into the study of new catalytic processes, such as the well-known Haber-Bosch process[4], but only starting from the middle of 1960 it was possible to investigate and completely understand the mechanism of some catalytic processes thanks to the development of new surface science tools[5].

Later, in 1972, after the birth of the electrocatalysis (term coined and defined by Grubb in 1964)[6] and the very previous discovery of the water electrolysis (at the end of the 18th century)[7], Fujishima and Honda observed for the first time the light-induced water electrolysis using TiO_2 (rutile) photoanodes[8].

This groundbreaking discovery became famous as the beginning of a new era: the birth of the heterogeneous photocatalysis. However, this phenomenon was not immediately accepted, in particular by electrochemists which maintained that water electrolysis takes place at 1.5-2 V and the idea that light could also be employed as an energy source to generate oxygen was not believed possible. From here, extensive research was carried out by chemists, chemical engineers and physicists for understanding the mechanism of this process and how to increase its efficiency. Thus, this discovery paved the way for the development of a new chemistry branch, called photoelectrochemistry.[9–12] As shown in Figure 1, after the pioneering work of Fujishima and Honda (1972), the scientific interest in photocatalytic processes exponentially increased up to nowadays (while the number of published works regarding catalytic processes was already over 100 publications per year starting from 1960).

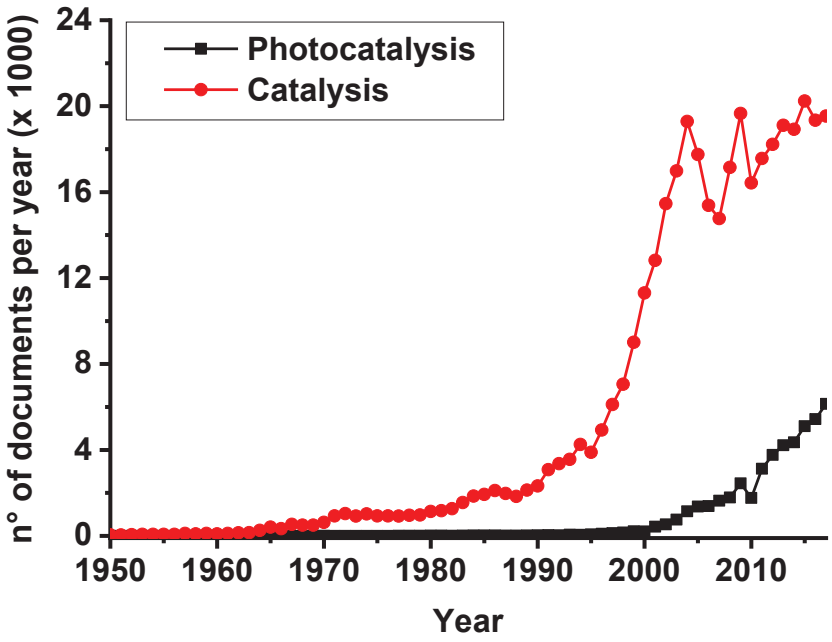

Figure 1. Trend of the published papers that contains the terms "photocatalysis" or "catalysis" obtained by "Analyze search results" section on Scopus.com website.

The recent rapid growth of heterogeneous photocatalysis is related to its several advantages such as attractive efficiency, cost-effectiveness and the employment of renewable energy sources. This method represents one of the major expression of sustainable and green chemistry which can be applied for several applications in environmental systems[13–15].

Mechanisms of action, some applications and different photocatalytic materials will be investigated and discussed in detail in the following chapters.

1.2. Basic principles of photo(electro)catalysis

The etymology of the word "photocatalysis" can be partially traced back to the Greek language as the composition of two parts:

•*"Phôs":* (from Ancient Greek) which means light.

•*"Catalysis":* (term used for the first time by Berzelius in 1836)[1] a process in which a foreign substance increase the rate of a chemical reaction (by reducing the activation energy) without being altered after the reactants transformation.

Thus, photocatalysis can be defined as "catalysis driven acceleration of a light-induced reaction".

Photocatalytic processes are commonly classified into two main categories: homogeneous and heterogeneous photocatalysis[14–16].

The first group generally requires the presence of transition metal complexes (such as complexes of iron, chromium, copper, etc.) as photocatalyst. This method can be used to produce, under proper illumination, highly reactive intermediates (e.g. hydroxyl radicals) which, for instance, can immediately react with organic substances present in solution and degrade them. However, the employment of homogeneous photocatalysts has several drawbacks such as i) waste disposal problems, ii) high costs, iii) necessity of controlled (and not always mild) pressure and temperature conditions.

These drawbacks can be theoretically overcome using heterogeneous photocatalysts which are currently widely employed for several fields of application.

The most common heterogeneous photocatalytic materials are metal oxide semiconductors (e.g. TiO_2, α-Fe_2O_3) because of their favorable electronic structure which, unlike metals (continuum of electronic states), are characterized by a fully occupied low-energy level (valence band, VB) and an empty level (conduction band, CB) at higher energy. These bands are separated by a void energy region which extends from the top of the filled VB to the bottom of the vacant CB. Within this void region no energy levels are permitted. The difference between the top of the VB and the bottom of the CB is called energy band gap (E_g)[17] and, for the most used semiconductor photocatalysts, its value is usually in the range 2-4 eV (i.e. 620-310 nm).

A generic semiconductor to be a good photocatalyst should be: i) photoactive in the visible and/or near-UV region, ii) chemically and biologically inert, iii) stable toward corrosion and photo-corrosion, iv) inexpensive, and v) non-toxic.

As shown in Figure 2, when a semiconductor is irradiated with a photon beam having energy equal to or higher than the E_g of the semiconductor, electrons can be promoted from the VB to the CB, leaving available holes in the VB. These charge carriers can be exploited to induce several redox reactions. More in detail, photo-promoted electrons have the reducing potential of the CB energy, and holes have the oxidation potential of the VB energy.

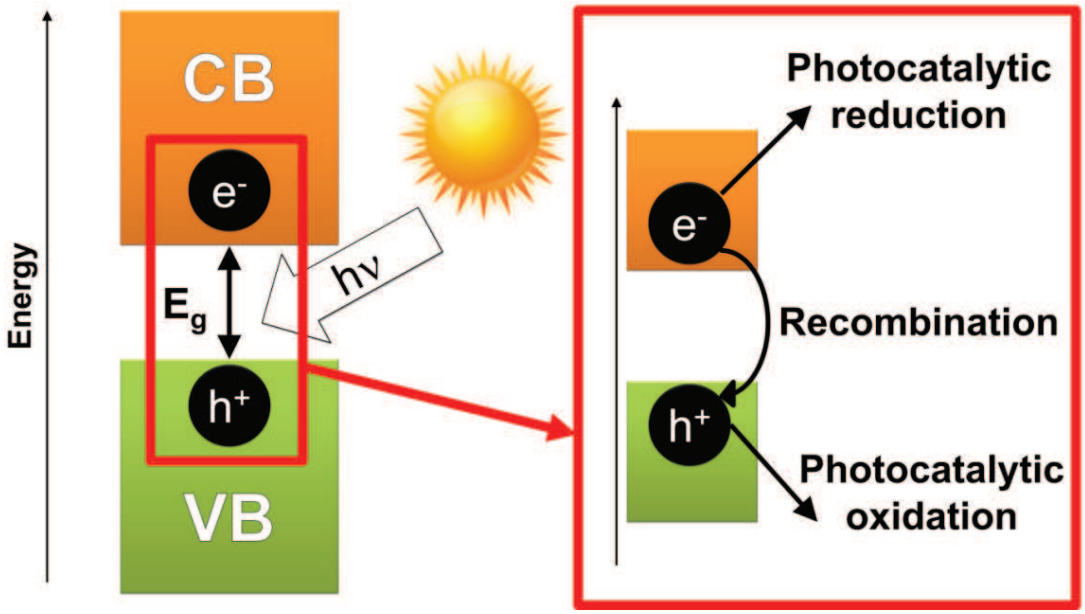

Figure 2. Scheme of light absorption and carrier generation processes in a generic semiconductor. In the red box the possible fates of the photo-generated charge carriers.

A photo-generated electron-hole pair is termed an "exciton" and its fate may be:

- Recombination (i.e. an electron "reacts" with a hole).
  This undesired process releases the energy gained from the photo-excitation of the electron as heat;
- Separation via suitable traps producing photo-corrosion (undesired process).
  It can occur when electrons and holes are separated through an irreversible trapping mechanism which involves elements of the semiconductor;
- Chemical reactions at the semiconductor surface (the goal of the photocatalytic process).

The exciton recombination can largely limit the charge carrier life-time, thus, high recombination rates lead to a significant decrease of the photocatalytic efficiency.[13–15]

Exploring more in detail the electronic structure of a semiconductor photocatalyst, it is important to define another peculiar parameter: the Fermi level. At temperatures higher than 0 K it is defined as the energy level with a 50% electron occupation probability. At absolute zero temperature a semiconductor acts as a perfect insulator, and, in this case the Fermi level represents the top of the most filled energy state of the system. However, as the temperature increases free electrons and holes are generated. At room temperature the Fermi level for a pure semiconductor lies in the middle of the forbidden band, while for an n-type semiconductor the Fermi level lies closer to CB and for a p-type semiconductor it lies closer to VB. (Figure 3)

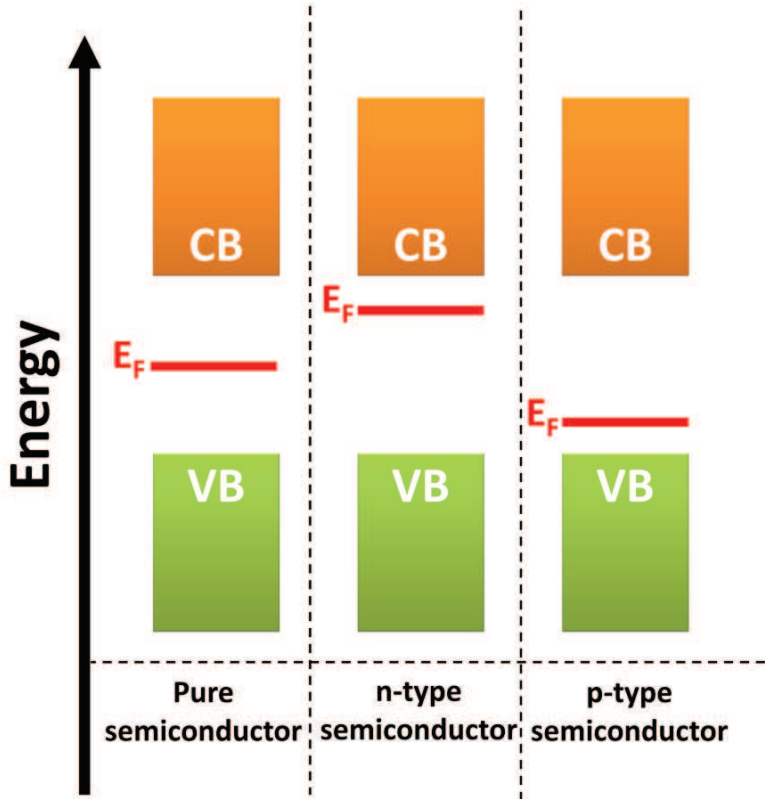

Figure 3. Schematic representation of the Fermi level position for the different type of semiconductor.

The hole-concentration in the VB can be obtained by the Equation 1a while the electron-concentration in the CB is given by Equation 1b.

$$p = N_V e^{\frac{-(E_F - E_V)}{K_B T}} \qquad \text{(Equation 1a)}$$

$$n = N_C e^{\frac{-(E_C - E_F)}{K_B T}}$$ (Equation 1b)

Where:

- K_B is the Boltzmann constant;
- T is the absolute temperature of the semiconductor;
- N_C and N_V are the effective density of states in the CB and in the VB, respectively;
- E_F is the Fermi level energy;
- E_C and E_V are the CB and VB energies, respectively.

Thus, as expressed by Equation 1a and 1b, the electron-carrier and hole-carrier concentration are strictly related to the energy difference between the band energy level (CB or VB) and the Fermi energy. Since for an n-type semiconductor the Fermi level lies closer to CB, the electron-carrier concentration is higher than the hole-carrier concentration (E_F-E_V > E_C-E_F).

The system can become more complex when a semiconductor of different charge (e.g. hetero-junction, two semiconductors with different E_F) or a redox system is in contact with the photocatalyst surface. In these conditions a change in the potential profile at the interface occurs due to a charge transfer process (diffusion). This effect on the electrical field in the near-surface region is called band-bending[18].

The same discussion can be applied both for the band-bending at an n-semiconductor/liquid contact and at a p-type semiconductor/liquid contact: the only one difference is the nature of the majority charge carrier (negative or positive) and, hence, the direction of the band-bending (i.e. upward or downward band bending).

More in detail, when a semiconductor is in contact with a redox electrolyte, charge carriers are transported at the semiconductor/electrolyte interface until the equilibrium is reached (i.e. when the Fermi energy is equal to the redox potential at the interface). The charge transfer can generate a depletion region in the semiconductor (compensated by opposite charge) and a potential barrier at the interface. Since the Fermi level of an n-type semiconductor electrode (at open circuit) is typically higher than the redox potential of the electrolyte, electrons will be transported from the semiconductor to the electrolyte. The positive charge associated with the space charge region causes the presence of upward bending of the band edges (Figure 4a). Vice versa, since the Fermi level of a p-type semiconductor is usually lower than the redox potential, electrons must be transported from the electrolyte to the semiconductor until the

equilibrium is reached. The negative charge in the space charge region causes a downward bending in the band edges. In both the cases the majority charge carriers (i.e. electrons for an n-type semiconductor and holes for a p-type semiconductor) in the space charge region are removed by these processes. For this reason, this region is also called "depletion layer".

The energy barrier generated by the upward band bending drives back the photoelectrons towards the bulk region, resulting in a hole accumulation (or electron depletion) layer at the surface[18]. Instead, the downward surface band bending of a p-type semiconductor causes an energy barrier for the photo-generated holes, creating an electron accumulation (or hole depletion). In few words, the upward band bending can be considered as a negative surface that repels electrons and attracts holes. The opposite consideration can be obviously made for downward band bending. The main consequence of this behavior is that a semiconductor with bent bands should react more efficiently (in comparison with the flat band situation). A stronger band bending and a wider space charge region should be beneficial for the efficiency of the photo-induced reaction.

In order to have an accurate knowledge of the strength of the upward or downward band bending, it is possible to use different photoelectrochemical methods to measure it[18,19].

Additionally, it is important to underline that band-bending can be induced and tuned also by applying an external bias voltage (E) to the semiconductor photoelectrode. As for metals, the variation of the potential applied to a semiconductor electrode shifts the Fermi energy level. The band edge positions in the bulk also shift thanks to the application of an external potential (in the same way as the Fermi level). Since the levels of the band edges at the interface are not influenced by variation in the applied potential, the modification of the energies of the band edges on going from the bulk to the interface (and thus of the extent and direction of band bending) is strictly dependent on the applied potential. As shown in Figures 4c and 4d for both n-type and p-type semiconductors, there are three different possible situations:

1) At a particular potential value ($E = E_{FB}$), the Fermi level is equal to the solution redox potential. In these conditions there is not a net transfer of charge, and so band bending does not occur. For this reason, this potential value is commonly called flatband potential (E_{FB}).
2) At potentials higher than E_{FB} for an n-type semiconductor and at potentials lower than E_{FB} for a p-type semiconductor, depletion regions appear.

3) At potentials lower than E_{FB} for an n-type semiconductor and at potentials higher than E_{FB} for a p-type semiconductor, accumulation regions appear. In this case, in fact, it is present an excess of the majority charge carrier (electrons for n-types and holes for p-types) in the space charge region.

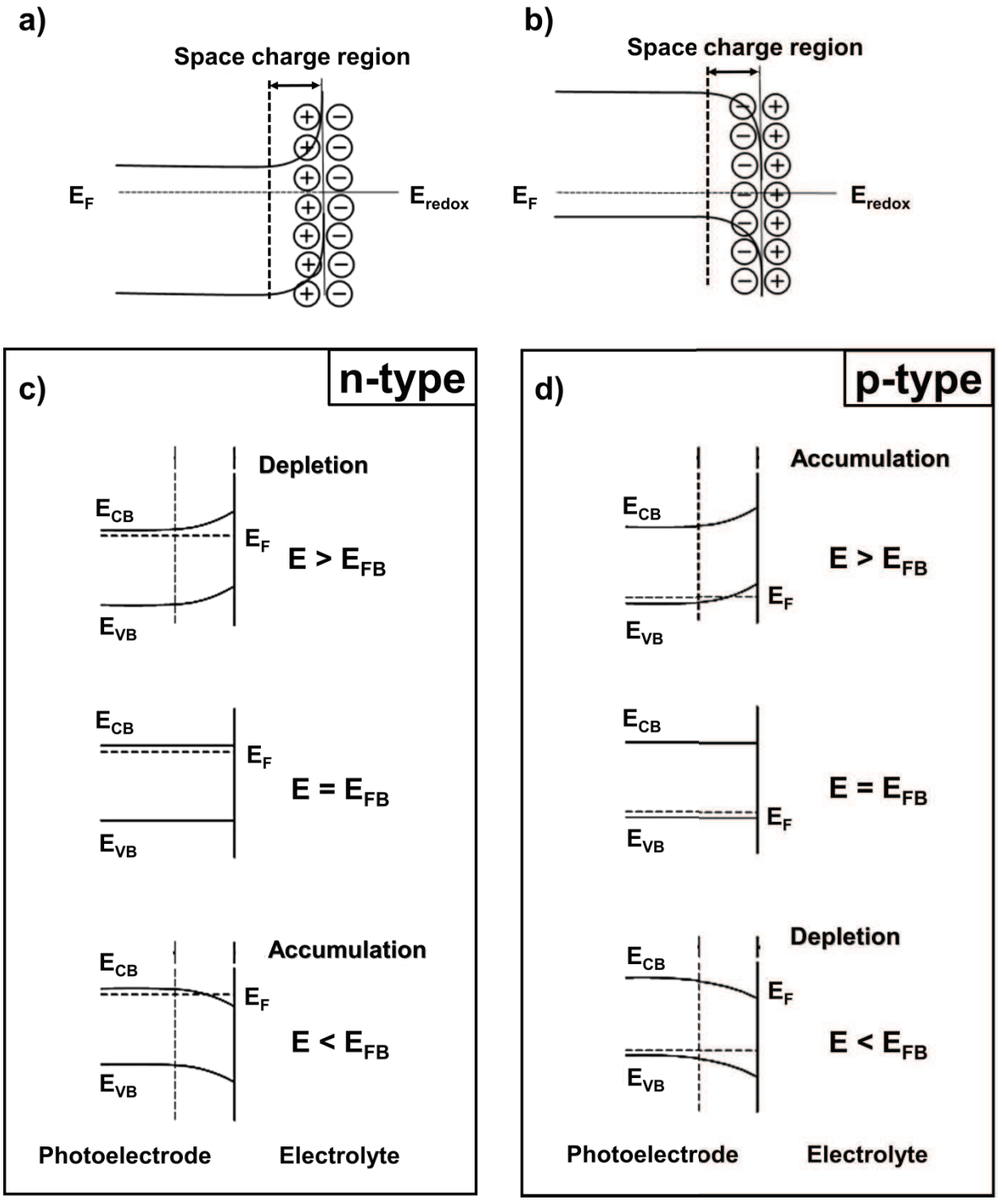

Figure 4. (a-b) Band bending for (a) an n-type and (b) a p-type semiconductor in equilibrium with a redox electrolyte. (c-d) Effect of varying the applied potential on (c) an n-type and (d) a p-type semiconductor.

Since band bending strongly influences the surface properties of a semiconductor, all the fundamental processes at the surface of a catalyst during heterogeneous photocatalytic processes (i.e. adsorption of reactants, photoreaction and desorption of products) can be significantly affected by band bending. Therefore, it can affect the efficiency of the overall photochemical process, which can be expressed by the quantum yield (Φ).

$$\Phi = \frac{rate\ of\ reactant\ consumption\ (or\ product\ formation)}{rate\ of\ photon\ absorption} \qquad \text{(Equation 2)}$$

The rate of reactant consumption (or product formation) is directly dependent on the rate of charge transfer (k_{CT}) from the semiconductor surface to the reactive species, and the rate of photon absorption is directly related to the sum of the rates of charges recombination (k_R) and the charge transfer (k_{CT}). Therefore, Φ can be expressed as:

$$\Phi \propto \frac{k_{CT}}{k_{CT} + k_R} \qquad \text{(Equation 3)}$$

The band bending effect can influence both k_{CT} and k_R. More in detail, the change in the near-surface electric field caused by upward or downward band bending increases the spatial separation of electron-hole pairs suppressing k_R and increasing k_{CT}. This is the reason why the efficiency of the overall photocatalytic process depends on the band bending effect.

Considering all the above described effects which may influence the efficiency of a photo-induced reaction, in the last years, a lot of efforts were put into the development of functional photocatalysts in order to improve the photochemical performances. These modified materials are usually designed to extend exciton lifetime by improving electron-hole separation and charge transport from the semiconductor to the reactants (i.e. to increase the quantum yield). These modifications have the ultimate goal of facilitating reactions between photo-generated electrons with oxidants to produce reduced products (reduction process), and/or reactions between the holes in the VB with reductants to produce oxidized products (oxidation process).

These photo-induced reactions can find application for a very wide range of purposes[20] among which the production of hydrogen from water (i.e. photocatalytic water splitting)[21],

the degradation of organic and inorganic pollutants in water (e.g. arsenic and mercury)[22,23], purification of air[24] and antibacterial activity[25].

1.3. Overview of the most common photocatalytic materials

In the last decades, nanomaterials have found great application as photocatalysts and they account for most of the existing research in this area. These materials provide several beneficial properties such as large surface areas, abundant surface states and the possibility to design various morphologies. In particular, nanostructured semiconductors have emerged as flexible materials to achieve high photocatalytic efficiency.

Although many efforts have been made in the development of novel nanostructured materials in the last years[26–29], their efficiency, especially under solar light irradiation, must be further enhanced in order to meet engineering requirements. The main challenge in this field is, in fact, to design and modify nanostructured semiconductor materials in order to obtain more efficient, stable and cheap photocatalysts.

In this chapter, it will be provided an overview of the properties of the most employed semiconductor photocatalysts and the state-of-art on their modifications.

As reported in Chapter 1.2, the most important aspect of a semiconductor is its energy band configuration which determines i) the minimum energy required for incident photons to activate the material and ii) the redox capabilities (defined by the energy of photo-generated electrons and holes)[29,30].

As shown in Figure 5, there are many semiconductor materials that need UV irradiation to be photo-activated (e.g. TiO_2 has an energy band gap of 3.0-3.2 eV which in terms of wavelength means 413.3-387.5 nm). These kinds of materials can efficiently exploit only less than ~ 5% of the solar light that reaches the earth. Instead, other materials, such as α-Fe_2O_3 (band gap ~ 2.3eV or 539.1 nm), can be photo-activated under visible light irradiation enabling a more efficient use of the solar light spectrum. Nevertheless, the recombination probability is higher for these metal oxides, and the energy of the band-edges is often not suitable to trigger specific redox reactions.

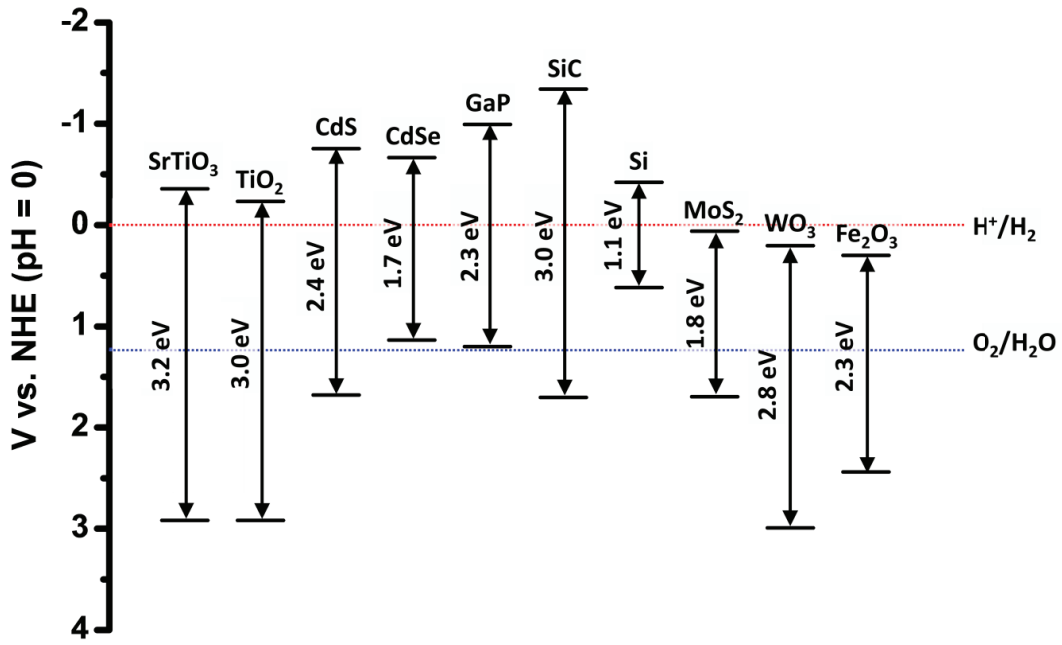

Figure 5. Summary of the energy band gap value and energy band edge positions of some of the main semiconductor photocatalysts reported in the literature.

For these reasons, the accurate knowledge of the position of CB and VB edges is fundamental to predict the feasibility of a specific redox reaction on a specific photocatalytic material. For instance, the feasibility of the water splitting reaction can be predicted by comparing the potential of H^+ reduction to H_2 and of H_2O oxidation to O_2 with CB and VB edge positions, respectively (see Figure 5).

Since for a reduction process electrons move from the semiconductor surface to reactants is necessary that the reduction potential is more positive than the CB edge energy. Vice versa, for an oxidation reaction (i.e. electrons move from the reactants to the semiconductor to react with holes in VB) the reduction potential must be more negative than the VB edge energy. Anyway, in order to make feasible theoretically not allowed reactions, it is possible to shift the band-edge positions by applying a bias potential (photoelectrocatalysis) or modifying the material in several ways, among which doping with foreign species (e.g. metals, non-metals) and solid-solution strategies.

Besides the energy situation, other properties such as the size and the structure of photocatalyst particles can play an important role in the photocatalytic efficiency. Reducing the particle size is in general beneficial for a photocatalytic process because it leads to the exponential growth of the specific surface area and, hence, to an increased number of reactive sites. However, this general rule is not always true (i.e. the smaller the particle size, not always the higher the efficiency). In fact, if the particle size and the electron mean free path

are of the same order of magnitude, the recombination probability can largely increase due to the quantum confinement effect. Instead, the structure and morphology of the photocatalyst can strongly influence the potential gradient (from the bulk to the surface of the particle) and the charge carrier migration. For these reasons, the comprehension of the relationship between the morphology and surface/photocatalytic properties has recently become a most interesting field of research. A properly designed shape-controlled synthesis of nanostructured photocatalysts can lead to the production of a material with significantly improved photocatalytic performances. This enhancement is generally ascribed to the increased separation of photo-generated electron-hole.

Additionally, the surface features of the material can regulate its adsorptive/desorpitive properties and stability against photo-corrosion[31,32]. As a general rule, the higher the surface energy, the higher the photocatalytic ability. For this reason, different semiconductor crystalline morphologies have been recently developed to provide a large fraction of highly reactive facets[33].

In conclusion, all the steps involved in a photocatalytic process (i.e. energy absorption from photons, migration of charge carriers to the photocatalyst surface, adsorption of reactants, redox reaction and desorption of products) are strongly dependent on intrinsic properties of the semiconductor. Proper structural, compositional and surface modifications can be carried out to tune these properties in order to achieve more efficient materials.

Since in this dissertation it will be reported the employment of supported TiO_2 nanotubes and nanostructured α-Fe_2O_3 for different environmental applications, particular attention will be dedicated to the detailed description of such materials and their modifications.

1.3.1. Titanium dioxide (TiO_2)

Since the pioneering work by Fujishima and Honda[34], TiO_2 has been widely employed for several UV-light driven photocatalytic applications thanks to its cost effectiveness, environmental friendliness, long-term stability against (photo)chemical corrosion and tunable electronic energy band gap[35,36].

TiO_2 is a transition metal oxide and more specifically an n-type semiconductor with a band gap of 3.00–3.20 eV (E_g strictly related to its crystallographic features). TiO_2 can be easily synthesized in two main crystalline forms (the most common ones for photocatalytic materials):

- Anatase (shown in Figure 6a, tetragonal structure, energy band gap ~ 3.20 eV)
- Rutile (shown in Figure 6b, tetragonal structure, energy band gap ~ 3.00 eV)

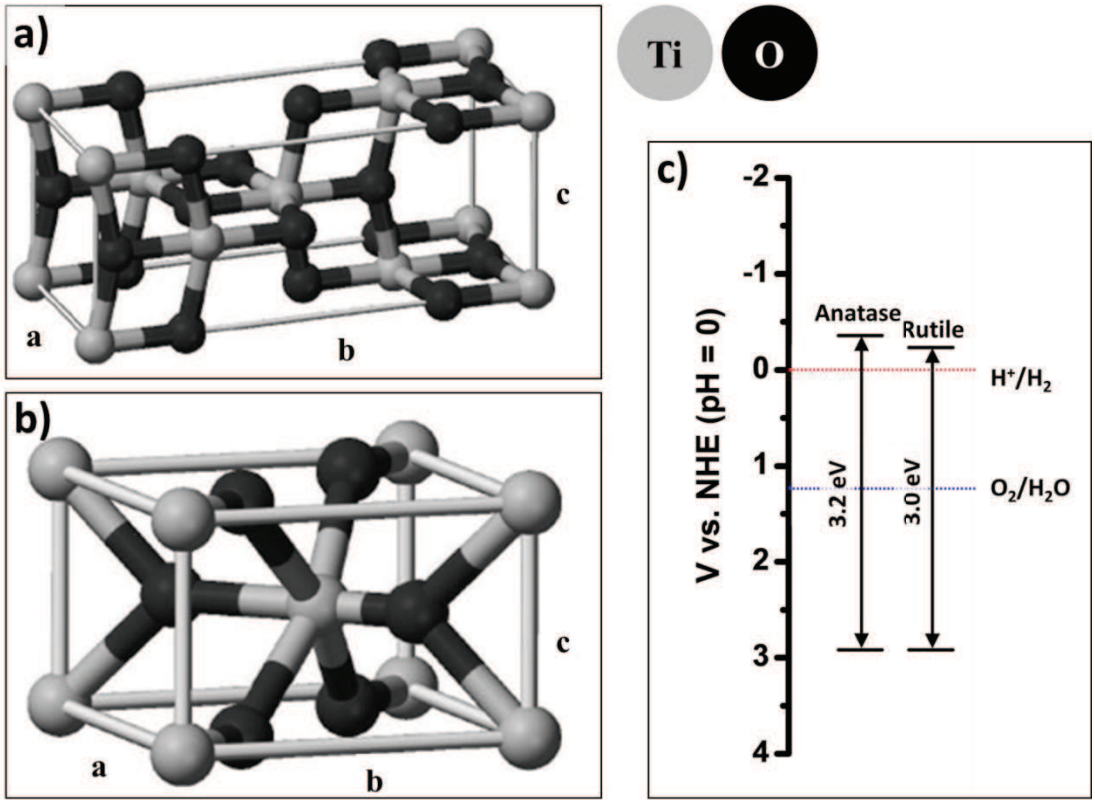

Figure 6. a) Anatase and b) Rutile TiO_2 crystal structures. c) Energy band edges situation for anatase and rutile.

Although anatase is commonly considered as the most photo-catalytically efficient polymorph[37], there is not a generally accepted elucidation for the different efficiency of rutile and anatase. However, some explanations can be found to tentatively justify this fact.

First of all, anatase TiO_2 having a larger band gap than rutile needs a more energetic light source to be photoactivated. On the other hand, anatase and rutile having different band gap energy have also a different position of CB and VB edge levels. Even if their relative position is still controversial, it is undoubted that the reduction and/or oxidation "power" of anatase is higher than the one of rutile (i.e. CB is more negative and/or VB is more positive than the ones of rutile). Moreover, the CB and/or VB shift can facilitate charge carriers transfer from anatase to adsorbed reactants molecules.

Another feature in favor of anatase is the fact that this polymorph has an indirect band gap narrower than its direct band gap while rutile exhibits an indirect band gap that is very similar to its direct band gap. Since it is well-known that the charge carrier life time of semiconductors with indirect band gap is longer than the life time of charges in direct gap materials, the exciton pair life in anatase is longer than in rutile. However, since only a fraction of electrons and holes are able to efficiently reach the semiconductor surface within their life time, also the charge carrier mobility needs to be considered for a complete description of the charge carriers participation to the reaction on the photocatalyst surface.

Additionally, preferential charge carriers diffusion along specific crystallographic directions is reported to be relevant to elucidate surface orientation dependencies in photocatalytic redox processes[37–39]. From preliminary measurements of exciton mobility with the polaron effective mass[37–39], it seems that anatase has a larger surface region that contributes to the photocatalytic reaction and this fact can surely contribute to the different photocatalytic activity of anatase and rutile.

Instead, the adsorptive/desorpitive properties cannot be considered as dependent only on polymorphism since the surface properties can largely differ for the same polymorph. A lot of synthesis-dependent contributions may affect such properties and their effect on photocatalytic efficiency.

Finally, a general drawback which unites these polymorphs is the rapid charge carrier recombination that leads to the dissipation of unproductive energy. In order to enhance the charge carrier separation (and hence to extend their life time), anatase and rutile are often mixed. The mixture of different phases, in fact, is reported to have synergistic positive effects on photocatalytic performances[40,41]. As proof of this fact, the most employed powdered TiO_2 photocatalyst is a phase mixture which contains anatase and rutile in a ratio of 3:1. This commercial photocatalyst is called Degussa P-25[42].

However, TiO_2, even if used as a mixture of polymorphs, is active only under UV light irradiation. This represents a major limitation since this photocatalyst only enables to use

~5% of the solar light that reaches the earth. To extend the light harvesting to the visible light region and to reduce the probability of the recombination process of photo-generated excitons, suitable modifications of TiO_2 photocatalysts must be performed (e.g. structural/surface changes, doping with foreign elements and decoration of the substrate making heterojunctions with other semiconductors or metals).

As mentioned above, it is essential to maximize the specific surface area to increase the overall photocatalytic efficiency, and for this reason, powdered TiO_2 nanoparticles (e.g. commercial Degussa P-25) find wide application. The increase of the specific surface area by reducing dimensions to the nanoscale leads to significant changes in the electronic properties (e.g. quantum size effects) and surface properties (e.g. interaction between TiO_2 and adsorbed molecules). These improvements can strongly enhance the kinetic reaction or can even enable for entirely new reaction mechanisms.

However, some drawbacks are related to the fabrication of powdered photocatalysts, such as poor morphological control and difficult disposal and regeneration of the exhausted photocatalyst. In order to overcome these limitations, several supported nanostructured photocatalysts have recently emerged as promising materials. In particular, one-dimensional (1D) nanostructures such as nanotubes and nanorods, allow for a much higher control of physico-chemical features[43,44] which lead to improved and more tunable photocatalytic properties. Even if these materials enable an enhanced charge carrier separation, the modification of such nanostructures should be performed to further increase the photocatalytic efficiency.

Doping TiO_2 with other elements such as non-metals (e.g. N, C, S)[45] and transition metals (e.g. Fe, Cr, Co)[46] is a widely used technique to shift the band-edges energy with the aim of extending the light harvesting to the visible light irradiation and enabling more redox reactions.

Instead, the construction of hetero-junctions with other semiconductors (e.g. WO_3, RuO_2, NiO or CdS) or with metals (e.g. Pt, Pd, Au) can significantly improve the electron transfer to reactants and the charge carrier separation[47,48]. Such effects cause a decrease of the charge recombination probability extending excitons life time and leading to increased efficiency. The choice of the proper semiconductor or metals needs a very good knowledge of the band alignments between TiO_2 and the second species in order to induce the charge carriers transfer in the desired direction.

After this brief introduction on TiO_2-based photocatalytic materials, a more detailed description about synthesis, properties, modifications and applications of TiO_2 nanotubes photocatalysts will be provided in the following chapter.

1.3.1.1. Titanium dioxide nanotubes (TiO_2 NTs)

The feasibility to grow TiO_2 nanotubes arrays with a high order level was reported for the first time in 1999[49] by performing a simple electrochemical anodization of a titanium metal sheet in optimized conditions. This discovery inspired many researchers to focus their work on the growth, modification, investigation of the properties, and application of these fascinating 1D nanostructures. The great interest in these materials is ascribed to their exceptional morphological and electronic properties, such as large specific area, quantum size effects, facilitated electron mobility, and even a very high mechanical strength[35,50].

These 1D TiO_2 nanostructures can be obtained by numerous routes including hydrothermal or solvothermal methods, sol–gel techniques, template-assisted approaches, and by electrochemical means[44,51–53].

Template-assisted and Ti precursor solution synthetic methods lead to the formation of single tubes or poor tubes agglomeration with a low-controlled length distribution. The formed tubes are suspended in the solution and so, they must be deposited on a conductive surface in order to use these nanostructures in electrical devices. The deposition process usually induces a random nanotubes orientation that eliminates many advantages of the 1D directionality typical of an ordered TiO_2 nanotubes layers. For this reason, the most used 1D TiO_2 nanostructures are anodically grown and self-organized TiO_2 nanotube layers.

A simple electrochemical oxidation of a titanium (metal) sheet substrate in an appropriate electrolyte, in fact, leads to the growth of perpendicularly aligned and well-defined TiO_2 nanotubes layer with a tunable and highly controllable geometry (in Figures 7 a-f are shown SEM images of different TiO_2 nanotubes obtained in different conditions). Moreover, it is not necessary to perform a deposition method to attach the tubes to a conductive surface since they are already attached to the metal surface (electrical contact). This method is extremely versatile and easy to scale up since it practically allows to coat with a uniform and dense nanotube layer any shape of titanium.

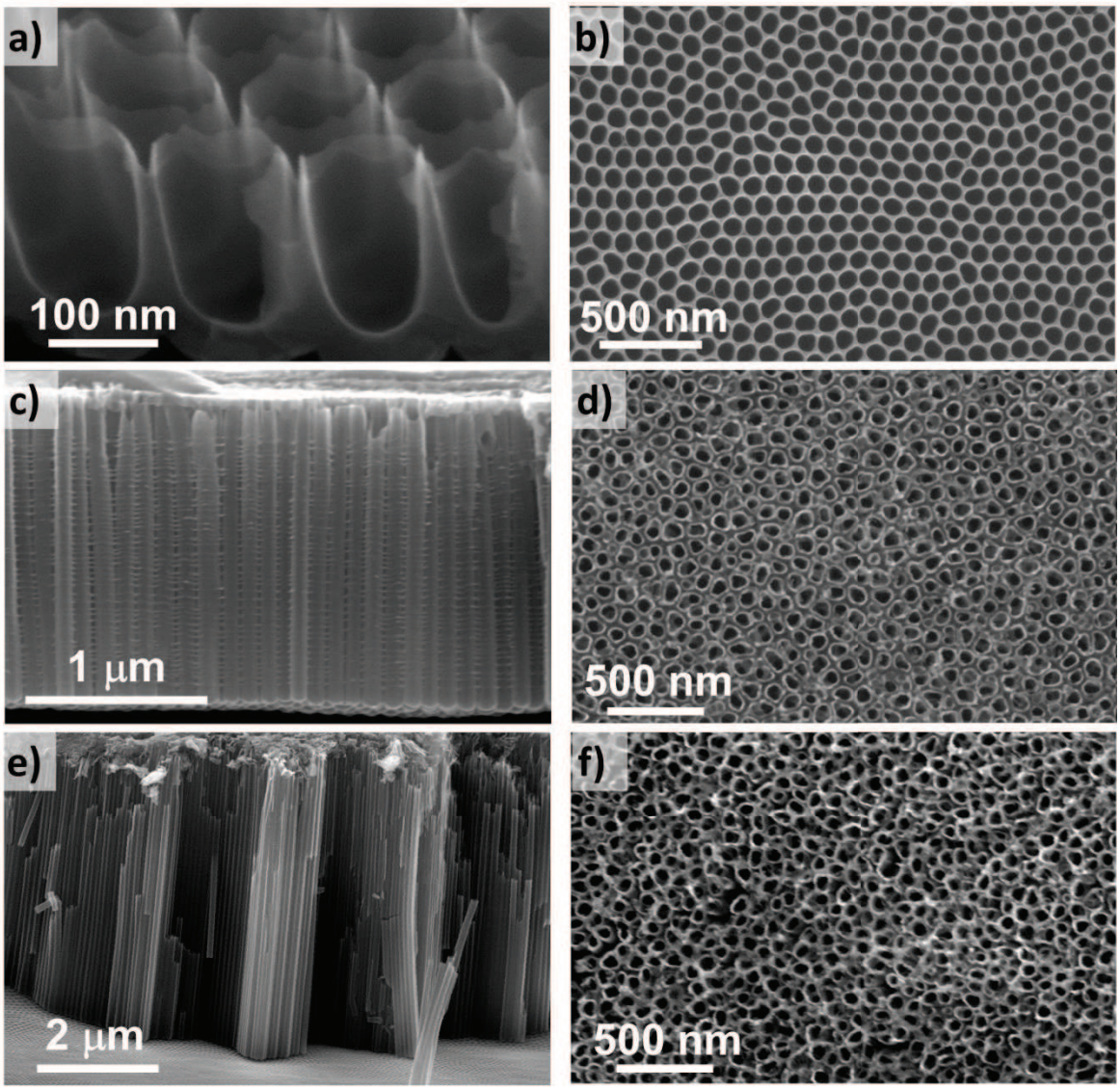

Figure 7. a) Cross-section and b) top view of TiO_2 nanotubes prepared in an H_3PO_4/HF electrolyte (nanotubes used for the works reported in this dissertation). c,d) Cross-sections and e,f) top views of nanotubes prepared in an electrolyte containing ethylene glycol and NH_4F using different anodization times.

The variation of anodization conditions (i.e. electrolyte, temperature, applied voltage and time of anodization) as shown in Figures 7 a-f, can lead to the formation of a wide variety of TiO_2 NTs with an internal diameter in the order of tens nanometers and a thickness in the range from hundreds nanometers to tens micrometers[54,55].

As mentioned above, the growth of TiO_2 nanotubes layers starting from a titanium substrate by electrochemical anodization was reported for the first time by Zwilling et al. in 1999[49]. The electrolyte used was a chromic acid solution containing a low concentration of hydrofluoric acid. It was demonstrated that the key of this process is the small addition of

fluoride ions. In fact, in absence of them, the formation of a compact TiO_2 layer occurs at the metal surface.

The idea to use fluoride for this purpose was born out of the observation, by Kelly et al. in 1979[56], that a low fluoride concentration can lead to the formation of porous TiO_2.

After Zwilling's findings, several different anodization conditions were explored in order to obtain a wide variety of TiO_2 nanotubes layers with improved morphology[57,58].

To understand the reason why a simple anodization can lead to a such high morphological control, in Figure 8 the anodization setup (Figure 8a), the growth mechanism (Figure 8b) and the steps of the anodic growth of TiO_2 nanotubes (Figure 8c) are reported in a schematic way to completely describe the mechanism of all the steps involved in this process.

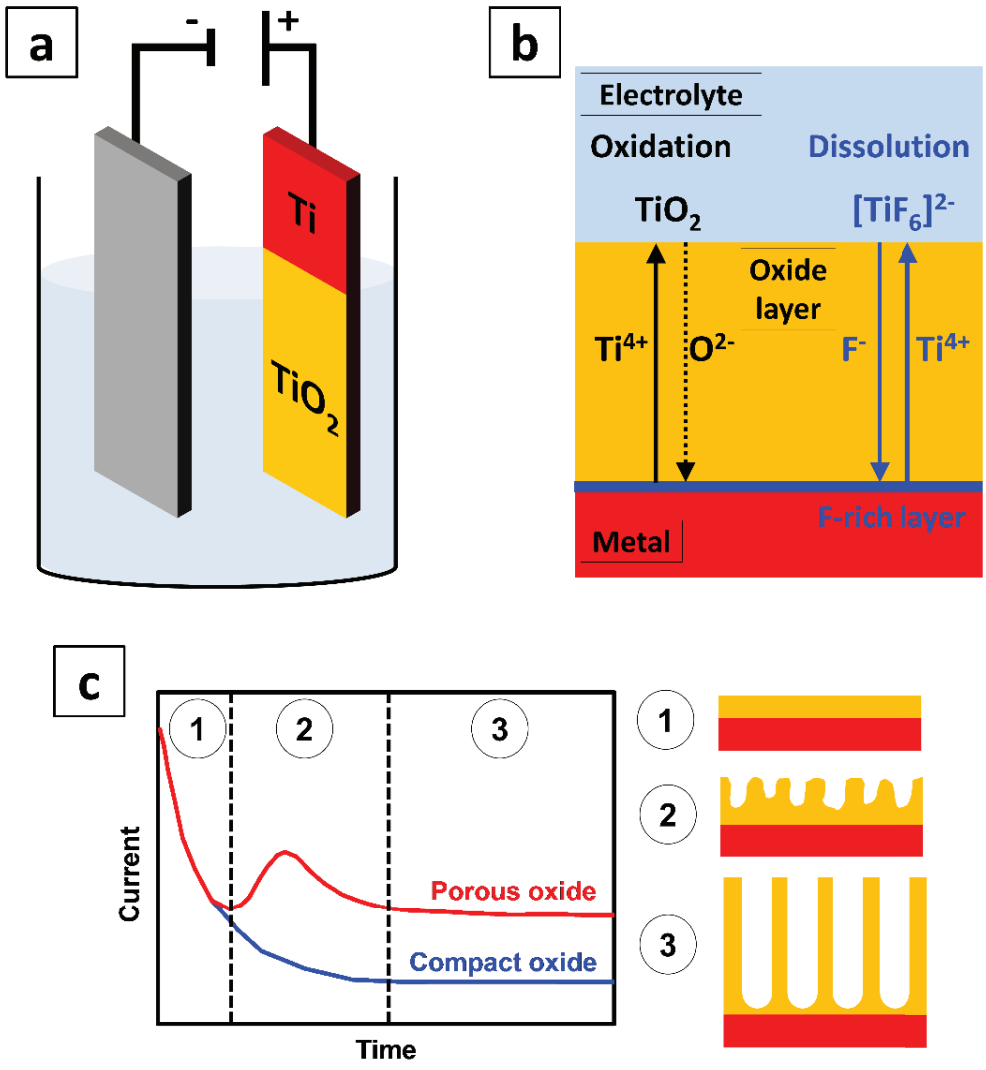

Figure 8. a) Schematic representation of the anodization process (the grey counter-electrode is commonly a platinum or graphite electrode). b) Mechanism of simultaneous anodic growth of the TiO_2 layer and dissolution by fluoride ions. c) Current versus time trends for the anodic growth of a compact and porous oxide layer. This last process can be divided into 3 steps (as discussed in detail here below).

When titanium is immersed in an electrolyte and it is exposed to a sufficiently high anodic (i.e. positive) voltage in a proper electrochemical configuration (see Figure 8a), an oxidation reaction (for a generic metal, $M \rightarrow M^{n+} + ne^-$) occurs.

The progress of this reaction can significantly change by varying synthetic conditions such as the electrolyte and anodization parameters. More in detail:

- If formed metal ions are strongly solvated by the solvent, the metal is constantly dissolved (corrosion or electropolishing of the metal);
- If metal ions react with O^{2-} and/or if the metal oxide cannot be dissolved in the solution, a compact oxide layer is formed.
- If there is a competition between the metal/metal oxide dissolution and the growth of an oxide layer, the formation of porous metal oxides can occur.

The latter case is the suitable situation for the growth of self-organized TiO_2 nanotubes layers. As reported in Figure 8b, in fact, the migration of the ionic species involved in the oxidation (Ti^{4+}, O^{2-}) and in the dissolution (Ti^{4+}, F^-) creates a competition between the growth of the oxide layer and titanium solubilization (Equations 4-9).

Oxidation reactions

$Ti \longrightarrow Ti^{4+} + 4e^-$ (Equation 4)

$Ti + 2H_2O \longrightarrow TiO_2 + 4H^+ + 4\,e^-$ (Equation 5)

$Ti^{4+} + 4H_2O \longrightarrow Ti(OH)_4 + 4H^+$ (Equation 6)

$Ti(OH)_4 \longrightarrow TiO_2 + 2H_2O$ (Equation 7)

Dissolution reactions

$Ti^{4+} + 6F^- \longrightarrow [TiF_6]^{2-}$ (Equation 8)

$TiO_2 + 6F^- \xrightarrow{H^+} [TiF_6]^{2-} + 2H_2O$ (Equation 9)

If on one hand, the oxidation leads to the growth of new oxide, on the other hand, the reaction between Ti^{4+} and fluoride ions can immediately occur to form the soluble species $[TiF_6]^{2-}$. Since the dissolution is a very aggressive process, in the presence of a too high fluoride concentration (over ~ 1 wt.%) no oxide formation can be observed (i.e. complete dissolution of TiO_2). Instead, for lower fluoride levels, the formation of porous TiO_2 or TiO_2 nanotube can be observed.

The growth of TiO_2 nanotubes can be also checked by recording in real time the typical current vs. time plot (Figure 8c). In this graph, it is possible to identify three different trends of the current which correspond to three different phases occurring during the formation of TiO_2 nanotubes.

- Step 1: Compact oxide layer formation: it causes a continuous decrease of the current.
- Step 2: Formation of irregular nanosized pores with partial penetration of the formed compact oxide layer: it causes an increase of the current.
- Step 3: Formation of a regular nanotubes layer. The tubes can continue to grow under steady-current conditions due to the competition between the etching at the top (action of fluorides) and the tube formation at the bottom. Under this steady-state situation, the thickness of the tubes is linearly dependent on the anodization time. At some point, an equilibrium between the formation of the oxide layer and its solubilization is reached.

In view of this last explanation, the tube length can be controlled by the anodization time and etching rate (i.e. fluoride concentration), while the diameter of the nanotubes is linearly dependent on the applied voltage[59–61].

The electrochemical anodization is commonly performed by applying a constant voltage (which can be reached by a single potential step or a ramp) in the range 1–30 V in aqueous electrolyte or by applying a higher voltage (5–150 V) in non-aqueous electrolytes containing around 0.1–1 wt.% fluoride ions. In these electrolytes can be added other ion species to dope the material or to induce particular morphologies and properties. Some typical morphologies which can be obtained using different electrolytes are shown in Figures 7a-f. The main difference between these solutions is their conductivity. In fact, organic electrolytes have a lower conductivity and consequently, a different IR-drop effect[62,63]. This is the reason why the employment of organic solutions can lead to the growth of nanotubes of several micrometers.

Another key factor that influences the formation of these nanostructures is the different size and migration rate of fluoride ions and O^{2-}. In fact, since F^- is smaller than O^{2-}, the migration rate of fluoride ions towards the bottom of the TiO_2 nanotubes is almost twice the

O^{2-} one[43,64,65]. Consequently, as reported in Figure 8b, a fluoride-rich layer is usually formed at the Ti/TiO_2 interface.

Independently by the employed anodization conditions, as-formed TiO_2 nanotubes layers can be modified by i) heat treatments, ii) introducing foreign elements (doping), or iii) creating hetero-junctions at the oxide surface. The aim of these treatments is to improve (photo)chemical, optical and electronic properties of the material in order to fabricate a more efficient system for a wide variety of applications.

First of all, since the as-prepared TiO_2 nanostructures are amorphous a thermal treatment is necessary to convert the amorphous phase to anatase or rutile[66,67]. This process can be carried out under oxidizing, inert or even reducing conditions (using gases such as air, O_2, Ar, N_2, H_2 or a mixture of these) at temperatures in the range 250-700°C. The annealing process has an important effect on electronic and surface properties since it leads to a significant change in conductivity, life-time of charge carriers and surface energy. This last parameter is strictly dependent on the number of uncoordinated Ti cation sites (fourfold- or fivefold-coordination). Less coordinated center, in fact, has higher surface energy and the global surface energy rises with the number of uncoordinated (fourfold coordination) centers. Anatase crystals surface energy is generally lower compared to the one of rutile crystals, while the stress energy exhibits the opposite behavior.

XRD studies revealed that anatase crystals start to appear at ~ 280°C and that the increase of the annealing temperature leads to an improved anatase formation[68]. Instead, above ~ 500°C rutile crystals can be formed directly from amorphous TiO_2 or from converted anatase crystals. The duration of the thermal treatment and the temperature ramp can significantly influence crystallographic properties and composition of TiO_2 nanotubes (e.g. phases, crystallite size). Additionally, the presence of dopants or co-catalysts is reported to have an important effect on the crystallization process. Some elements such as Nb, Al and Ni can retard the growth of TiO_2 crystallites and the anatase-to-rutile conversion[69,70]. Instead, other elements, among which Mn, Fe and Cu, are able to promote and accelerate the crystallization process.

Regarding the doping process, in the last 15-20 years a lot of effort was directed to introduce a foreign electronically active element into TiO_2 lattice. The doping process can have significant effects on the band-structure of TiO_2 which can be exploited to cause a decrease of the onset energy for light absorption (extending light absorption to the visible light region). This is a fundamental feature for solar light-driven photocatalytic applications.

The first band-structure modification through a doping process dates back to 2001[71]. In this case, the mixing of the nitrogen p states with the O 2p states led to a rise of the VB level, and thus, a decrease of the energy band gap. After this discovery, several doping elements were investigated to activate a photo-response to visible light, including transition metals (e.g. V, Cr)[72,73] and non-metals (e.g. C, S)[74–76].

The most common ways to dope TiO_2 NTs are: i) treatment of as-formed TiO_2 nanostructures with a solution containing the dopant or its precursor (e.g. hydrothermal or sol-gel processes)[77,78]; ii) thermal treatment (annealing) in the presence of a gas containing the doping species (e.g. Nitrogen doping using NH_3)[79,80]; iii) co-sputtering or sputtering in a dopant-containing atmosphere[45]; iv) implantation of high energy ion[81]; v) electrochemical anodization of an alloy substrate or incorporation of doping species from electrolyte. The last method is peculiar for anodically grown nanotubes since a metal doping can be easily carried out by creating an alloy substrate (TiX) and then to electrochemically grow a TiX nanotubes array (in which X is the metal dopant).

Another successful way to modify as-formed TiO_2 NTs is the decoration of their top, side-walls and/or bottom with metals, metal oxide semiconductors or polymers nanoparticles (usually of size lower than ~ 100 nm in order to avoid a shadow effect, see nanotubes diameter). This approach was already well-established for bulk and powdered TiO_2 NPs and it involves the creation of a solid-state heterojunction which, if properly designed, can lead to significant beneficial catalytic effects: i) changes in the band bending which can promote charge transfer processes (e.g. Pt for H_2 evolution); ii) surface plasmon effects which can further increase the charge transfer efficiency in proximity of metal NPs; iii) creation of new (photo)catalytic sites.

Special attention should be paid to identify a metal oxide (M_xO_y) semiconductor having a suitable band alignment with TiO_2 bands in order to design an efficient Schottky-type junction. An appropriate band alignment, in fact, can lead to a more efficient charge separation due to charge carriers transfer from TiO_2 to M_xO_y (or vice versa). From the observation of the energy band levels of some of the most employed photocatalysts (in Figure 5), a particularly interesting combination could be represented by TiO_2 and WO_3[82–84]. WO_3 is an n-type semiconductor with E_g ~ 2.8 eV (i.e. ~ 450 nm) [85,86] and, in the literature, several advantages are reported for such combination. The favorable band alignment (i.e. CB_{WO3} more positive than CB_{TiO2}) at the metal oxides interface enables an efficient electron transfer from the CB of TiO_2 to the CB of WO_3.[82,87–89] Additionally, the deposited WO_3 layer can contribute to the enhancement of the photocatalytic performances also through an increased

photo-response under visible light irradiation. The decorating metal oxide, in fact, is in turn a semiconductor photocatalyst and as such can improve the global photon harvesting[90,91]. Other surface properties are related to the decoration with tungsten trioxide such as surface acidity[83,92–96] and hydrophilicity[97] which can strongly influence the reactants adsorption/products desorption process.

Besides the metal oxide decoration of TiO_2 NTs, the formation of a Schottky-type heterojunction with noble metal nanoparticles (e.g. Au, Pt, Pd NPs) at the TiO_2 surface is reported to be extremely beneficial for photocatalytic processes[98,99]. An enhanced electron transfer at the photocatalyst/electrolyte interface, in fact, is enabled thanks to the formation of such favorable solid-state junction to TiO_2. This improvement is essentially related to the relative position of the work function of the noble metal and the TiO_2 energy bands[100]. The formation of such a contact barrier has great influence on the migration and lifetime of the photo-generated charge carriers. The most employed and efficient noble metal co-catalyst is undoubtedly Pt, mostly for the H_2 generation reaction[101–104]. This metal is commonly preferred not only for its favorable electronic structure, but also for its pure catalytic properties (catalysis of hydrogen atom recombination)[105,106]. However, the high cost of noble metals has recently shifted the attention to low-cost alternative co-catalysts such as non-noble metals (e.g. Ni and Cu). The principle of action is the same reported for noble metal co-catalysts but the photocatalytic performances obtained using non-noble metals are typically much lower than the ones achieved by Pt-decorated TiO_2 NTs under comparable deposition conditions[107–111]. To further improve the photocatalytic activity, it is possible to use metal alloy NPs as co-catalysts (e.g. Ni-Cu, Au-Pd). The decoration with these species can lead to significantly higher performances compared to the ones obtained with a single metal co-catalyst thanks to enhanced surface properties (i.e. different adsorption/desorption of species) and a favorable shift of the work function (from theoretical calculations the new work function is a linear combination of the work functions of the two metals present in the alloy)[112–114].

Additionally, metals and metal oxides can be combined into composite materials (i.e. TiO_2-M_xO_y-M or TiO_2-M-M_xO_y) in order to achieve higher efficiency exploiting both the beneficial effects provided by these co-catalysts (i.e. charge separation with metal oxides and electron transfer with metals). In recent studies, TiO_2-WO_3-noble metal (Au, Pt) powders were investigated in view of their photocatalytic performance[115–118]. The outcomes of these works proved that such a combination is particularly advantageous in terms of photocatalytic efficiency.

Several techniques for the decoration of TiO_2 nanotubes with metal and metal oxides have been reported in the literature such as i) electrodeposition (e.g. p-n heterojunctions, Cu_2O-TiO_2)[119], ii) photocatalytic reduction (e.g. Ag reducing Ag^+ by UV illumination), iii) ultra-high vacuum (UHV) evaporation, iv) chemical or physical vapor deposition (CVD or PVD) and v) sputtering or co-sputtering deposition.

In any case, a high control over the morphology and the proper stacking of co-catalysts (in particular in the case of composite materials TiO_2-M_xO_y-M or TiO_2-M-M_xO_y) are fundamental to achieve the desired electron cascade transfer from the photoactive substrate (TiO_2) to co-catalysts and reactants.

In this context, solid-state templated-dewetting is emerging as a promising technique to decorate with a fine control TiO_2 NTs with small sized NPs[120,121]. For virtually any M-TiO_2 combinations, after the deposition of a thin metal layer (up to few tens of nm) by any classic method (e.g. CVD, PVD, evaporation, sputtering), a thermal treatment at sufficiently high temperature (as a general rule around half the metal's melting point) is performed in order to cause the breakup of the metal layer into patches and then into individual nanoparticles. As an additional effect, the heat treatment lead also to the crystallization of TiO_2.

The "dewetting", in few words the formation of metal "islands" starting from a thin conformal layer (Figures 9a and 9b), is a process that occurs in the solid state and it allows for a fine morphological control with nanoscopic precision (i.e. predictable and narrow size distribution and site selective placement), mostly when the metal layer is deposited on a highly ordered and periodic substrate such as self-organized TiO_2 NTs (templated-dewetting).

The solid-state dewetting mechanism involves the creation of holes in the thin metallic film (preferentially at specific defects) and the retraction of the film from the edges of the holes. After the holes formation, the dewetting process spontaneously proceeds driven by capillary forces and surface curvature that lead to the formation of isolated metal NPs. The initiation of this mechanism (formation of holes) is probably the most important step of this thermally-driven process and it is strongly influenced by the deposition method employed. In fact, it is known that layers deposited by sputtering and evaporation provide a higher inhomogeneity and surface defectivity degree and it is also known that the dewetting process preferentially initiates from intrinsic defects present on the thin metal film.

Besides the metal deposition technique, there are other parameters which can play an important role in controlling the entire dewetting process: i) working temperature, ii) metal film thickness, iii) metal/substrate couple, iv) surface and capillary energy and v) crystallographic features.

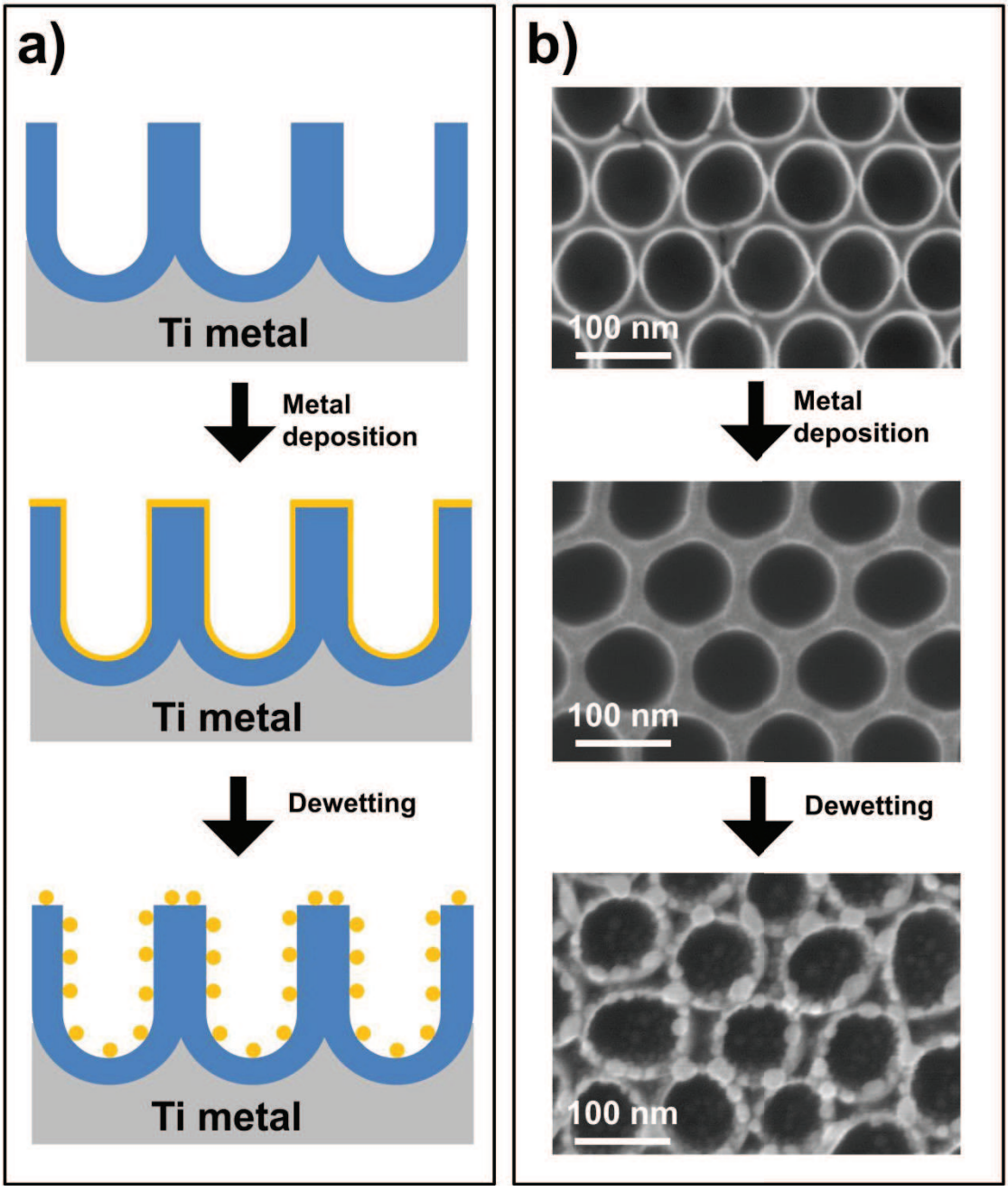

Figure 9. a) Schematic representation and b) SEM images of the steps involved in the solid-state templated dewetting process on TiO_2 nanotubes.

Considering that the key of this process is the metal atoms surface mobility and that this parameter exponentially increases with increasing temperature, the dewetting temperature (T_d) significantly affects the dewetting kinetic. Since the process occurs in solid-state, the working temperature is necessarily lower than the metal's melting point. From experimental observation, T_d was found to be between 0.3 (Huttig temperature) and 0.5 (Tammann temperature) times the melting point of the metal. The first one (T_{Huttig}) is the temperature at which metal atoms at defects become mobile, while the Tammann temperature concerns the

atoms diffusion in the bulk metals[122]. For instance, Au has a lower melting point (1064°C) compared to Pt (1768°C), meaning that a lower temperature is required to induce surface diffusion and dewetting for Au[121]. Additionally, since the dewetting process involves the surface diffusion of metal atoms, if two (or more) metals are deposited on the same substrate the complete or partial formation of alloys can occur.

Besides the working temperature, the nature of the metal can pose a limitation to the choice of the heat treatment environment. A thermal treatment under inert or even reductive conditions, in fact, is usually preferred when the metal is easily oxidizable[102,123,124]. The metal oxide formation (if not desired) should be avoided since it may limit surface diffusion and, hence, it may partially hinder defined dewetting[125].

T_d is also strictly related to the metal film thickness (T_d decreases with film thickness). This relationship can be ascribed to the inverse variation of the density of holes with the film thickness[126,127]. In other words, to initiate the breakup of a thinner metal film it is necessary to overcome a lower energy barrier[121,126]. The energy barrier for the dewetting of a very thin (~1 nm) layer can become so low that the dewetting process can even occur at room temperature[120].

Moreover, dewetting on corrugated surfaces usually takes place at lower temperatures compared to flat substrates. The employment of a periodic surface as a substrate can lead to the formation of size-controlled and site-selectively placed metal NPs. For this reason, highly-ordered TiO_2 nanotubes arrays are considered as ideal surfaces for template-guided solid-state dewetting of thin metal films. If metal layers of equal thickness are deposited on self-organized anodic TiO_2 NTs and a flat TiO_2 surface, the dewetted metal NPs (and their particle-to-particle distance) are much smaller in the first case and they are also almost monodisperse in size (see an example in Figure 10).

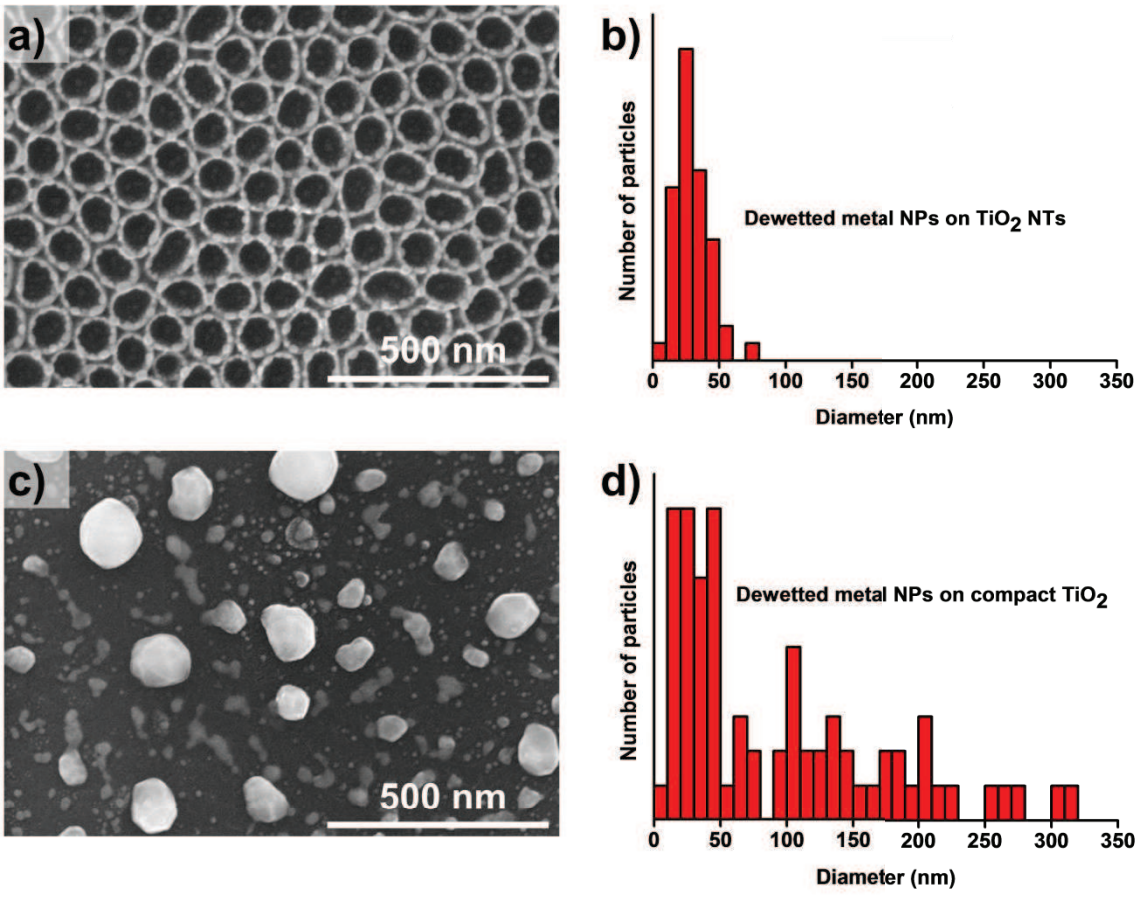

Figure 10. a) SEM top view of dewetted metal NPs on TiO_2 NTs and b) their size distribution. c) SEM top view of dewetted metal NPs (starting from an equally thick metallic layer) on a compact TiO_2 layer and d) their size distribution.

Finally, it is possible to calibrate the thickness of the deposited metal layer and the deposition configuration (e.g. angle of the substrate during sputtering deposition) with the respect to the topographical features and geometry of the nanocavities in order to control with nanoscopic precision the dewetting process in terms of NPs size and their relative placement.

Since the structures resulting from a sputtering/dewetting approach have fascinating features and functionalities, this decoration method was employed in the works reported in this thesis on highly-ordered anodic TiO_2 NTs to fabricate efficient photocatalytic materials both for hydrogen evolution and inorganic mercury removal from water.

1.3.2. Hematite (α-Fe_2O_3)

Iron oxides can be found in different crystalline and stoichiometric structures, among which magnetite (Fe_3O_4), wüstite (FeO), maghemite (ν-Fe_2O_3) and hematite (α-Fe_2O_3).

The most stable form of iron oxide at ambient conditions is α-Fe_2O_3 that, as shown in Figure 11a, is a hexagonal crystal system consisting of Fe atoms surrounded by six O atoms.

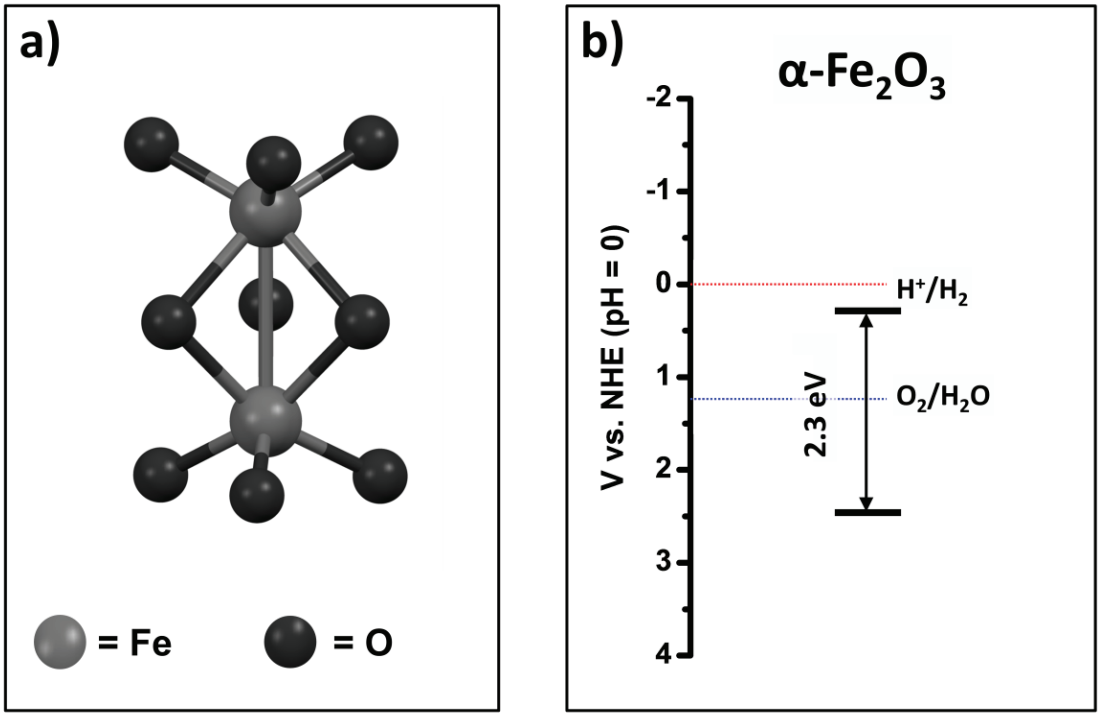

Figure 11. a) Hematite crystal structure and b) its energy band situation.

Hematite is weakly ferromagnetic at room temperature, while at temperatures below 260 K it is antiferromagnetic. Nevertheless, the magnetic properties of hematite do not play an important role in its photoelectrochemical properties, the Fe spin configuration affects its optoelectronic and charge carrier transport properties of hematite.

The light absorption by α-Fe_2O_3 starts with weak absorption bands in the near-infrared (NIR) region caused by transition states electron between two d orbital energy levels of the Fe^{3+} ion, which are split by an intrinsic crystal field[128].

This metal oxide is an earth-abundant, non-toxic, low-cost and stable in most aqueous solutions (pH ≥ 3) n-type semiconductor which finds wide application in many fields such as photocatalysis[129,130], gas sensors[131,132], lithium-ion batteries[133] and water treatment[134].

The narrow band gap value of α-Fe_2O_3 (2.3 eV) and its favorable VB edge position (considerably more positive than water oxidation potential, see Figure 11b) make this material a promising photoanode for photoelectrochemical (PEC) water splitting.

As mentioned in Chapter 1.3, there are many semiconductor metal oxides which exhibit photocatalytic activity, but, most of these have an absorption edge only in the UV region which largely limits the exploiting of most of the solar light spectrum. In this context, hematite is a very interesting material since it can absorb visible photons up to ~550 nm, collecting up to 40% of the solar spectrum. Thanks to its narrow band gap value, hematite can exhibit a theoretical photocurrent density of ~12.5 mA cm^{-2} under Air Mass Filter 1.5G solar irradiation (AM 1.5G) with a theoretical solar-to-hydrogen (STH) efficiency of ~ 15.5%[135] in an ideal PEC cell[136,137], that matches the requirements for practical applications[138].

The theoretical STH efficiency (η_{STH}) can be calculated as shown in Equation 10[139].

$$\eta_{STH} = J\,(1.23V - \eta) / P_{in} \qquad \text{(Equation 10)}$$

In which:

- J is the current density of the cell;
- 1.23 V is the Nernstian potential difference for the conversion of H_2O to H_2 and $½O_2$ under standard conditions;
- η is the additional overpotential to be applied to generate the current density J;
- P_{in} is the incident light power density (commonly 100 mW cm^{-2}).

However, unfavorable properties of hematite such as high charge carrier recombination rate, very short diffusion of holes (~ 4 nm) and poor conductivity lead to low efficiency and large demanded overpotential for PEC water oxidation[140,141]. In order to overcome these limitations, many attempts have been made by researchers in the last years. The formation of α-Fe_2O_3 nanostructures was recently explored to decrease the recombination rate while doping with appropriate metals was employed to improve the charge transfer ability and enhance the conductivity of the material[142].

The great interest over this material and its applications derives from the fact that PEC water splitting intermediates and products can be exploited for the elimination (generally through oxidative mechanism) of organic or inorganic pollutants from water. The reactions

induced by photo-stimulated α-Fe_2O_3 in water during the degradation of an organic red dye (Congo Red) were investigated in detail by Sundaramurthy et al.[143].

Electrons and holes generated by irradiating hematite (Equation 11) can induce several reactions which are briefly summarized in the following Equations 12-15.

$$\alpha\text{-}Fe_2O_3 + h\nu \longrightarrow \alpha\text{-}Fe_2O_3\ (e_{CB}^- + h_{VB}^+) \qquad \text{(Equation 11)}$$

$$e_{CB}^- + O_2 \longrightarrow O_2^{\bullet -} \qquad \text{(Equation 12)}$$

$$O_2^{\bullet -} + H^+ \longrightarrow HO_2^{\bullet} \qquad \text{(Equation 13)}$$

$$HO_2^{\bullet} + HO_2^{\bullet} \longleftrightarrow H_2O_2 + O_2 \qquad \text{(Equation 14)}$$

$$h_{VB}^+ + OH^- \longrightarrow OH^{\bullet -} \qquad \text{(Equation 15)}$$

First of all, photo-generated electrons can produce super-oxide radicals ($O_2^{\bullet -}$) by reacting with chemisorbed oxygen on the semiconductor surface (Equation 12). The intermediate super-oxide radicals produced can react with hydrogen ions (H^+) forming hydroperoxyl radicals ($HO_2^{\bullet}$) (Equation 13) and then H_2O_2 can be formed from the coupling reaction between hydroperoxyl radicals (Equation 14). Finally, hydroxyl ions (OH^-) on the surface of the catalyst can react with photogenerated holes (h_{VB}^+) to produce $OH^{\bullet -}$. (Equation 15)

These radicals and intermediate species are very reactive towards organic and inorganic compounds (e.g. pollutants in water) and they can degrade these molecules or produce other species with different properties (e.g. less or non-toxic species).

Given the fundamental impact of these photo-activated processes, researchers have spent a lot of efforts in the production of nano-scaled hematite with enhanced photocatalytic properties.

Nanocrystalline hematite can be prepared as powdered photocatalyst or as a thin film deposited on a conductive support (e.g. Fluorine doped tin oxide-coated glass, FTO-coating).

Many methods to synthesize different forms of nanocrystalline powdered α-Fe_2O_3 are reported in the literature, including hydrothermal methods[144,145], solvothermal methods[146], co-precipitation[147], hydrolysis[148], ionic liquid assisted synthesis[149], thermal decomposition[150] and combustion methods[151].

Instead, the fabrication of supported hematite films can be carried out by atmospheric pressure chemical vapor deposition (APCVD)[152], thermal evaporation[153], electrodeposition[154,155], spin coating [156] and solution methods[135,157].

Since composition, porosity, crystallite size and specific surface area of the material play a key role in the electronic and surface properties, several modified α-Fe_2O_3 nanostructures were investigated in view of their photocatalytic activity. Recent works have proved that the small carrier harvesting depth of hematite can be enhanced by producing highly photoactive nanostructured α-Fe_2O_3 morphologies. Most of the photo-generated charge carriers, in fact, vanish due to recombination using a thick planar hematite layer and, consequently, the photocurrent produced by this kind of material is negligible. For this reason, several interesting nanostructured α-Fe_2O_3 forms have been recently investigated in view of their photocatalytic activity. Among these systems are included nanoplatets[158], nanospindles[159], nanofibers[160], nanocubes[159], nanoworm-like structures[135,157], nanorods[159] and nanotubes[161]. These high aspect ratios structures with large specific surface area are able to enhance charge carrier collection by shortening their mean pathway and, thus, decreasing recombination losses at grain boundaries[162]. Further detailed investigation of the photocatalytic properties of 1D and ultrathin film nanostructures[163] revealed that it is possible to achieve better photo-response using 1D nanostructured electrode.

As previously reported for TiO_2, charge separation and transfer properties of hematite can be improved in several other ways. In particular, the electronic properties of α-Fe_2O_3 can be enhanced by doping (increasing donor density[46,141]) with metals (e.g. Pt[164], Al[165], Au[166], Ti[167]) or anionic materials (e.g. Fluorine and nitrogen[168]). The improvement of the photocatalytic activity by forming metal-α-Fe_2O_3 nanostructures is due to: i) modification of the crystal structure and surface properties, ii) increase of the charge separation with increased surface metal atoms, iii) enhanced interactions between reactants and photocatalyst surface, and iv) concentration of the light energy at the near hematite surface thanks to the presence of metal nanostructures which can act as optical antenna[129]. Instead, doping hematite with elements like fluorine (F) and nitrogen (N)[168] can increase the photocatalytic activity by introducing an additional acceptor level, which leads to an improvement of the charge separation and a decrease of the recombination rate. The modification in the band alignment due to N-doping of hematite can also allow to approach the hydrogen evolution level, thus enabling pure photocatalytic H_2 production (as shown in Figure 11b the CB edge position of unmodified hematite makes this reaction thermodynamically infeasible).

Other promising strategies to enhance the photocatalytic performance of hematite are the loading of a metal/metal oxide co-catalyst on the α-Fe_2O_3 surface[169] or the formation of a hetero-junction with a suitable semiconductor[170].

The aim of loading a co-catalyst on the semiconductor surface is the enhancement of the oxygen evolution reaction (OER) by accommodating excited charge carriers and improving redox reaction kinetics. One of the most common catalytic mechanism of action is the oxidation of the metallic element of the co-catalyst which can significantly promote hole transport from the α-Fe_2O_3 surface to the reactants. Noble metal oxides like RuO_x[171] and IrO_x[172] were widely investigated as water oxidation co-catalysts. In particular, iridium oxide is considered one of the best co-catalysts for this application, but its high cost represents a major limitation. For this reason, the attention of researchers was recently shifted on earth abundant, low-cost and non-noble metal-based co-catalysts. Co-based (e.g. cobalt hydroxides, cobalt oxide and cobalt phosphate)[173–175] and Ni-based (e.g. nickel oxide, nickel hydroxide, and nickel borate)[173,176] catalysts have attracted a lot of interest thanks to their high turnover frequency (TOF), high stability, low toxicity, low cost and efficient catalytic performance.

Even if no catalytic sites are introduced, the deposition of non-catalytic semiconductor material layers (e.g. 13-group oxides such as Al_2O_3, Ga_2O_3, or In_2O_3) on the hematite surface can influence OER performance by enhancing the charge carrier transfer[177]. This modification can lead to a decrease of the overpotential for PEC water splitting and a significant increase of the produced photocurrent.

Besides these co-catalysts, other semiconductor materials such as TiO_2, WO_3 and $BiVO_4$ have been reported to improve the PEC performance of the hematite photoanode. Their suitable band edge positions can facilitate the transfer of photo-generated electrons reducing the recombination rate (as previously reported for hetero-junctions with titanium dioxide).

Finally, other methods to reduce the onset potential and increase the photocurrent are H_2 treatment and surface corrosion by HCl. In the first case, the improvement of the photocurrent may be ascribed to an increase of the surface oxygen vacancies, while the enhancement induced by surface corrosion of hematite is due to a change of the surface chemical state of the photoanode.

In conclusion, hematite photoanodes can find application for a wide range of purposes such as PEC water splitting, degradation of organic and inorganic compounds[129]. The main advantage deriving by the employment of this material is the efficient exploiting of the solar-simulated light irradiation.

Since hematite exhibits also very good adsorptive capability towards several species, among which arsenic compounds[178–184], the feasibility of the PEC oxidation of As(III) to

As(V) over nanostructured worm-like α-Fe_2O_3/FTO photoanodes was investigated in detail during this Ph.D. and the outcomes and related discussion will be reported in this dissertation.

1.4. Overview of photocatalytic applications

The sustainable progress of human society has gained much more attention in the last decades and several efforts have been directed to the development of new alternative clean energy supplies and "green" environmental remediation for pollution.

In this context, semiconductor photocatalysis has emerged as one of the most promising approaches to convert renewable energy (e.g. natural sunlight or artificial UV or visible irradiation) to more useful energy (e.g. chemical energy).

A fundamental requirement for large scale environmental applications is a high efficiency under solar light irradiation. Thus, in order to simulate the behavior of a photocatalyst under such illumination, the sunlight spectrum has to be modeled and standardized with the aim of reproducing it with bench-top instrumentation (solar simulator) for small scale and lab applications.

The sun is conventionally modeled as a ~ 6000K blackbody radiator[185] (see Figure 12b) with an intensity of 1366.1 W m^{-2} at the border of Earth's atmosphere[186]. However, scattering and absorption of the radiation by suspended particulates and molecules such as ozone (O_3), H_2O and CO_2 attenuate the sun light intensity. This attenuation strongly depends on the light path length through the atmosphere and on several atmospheric parameters (e.g. humidity, pressure). Thus, the resulting spectrum reaching the Earth's surface is a function of all these parameters.

To define the solar spectrum is commonly employed the air mass (AM) notation that is defined as follows:

$$AM = L / L_0 \approx 1 / \cos(z) \qquad \text{(Equation 16)}$$

In which:

- L is the path length of the radiation through the atmosphere;
- L_0 is the zenith path length (i.e. perpendicular to the Earth's surface) of the radiation at the sea level;
- z is the angle (in degrees) between the vector normal to the Earth's surface and the vector towards the sun (see Figure 12a).

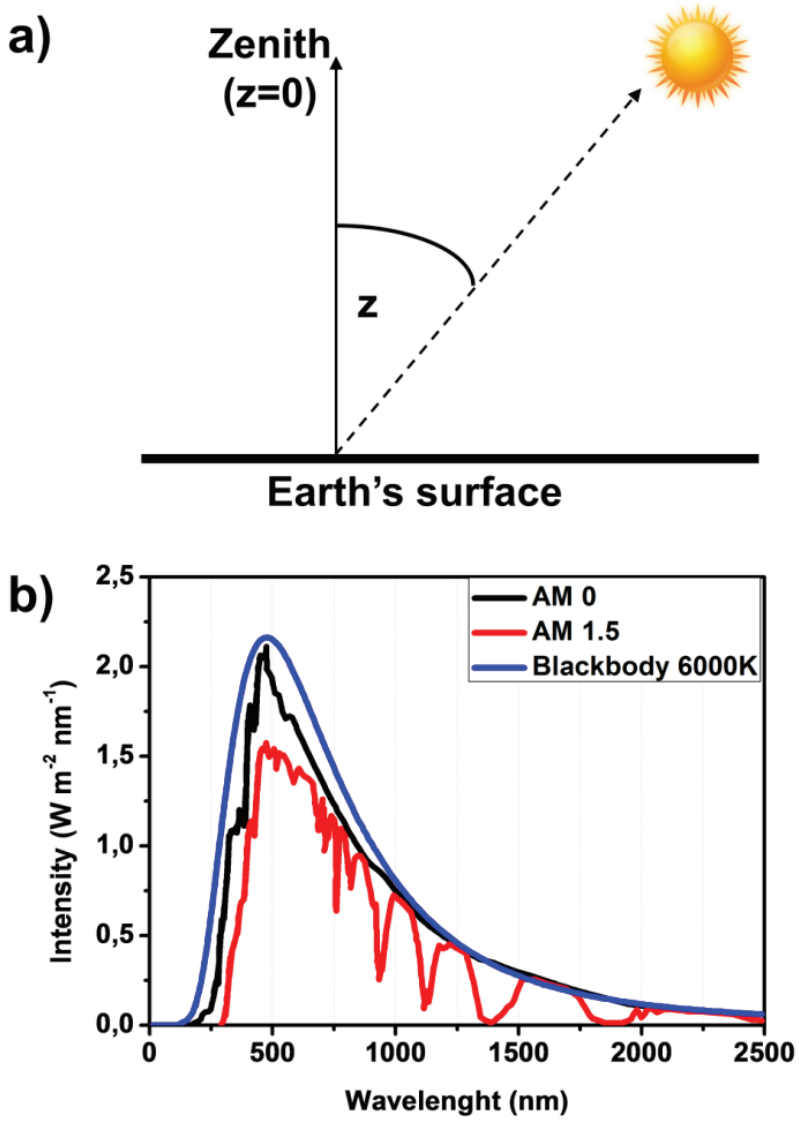

Figure 12. a) Schematic representation of the estimation of the Zenith angle and b) emission spectra for a blackbody at 6000K (blue), AM 0 irradiation (black) and AM 1.5 irradiation (red).

Since the AM number depends on the angle "z" and on the radiation path length, it depends on the latitude of the observer, time of day and seasons of the year. Using this notation, AM 0 is defined as the spectrum outside the atmosphere (L = 0) and AM 1 is defined as the solar spectrum at the sea level when the sun is normal to Earth's surface (i.e. $L=L_0$).

From 1977, AM 1.5 (z = 48.2°) was chosen to be the reference standard spectrum for photovoltaic and photocatalytic applications[186]. Thus, solar simulators are commonly equipped with a 1.5 AM filter which reproduces this standard spectral distribution (see Figure 12b). The total irradiance can be tuned and chosen depending on application needs, but for

photocatalytic purposes, it is conventionally adopted a power density of 100 mW cm^{-2} (defined as 1 Sun).

Unfortunately, this solar light source is often incompatible with some of the most employed photocatalyst (e.g. TiO_2) since in the absence of suitable modifications they are photo-active only under UV irradiation (i.e. small portion of the solar spectrum). Therefore, besides the employment of solar simulators as light sources, Light Emitting Diodes (LEDs) and Lasers find wide application, especially for UV-driven photocatalytic applications.

Regardless of the light source employed, photocatalysis advantages such as simplicity, cost-effectiveness and high flexibility of application make this technique a most interesting field of research.

In particular, semiconductor photocatalysis finds application for a very extensive range of purposes such as the production of clean energy (e.g. photocatalytic water splitting)[21], removal of various organic and inorganic pollutants in natural water[22,23], purification of air[24] and antibacterial activity[25]

Since photocatalytic hydrogen evolution from water/ethanol mixtures and highly toxic inorganic pollutants removal (inorganic arsenic and mercury species) from water were investigated in this thesis, principles and the current state-of-art of these fields of application will be described in the following chapters.

1.4.1. Photocatalytic hydrogen evolution and PEC water splitting

Since the ground-breaking work of Fujishima and Honda[8] in 1972, the H_2 generation by photocatalytic water splitting on semiconductor materials has been widely investigated by researchers. Around twenty-five years later, in 1998, Khaselev and Turner[187] proved a PEC STH efficiency of 12.4%, demonstrating the great potential of the combination of the harvesting of solar energy and the electrolysis of water in a single device.

Photocatalytic (or PEC) decomposition of water is a complex and powerful process that needs several requirements to be efficiently and sustainably carried out: i) the semiconductor must absorb a significant portion of the solar spectrum (see energy band gap value), ii) the band edge levels must be suitable for both hydrogen and oxygen generation, iii) the photocatalytic material should have long-term stability against corrosion and photo-corrosion in water, and finally iv) it is necessary an efficient charge transfer from the semiconductor surface to reactants to minimize energy losses.

Unfortunately, up to now, no cost-effective photocatalytic materials meet all these requirements for practical large-scale H_2 production from water.

In order to compare photo(electro)catalytic water splitting performances obtained by different materials, it is fundamental to find a conventional definition of the efficiency for this process. The definition of the photocatalytic efficiency is one of the most discussed topics in this field of research since it can be estimated primarily in four ways (divided into two categories):

- Benchmark efficiency definition (to define the water splitting capability):
    - solar-to-hydrogen conversion efficiency (STH).
- Diagnostic efficiency definitions (to define materials performance):
    - applied bias photon-to-current efficiency (ABPE);
    - incident photon-to-current efficiency (IPCE);
    - absorbed photon-to-current efficiency (APCE).

Among these definitions, STH and IPCE are undoubtedly the most common and used estimation of the efficiency.

More in detail, STH efficiency is defined as the ratio between the chemical energy of the H_2 produced and the radiative energy input from incident sunlight.

The chemical energy of the hydrogen produced can be calculated as follows:

$$E_{H_2} = (mmol_{H_2\ produced}/s) * \Delta G^0_{H_2} \quad \text{(Equation 17)}$$

In which:

- $(mmol_{H_2\ produced}/s)$ → rate of H_2 production
- ΔG^0 → Gibbs free energy per mole of hydrogen (ΔG^0 = 237 kJ/mol at 25 °C).

So, STH can be easily calculated by divided E_{H_2} by the product between incident illumination power density (P, expressed in mW/cm^2) and illuminated photocatalyst area (A, expressed in cm^2).

$$STH = E_{H_2} / (P*A) \quad \text{(Equation 18)}$$

It is important to note that Equation 18 and 10 (an alternative way to calculate STH) are considered valid only in absence of sacrificial donors or acceptors since the stoichiometry of gas evolution (H_2 and O_2) plays a key role in these definitions.

Instead, the Incident Photon-to-Current Efficiency (IPCE) is a function of the irradiation wavelength and it represents the photocurrent collected per incident photon flux. The IPCE can be calculated as follows:

$$IPCE(\lambda) = \frac{\frac{electrons/cm^2}{s}}{\frac{photons/cm^2}{s}} = \frac{j_p * hc}{P_m * \lambda} \quad \text{(Equation 19)}$$

In which:

- j_p → is the photocurrent density expressed in mA/cm^2;
- hc → is the product between h (Planck's constant) and c (speed of light) and it is equal to 1239.8 V*nm;
- P_m → is the calibrated power intensity for each specific λ, it is expressed in mW/cm^2;
- λ → is the wavelength at which the measurements are carried out, it is expressed in nm.

Besides the estimation and definition of the efficiency, it is essential to have a detailed knowledge of the reactions involved during photocatalytic or PEC water splitting as well as the nature of the semiconductor for a complete description of the photocatalytic system.

As briefly mentioned in previous chapters, the thermodynamic feasibility of water splitting is related to the band edge positions of the semiconductor. In fact, to initiate the redox reaction, the band edge level of the VB must be more positive than water oxidation potential (see Equation 20 and Figure 5), while the band edge position of the CB must be more negative than the H_2 evolution potential (see Equation 21).

$H_2O + 2\ h^+ \longrightarrow 2H^+ + ½\ O_2$ $E^0_{ox} = -1.23$ V (vs. NHE) (Equation 20)

$2H^+ + 2\ e^- \longrightarrow H_2$ $E^0_{red} = 0$ V (vs. NHE) (Equation 21)

$H_2O + 2\ h^+ + 2\ e^- \longrightarrow H_2 + ½\ O_2$ (Equation 22)

Thus, it is not sufficient that a semiconductor has a band gap energy higher than 1.23 eV to induce the photocatalytic degradation of water. Only CB and VB edge positions can define the feasibility of both these reactions.

This is one of the reasons why TiO_2 is the most employed semiconductor material for such a process. In fact, both oxygen and hydrogen evolution can occur at the surface of this material (Equations 20-22 and Figure 5).

Other materials, such as α-Fe_2O_3, have a suitable band gap energy (i.e. higher than 1.23 V) but, as shown in Figure 5, the band alignment is not favorable for H_2 evolution. In this case, the water splitting process can be carried out in a PEC system by applying an onset potential (V_{onset}, the lowest potential which produces photocurrent) to the photoelectrode. Additionally, the strongly improved charge carriers separation (and their transportation through an external circuit) causes a significant decrease of the recombination probability which enables a more efficient water splitting process. The proper V_{onset} is usually taken by recording a J-V curve (photocurrent-voltage curve) with a conventional three-electrode system, and this value is essentially dependent on the surface energy situation at the semiconductor/electrolyte interface.

As reported in Equations 11-15, hematite is able to photo-oxidize water and generate highly oxidant species thanks to the application of a positive V_{onset}, while hydrogen evolution occurs at the counter-electrode surface (e.g. Pt) by driving photo-generated electrons towards the external circuit which connect the counter-electrode to the photoanode.

Anyway, independently of the employed semiconductor material, photocatalytic performances are often improved by mixing water with low-cost sacrificial agents which can be easily oxidized by photo-generated holes. These species are commonly simple organic compounds (e.g. ethanol, methanol) or a mixture of them and, as reported in Equation 23, their hole scavenging action leads to an enhancement of the photocatalytic performances.

$$H_xC_yO_z + h^+ \longrightarrow CO_2 + H_2O \qquad \text{(Equation 23)}$$

In this dissertation, it will be discussed in detail the performances of decorated-TiO_2 nanotubes towards photocatalytic hydrogen evolution from water/ethanol mixtures under UV-light irradiation.

1.4.2. Photocatalytic mercury removal from water

Mercury (Hg, atomic number 80) is a heavy metal of well-known toxicity.

Its presence in the environment, as organic or inorganic species, is mostly due to human activities such as coal burning, mining and industrial emission[188,189]. Inorganic Hg species include elemental mercury (Hg^0, metallic or vapor), mercurous (Hg_2^{2+} or Hg(I)) and mercuric (Hg^{2+} or Hg(II)) salts (such as chloride, sulfate). Instead, in its organic forms, mercury is bonded to a carbon-containing structure (such as methyl, ethyl, or analogous groups).

Inorganic mercury present in water bodies (commonly as dissolved Hg(II) or settled Hg(0)) can be converted by several anaerobic bacteria and microorganism into organic Hg forms like methylmercury, that is a well-recognized neurotoxin. This highly toxic species can be ingested by small sea creatures which in turn can be eaten by larger fishes. Considering that mercury has a very strong interaction (i.e. high adsorption and slow elimination) with biological systems, the food chain leads to a significant bioaccumulation and biomagnification, that is a considerable increase of Hg concentration in the tissues of fishes at the top of the chain (e.g. shark, tuna). Additionally, mercury cannot be degraded by biological or chemical agents, thus, Hg is considered a serious health hazard since it is a cumulatively toxic element.

For this reason, nowadays mercury contamination is still a problem of major concern.

The toxic effect due to the presence of high levels of mercury at Minamata (Japan) and Iraq was well investigated[190,191].

More recent cases regard also the contamination of water bodies in the United States, where fishing was forbidden in over three thousand lakes due to Hg pollution[189] and several ocean fishes were found to be tainted with significant concentrations of mercury[192,193].

So, in order to limit the toxicological problems related to the presence of mercury in water bodies, contaminated water treatment should be designed to remove mercury without creating other toxic species.

Up to now a lot of technologies useful to treat highly concentrated wastewaters are known. Among these methods are included membrane filtration, precipitation and ion exchange[194–197]. However, all these techniques are very poorly efficient and exorbitantly expensive and they can be used efficiently only to treat Hg concentrations below ~ 100 ppm[194,195,198].

For this reason, photocatalysis is recently emerged as a promising technique for mercury removal from aqueous solution, even at low concentration levels. Several photocatalytic

materials have been employed for this purpose and as reported for other applications, titanium dioxide is one of the most used photocatalysts for mercury removal.

As reported in Equations 11-15 photo-generated holes can produce several oxidant species while photo-promoted electrons are able to cause the reduction of oxygen and/or metallic ions (M_{ox}) present in aqueous solution.

The feasibility of the photocatalytic reduction process can be thermodynamically evaluated by comparing the relative position of the CB edge level of TiO_2 and the standard reduction potential of the M_{ox}/M_{red} couple[199]. Since the standard reduction potential reported in the literature for the couple Hg(II)/Hg(0) is equal to 0.851 V (vs NHE)[200,201] and the CB edge level of TiO_2 have been reported ≈ - 0.50 V (at pH 7 vs NHE)[202] the photocatalytic reduction from Hg(II) to Hg(0) is theoretically achievable (i.e. CB edge potential is more negative than the mercury reduction potential).

However, a relatively poor number of works on photocatalytic reduction of Hg(II) in aqueous solution can be found in the literature[198,203–208] and the number becomes even lower in the case of supported photocatalysts (e.g. TiO_2 nanotubes). In addition, UV irradiation was employed for all these works and no solar light-driven photocatalytic reduction of Hg(II) can be found in the literature up to now.

The first attempts to photoreduce Hg(II) on powdered TiO_2 photocatalysts have been made by using commercial Degussa P25 and Hombikat UV100 (100% anatase) under UV light illumination[204–206]. A few years later Lenzi et al.[207] tried to improve the adsorption and photocatalytic performances by preparing sol-gel and impregnation Ag/TiO_2 with higher specific surface area. Only more recently supported TiO_2 nanotubes (WO_3-decorated TiO_2 NT arrays) were used by Lee at al.[198] for mercury removal achieving quite good photocatalytic mercury abatement performances (~76% of initial Hg(II) removed after 2 hours UV irradiation).

In this thesis, Au-decorated TiO_2 nanotubes were employed for the first time for the photocatalytic reduction and scavenging of inorganic Hg(II) in natural water-like solutions under solar light irradiation.

1.4.3. Photocatalytic arsenic removal from water

Arsenic (As, atomic number = 33) is a ubiquitous element that can be found in water, soil and air. Its presence in the environment is predominantly due to natural sources (e.g. volcanoes, weathering of arsenic-containing minerals) and, to a minor extent, to industrial wastes.

Arsenic is a well-known toxin for both plants and animals and, in particular, inorganic arsenic compounds are recognized as carcinogens in humans[209]. In fact, prolonged chronic exposure to these compounds by drinking or eating food prepared with arsenic-containing waters can cause cancer of the brain, kidney and stomach as well as skin lesions and other diseases[210–213]. For this reason, very low accepted concentration limits (10 μg/L) have been established for total As in drinking water by EU regulations[214].

Since arsenic compounds toxicity is strictly related to arsenic speciation it is fundamental to distinguish these species into 2 main categories:

- *Inorganic compounds*
  Inorganic arsenic species (iAs) in water are commonly present as oxyacids, namely H_3AsO_3 (As(III)), H_3AsO_4 (As(V)) and their relative oxyanions.
  Although arsine (AsH_3) is the most toxic arsenic compounds, it can't be found in water at high concentration levels since it is volatile.

- *Organic compounds*
  In these compounds, arsenic is combined with carbon and in some cases also with other elements. The most important species present in water are the methylated forms of inorganic arsenic oxyacids such as mono-, di- and tri-methylarsinic (or –methylarsenous) acids.

This distinction is very important as organic compounds are much less toxic than the iAs species and, for this reason, they are not considered to be connected to cancer. Instead, iAs species are recognized as very toxic and carcinogenic to human organisms[209,215,216] and the oral Lethal Dose 50 (LD50) for iAs compounds is between 15 and 293 mg/kg[209].

Investigating more in detail within iAs compounds, As(III) is recognized as ~15-20 times more toxic than As(V), and the ingestion of ~80 mg of arsenic trioxide (As_2O_3) has been reported to be deadly for humans[217].

The relative abundance of As(III) and As(V) is strongly influenced by the presence of oxidizing or reducing conditions. The knowledge of the standard reduction potentials (see Equations 24-26) of iAs species[201] allows for a rough prediction of the redox speciation of iAs.

$H_3AsO_4 + 2H^+ + 2e^- \longleftrightarrow H_3AsO_3 + H_2O$ $E^0 = +0.575$ V[201] (Equation 24)

$H_3AsO_3 + 3H^+ + 3e^- \longleftrightarrow As(s) + 3H_2O$ $E^0 = +0.247$ V[201] (Equation 25)

$As(s) + 3H^+ + 3e^- \longleftrightarrow AsH_3(g)$ $E^0 = -0.238$ V[201] (Equation 26)

Besides the organic/inorganic nature and the oxidation state of arsenic species, it is fundamental to define the pH effect on acid-base iAs speciation in order to have a complete toxicological and chemical description. As shown in Figures 13a and 13b, the presence of neutral or anionic As(III) and As(V) species is exclusively dependent on the pH value of the solution.

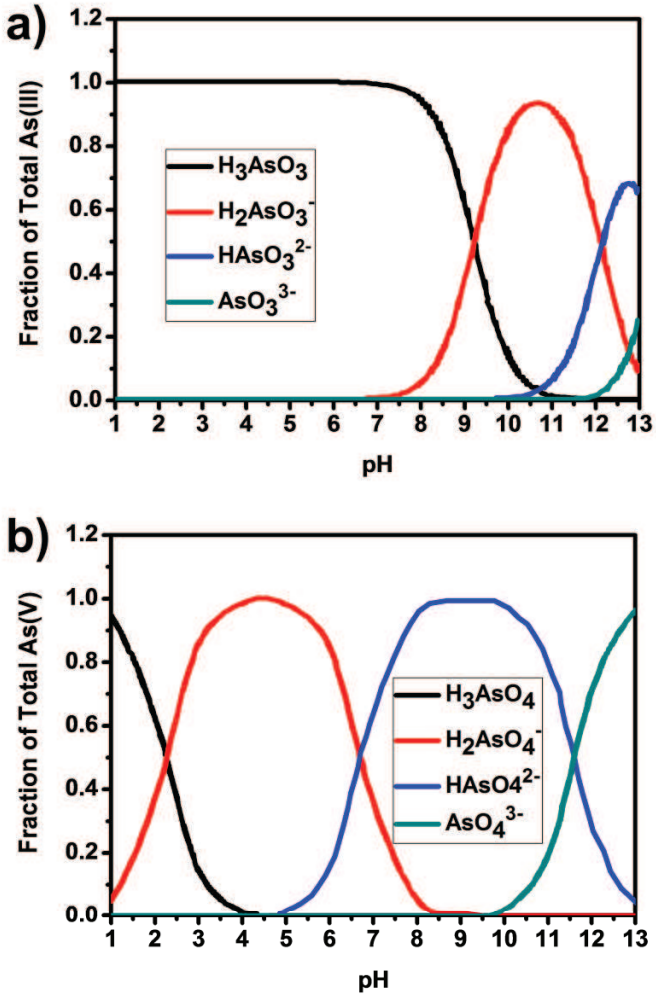

Figure 13 α-plots for a) arseneous acid and b) arsenic acid.

In particular, $As(OH)_3$ starts to dissociate only at pH > 7.50 (Figure 13a), and for this reason in natural waters (pH in the range 6.50-8.50) $As(OH)_3$ (neutral species) is the dominant compound of As(III) while the contribution of other As(III) species is usually negligible. This behavior is evident also by observing its acid dissociation constant values (Equations 27-29)[215,218].

$$As(OH)_3 \longleftrightarrow As(OH)_2O^- + H^+ \qquad pK_{a1} = 9.2 \qquad \text{(Equation 27)}$$

$$As(OH)_2O^- \longleftrightarrow As(OH)O_2^{2-} + H^+ \qquad pK_{a2} = 12.1 \qquad \text{(Equation 28)}$$

$$As(OH)O_2^{2-} \longleftrightarrow AsO_3^{3-} + H^+ \qquad pK_{a3} = 12.7 \qquad \text{(Equation 29)}$$

Instead, as shown in Figure 13b, As(V) is present at neutral pH values as an equilibrium between its mono-anionic and di-anionic species (see pK_{a2} value ~ 7 in Equation 31).

$$AsO(OH)_3 \longleftrightarrow AsO_2(OH)_2^- + H^+ \qquad pK_{a1} = 2.3 \qquad \text{(Equation 30)}$$

$$AsO_2(OH)_2^- \longleftrightarrow AsO_3(OH)^{2-} + H^+ \qquad pK_{a2} = 6.8 \qquad \text{(Equation 31)}$$

$$AsO_3(OH)^{2-} \longleftrightarrow AsO_4^{3-} + H^+ \qquad pK_{a3} = 11.6 \qquad \text{(Equation 32)}$$

Thus, arsenous acid (H_3AsO_3) and As(V) ions ($HAsO_4^{2-}$, $H_2AsO_4^-$) are the species of major interest and concern in natural waters.

In light of their toxicity, several efforts have been made to decontaminate natural and drinking waters from iAs species. Some traditional physico-chemical processes have found application for As removal including oxidation, adsorption, precipitation/co-precipitation, ion exchange and reverse osmosis[219]. Among these techniques, adsorption of arsenic species on metal oxides phases has attracted particular interest as an efficient method for As removal in contaminated natural and drinking waters. Additionally, As determination and speciation methods can be based on this metal oxides property.

The idea of using oxides and hydroxides was born out of the observation of the crucial role played by them in arsenic geochemistry. In this context, the nature of iAs species and the competition with other ions must be carefully considered for an accurate description of the adsorptive behavior[180].

One of the most employed material for this application is iron oxide (i.e. hematite, amorphous oxide, goethite and magnetite) and several works regarding As/Fe_xO_y chemical and physical interaction were reported in the literature[178–184]

In fact, since As(III) naturally occurs as a neutral species in water (see Figure 13a), is generally less strongly adsorbed than As(V) by oxide surfaces[179,220] and considering also that As(III) is much more toxic compared to As(V)[221] a preliminary oxidation of arsenite to arsenate is often desirable.

The oxidation process is traditionally performed by using stoichiometric oxidants including oxygen, ozone, hydrogen peroxide, chlorine dioxide, permanganate and ferrate[215] which result in limited efficiency, potential dangerous disposal of wastes and high cost due to the massive usage of these chemicals[222]. To overcome these critical aspects, photocatalysis has emerged as an attractive alternative oxidation method in the last decades[223]. In the literature, it is possible to find the application of different photocatalytic materials, including TiO_2[223–226], Fe_2O_3/TiO_2[227,228] and WO_3[229].

A particular approach, that involves photocatalytic oxidation of As(III) to As(V) followed by adsorption of As(V) using TiO_2 suspensions, was proposed for the first time by Dutta et al.[230,231]. Afterwards, Zhang and Itoh[232] investigate the adsorption properties of a slag-iron oxide-TiO_2 material for arsenic removal and photocatalytic oxidation of As(III). In this case at least 2 g/L of photocatalyst was required to remove of 20 mg/L of As(III) by adsorption.

The photo-oxidation mechanism of As(III) with powdered TiO_2 has been extensively investigated and several studies proposed hydroxyl radicals and superoxide ions (produced by water splitting reaction, as reported in Equations 12-15) as the major oxidant species for As(III) oxidation[224,230].

In this dissertation, the PEC As(III) oxidation over nanostructured hematite photoanodes in aqueous solutions under solar light illumination was tested for the first time. The outcomes and the related discussion will be provided in the following chapters.

2. Research projects

As mentioned in previous chapters, the focus of this thesis was to explore properties and photo(electro)catalytic performances of different metal oxide semiconductor materials towards environmental applications.

In particular, the production of clean energy through hydrogen gas evolution from water-ethanol mixtures and the abatement of highly toxic inorganic pollutants (i.e. arsenic and mercury) from water were investigated.

The first two studies reported in this dissertation have regarded the enhancement of photocatalytic performances towards hydrogen evolution under UV irradiation thanks to the employment of highly-ordered anodic TiO_2 nanotubes decorated by sputtering/templated-dewetting. The decoration was carried out using a double-layered co-catalyst (WO_3-Pt, Chapter 2.1) and metal alloy NPs (NiCu, Chapter 2.2).

The same decoration approach was employed also to fabricate TiO_2-Au photocatalysts which were employed for the first time for the reduction/scavenging of inorganic Hg(II) from water under solar light irradiation (Chapter 2.3).

Finally, a novel PEC approach for the oxidation/abatement of inorganic As(III) over nanostructured worm-like hematite photoanodes under solar light illumination was investigated in detail (Chapter 2.4).

Since the results of all these works have led to scientific publications during my Ph.D., they will be reproduced and adapted with permission from the relative journals and publishers.

2.1. Site-selective Pt dewetting on WO_3-coated TiO_2 nanotube arrays: An electron transfer cascade-based H_2 evolution photocatalyst

Reproduced and adapted with permission from *Applied Catalysis B: Environmental* 237 **(2018)** 198–205, **DOI**: 10.1016/j.apcatb.2018.05.061, **Copyright © 2018 Elsevier B.V.**.

The results reported in this chapter were entirely obtained during my six-month period in Friedrich-Alexander University (FAU) of Erlangen-Nuremberg. My contribution has concerned the fabrication of all the employed photocatalytic materials and the evaluation of their performances towards photocatalytic hydrogen evolution and acid orange 7 degradation. I contributed partially in the characterization of these photocatalysts and extensively in the drafting and finalization of the published article.

Abstract

Among several parameters that affect the yield of a photocatalytic process mediated by a metal oxide semiconductor, key is the efficient separation and transfer of photogenerated charge carriers. To overcome kinetic limitations and enable charge transfer, an effective strategy is to decorate the photocatalyst surface with cocatalytic nanoparticles of either a second semiconductor metal oxide or a noble metal. Nevertheless, classical deposition technique (based on common powder technology approaches) lead to randomly placed cocatalytic nanoparticles at the photocatalytic surface. The poor control over cocatalyst placement can drastically hamper the photocatalytic efficiencies, and also prevents a full understanding of the charge carrier dynamics and photocatalytic mechanism. Here we introduce a highly defined charge separation platform for photocatalytic H_2 evolution based on a Pt-WO_3-TiO_2 "stacked" structure constructed on anodically grown TiO_2 nanotube arrays. Key is the formation of a site-selective and sequential W and Pt metal sputter-decoration only at the mouth of highly-ordered TiO_2 nanotubes. After placing the W-Pt bilayer at the nanotubes mouth, a suitable thermal treatment forms a WO_3 layer atop the nanotubes while the Pt film undergoes solid state dewetting into 2-6 nm-sized Pt nanoparticles. These structures show strongly improved photocatalytic H_2 evolution efficiency compared to any other single-cocatalyst system (Pt-TiO_2 and WO_3-TiO_2) and pristine TiO_2 nanotubes. This significant improvement is ascribed to an enhanced charge carrier separation enabled by the well-defined TiO_2-WO_3-Pt cascade that provides swift electron transfer through WO_3 and towards Pt for H_2 evolution.

Introduction

Since the pioneering work of Fujishima and Honda [8] in 1972, the production of H_2 by photocatalytic splitting of H_2O on semiconductors has been extensively investigated. Among the different studied photocatalysts, titanium dioxide (TiO_2) received large attention owning to its suitable conduction (CB) and valence band (VB) edge positions, as well as for its nontoxicity and stability against corrosion and photo-corrosion [35,36]. The bottom of TiO_2 conduction band (CB) lies higher than the redox potential of water (-0.45 and 0 V vs. NHE, respectively, at pH 0) [119]. Therefore, by promoting electrons in TiO_2 CB through UV light irradiation ($E_{g\ TiO2} \sim 3.0$-3.2 eV), it is possible to reduce H_2O to H_2.

However, pristine TiO_2 shows low efficiencies for H_2 production because of trapping and recombination of charge carriers, and owing to a kinetically slow electron transfer to reactants. Nanostructured photocatalysts can be employed in order to improve the electron transfer efficiency. Particularly, one-dimensional (1D) nanostructures, such as anodic TiO_2 nanotubes (NTs), have attracted great attention in the last decades [49,233,234]. Vertically aligned arrays of self-organized NTs can be grown by a simple anodization of Ti metal in a suitable electrolyte [35,36,235]. The electrochemical conditions can be adjusted in order to lead to a large palette of nanotubular morphologies [235,236]. These highly-ordered 1D TiO_2 structures can promote directional charge transport and orthogonal electron-hole separation that allow for enhanced photo-electrochemical and photocatalytic performances [36,237].

In addition, cocatalysts that aid charge separation and transfer by forming a heterojunction on TiO_2, such as a suitable semiconductor or noble metal nanoparticles (e.g. Au, Pd, and Pt) can be also employed to further improve the performance of titania-based photocatalysts.

In view of constructing a composite photocatalyst, a particularly interesting constellation is obtained when TiO_2 is combined to WO_3, an n-type semiconductor with a band gap $E_{g\ WO3} \sim 2.6$-2.8 eV [85,86]. With such a combination, a favorable band alignment at the TiO_2-WO_3 interface is generated that enables efficient charge separation [84] by transfer of TiO_2 CB electrons into the WO_3 CB [82,87–89]. The photocatalytic enhancement obtained when WO_3 is combined to TiO_2 is typically discussed also in terms of a WO_3 contribution to visible-light absorbance ($\lambda_{abs\ WO3} < \sim 450$ nm – i.e. larger photon harvesting) [90,91], enhanced surface acidity that can yield improved adsorption of reactants [83,92–96], higher hydrophilicity [97], and the possibility of enabling a "z-scheme" for charge separation [238].

While the placement of a suitable metal oxide semiconductor (WO_3) at the TiO_2 surface can enhance charge-separation, localized Schottky-type junctions are also commonly formed

by placing noble metal cocatalytic nanoparticles on the individual oxides. For example, Pt is typically a most efficient cocatalyst for the H_2 generation reaction [101–104]. Pt nanoparticles at the TiO_2 surface can enable efficient electron transfer at the catalyst/environment interface by providing a favorable solid state junction to TiO_2 [119], hence improving the electron transfer to reactants while additionally catalyzing hydrogen atom recombination reaction, and thus facilitating H_2 gas formation ($2H^0 \rightarrow H_2$) [105,106].

These two cocatalyst principles, i.e. a charge separation cocatalyst (WO_3) and a charge transfer cocatalyst (Pt), can, based on an anticipated synergistic effect, be combined into a composite photocatalyst, e.g. in a TiO_2-WO_3-noble metal combination. The benefit of combining these three catalytic elements has been used also in thermal catalysis, e.g. by using TiO_2-WO_3-Pt composites as de-NOx catalysts [239].

In some recent studies, such as the work of Pap et al., TiO_2-WO_3-noble metal (Au, Pt) powders were investigated in view of their photocatalytic performance [115–118]. These works pointed out the potential of combining the two cocatalyst principles for efficient photocatalysis, but the chosen preparation method, based on a classical powder technology process, suffered from a poor control over morphology and stacking of the cocatalysts. Particularly, only a loose and undefined contact (junction) between the two oxides can by these classical approaches be obtained – this hampers the charge carrier separation: note in fact that in these works any noble metal-WO_3-TiO_2 combination was found less photocatalytically active for H_2 evolution than a simple noble metal-TiO_2 configuration.

Moreover, similar synthesis methods for noble metal-WO_3-TiO_2 structures lead in general to a photocatalyst configuration characterized by undefined interfaces, which can bring about several uncontrolled charge carrier dynamics and enable various photocatalytic mechanisms – in this case, given that a photocatalytic enhancement can be observed, an accurate understanding of the photocatalytic mechanism is almost impossible.

In contrast, with the present work, we introduce a reliable fabrication strategy of a synergistic Pt-WO_3-TiO_2 photocatalyst for H_2 generation constructed with nanoscale precision on an array of highly-ordered TiO_2 nanotubes. This architecture, owing to its highly-defined geometry obtained by site-selective placement of Pt and WO_3 cocatalysts, induces an electron transfer cascade from the TiO_2 NTs (light absorber) to the WO_3 junction (charge separation cocatalyst) and onward to the Pt nanoparticles (NPs) (charge transfer cocatalyst). The result is a facilitated electron transport towards the nanotube top for H_2 evolution, while the uncoated bottom of the TiO_2 cavities is a suitable site for hole-mediated oxidation reaction. We show that, in contrast to previous works, a morphologically controlled

TiO_2-WO_3-Pt design leads to enhanced photocatalytic H_2 evolution efficiencies, which are higher than those measured for classic noble metal-TiO_2 photocatalysts.

Experimental

Fabrication of the TiO_2 nanotube array

Ti foils (Advent Research Materials, 0.125 mm thickness, 99.6+% purity) were degreased by sonicating in acetone, ethanol, and deionized water, and were then dried in a N_2 stream. Then, the Ti foils were anodized to fabricate the highly ordered TiO_2 nanotube arrays in a hot electrolyte based on 3 M HF in o-H_3PO_4 (Sigma- Aldrich) [240]. For the anodic growth, a two-electrode configuration was used, where the Ti foil (15 mm × 15 mm) and a Pt sheet were the working and counter electrodes, respectively. The anodization experiments were carried out by applying a potential of 15 V (for 2 h) using a DC power supply (VLP 2403 Voltcraft). After anodization, the TiO_2 nanotube arrays on Ti metal substrates were rinsed with ethanol and dried under N_2 stream.

W and Pt sputtering-coating and thermal treatment

In order to site-selectively place the cocatalytic Pt/WO_3 stack only atop the nanotubes, a plasma-sputtering machine (EM SCD 500, Leica) was used in a shallow angle configuration to sputter-coat W and Pt metal thin films (W-Pt bilayers) using a 99,8% pure W target (Hauner Metallische Werkstoffe) and a 99,99% pure Pt target (Hauner Metallische Werkstoffe), respectively. The applied sputtering current was 16 mA and the pressure of the sputtering chamber was set at 10^{-2} mbar of Ar. The amount of sputtered material was in-situ determined by an automated quartz crystal monitor, and is reported in this work as nominal thickness of the sputtered film. However in some previous works the deposition process for Pt was calibrated and a linear correlation between the nominal thickness of the sputtered layer (in nm) and the actual loading on the catalyst (in µg of Pt) was found [101,241]. Precisely, the Pt loading determined by ICP-OES measurements scales with the nominal thickness of the sputtered layer with a factor of 1.1 $\mu g_{Pt}\ nm^{-1}$. In this work, the sputter-coated Pt films have a nominal thickness of 1 nm, and are coated on an active surface (irradiated photocatalyst surface) of 0.785 cm^2. Thus, for Pt-leaded structures, the Pt loading is ~ 1.4 $\mu g_{Pt}\ cm^{-2}$.

The Pt film nominal thickness of 1 nm was selected based on previous works demonstrating that a thickness of the sputter-coated noble metal film < 5 nm leads after

dewetting to optimized cocatalyst loading and photocatalytic efficiency. More precisely, it was found that a minimal amount e.g. 1 nm can lead to a highest H_2 evolution rate [101].

Subsequently, the samples were annealed at 450°C in air for 1 h, using a Rapid Thermal Annealer (Jipelec Jetfirst 100 RTA), with a heating and cooling rate of 30°C min^{-1}. The thermal treatment formed a WO_3 layer on the TiO_2 nanotube arrays onto which Pt splits into nanoparticles by thermal dewetting.

Characterization of the structures

A field-emission scanning electron microscope (FE-SEM, Hitachi S4800) and a high resolution transmission electron microscope (HR-TEM, Philips CM300) were used to characterize the morphology of the samples. The chemical composition of the samples was analyzed by X-ray photoelectron spectroscopy (XPS, PHI 5600, US). X-ray diffraction (XRD) with an X′pert Philips MPD (equipped with a Panalytical X'celerator detector) was employed to examine the crystallographic properties of the materials. The light absorption properties (diffuse reflectance) of the samples were measured by a UV-Vis Spectrometer (Lambda 950, Perkin Elmer).

Photocatalytic experiments

The photocatalytic H_2 generation measurements were carried out by irradiating the oxide films with UV light (LED Opsytec, λ = 365 nm, beam size = 0.78 cm^2, power of 80 mW cm^{-2}) in a 20 vol% ethanol–water solution (ethanol was used as hole-scavenger) in a quartz tube sealed with a gas-tight cap. The ethanol-water solution (kept under static conditions during the runs) and the cell head-space (volume = 6.22 mL) were purged with N_2 gas for 15 min prior to photocatalysis. N_2-purging is strictly needed as O_2, if present, would reduce the efficiency of H_2 generation by competitively reacting with conduction band electrons forming $O_2^{-\bullet}$.

The amount of produced H_2 (which was accumulated over the irradiation time in the head space of the tube) was measured by using a gas chromatograph (GCMSQO2010SE, Shimadzu) equipped with a thermal conductivity detector and a Restek micropacked Shin Carbon ST column (2 m × 0.53 mm). GC measurements were carried out at a temperature of the oven of 45 °C (isothermal conditions), with the temperature of the injector set at 280 °C and that of the TCD fixed at 260 °C. The flow rate of the carrier gas, i.e., argon, was 14.3 mL min^{-1}. The majority of the experiments lasted 5 hours, and the amount of evolved H_2 was measured at the end of the experiments. Photocatalytic measurements of Acid Orange 7

(AO7) degradation were carried out with the same instrumental setup and using a 0.125 mM AO7 solution. The light absorbance of the solution was measured by using a UV-Vis spectrophotometer (Lambda XLS+, Perkin Elmer) at 485 nm wavelength (maximum absorbance value) in order to determine the AO7 concentration.

Results and discussion

Figure 14a shows the morphology of the highly-ordered anodic TiO_2 NTs used in this work, which are grown on Ti metal foils by anodization in a hot H_3PO_4/HF electrolyte [240]. These NTs have an almost ideal hexagonal packing, an average inner diameter of ~ 80-90 nm and a length of ~ 190-200 nm (see Inset in Figure 14a). This well-defined structure with short aspect-ratio allows for the site-selective decoration of only the NT top, with e.g. metal bilayers (Pt and W in this work) using a grazing-angle sputtering technique.

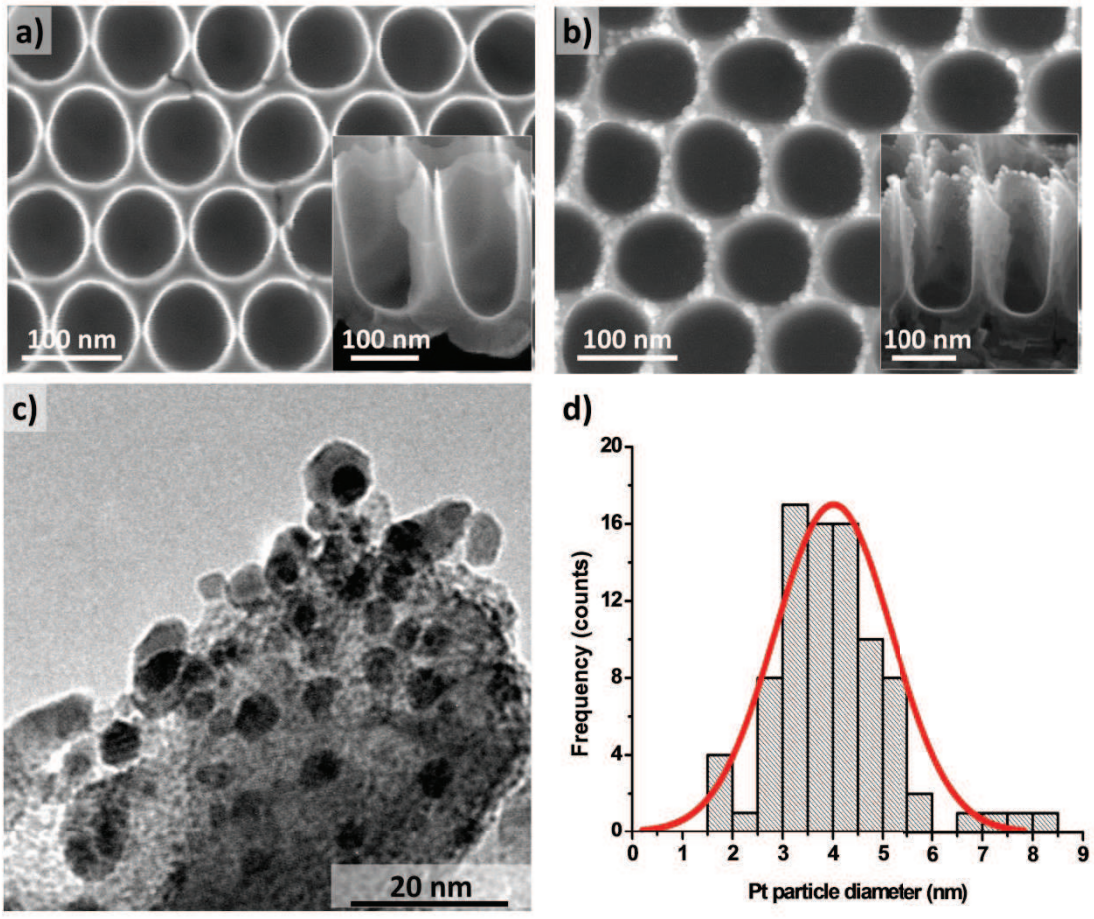

Figure 14. (a-f) SEM images of various TiO_2 structures: (a) arrays of pristine TiO_2 nanotubes. Inset: cross-sectional view of the pristine NTs; (b) TiO_2 NTs coated with a sputtered 1 nm-thick Pt film after dewetting (thermal treatment at 450°C, air, 1h). Inset: cross sectional view. (c) TEM image of the very top of a nanotube decorated with a sputtered-dewetted 1nm-thick Pt film; (d) Pt NPs size distribution.

After the sputter-deposition of a metal film, e.g. a 1 nm-thick Pt film, a thermal treatment is carried out to crystallize the TiO_2 NTs. Worth nothing, as illustrated in Figure 14b, such a thermal treatment leads at the same time to solid state dewetting of Pt, that is, to the conversion of the sputtered Pt film into Pt nanoparticles, with spherical shape and average diameter of 2-6 nm (as shown in Figure 14c and d). The driving force for dewetting [121] is the minimization of the free surface energy of the metal (Pt) film, of the substrate (oxide surface) and of the metal-substrate interface (Pt/oxide). Since the thinner the metal film the higher its surface-to-volume ratio and thus its surface energy, the dewetting of e.g. few nm-thick metal films can occur also at temperature far below the metal melting point – that is, the film can dewet while remaining in the solid state [120].

The NT structures can also be decorated by sputtering a W film firstly (nominal thickness of 0-30 nm), followed by sputter-deposition of a thin Pt metal layer (nominal thickness of 1 nm) – i.e. using a sequential metal sputter-coating approach that form a W-Pt bilayer at the TiO_2 NT surface. A subsequent thermal treatment of these structures in air at 450 °C for 1 hour forms the architectures illustrated in Figure 15 (additional SEM images of similar structures are reported in Figure 16).

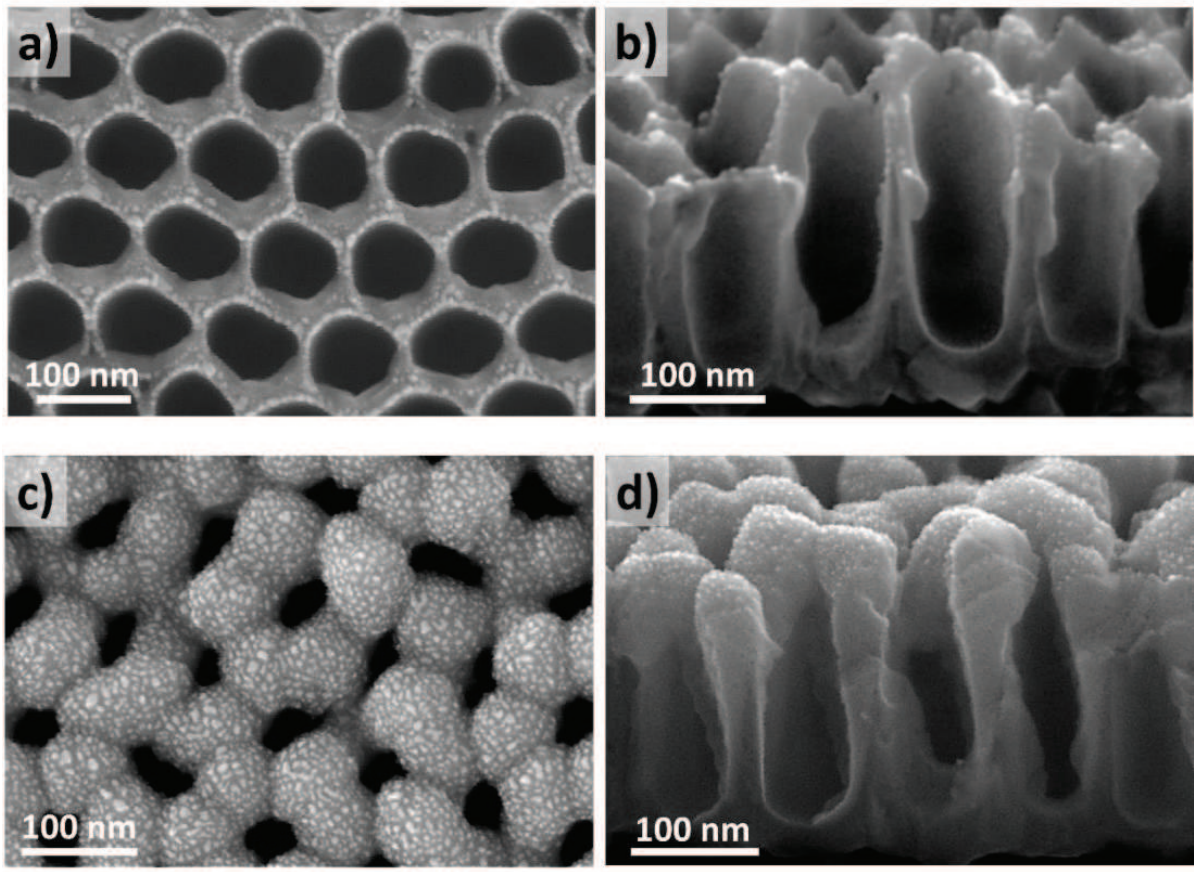

Figure 15. (a, c) Top and (b, d) cross sectional views of TiO_2 NTs coated with (a, b) 5 nm-thick and (c, d) 30 nm-thick W film and then with Pt (1 nm-thick) film after thermal treatment.

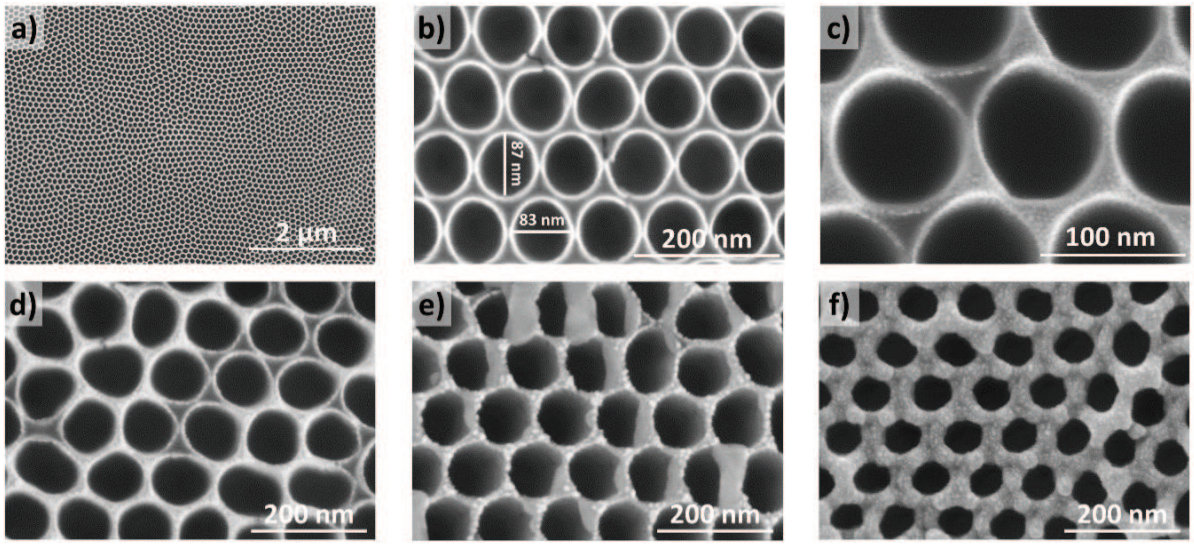

Figure 16. Top view SEM images of various TiO_2 structures: (a,b) pristine highly-ordered TiO_2 nanotubes; (c) TiO_2 NTs coated with a sputtered 1 nm-thick Pt film without any thermal treatment; (d-f) TiO_2 NTs sequentially coated with (d) 1, (e) 3 and (f) 10 nm-thick W film and then 1 nm-thick Pt films, followed by a thermal treatment (450°C, air, 1h).

In the case of small amounts of shallow-angle sputtered W (nominal thickness < 10 nm, e.g. Figure 15a and b), it is possible to observe from the cross-sectional SEM picture (Figure 15b) that the deposition of the W film occurs only at the rim of the tubes, thus leaving the tube bottom uncovered (free TiO_2 surface). However, for thicker W films (≥ 10 nm, Figure 15c and d) a certain amount of W is deposited also deeper in the NTs – e.g. Figure 15d shows that WO_3 is formed also close to the NT bottom.

The structures in Figure 14 and 15 were characterized by XRD, HR-TEM in view of their composition and structure. The results are compiled in Figure 17a,b. The intense XRD peaks (Figure 17a) at $2\theta = 25.4°$ and 27.6° can be assigned to TiO_2 (101) anatase and (110) rutile reflections [242,243], respectively, while peaks at $2\theta \sim 23\text{-}24°$ can be ascribed to the monoclinic WO_3 phase [244].

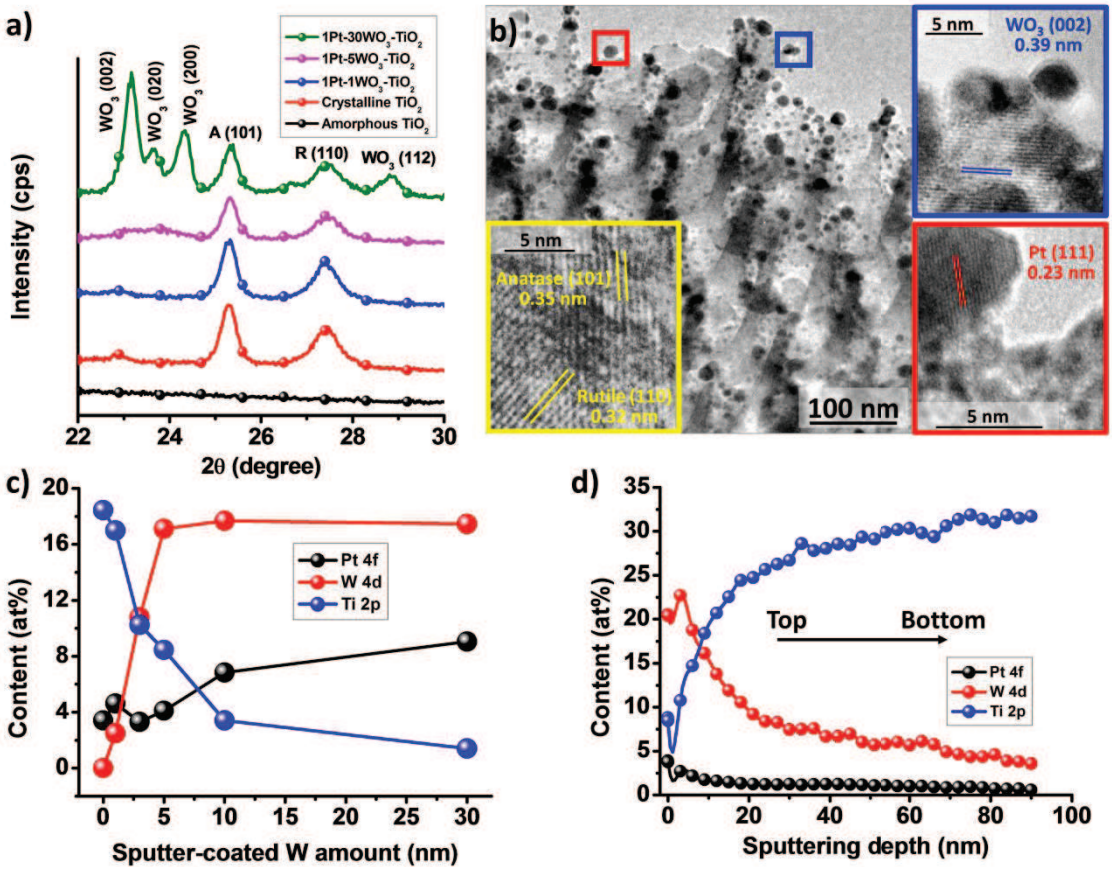

Figure 17. (a) Magnified view of the XRD patterns showing the main reflections of anatase (A) and rutile (R) TiO_2 and monoclinic WO_3, (XRD patterns measured in the 20-80° 2θ range are in Figure 18). (b) TEM images of sample 1Pt-5WO_3-TiO_2. Insets: HR-TEM images: (yellow) crystal planes of (101) anatase TiO_2 and (110) rutile TiO_2 in the sidewalls and bottom of the nanotubes; (blue) crystal planes of (002) monoclinic WO_3 and (red) crystal planes of (111) cubic Pt at the very top of the nanotubes. (c,d and e) Ti, W and Pt content determined from XPS analysis: (c) surface content as a function of the nominal thickness of the sputter-coated W films, (d) depth profile (content measured along the depth of the nanotubes; the Pt signal in the plot is magnified by a factor 5x) and (e) Ti, W and Pt surface content of three differently decorated TiO_2 NT layers showing the change in surface composition after the different steps of the W and Pt sputter deposition approach and thermal treatment.

The relatively intense reflections at 2θ ~ 23-24° observed for the structure 1Pt-30WO_3-TiO_2 is well in line with the larger amount of sputtered W metal (additional XRD patterns are shown in Figure 18). In any case, no XRD signal for Pt can be seen, probably owing to the little amount of sputtered noble metal.

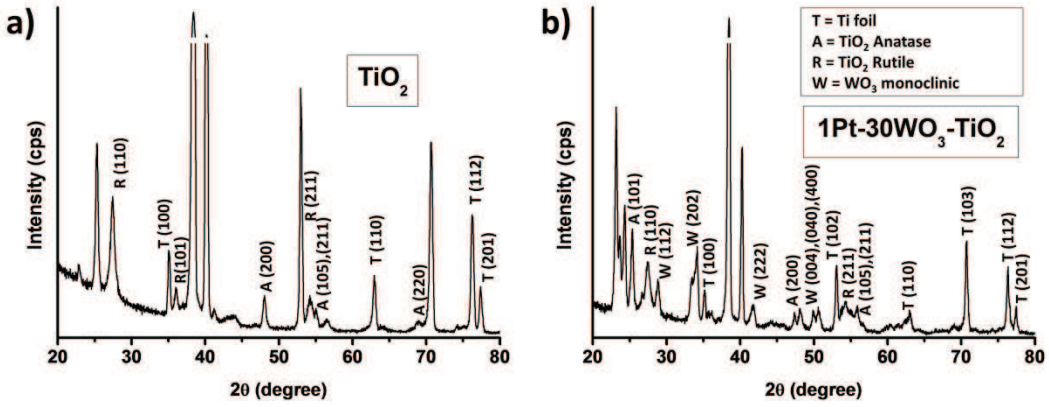

Figure 18. (a,b) XRD patterns of (a) crystalline TiO_2 and (b) *1Pt-30WO_3-TiO_2*.

The TEM images in Figure 17b clearly show the decoration of the top of the tubes with the two cocatalysts (i.e. Pt and WO_3). The HR-TEM images (insets in Figure 17b) reveal the presence of both anatase TiO_2 (101) and rutile TiO_2 (110) in the sidewalls and bottoms of the tubes, and, confirm the site-selective placement of the monoclinic WO_3 layer and Pt NPs on the top of the tubes. For example, the HR-TEM image in the blue box in Figure 17b clearly shows the WO_3 lattice planes – in the same image one can also identify, owing to a clearly different contrast, various Pt nanoparticles the size of which matches the size distribution shown in Figure 14d. Thus, SEM analysis along with XRD and TEM results (as well as XPD data below) confirm the presence of Pt nanoparticles as well as of the conversion of the sputtered W metal into crystalline WO_3 layer atop the architecture.

In addition, XPS analysis was carried out to investigate the composition of these structures and to gain information of the interfaces constructed in the Pt/WO_3/TiO_2 stack. The XPS surveys (Figure 19a) show that the structures are composed of Ti, O, W and Pt, with small traces of adventitious carbon and P (due to the anodization in highly-concentrated o-H_3PO_4). The XPS doublet with signals peaking at ~71.3 and 74.7 eV (Figure 19b) can be assigned to $Pt4f_{7/2}$ and $Pt4f_{5/2}$, respectively [245], and confirms the metallic state of the dewetted Pt nanoparticles. The XPS doublet peaking at ~ 36.5 and 38.7 eV (Figure 19c) can be attributed to WO_3 [246,247].

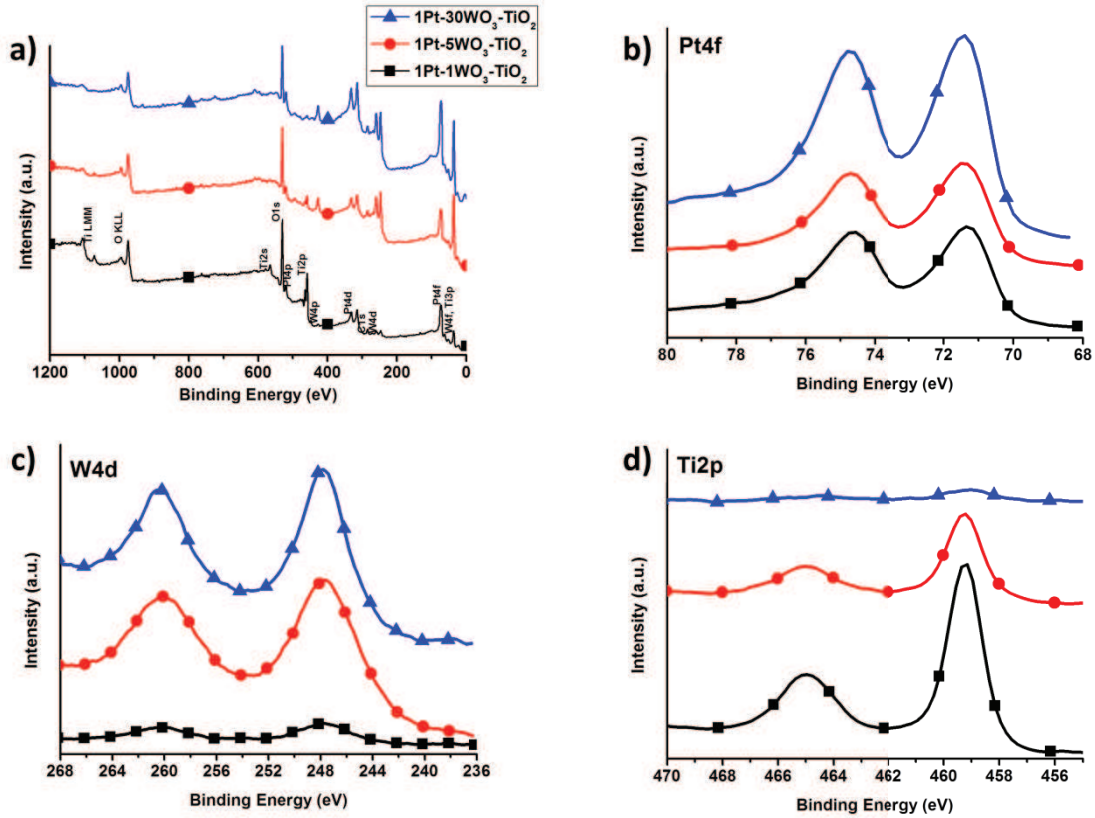

Figure 19. (a) XPS survey of different TiO_2 structures and high resolution XPS spectra of the (b) Pt4f, (c) W4d and (d) Ti2p regions.

Note that in contrast to what is observed for Pt (i.e. solid-state thermal dewetting leading to rupture of the Pt film into Pt NPs), the sputter-coated W film is subjected to a different fate when annealed in air: it reacts with O_2 gas and forms a crystalline WO_3 layer atop the NTs [248].

The XPS data reported in Figure 17c show that the Ti2p signal for the NT structures decreases with increasing the amount of sputtered W. This is well in line with data in Figure 19d, and indicates that the WO_3 layers formed from W sputtered films > 10 nm cover almost totally the TiO_2 NT surface. The weak Ti signal is in this case attributed to the uncovered TiO_2 surface at the very bottom of the tubes. A side effect of sputter-coating W film > 5 nm is the increase of the surface content of Pt at the top of the structures. This can be ascribed to the narrowing of the tube mouth (as clearly shown in Figure 15c and d). Hence, the relatively large amount of deposited W makes available a larger surface on the top of the cavities for Pt deposition.

The XPS depth profiling (Figure 17d) corroborates the stacked architecture of the photocatalyst, with the presence of Pt and WO_3 only at the very top of the tubes, i.e. the signals of Pt and W decrease sharply from the NT top towards the bottom of the cavities.

The XPS data in Figure 17e show the change in surface composition after each step of sputter-deposition and thermal treatment, i.e. in order to form the structures $3WO_3$-TiO_2 and 1Pt- WO_3-TiO_2. The Ti signal drops significantly after the sequential W and Pt sputter coating, confirming that the WO_3 layer firstly and then the Pt nanoparticles are deposited atop the TiO_2 nanotubes. Moreover, the amount of W in 1Pt-WO_3-TiO_2 and WO_3-TiO_2 is comparable, which confirms not only the reliability of the cocatalyst deposition method (fine control over amount and placement), but also that Pt cocatalyst is deposited atop the nanotube structure. The atomic concentrations of the various elements in the structures are summarized in Table 1.

Table 1. Surface composition of different decorated TiO_2 systems determined from XPS analysis.

	Surface composition (at%)					
Structure	**Ti**	**O**	**W**	**Pt**	**C**	**P**
TiO_2	21.06	69.29	-	-	1.24	6.64
1Pt-TiO_2	20.95	60.69	-	10.15	3.43	3.72
$3WO_3$-TiO_2	16.24	69.98	9.03	-	1.20	2.96
1Pt-$3WO_3$-TiO_2	9.04	63.16	10.56	12.01	3.54	1.33

In order to evaluate the interaction of Pt, WO_3 and TiO_2 with each other at the different formed interfaces, the high resolution XPS spectra in the W4f and Pt4f regions for different structures (TiO_2, Pt-TiO_2, WO_3-TiO_2 and Pt-WO_3-TiO_2) are overlaid in Figure 20a and b, respectively. The W state (Figure 20a) is virtually identical in WO_3-TiO_2 and Pt-WO_3-TiO_2. The peak at 36.48 eV observed for pristine TiO_2 is ascribe to the Ti3p signal, which falls in the W4f signal region. Also, as it is evident from Figure 20b, Pt is present in its metallic form, and no shift could be detected in the Pt4f doublets of structures Pt-TiO_2 and Pt-WO_3-TiO_2. In other words, the XPS data confirm the stacked architecture of the Pt-WO_3 cocatalyst atop the NTs, and the sequential deposition of the WO_3 and Pt cocatalytic elements does not affect their chemical state, which is comparable for different structures.

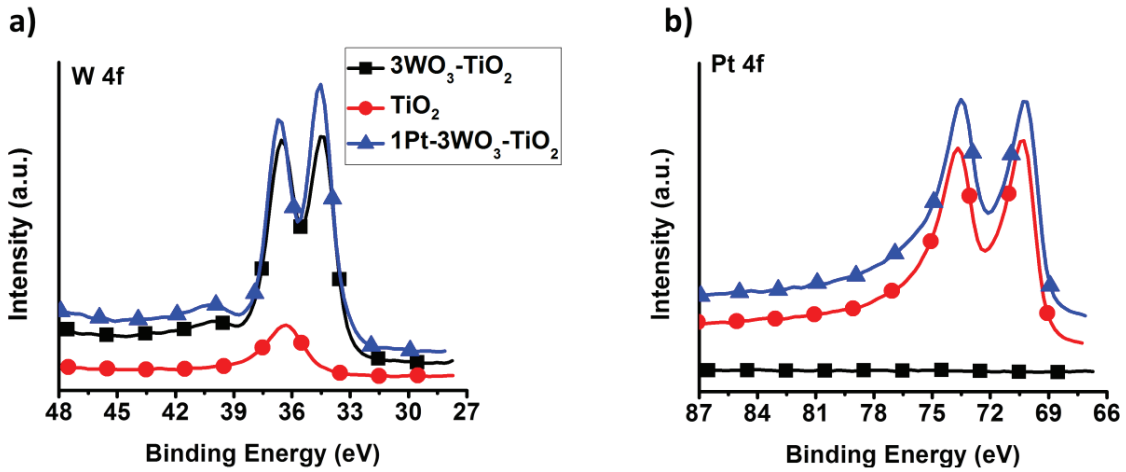

Figure 20. HR-XPS spectra of different decorated TiO_2 systems in two specific XPS region: (a) W 4d, (b) Pt 4f

These structures were assessed in view of their photocatalytic H_2 evolution performance, from water-ethanol (20%) solution under UV light irradiation (LED light, 365 nm). The results are shown in Figure 21a-c. From these data it is clear that, for these stacked structures, an optimized amount of sputtered W leads to significantly higher photocatalytic H_2 generation efficiency than any other combination (Pt-TiO_2, WO_3-TiO_2 and pristine TiO_2). More precisely, both pristine TiO_2 NTs (TiO_2) and TiO_2 NTs modified only with WO_3 ($3WO_3$-TiO_2) exhibit a negligible photocatalytic H_2 generation (0.06 µL h^{-1} cm^{-2} and 0.14 µL h^{-1} cm^{-2}, respectively). The slight improvement of the r_{H2} may be ascribed to electron-hole separation at the TiO_2/WO_3 interface, which can make electrons more available for the H_2 evolution (spatially separated charges). As expected, Pt-TiO_2 photocatalyst (1Pt-TiO_2) shows an improved H_2 evolution compared to pristine TiO_2, i.e. leading to a r_{H2} of 3.4 µL h^{-1} cm^{-2}. This effect is due to the formation of Pt/TiO_2 Schottky junctions at the TiO_2 nanotubes top.

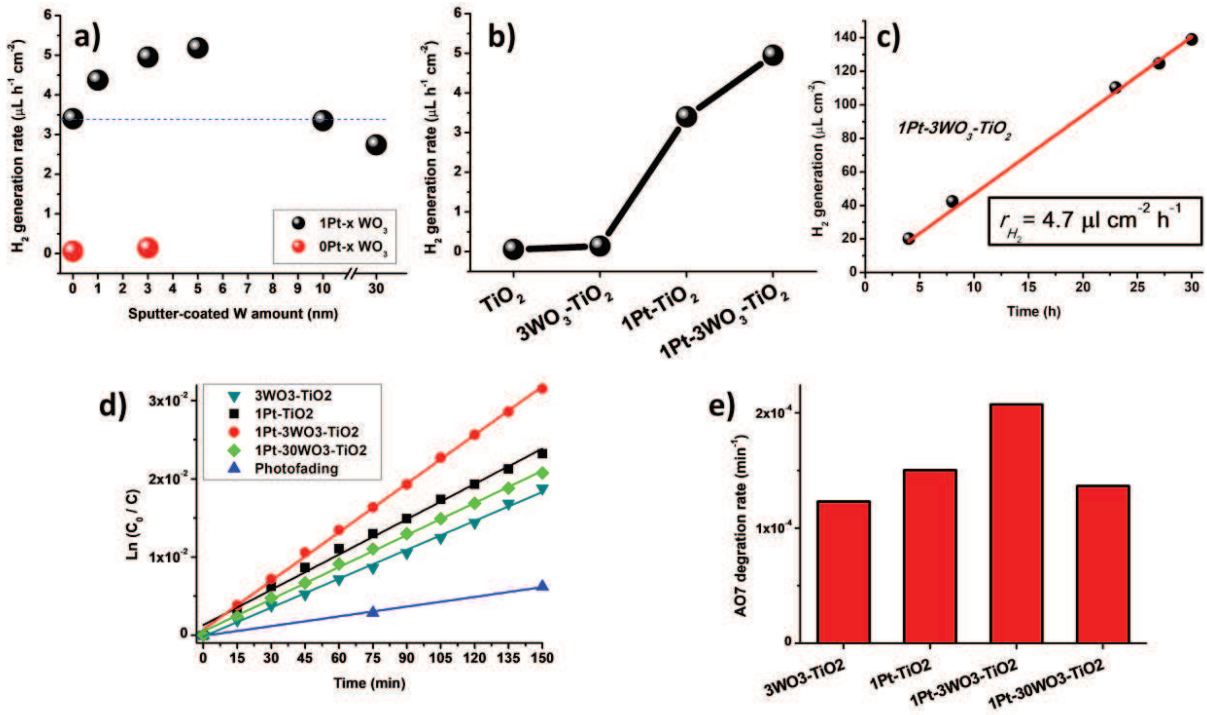

Figure 21. (a) Photocatalytic H_2 evolution results of different TiO_2 nanotube structures as a function of W sputtered amount; (b) summary of the r_{H2} improvement achieved with an optimized Pt and WO_3 decoration on the top of the TiO_2 NT arrays. (c) Evaluation of the photocatalytic H_2 evolution performance of 1Pt-3WO_3-TiO_2 over an irradiation time of 30 h. (d) First-order kinetic fitting for the photocatalytic degradation (oxidation) of AO7 (Acid Orange 7) under LED 365 nm irradiation using different TiO_2 nanotube structures and in absence of photocatalyst (photofading). (e) AO7 degradation rates for the different samples.

Nevertheless, a substantial further enhancement of the photocatalytic performance is obtained modifying TiO_2 with both WO_3 and Pt (1Pt-xWO_3-TiO_2), that is, by constructing a stacked Pt-WO_3-TiO_2 architecture at the NT top. In particular, photocatalysts with 1, 3 and 5 nm of WO_3 lead to the highest H_2 generation rates, that is, of 4.4, 5,0 and 5.2 µL h^{-1} cm^{-2}, respectively, which correspond to apparent quantum efficiencies (AQE) of 0.041, 0.047 and 0.049%, respectively (see more detail from Equations 33-37 reported in Chapter 2.2). Note that these r_{H2} can be up to a factor 1.5 higher than that of 1Pt-TiO_2. Long-run photocatalytic tests (carried out by continuous irradiation for 30 h – Figure 21c) reveal that the r_{H2} remains constant and thus, deterioration phenomena such as photo-corrosion of the photocatalyst or fall-off of the cocatalytic Pt NPs can be ruled out.

Taking into account the band edge alignment and energetic situation of the elements of the Pt-WO_3-TiO_2 triad, one can interpret these photocatalytic results assuming that the defined Pt-WO_3-TiO_2 architecture constructed at the top of the NT walls enables efficient electron transfer from the TiO_2 NTs (light absorber and charge carrier generator) to the WO_3 top layer, and then onward to the Pt cocatalytic NPs. This "electron transfer cascade" is therefore the main cause for the observed synergistic r_{H2} enhancement.

A side effect of the site-selective decoration of the NT top only (W films < 10 nm) is that the bottom of the TiO_2 nanocavities is left uncoated, i.e. free TiO_2 surface. This situation, along with the intrinsic upward band bending in the nanotube walls [249] and the typically short diffusion length of holes in TiO_2, leads to direct hole-transfer to the reactants (ethanol), which reduced the electron-hole recombination in the NTs.

In order to corroborate the results of photocatalytic H_2 evolution and their interpretation, photo-degradation tests of Acid Orange 7 (AO7) under 365 nm UV light irradiation were carried out with the reference materials 1Pt-TiO_2 and 3WO_3-TiO_2, and different three-layered structures, i.e., 1Pt-3WO_3-TiO_2 and 1Pt-30WO_3-TiO_2. The results are reported in Figure 21d and e. Noteworthy, also in this case, for single-cocatalyst structures, the deposition of a noble metal (1Pt-TiO_2) leads to a significantly higher AO7 photocatalytic degradation rate compared to the modification with WO_3 (WO_3-TiO_2). More importantly, the Pt-WO_3-TiO_2 triad with optimized amount of W (~1-5 nm) leads to a higher photocatalytic performance (AO7 degradation) compared to 1Pt-TiO_2. However, a too large amount of W (~30 nm) leads to a lower A07 degradation rate. In other words, these data mirror the H_2 evolution results.
In order to understand the role of the WO_3 top layer and of the thickness on the photocatalytic performance, the light absorption properties of the different structures along with their photo-electrochemical behavior were investigated by measuring UV-Vis diffuse reflectance (DR-UV-Vis) and photocurrent spectra (see Figure 22 and Figure 23, respectively).

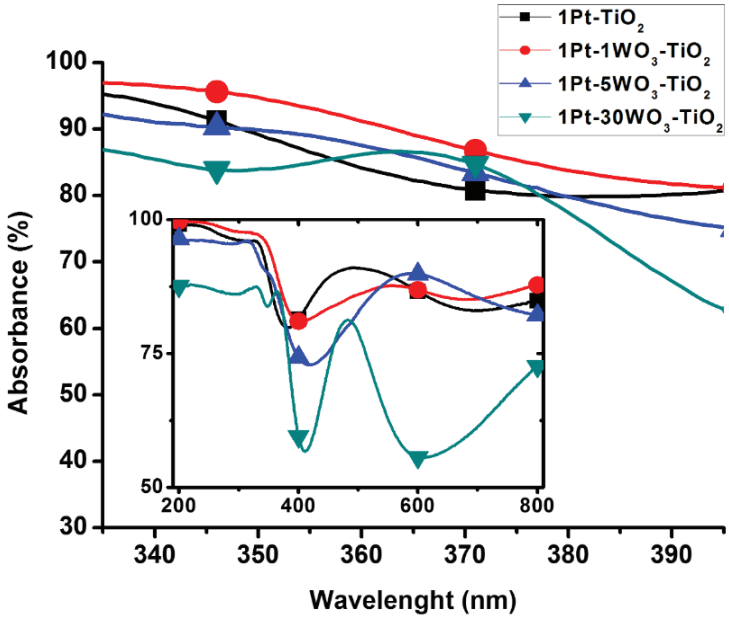

Figure 22. Detail of the DR-UV-Vis spectra of different TiO_2 structures in the region around 365 nm (i.e. wavelength used in this work for the photocatalytic experiments). Inset: DR-UV-Vis spectra measured in the 200-800 nm wavelength range.

Interestingly, only minor differences in terms of light absorbance between the various morphologies were observed at 365 nm (Figure 22).

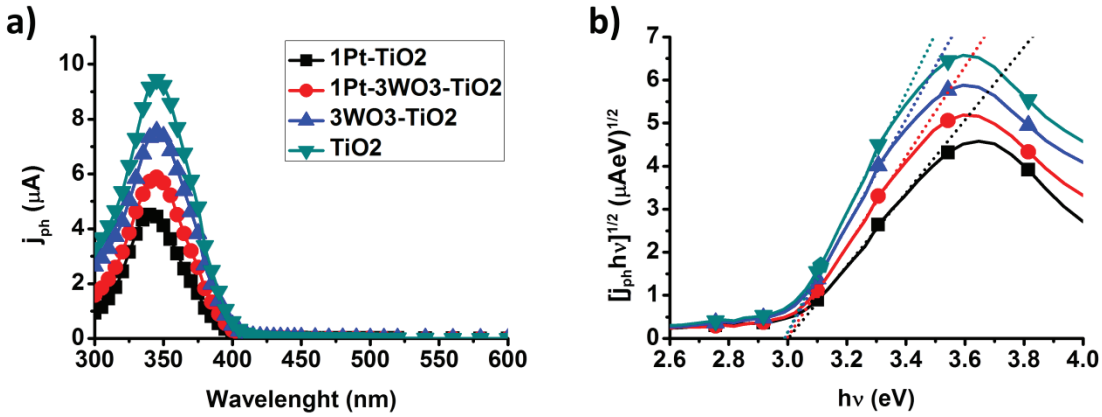

Figure 23. (a) Photocurrent spectra of different decorated TiO_2 systems. (b) Estimation of energy band-gap values from photocurrent spectra.

The observed photocurrent trend is: TiO_2 > $3WO_3$-TiO_2 > 1Pt-$3WO_3$-TiO_2 > 1Pt-TiO_2 (Figure 23a).

That is, pristine nanotubes outperform any other cocatalyst-decorated structures. Moreover, a virtually identical bandgap (~3.3 eV) can be estimated for the different structures (Figure 23b) [250].

The reason can be ascribed to:

- the band alignment (energetic situation) of the TiO_2/WO_3 interface with respect to the photo-anode architecture (Ti/TiO_2/WO_3) is in principle not adequate for efficient electron collection. In a photo-anode, an electron transfer cascade can be enabled by a heterojunction stack if photo-generated electrons are owing to the band alignment driven towards the electron collector scaffold (Ti metal substrate) – and holes are driven towards the semiconductor/electrolyte interface. However, since the WO_3 CB lies below the TiO_2 CB, photo-generated TiO_2 electrons may accumulate in WO_3 without contributing to photocurrent. This explains the lower photocurrent of WO_3-decorated structures compared to pristine TiO_2.
- Pt is in principle not needed at the photo-anode surface – electrons photo-generated in TiO_2 or WO_3-TiO_2 that are trapped by Pt nanoparticles cannot contribute to photocurrent. This explains the lower photocurrent of Pt-decorated structures compared to TiO_2 or WO_3-TiO_2. In addition, Pt nanoparticles may scatter light, and the underneath semiconductor (TiO_2 or WO_3-TiO_2 structures) could be exposed to a lower photon flux.

Under photo-electrochemical conditions, i.e. by applying a bias to the TiO_2 structures which is more positive than the TiO_2 flat band potential, the charge dynamics is dominated by electron diffusion towards the photo-anode back-contact (H_2 evolution takes place at a Pt counter electrode) while holes are driven, owing to the upward band bending, towards the TiO_2/electrolyte interface for water oxidation.

This is a completely different situation compared to the photocatalytic experiments carried out in the present work under open circuit conditions. Under these experimental conditions, electrons can be transferred by a cascade effect from TiO_2 to WO_3 and then onward to Pt; Pt nanoparticles are the electron reaction site where H_2 evolution takes place.

While it is commonly reported that the CB minimum of WO_3 lies below the CB minimum of TiO_2, the exact position of CB minimum and VB maximum of WO_3 can vary with experimental parameters, e.g. crystallographic phase [17,53,86,87,119,251–254], but even more importantly, the band positions can deviate significantly from "bulk" to nanostructured (supported) materials [255,256].

Owing to the natural upward bending of TiO_2 valence band in the nanotube walls (the walls are < 10 nm-thick), the most plausible fate for holes generated deep in TiO_2 is a facilitated transfer to the environment (oxidation site for hole-scavenger molecules). A dominant TiO_2 hole transfer to WO_3 is excluded since this would be in contrast to the evident electron accumulation observed for WO_3-TiO_2 architectures by EIS measurements under light irradiation (and considering also the short diffusion length of holes in TiO_2) [257]. ESI measurements on similar architectures demonstrated that under UV light illumination, TiO_2 CB electron are transferred from TiO_2 to WO_3 and then to the noble metal for H_2 evolution – this confirms that WO_3-TiO_2 energetic situation [251] is compatible with an electron transfer cascade mechanism for H_2 evolution.

Considering these results, it is clear that the light harvesting ability of the different structures (i.e. different W loadings) does not have a dominant effect on the photocatalytic performance – in other words, it is reasonable to assume that WO_3 is not the photoactive material in photocatalytic architecture but acts only as a buffer (transfer) layer for TiO_2 electrons, and the contribution to H_2 evolution of charges generated directly in WO_3 is negligible (also owing to the minimized amount of WO_3).

Thus, one can assume that the Pt-WO_3-TiO_2 structure is properly constructed only when the WO_3 top layer is sufficiently thin: in this case it can favor charge carrier separation by

electron transfer towards the top of the tube, through the WO_3 buffer layer, and then onward to the Pt NPs for H_2 evolution (as illustrated in Figure 24).

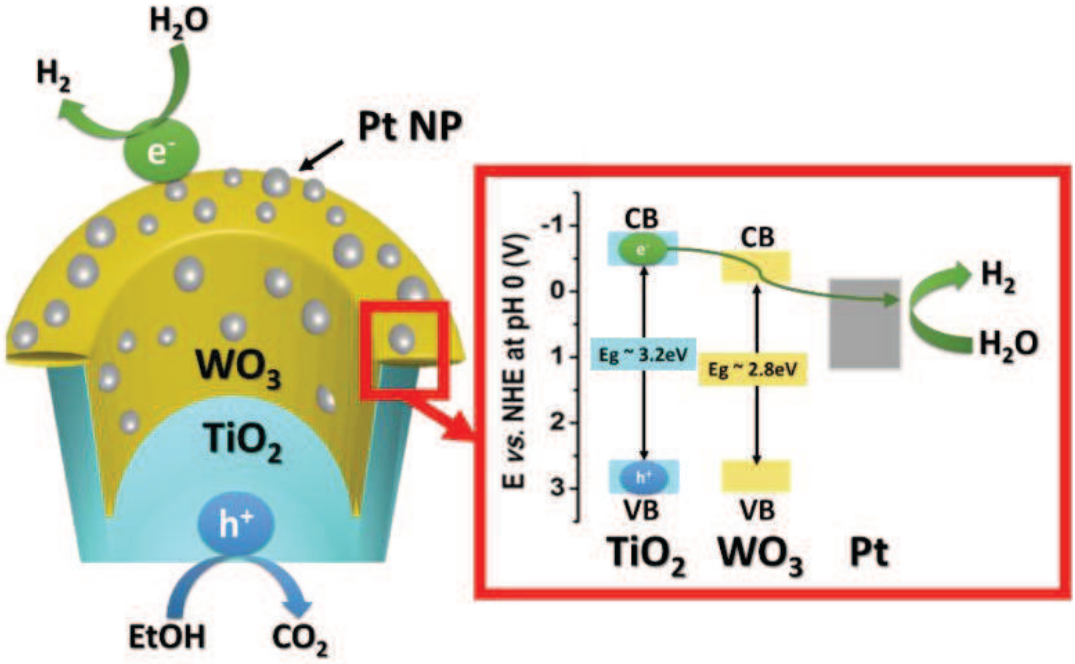

Figure 24. Scheme of the structure of the three-layered photocatalyst illustrating the band alignment (TiO_2-WO_3 [251] energetic situation) that allows for the proposed mechanism of electron transfer cascade.

In this construction, crucial is also the uncoated bottom of the TiO_2 cavities that allows for direct hole-transfer to the reaction phase (hole-scavenging). This explains also the low H_2 yield of the sample 1Pt-30WO_3-TiO_2, that is, a too thick WO_3 buffer layer not only blocks TiO_2 hole-transfer to the environment at the tube bottom, but also can make the electron transport across the WO_3 layer less efficient owing to an increased charge transfer resistance. These findings are in line with the proposed electron transfer cascade mechanism and well support EIS results obtained for similar stacked-architectures [84] for which charge accumulation can be observed in WO_3-TiO_2 structures under UV light illumination (TiO_2 CB electrons are transferred to WO_3), while the accumulated charge is depleted when Pt nanoparticles are decorated atop the WO_3 buffer layer (in the Pt-WO_3-TiO_2 architecture electrons are extracted by Pt and transferred to the environment for H_2 evolution).

Conclusions

We introduced the fabrication of an efficient photocatalytic platform based on an electron transfer cascade mechanism designed by site-selective decoration of the top of highly-ordered TiO_2 nanotubes with a well-defined WO_3-Pt cocatalyst stack. In contrast to previous works, we show that a morphological control with nanoscale precision of the cocatalyst-catalyst structure not only allows for a systematic assessment of the charge carrier dynamics and photocatalytic mechanism, but also is key to design functional composite architecture that can achieve strongly enhanced photocatalytic H_2 evolution efficiencies.

2.2. Templated dewetting-alloying of NiCu bilayers on TiO_2 NTs: an efficient noble metal-free photocatalyst for H_2 evolution

Reprinted (adapted) with permission from *ACS Catal.*, **2018**, *8* (6), pp 5298–5305, **DOI:** 10.1021/acscatal.8b01190, **Copyright © 2018 American Chemical Society**.

The results reported in this chapter were entirely obtained during my six-month period in Friedrich-Alexander University (FAU) of Erlangen-Nuremberg. My contribution has concerned the fabrication of all the employed photocatalytic materials and the evaluation of their performances towards photocatalytic hydrogen evolution. I contributed partially in all the characterizations here reported which were carried out in FAU except for TEM images which were collected in the Regional Centre of Advanced Technologies and Materials (RCPTM) of Olomouc. Finally, I contributed extensively in the drafting and finalization of the published article.

Abstract

Photocatalytic H_2 evolution reactions on pristine TiO_2 are characterized by low efficiencies due to trapping and recombination of charge carriers, and due to a sluggish kinetics of electron transfer. Noble metal (mainly Pt, Pd, and Au) nanoparticles are typically decorated as cocatalyst on the TiO_2 surface to reach reasonable photocatalytic yields. However, owing to the high cost of noble metals, alternative metal cocatalysts are being developed. Here we introduce an approach to fabricate an efficient noble metal free photocatalytic platform for H_2 evolution based on alloyed NiCu cocatalytic nanoparticles at the surface of anodic TiO_2 nanotube arrays. NiCu bilayers are deposited onto the TiO_2 nanotubes by plasma sputtering. A subsequent thermal treatment is carried out that leads to dewetting, that is, owing to surface diffusion the Ni and Cu sputtered layers simultaneously mix with each other and split into NiCu nanoparticles at the nanotube surface. The approach allows for a full control over key features of the alloyed nanoparticles such as their composition, work function and cocatalytic ability towards H_2 generation. Dewetted-alloyed cocatalytic nanoparticles composed of equal Ni and Cu amounts not only are significantly more reactive than pure Ni or Cu nanoparticles, but also allow to reach H_2 generation rates that can be comparable to those obtained by conventional noble metal (Pt) decoration of TiO_2 nanotube arrays.

Introduction

Since the ground-breaking work of Fujishima and Honda[34] in 1972, the photocatalytic production of H_2 by splitting of H_2O has been widely investigated. Among the different photocatalytic materials developed in the last decades, TiO_2 still represents one of the most explored and promising semiconductor metal oxides. In fact, not only is TiO_2 cheap, easily available, non-toxic, and stable against corrosion and photo-corrosion, [35,65] but most importantly, it has a suitable conduction band edge position to allow H_2O reduction to H_2, the fuel of the future. For TiO_2, the conduction band (CB) edge lies 0.45 eV higher than the redox potential of water. [258] Therefore, photo-generated conduction band electrons, promoted by UV light irradiation ($E_{g\,TiO_2}$~ 3.0-3.2 eV), are thermodynamically able (in terms of electron "exit" energy) to reduce H_2O to H_2. However, this reaction is characterized by low efficiencies owing to trapping and recombination of charge carriers, and due to a sluggish kinetics of electron transfer from TiO_2 to reactants.

A successful strategy to limit charge recombination in TiO_2 is provided by nanostructuring the semiconductor. Particularly, one-dimensional (1D) nanostructures, such as anodic TiO_2 nanotubes (NTs), have attracted great attention in the last years. [49,233] Aligned arrays of self-organized NTs with controllable morphology can be grown by a simple electrochemical anodization of Ti metal in a suitable electrolyte.[35,65,235] These highly-ordered and defined 1D structures promote directional charge transport and orthogonal electron–hole separation that lead to enhanced photocatalytic and photo-electrochemical efficiencies, owing to a more efficient charge separation and improved electron transport properties.[259]

On the other hand, limitations in charge transfer can be tackled by using a suitable cocatalyst, mostly noble metal nanoparticles (NPs), e.g. Pt, Au and Pd. [104] The most efficient metal-cocatalyst is Pt, which not only enables an efficient electron transfer at the TiO_2/environment interface yielding a favorable solid state (Schottky type) junction to TiO_2,[258] but also provides catalytic sites that enhance the hydrogen recombination reaction ($2H^0 \rightarrow H_2$).[260]

However, the high cost of Pt (or in general of noble metals) has meanwhile shifted the attention to alternative catalysts and cocatalysts composed of non-noble and cheaper metals. Interesting candidates are e.g. Ni and Cu. Nevertheless, the photocatalytic activity of TiO_2 decorated with non-noble metal cocatalysts is typically lower than that achieved by Pt decoration (under comparable deposition conditions).[107–111]

In recent work, photocatalysts composed by co-loaded Ni and Cu NPs on powdered titania were shown to enhance the H_2 evolution rate more than pure Ni or Cu particles,[261–264] Co-loaded NiCu NPs found also promising application in sensors,[265,266] dye photo-degradation processes [267] and selectively catalyzed organic reactions. [268–270] NiCu-TiO_2 structures are commonly prepared by a powder technology approach based on wet impregnation,[267,269] hydrothermal deposition,[262,270] thermal deposition followed by a chemical reduction,[263,268] laser ablation in liquid[261] and electrodeposition.[265]

Here we propose an alternative approach based on a templated dewetting-alloying principle of sputtered Ni and Cu metal bilayers on a highly defined TiO_2 nanotube surface.[120,271] The amount of Ni and Cu metal can be adjusted by the thickness of the metal sputtered layers (nm range). With a suitable thermal treatment, the metal films can, owing to surface diffusion, mix (alloy) with each other and simultaneously dewet, i.e. split into NiCu NPs of controllable composition, size and spacing, [120] at the surface of TiO_2 nanotubes. We show that dewetted-alloyed NiCu nanoparticles of an optimized composition lead to a significantly higher photocatalytic H_2 evolution efficiency compared to pure Ni or Cu nanoparticles that are decorated on the nanotubes under similar conditions. Even more remarkable, the H_2 generation rate of NTs decorated with dewetted-alloyed NiCu NPs is comparable with that obtained by Pt decoration (under optimized Pt deposition conditions), particularly under solar light irradiation.

Experimental Section

Fabrication of the TiO_2 nanocavity array

Ti foils (Advent Research Materials, 0.125 mm thickness, 99.6+% purity) were degreased by sonicating in acetone, isopropanol, and deionized water and then were dried in a N_2 stream. Then, the Ti foils were anodized to fabricate the highly ordered TiO_2 nanotube arrays in a hot electrolyte based on 3 M HF in o-H_3PO_4 (Sigma- Aldrich). For the anodic growth, a two-electrode configuration was used, where the Ti foil (15 mm × 15 mm) and a Pt sheet were the working and counter electrodes, respectively. The anodization experiments were carried out by applying a potential of 15 V (for 2 h) using a DC power supply (VLP 2403 Voltcraft). After anodization, the TiO_2 nanotube arrays on Ti metal substrates were rinsed with ethanol and dried under N_2 stream. The compact TiO_2 layers were prepared by anodization of Ti foils in aqueous 0.5 M H_2SO_4, at 20 V and room temperature, for 30 min.

Metal sputtering-coating and thermal treatment

In order to form Ni, Cu, alloyed NiCu and Pt nanoparticles on the TiO_2 nanotube arrays, a plasma-sputtering machine (EM SCD 500, Leica) was used to sputter-coat Cu, Ni and Pt metal thin films using a 99,90% pure Cu target (Baltic Praeparation e.K.), 99,98% pure Ni target (Hauner Metallische Werkstoffe) and a 99,99% pure Pt target (Hauner Metallische Werkstoffe), respectively. In any case the applied sputtering current was 16 mA and the pressure of the sputtering chamber was set at 10^{-2} mbar of Ar. The amount of sputtered material was in-situ determined by an automated quartz crystal monitor, and is reported in this work as nominal thickness of the sputtered film. Subsequently, the samples were annealed at 450°C (1 h) in Ar atmosphere (Ar flux = 10 L h^{-1}) to induce dewetting.

Characterization of the structures

X-ray diffraction (XRD) with an X′pert Philips MPD (equipped with a Panalytical X'celerator detector) was employed to examine the crystallographic properties of the materials. A field-emission scanning electron microscope (FE-SEM, Hitachi S4800) and a transmission electron microscope (TITAN 60–300, FEI, USA) were used to characterize the morphology (by SEM and HAADF-TEM) and chemical composition (by EDS-TEM) of the samples. The chemical composition of the samples was analyzed by X-ray photoelectron spectroscopy (XPS, PHI 5600, US) and peak positions were calibrated with respect to the Ti2p peak at 458 eV. UV-Vis diffuse reflectance spectra of the different Ni-, Cu- and NiCu-decorated TiO_2 nanotubes were measured with an Avantes spectrophotometer (AvaSpec-ULS2048L-USB2/16S-002-300), equipped with deuterium-halogen lamp (AvaLight-DH-S-BAL) and integrating sphere (AvaSphere-30-REFL).

Photocatalytic measurements

Photocatalytic measurements for H_2 generation were carried out by irradiating the oxide films in a 20 vol% ethanol–water solution (ethanol was used as hole-scavenger) in a quartz tube sealed with a gas-tight cap. As light sources we used a LED UV light (Opsytec, λ = 365 nm, beam size = 0.785 cm^2, power of 105 mW cm^{-2}) and a solar simulator (simulated AM 1.5 illumination provided by a 300 W Xe with a Solarlight optical filter) with an irradiation power of 100 mW cm^{-2} (the light intensity was measured prior to the experiments using a calibrated Si photodiode). The ethanol-water solution (kept under static conditions during the

runs) and the cell head-space (volume = 5.12 mL) were purged with N_2 gas for 15 min prior to photocatalysis. N_2-purging is needed to remove O_2 from the liquid phase and from the head space – O_2 would reduce the efficiency of H_2 generation by competitive photocatalytic reduction to $O_2^{-\bullet}$ (O_2 can react with conduction band electrons).

The amount of produced H_2 (which was accumulated over the irradiation time in the head space of the tube) was measured by using a gas chromatograph (GCMSQO2010SE, Shimadzu) equipped with a thermal conductivity detector and a Restek micropacked Shin Carbon ST column (2 m × 0.53 mm). GC measurements were carried out at a temperature of the oven of 45 °C (isothermal conditions), with the temperature of the injector set at 280 °C and that of the TCD fixed at 260 °C. The flow rate of the carrier gas, i.e., argon, was 14.3 mL min^{-1}. The experiments lasted 4-30 hours.

Apparent quantum efficiency (AQE)

The apparent quantum efficiency (AQE) was determined for the most active photocatalyst under monochromatic UV light illumination taking into account the following experimental details:

Illumination source = LED UV light, λ = 365 nm, power density = 105 mW cm^{-2}

Sample 5Ni5Cu-TiO_2 leads to the highest H_2 evolution rate = 6.0 μL h^{-1} cm^{-2} (data in Figure 30b)

The apparent quantum efficiency can be calculated as in Equation 33:

$$AQE\ \% = \frac{2 \times generated\ H_2\ molecules}{\varphi\ (photon\ flux)}\ 100\% \qquad \text{(Equation 33)}$$

Taking into account the following equations:

$$r_{H_2} = \frac{V}{t\ A} \qquad \text{(Equation 34)}$$

$$p\ V = n\ R\ T \qquad \text{(Equation 35)}$$

$$\varphi\ (photon\ flux) = \frac{H\ \lambda}{h\ c} \qquad \text{(Equation 36)}$$

Where:

r_{H2} = H_2 generation rate $[\frac{L}{s\ m^2}]$

t = illumination time [h]

A = illuminated sample area [m^2]

p = pressure [atm]

V = volume of generated H_2 [L]

n = moles of generated H_2 [mol]

R = gas constant [0.0821 $\frac{L\ atm}{K\ mol}$]

T = temperature [K]

φ = photon flux [$\frac{\#\ of\ photons}{s\ m^2}$]

H = power density [$\frac{W}{m^2}$]

λ = wavelength [m]

h = Planck's constant [6.63 x 10^{-34} J s]

c = speed of light [3.0 x 10^8 $\frac{m}{s}$]

Equation 33 can be expressed as follows, using Equations 34-36:

$$AQE\ \% = \frac{2\, r_{H_2} \frac{p}{RT} N_A}{\frac{H\,\lambda}{h\,c}}\ 100\% \qquad \text{(Equation 37)}$$

Where:

N_A = Avogadro's number [6.022 x 10^{23} $\frac{\#\ of\ molecules}{\#\ of\ moles}$]

2 = correction factor assuming that 2 photons are required to generate 1 H_2 molecule

The resulting AQE is ~ 0.043%. The value is relatively low compared to data in the literature (e.g. [241]). This can be explained considering that the short depth of the TiO_2 nanotubes used in the present work (~ 200 nm) may not lead to full light absorption and also by taking into account that that a non-noble metal cocatalyst was used – in contrast, in ref. [241] longer nanotubes (15 μm) are used that are loaded with noble metal (Pt) cocatalyst nanoparticles.

Optimization of the annealing, TiO_2 crystallization and metal dewetting parameters

The effect of dewetting time (as well as of other parameters e.g. temperature, metal film thickness) on kinetics and morphological evolution of metal thin films has been discussed in the literature by various authors (e.g. [272–274]). In general, for polycrystalline metal layers with a thickness of few tens of nm exposed to T in the 400-600°C (i.e. under experimental conditions that are comparable to those adopted in our work), the morphological evolution of metal films occurs to a large extent within the first 10-20 minutes. Typically, thinner layers dewet faster. Dewetting may be considered completed when parameters such as substrate coverage, metal particle size and crystallographic domain size remain constant with increasing annealing time.

In the present work key is that NiCu dewetting-alloying takes place at the same time of TiO_2 NT crystallization. While dewetting may be completed within < 30 minutes, previous work on anodic TiO_2 nanotube layers [35,65,258] for photocatalysis and photo-electrochemical application reveals that a set of most suitable annealing conditions to reach an optimized crystallization of TiO_2 is a temperature of ~ 450°C and an annealing time of ~ 1 h. Shorter times may lead to poor TiO_2 crystallization and also to an uncompleted metal dewetting. On the other hand, annealing time > 1 h lead to an extensive formation of TiO_2 rutile phase in the NTs that was found detrimental for photocatalytic H_2 evolution [275].

The heating rate may have an effect on the morphology of the dewetted metal films (and therefore on the photocatalytic activity of the metal/TiO_2 NT structures) if the dewetting process has not reached the equilibrium for a given dewetting time and/or dewetting temperature.

Calculation of cell parameters from XRD data

The predicted and experimental cell parameter data are obtained from the XRD data by applying the equations below.

According to the Bragg's law: $2\,d\sin\theta = n\,\lambda$ (Equation 38)

Thus: $d = \lambda / (2\sin\theta)$

Where d is the lattice spacing, λ = 1,5406 Å, and θ is determined as the maximum of the lorentzian fitting of the (111) reflection for each sample (data in Table 3 and Figure 30d).

In the case of Ni, Cu and NiCu alloys: $d = a / (h^2 + k^2 + l^2)^{1/2}$ (Equation 39)

Where “a” is the lattice parameter, and the Miller indices h, k and l = 1.

Thus: $a = d / (3)^{½}$

According to the Vergard’s law: $a_{AB} = x\ a_A + (1-x)\ a_B$ (Equation 40)

Where x is the molar fraction of A in the AB alloy.

Results and Discussion

In the present work we use short aspect ratio TiO_2 NTs as photocatalytically active surface and patterned substrate for dewetting. The TiO_2 NT arrays are grown on Ti foils by self-organizing electrochemical anodization in a hot H_3PO_4/HF electrolyte.[271] Figure 25a and Figure 26a shows that these NTs are almost ideally hexagonally packed, and each NT has an individual inner diameter of ~ 90 nm, a depth of ~ 180 nm and wall thickness of ~ 10 nm. These short and well-defined nanotubes can easily be coated with metal films (Ni and Cu in this work) by a plasma sputtering technique.[257,276]

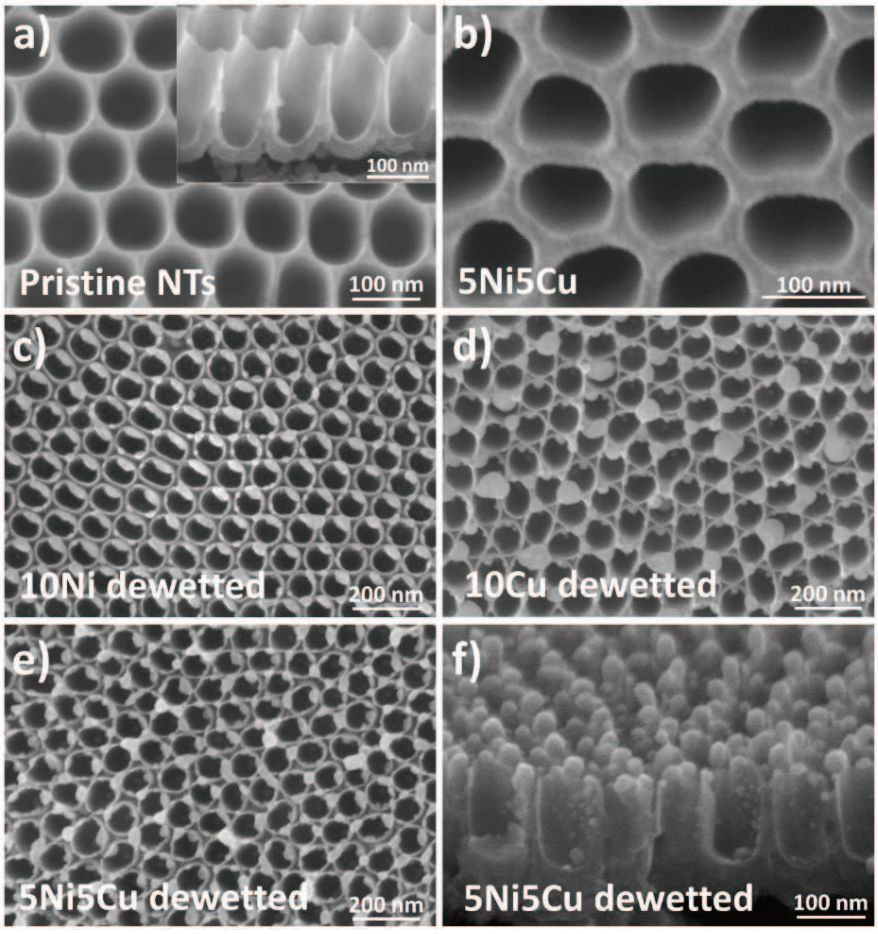

Figure 25. SEM images of various TiO_2 nanotube arrays. (a) pristine (Inset: cross-sectional view); (b) coated with a NiCu bilayer (5 nm Ni – 5 nm Cu); (c) coated with a 10 nm thick Ni layer and dewetted at 450°C; (d) coated with a 10 nm thick Cu layer and dewetted at 450°C; (e,f) coated with a NiCu bilayer (5 nm Ni – 5 nm Cu) and dewetted at 450°C (f shows the cross-sectional view).

Examples of the resulting structures are illustrated in Figure 25b and Figure 26b,c. These structures are formed by sputter-coating on the TiO_2 NTs a Cu film (nominal thickness 10 ± 0.5 nm), a Ni film (10 ± 0.5 nm) or a NiCu bilayer deposited by sequential sputtering (5 ± 0.5

nm for each metal, for an overall nominal thickness of ~ 10 nm). In any case the as-sputtered metal films homogeneously coat the TiO_2 NT surface.

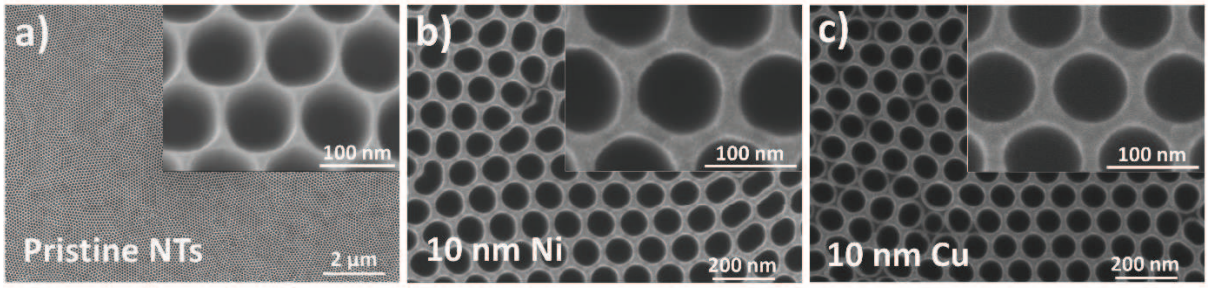

Figure 26. SEM images of different TiO_2 nanotube arrays: (a) pristine nanotube; (b) nanotube coated with a 10 nm thick Ni layer; (c) nanotube coated with a 10 nm thick Cu layer.

Afterwards, a thermal treatment at 450°C (1 h) leads to dewetting (Figure 25c-e) of the metal films at the TiO_2 NT surface. Dewetting takes place as thin metal films are unstable when heated up, and tend to split-open and agglomerate forming metal islands (particles) via surface diffusion. Dewetting of a given metal thin film typically initiates at temperatures between 1/3 and 2/3 of the metal melting point [121]; thus, the occurrence of Ni and Cu dewetting at 450°C is well in line with their melting point (T_m Cu = 1085°C; T_m Ni = 1455°C). Such thermal treatment leads at the same time to the crystallization of the NT substrate into a mixed anatase-rutile TiO_2 phase (see XRD data in Figure 27).

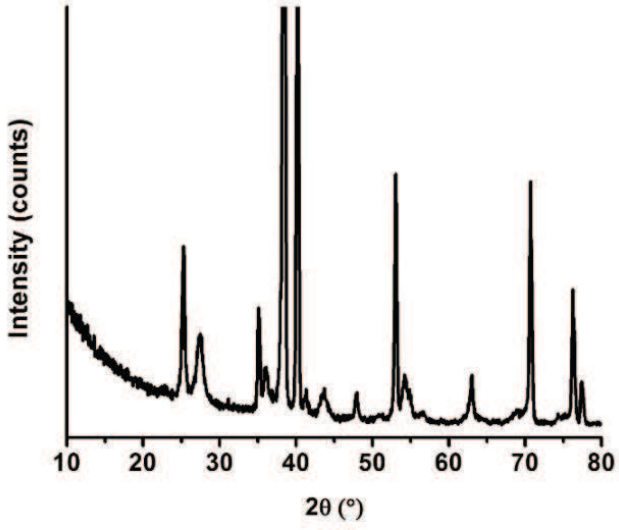

Figure 27. XRD pattern of sample 5Ni5Cu crystallized (and dewetted) in argon at 450°C. TiO_2 NTs annealed at 450°C in argon gas are converted into an anatase-rutile mixed phase. The XRD peaks at 2θ = 25.3° and 27.5° can be assigned to TiO_2 (101) anatase and (110) rutile reflections, respectively.

The average size of the dewetted metal particle is found to be independent of the initial composition of the metal film. Both Ni and Cu layers, as well as NiCu bilayers, dewet into ~ 30-40 nm-sized NPs (see NP size distribution in Figure 28a-c). Compared to the dewetted Ni

NPs that are relatively close to each other and homogeneously decorated on the substrate, the dewetted Cu NPs are less densely distributed and more scattered at the TiO_2 NT surface. This may suggest that Ni and Cu exhibit slightly different dewetting "modes", e.g. owing to a different surface diffusion or substrate wettability, and the dewetting behavior of NiCu bilayers may depend on the initial composition of the bilayer.

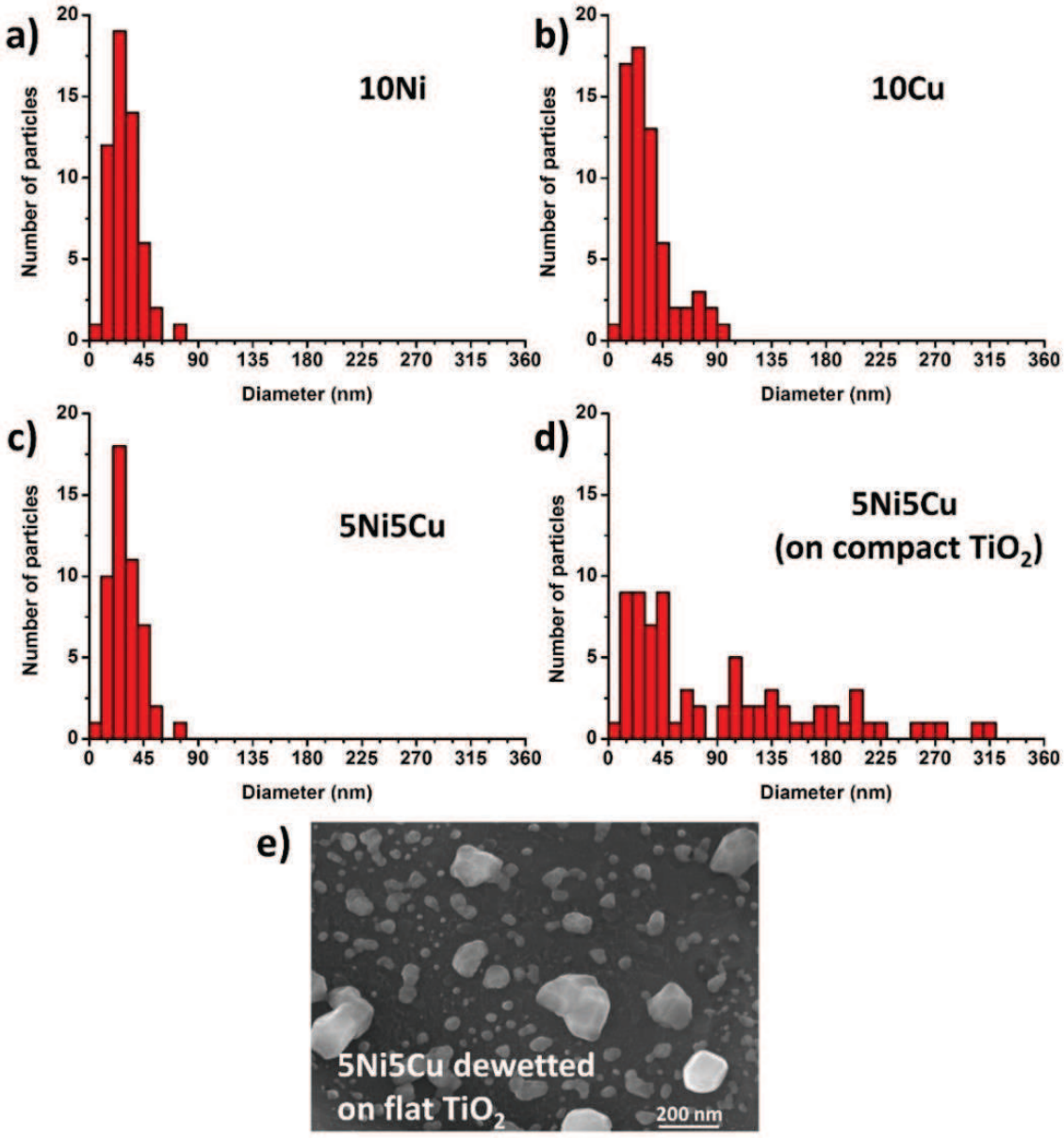

Figure 28. (a-d) Metal particle size distribution for samples (a) 10Ni, (b) 10Cu, (c) 5Ni5Cu and (d) 5Ni5Cu on compact TiO_2 (the corresponding structure is shown in (d)). The cocatalyst nanoparticle size was estimated from the SEM images of the various samples by using the software Image J. For each sample, the average size was determined from ~ 70 particles. (e) SEM image of a 5 nm Ni – 5 nm Cu bilayer sputter-dewetted on a compact TiO_2 anodic layer under identical experimental condition (450°C, 1 h, in argon atmosphere). The compact TiO_2 layers were prepared by anodization of Ti foils in aqueous 0.5 M H_2SO_4, at 20 V and room temperature, for 30min.

Key role in tailoring (limiting) the size of the dewetted metal particles to a few tens of nm is played by the patterned TiO_2 NT surface that provides high surface energy sites, such as the NT rims, that act as preferential locations that initiate dewetting – in other words, the defined TiO_2 NT morphology enables templated-dewetting.[121] Note in fact that, on a flat TiO_2 surface, NiCu bilayers of comparable composition and thickness split into particles that can be as large as ca. 300 nm, with an average size > 100 nm that is one order of magnitude bigger than on the TiO_2 NT surface (see Figure 28d,e). Such results are obviously of large interest e.g. in the field of heterogeneous catalysis, where metal particle size, distribution and composition are crucial parameters for reactivity control.[270]

By systematically varying the Ni and Cu relative amount (i.e. nominal thickness), we prepared a series of TiO_2 NT arrays decorated with dewetted NiCu particles with defined compositions – a summary of the prepared samples and nominal cocatalyst composition is in Table 2, while their morphology is illustrated in Figure 29. The structures were investigated as photocatalyst for H_2 evolution from ethanol-water under UV light illumination (365 nm, LED, 105 mW cm^{-2}).

Table 2. Summary of the samples tested in this work

Sample Name*	Nominal thickness (nm)		Nominal composition (x_{Ni})	Real thickness (nm)		Real composition (x_{Ni})
	Ni	Cu		Ni	Cu	
5Cu	5	-	0	-	4.3	0
10Cu	10	-	0	-	10.0	0
3Ni7Cu	3	7	0.3	2.8	6.5	0.30
5Ni5Cu 400°C	5	5	0.5	5.2	4.7	0.53
5Ni5Cu 450°C	5	5	0.5	4.5	5.2	0.46
5Ni5Cu 500°C	5	5	0.5	5.5	4.7	0.54

7Ni3Cu	7	3	0.7	6.6	3.5	0.65
10Ni	10	-	1	9.5	-	1.0
5Ni	5	-	1	4.2	-	1.0

*The order of the metals refers to the sputtering sequence.

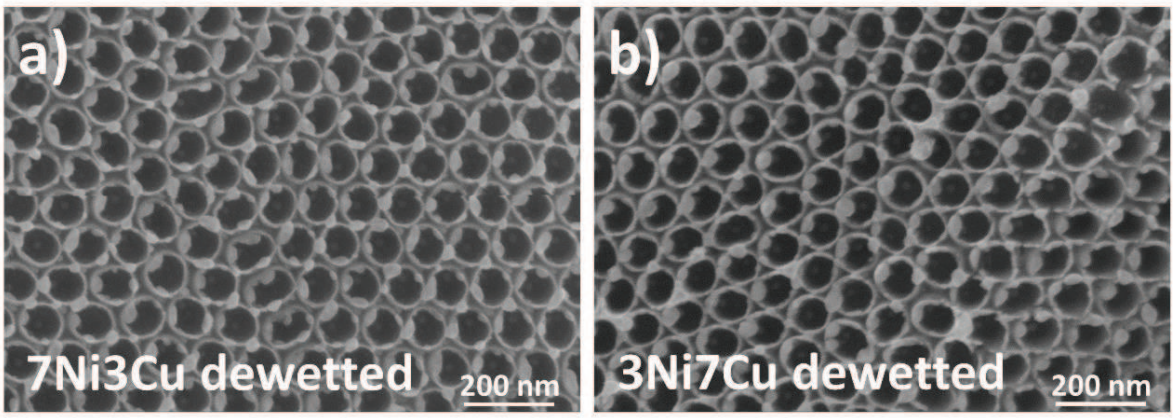

Figure 29. SEM images of TiO_2 nanotube arrays decorated with dewetted-alloyed NiCu nanoparticles of different compositions: (a) 7Ni3Cu and (b) 3Ni7Cu.

The photocatalytic results are summarized in Figure 30a. The data show that pristine TiO_2 NTs ("TiO_2") exhibit a negligible photocatalytic H_2 generation (0.04 µL h^{-1} cm^{-2}). TiO_2 NTs modified with dewetted pure Cu or Ni NPs ("10Cu" and "10Ni") show a slightly improved photocatalytic H_2 generation (1.62 µL h^{-1} cm^{-2} and 0.44 µL h^{-1} cm^{-2}, respectively).

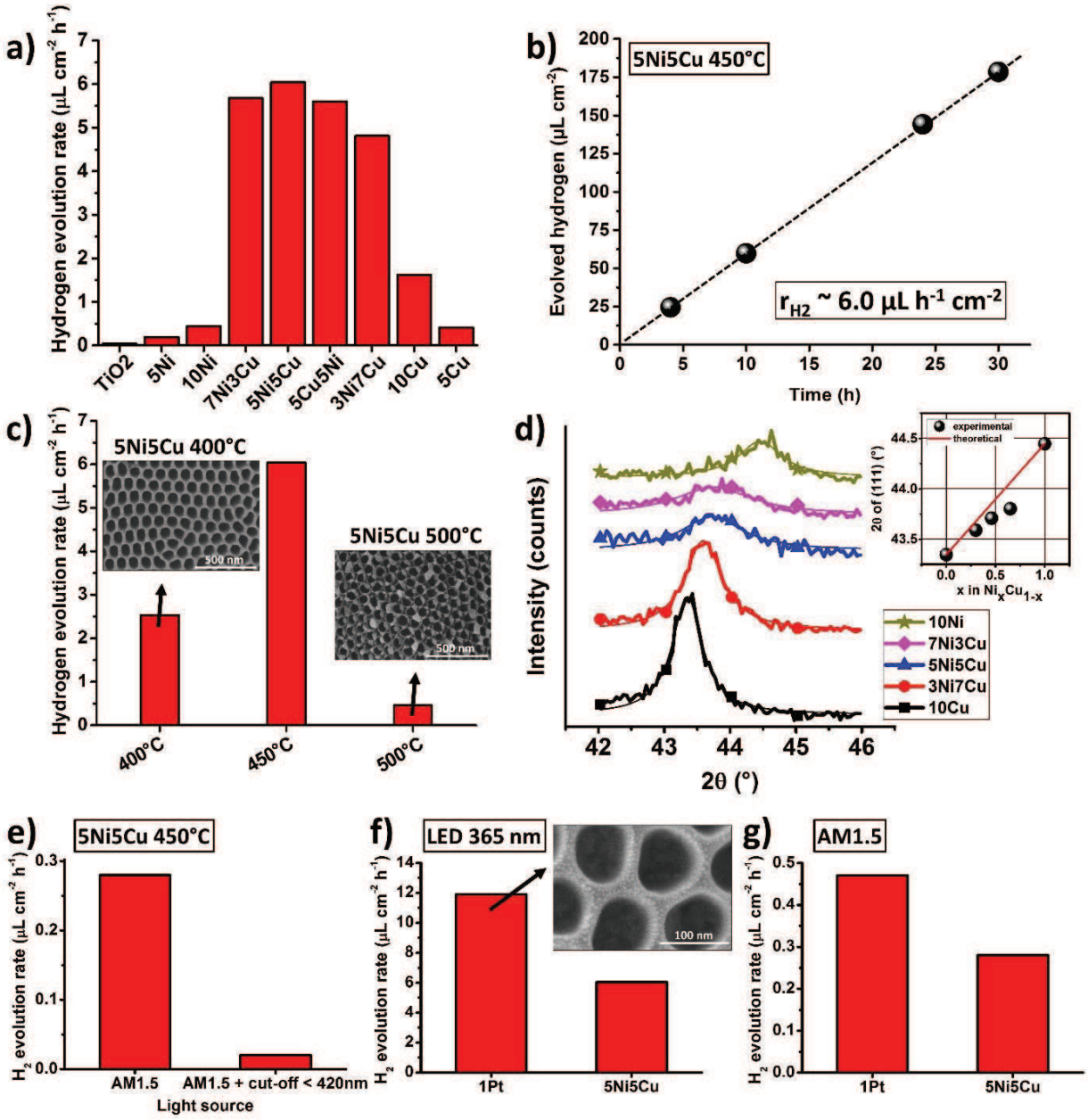

Figure 30. (a) photocatalytic H_2 evolution rate of different photocatalysts under UV light illumination (LED, 365 nm) as a function of loading, composition and sputter-deposition sequence of the metal cocatalyst; (b) H_2 amount evolved over time under UV light illumination (LED, 365 nm) for sample 5Ni5Cu dewetted at 450°C; (c) photocatalytic H_2 evolution rate for sample 5Ni5Cu under UV light illumination (LED, 365 nm) as a function of the annealing temperature; (d) XRD patterns of TiO_2 nanotube decorated with Ni, Cu or alloyed NiCu NPs of various compositions. Inset: shift of the (111) XRD reflection as a function of the composition of the NiCu alloy NPs; (e) photocatalytic H_2 evolution rate for sample 5Ni5Cu (dewetted at 450°C) under unfiltered and filtered (420 nm cut-off filter) simulated solar light illumination (AM1.5G); (f,g) photocatalytic H_2 evolution rate for sample 5Ni5Cu (dewetted at 450°C) compared to a Pt- TiO_2 benchmark photocatalyst under (f) UV light (LED, 365 nm) and (g) simulated solar light illumination (AM1.5G).

Remarkably, cocatalytic NPs formed by dewetting NiCu bilayers (7Ni3Cu, 5Ni5Cu and 3Ni7Cu) lead in any case to a clearly higher photocatalytic efficiency compared to pure Ni or Cu NPs (using a similar loading). The improvement in H_2 generation correlates with the Ni-Cu relative amount, and is maximized when Ni and Cu are in equal amounts; the highest

photocatalytic activity is measured for TiO_2 NT structures decorated by dewetting a sequentially sputtered 5 nm Ni – 5 nm Cu bilayer ("5Ni5Cu-TiO_2"). These structures lead to a H_2 evolution rate of 6.04 μL h^{-1} cm^{-2}, which is ~ 14 and ~ 4 times higher than that of "10Ni" and "10Cu", respectively. We also found that in this case the sputter deposition sequence of Ni and Cu metal films does not play a crucial role, i.e. samples 5Ni5Cu and 5Cu5Ni lead to almost identical H_2 evolution rates (6.04 and 5.60 μL h^{-1} cm^{-2}, respectively). The apparent quantum efficiency (AQE) for the most active photocatalyst (e.g. 5Ni5Cu) under monochromatic UV light illumination is ~ 0.043%.

The results of a 30 h long photocatalytic run (Figure 30b) reveal that H_2 is evolved at a constant rate. Also, SEM images of the photocatalyst taken after 30 h long photocatalytic runs are virtually identical to those of the as-prepared (not used) photocatalyst (Figure 31). This proves that the NiCu-TiO_2 photocatalysts are stable, and occurrence of deterioration phenomena such as (photo-)corrosion or fall-off decay of the metal cocatalyst are excluded.

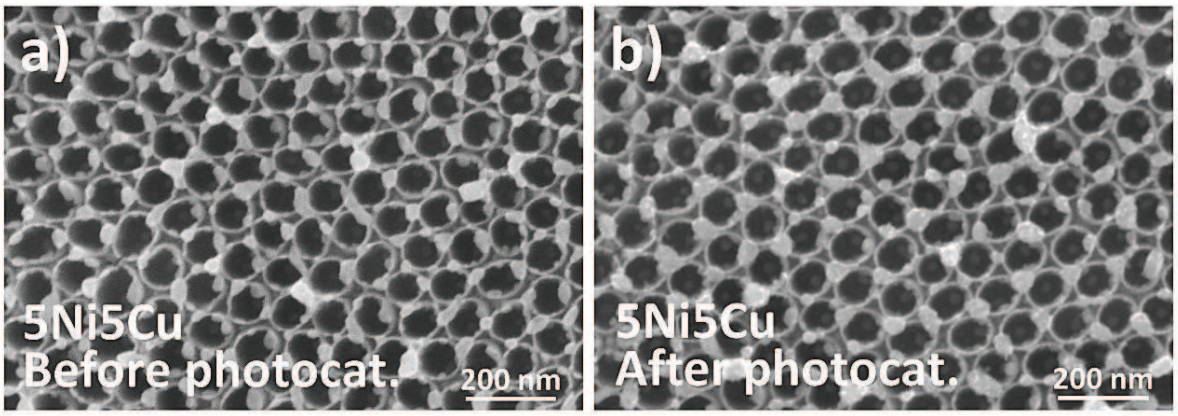

Figure 31. SEM images of TiO_2 nanotube arrays coated with a NiCu bilayer (5 nm Ni – 5 nm Cu) and dewetted at 450°C. The images are taken (a) before and (b) after the photocatalytic H_2 evolution runs.

The data in Figure 30c show that the photocatalytic improvement is a direct consequence of dewetting. The morphology of structures treated in Ar at 400°C is virtually identical to that of as-sputtered materials, i.e. such temperature does not induce dewetting of the NiCu bilayer, and the resulting H_2 generation rate is significantly lower than that of photocatalysts dewetted at 450°C. Reasons for the higher activity obtained upon annealing-dewetting at 450°C are various: (i) dewetting exposes free TiO_2 surface – this is crucial for the hole-mediated reaction (ethanol oxidation); (ii) metal nanoparticles formed by dewetting are alloyed (while the as-sputtered film is a Ni-Cu bilayer – discussed below); (iii) dewetted metal NP exhibit higher surface area compared to as-sputtered metal films; (iv) dewetting

forms localized Schottky junctions at the TiO_2 NT surface; and (v) upon dewetting, shading effects of the metal cocatalyst are reduced and a higher photon flux can reach the TiO_2 substrate. Nevertheless, although the annealing at 500°C also induces dewetting, it leads to a relatively low H_2 evolution performance – as reported by Yoo et al.,[275] this is due to an extensive formation of TiO_2 rutile phase in the NTs for annealing T > 450°C.

Reference samples fabricated by dewetting smaller amounts of Cu or Ni, e.g. samples "5Cu" and "5Ni", lead to H_2 generation rates (0.41 μL h^{-1} cm^{-2} and 0.19 μL h^{-1} cm^{-2}, respectively) that are even lower than that of 10Cu and 10Ni (Figure 30a). This means that the improved activity of TiO_2 NTs decorated with dewetted NiCu NPs cannot be simply ascribed to the Ni or Cu loading. Moreover, one may consider that if Ni and Cu could ideally be deposited on the TiO_2 NTs without undergoing alloying, the resulting H_2 evolution rate would virtually be the sum of those of samples 5Ni and 5Cu, i.e. 2.1 μL h^{-1} cm^{-2} which is still ~ 3 times lower than that obtained by alloying similar Ni and Cu cocatalyst amounts (sample 5Ni5Cu leads to ~ 6 μL h^{-1} cm^{-2}) – this results supports the synergy enabled by alloying Ni and Cu to form NiCu alloyed nanoparticles as TiO_2 cocatalyst for noble metal free photocatalytic H_2 evolution.

To clarify the reason for the photocatalytic improvement, we characterized the different samples by UV-Vis diffuse reflectance spectra, XRD, XPS and TEM, particularly in view of the morphology and physicochemical features of the dewetted Ni, Cu of NiCu particles.

The UV-Vis diffuse reflectance spectra of the different Ni-, Cu- and NiCu-decorated TiO_2 nanotubes are shown in Figure 32. While the spectra differ from each other, probably as a consequence of the different composition of the metal cocatalyst nanoparticles, the trend of light absorption at 365 nm (i.e. λ used for the photocatalytic experiments) does not support the trend of photocatalytic efficiency (see Figure 32b) – in other words, the photocatalytic enhancement caused by TiO_2 decoration with alloyed NiCu nanoparticles cannot be only ascribed to light absorption features.

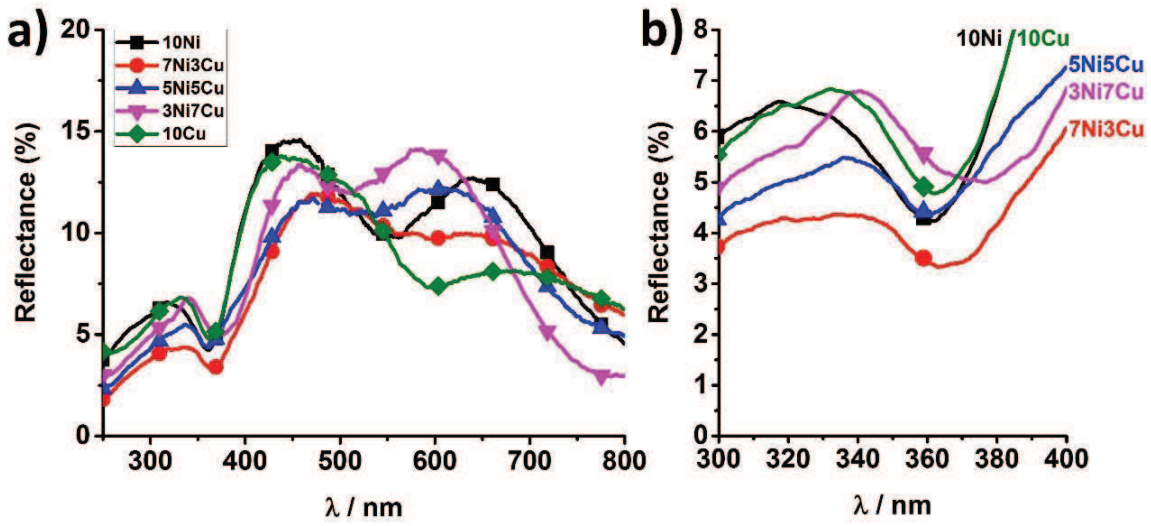

Figure 32. UV-Vis diffuse reflectance spectra of various Ni-, Cu- and NiCu-decorated TiO_2 nanotubes measured in the (a) 250-800 nm and (b) 300-400 nm range.

XRD results are compiled in Figure 30d. For TiO_2 NTs decorated with dewetted Cu NPs (10Cu), the peaks at 43.3° and 50.4° are indexed as the Cu (111) and (200) planes.[277] For Ni NP decorated TiO_2 NT (10Ni), the XRD signals at 44.4° and 51.9° are assigned to Ni (111) and (200) diffraction peaks.[278]

Interestingly, for TiO_2 NTs decorated with dewetted NiCu particles of various compositions, the (111) diffraction peak shifts from 43.3° (pure Cu) to 44.4° (pure Ni) with increasing the Ni loading, while no reflection of pure Ni or Cu could be detected. In other words, the (111) diffraction signal for dewetted NiCu particles shows a shift that correlates well with the composition of the NiCu bilayer. These results fit well the Vegard's law [261,279] that describes the correlation between the XRD peak position of a binary AB metal alloy with respect to the content of the alloying metal elements A and B (see Figure 33 and data in Table 3).

Table 3. Summary of the XRD data obtained for samples with different Cu and Ni composition. (see equations reported in the Experimental section in "calculation of cell parameters from XRD data").

Sample name	Real composition (x_{Ni})	Peak position 2θ (°)	d (Å)	a predicted (Å)	a experimental (Å)
10Cu	0.00	43.347	2.086	3.613	3.613
3Ni7Cu	0.30	43.590	2.075	3.593	3.587
5Ni5Cu	0.46	43.709	2.069	3.584	3.573
7Ni3Cu	0.65	43.803	2.065	3.577	3.557
10Ni	1.00	44.447	2.037	3.528	3.528

Thus, one can conclude that dewetting of NiCu bilayers at the surface of TiO_2 NTs forms NiCu alloyed NPs. These results are in principle well in line also with the full miscibility for any composition of the NiCu alloy system. The results of the fitting based on Vegard's law (Figure 33 and Table 3) suggest that the composition of the alloyed NPs is in line with that of the NiCu bilayer – the small deviation from the predicted trend (Inset in Figure 30d and Figure 33) may originate from the fact that the thermodynamics of bulk NiCu alloys may not apply in the same way to nanosized alloyed particles.

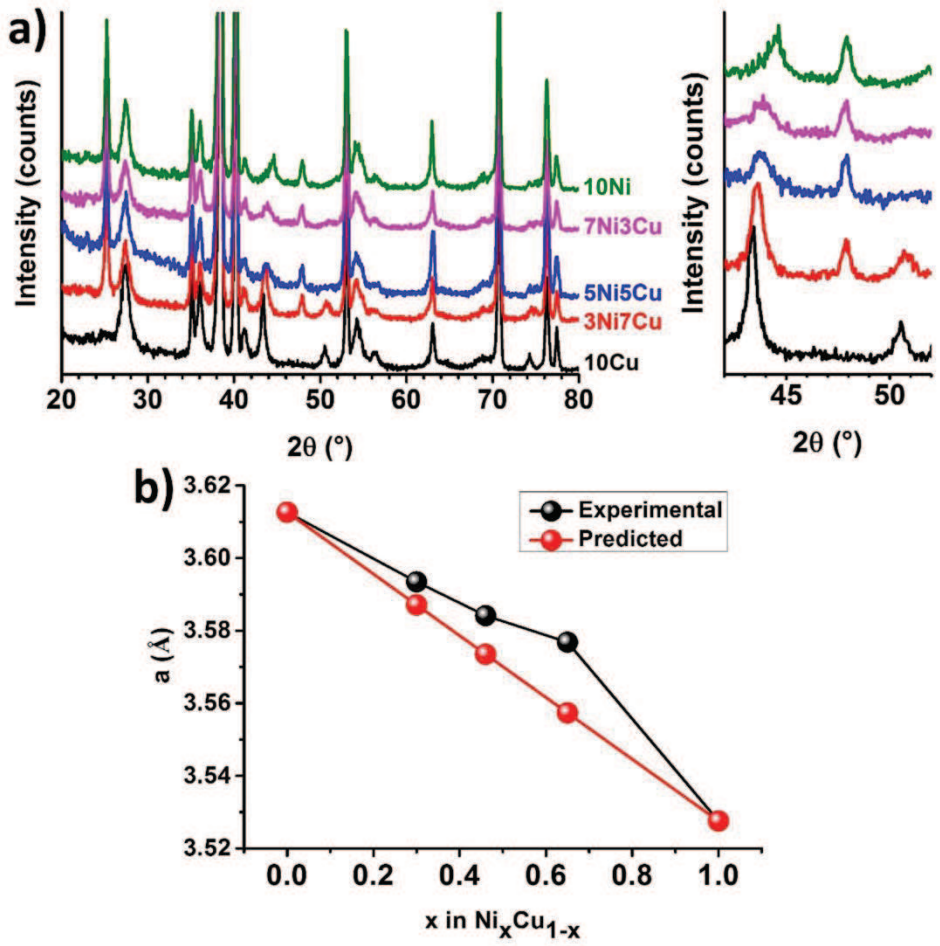

Figure 33. (a) XRD patterns of TiO_2 nanotube arrays decorated with dewetted-alloyed NiCu nanoparticles of different compositions. Inset: detail of the XRD patterns in the 42-52° 2θ range. (b) Predicted and experimental cell parameter (a) plotted as a function of the composition of the alloyed NiCu NPs. The composition is expressed as molar fraction of Ni. The predicted and experimental cell parameter data are obtained from the XRD results by applying the Vergard's law. Additional data and equations are reported in Table 3 and in the experimental section, respectively. The patterns are shown in the full range (i.e. 20-80°) as well as in the 42-50° range (Inset) to highlight the (111) and (200) reflections of the NiCu particles. The position of peak attributed to the (111) reflection (at 43.3-44.4°) is taken into account as reference signal to evaluate the NiCu composition. One can also notice that another series of peaks (attributed to the (200) reflection) appear in the 50.4-51.9° range. While also for these peaks a shift can be observed that correlates with the NiCu particle composition, this signal becomes weak with increasing the Ni composition (this is well in line with previous work[280]). Besides, we observed that in the presence of only Cu, the TiO_2 NTs undergo crystallization forming mainly rutile phase.

The improved photocatalytic activity of TiO_2 NTs decorated with dewetted-alloyed NiCu NPs is therefore attributed on the one hand to the specific cocatalyst composition that can lead to a faster H atom adsorption/recombination over Ni cocatalytic centers combined with a more favorable H_2 molecule desorption from adjacent Cu sites [281,282] – see Scheme 1. This mechanism can also take place in the case of NiCu particles with an inhomogeneous composition: H atoms may adsorb and recombine efficiently at Ni rich sites, while desorption of H_2 molecules may occur from the nearby Cu rich sites in the same cocatalyst nanoparticle.

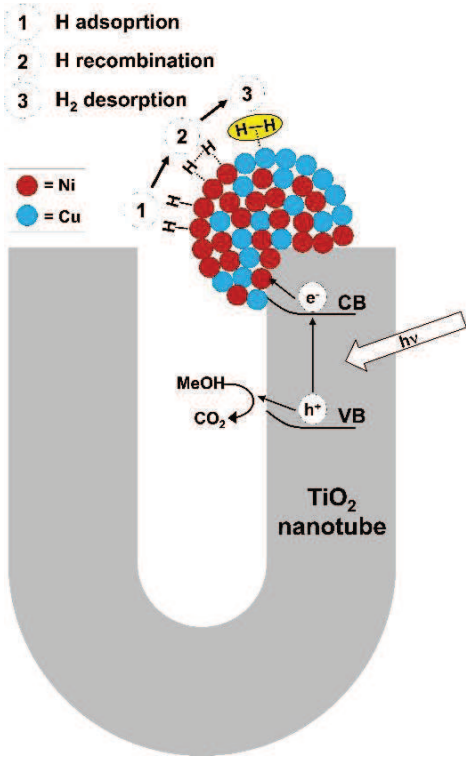

Scheme 1. The improved photocatalytic activity of TiO_2 NTs decorated with dewetted-alloyed NiCu NPs is attributed to the specific cocatalyst composition that can lead to a faster H atom adsorption/recombination over Ni cocatalytic centers combined with a more favourable H_2 molecule desorption from adjacent Cu sites [281,282].

On the other hand, an additional reason for the improved activity is the work function of NiCu alloyed particles with respect to that of pure Cu and Ni (i.e. 4.65 eV and 5.15 eV [283], respectively). According to theoretical calculations,[112–114] the work function of NiCu alloy increases linearly from 4.65 eV to 5.15 eV with increasing the Ni content. This leads in principle to an increase of the Schottky barrier height at the NiCu/TiO_2 interface, which can enable a more efficient electron-hole separation – see Scheme 2.

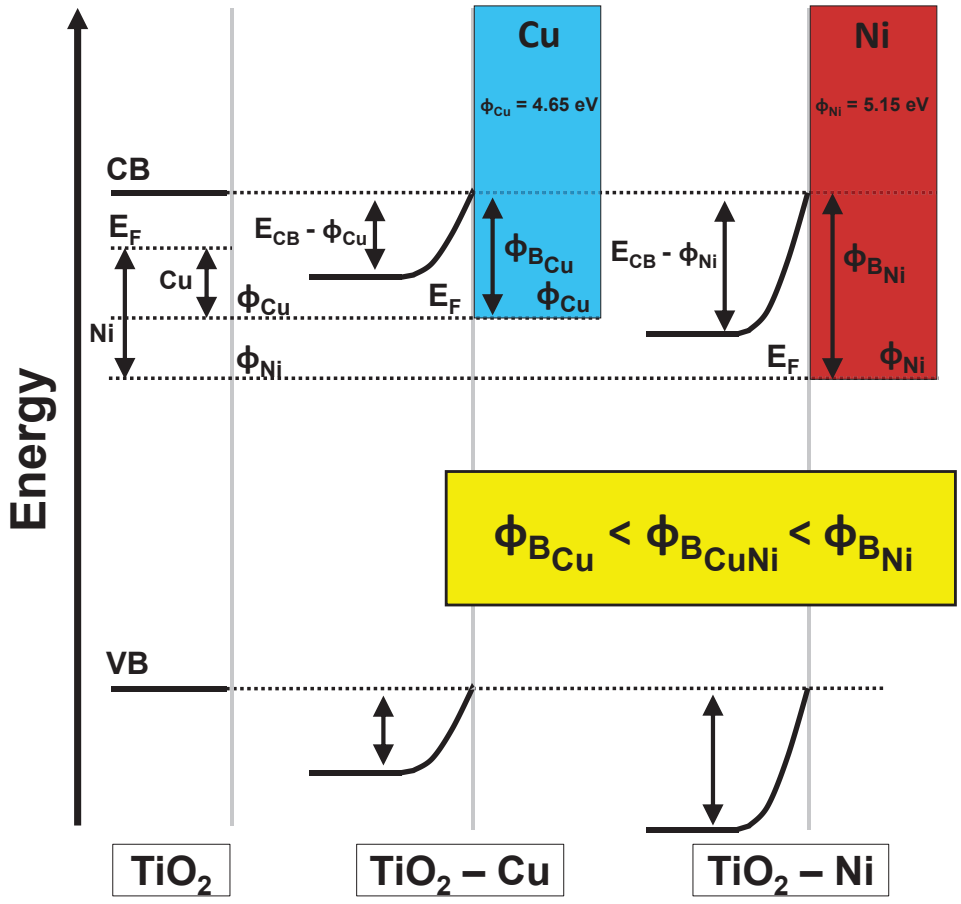

Scheme 2. An additional reason for the improved activity of TiO_2 NTs decorated with dewetted-alloyed NiCu NPs is the work function of NiCu alloyed particles with respect to that of pure Cu and Ni (i.e. 4.65 eV and 5.15 eV [283], respectively). According to theoretical calculations [112–114], the work function of NiCu alloy increases linearly from 4.65 eV to 5.15 eV with increasing the Ni content. This leads in principle to an increase of the Schottky barrier height (φ_B) at the NiCu/TiO_2 interface, which can enable a more efficient electron-hole separation. As the highest rate of H_2 evolution is achieved with a 1:1 Ni:Cu ratio, one can conclude that such composition of the NPs enables at the same time an efficient electron-hole separation (due to a higher Schottky barrier height compared to pure Cu), and a fast kinetics of hydrogen adsorption/recombination/desorption at the NiCu alloy surface (as outlined in Scheme 1).

As the highest rate of H_2 evolution is achieved with a 1:1 Ni:Cu ratio, one can conclude that such composition of the NPs enables at the same time an efficient electron-hole separation (due to a higher Schottky barrier height compared to pure Cu), and a fast kinetics of hydrogen adsorption/recombination/desorption at the NiCu alloy surface.

We also performed H_2 evolution experiments with the most active photocatalyst under illumination with unfiltered and filtered (420 nm cut-off filter) simulated solar light (AM1.5G). As shown in Figure 30e, under filtered illumination ($\lambda > 420$ nm) the NiCu-TiO_2 photocatalyst exhibits a negligible H_2 generation (0.02 $\mu L\ h^{-1}\ cm^{-2}$), while the activity is significantly higher (0.28 $\mu L\ h^{-1}\ cm^{-2}$) under full lamp illumination. This indicates that the photocatalyst is active only under UV light illumination ($\lambda < 420$ nm). Thus, the light

absorber and charge carrier generator is TiO_2, while the NiCu NPs act as electron transfer mediator and hydrogen recombination center.

A comparison between the photocatalytic activity of NiCu-TiO_2 NTs with noble metal decorated TiO_2 structures is shown in Figure 30f,g. As benchmark photocatalyst we fabricated Pt decorated TiO_2 NTs. The approach used for the fabrication of Pt-TiO_2 structures is in principle the same used for NiCu-TiO_2, i.e. a Pt film of an optimized thickness (1 nm, based on previous work)[101] is sputter-coated on TiO_2 nanotube arrays that are then annealed at 450°C in argon – this treatment simultaneously leads to nanotube crystallization and Pt dewetting into nanoparticles. The H_2 evolution rate of NiCu-TiO_2 NTs is ~ 60% and 50% of that measured for Pt-TiO_2 NTs under solar light illumination with and without the 420 nm cut off filter, respectively. This result is remarkable if one takes into account the substantially lower fabrication cost of the NiCu cocatalyst.

The most active photocatalyst (5Ni5Cu-TiO_2) was further investigated by HAADF-TEM and EDS-TEM. The HAADF-TEM images in Figure 34a show that the dewetted metal particles at the TiO_2 NT surface are ~ 30-40 nm in size. This result matches well the size distribution estimated from the SEM images (Figure 25e and Figure 28). From the EDS-TEM mapping data in Figure 34b, it seems that each particle results from welding of two different entities, one mainly composed of Cu, and the other of Ni. However, the zone where the two entities are welded into a single particle shows a mixed NiCu composition – see Figure 34c-e. This is well in line with the XRD results supporting the formation of NiCu alloyed NPs.[280] Please also note that in spite of the partially inhomogeneous composition of these particles, no XRD peak attributable to pure Ni or pure Cu phase could be detected (discussed above).

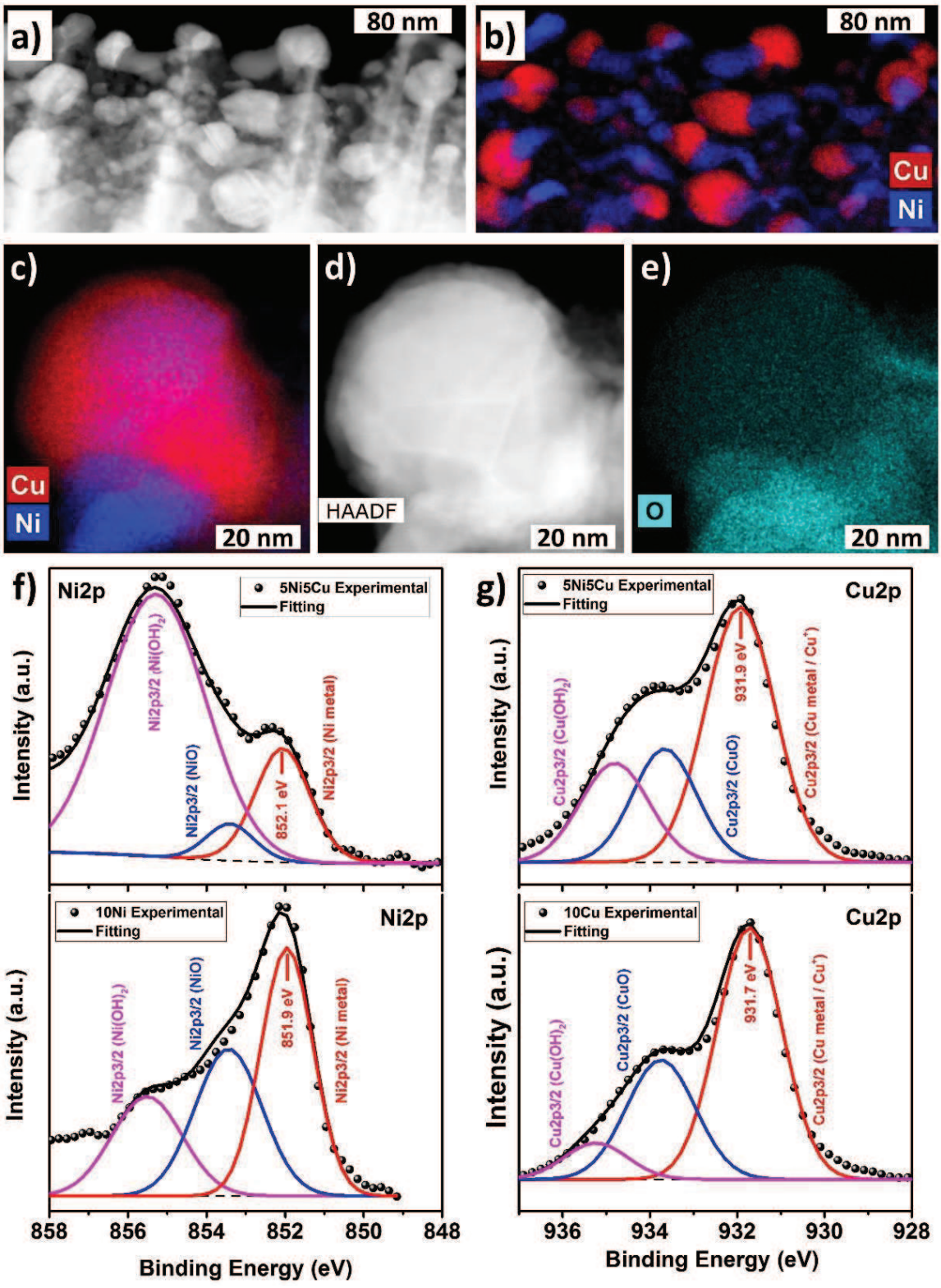

Figure 34. (a-e) TEM data for sample 5Ni5Cu dewetted at 450°C: (a,d) HAADF-TEM images; (b,c,e) EDS-TEM images with (b,c) Cu and Ni and (e) O elemental distribution. (f,g) XPS spectra for sample 5Ni5Cu, 10Ni and 10Cu (dewetted at 450°C) in the (f) Ni2p and (g) Cu2p region. The spectra are deconvoluted and peaks of Ni and Cu metal, oxide and hydroxide are indicated. The Cu2p3/2 signal at 931.7-931.9 eV (g) is attributed to Cu metal (based on XRD and TEM results) although the Cu2p3/2 signal of Cu(I) oxide typically peaks at similar B.E. values.

The EDS-TEM mapping in Figure 34e, suggests that the NiCu metal particles may be partially oxidized at their surface, probably due to surface oxidation of the metal NPs under ambient conditions or due to interaction with the TiO_2 substrate.[270] These structures were further characterized by XPS and compared to non-alloyed Ni and Cu NPs on TiO_2 NTs. The results are compiled in Figure 34f,g, where the Ni2p and Cu2p signals are deconvoluted into various contributions. While the signals of Ni and Cu oxides and hydroxide are present in any structure, the bands at 852.1 and 931.9 eV in the spectra of sample 5Ni5Cu can be assigned to Ni and Cu metals, respectively.[270,284–286] Both the Ni and Cu metal signals for the dewetted-alloyed NiCu NPs show a positive shift of 0.2 eV, compared to particle dewetted from pure Ni and Cu layers. These results, along with XRD and TEM data, further corroborate the formation of NiCu alloyed NPs.

Conclusions

We introduced an approach to fabricate an efficient noble metal free photocatalytic platform for H_2 evolution formed by dewetting NiCu bilayers into alloyed NiCu cocatalytic nanoparticles at the surface of TiO_2 nanotube arrays. This strategy allows for a full control over the alloyed nanoparticle size, loading and distribution, which enables the tuning of the metal cocatalyst work function as well as its catalytic ability in terms of kinetics of hydrogen adsorption, recombination and desorption. We showed that an equal Ni and Cu content in the alloyed nanoparticles is key to achieve a strong enhancement of the photocatalytic H_2 evolution compared to TiO_2 decorated with pure Ni or Cu nanoparticles. The alloyed NiCu cocatalyst on TiO_2 nanotubes allows to reach H_2 generation rates that are comparable to those delivered by conventional noble metal (Pt) decoration of TiO_2. From a more general point of view, it is anticipated that the dewetting-alloying approach can be adapted to other alloy systems and will therefore find wide application e.g. in heterogeneous catalysis.

2.3. Photocatalytic reduction and scavenging of Hg(II) over templated-dewetted Au on TiO_2 nanotubes

Reproduced from *Photochem. Photobiol. Sci.*, **2019**, **DOI:** 10.1039/c8pp00424b with permission from the European Society for Photobiology, the European Photochemistry Association, and The Royal Society of Chemistry.

The results reported in this chapter were obtained both at the University of Insubria and FAU. More in detail, my contribution has concerned the fabrication of all the photocatalytic materials (carried out in Erlangen), their characterization (carried out both in Erlangen and Como) and the evaluation of their performances towards photocatalytic mercury abatement (carried out in Como). Finally, I contributed extensively in the drafting and finalization of the published article.

Abstract

Gold-decorated TiO_2 nanotubes were used for the photocatalytic abatement of Hg(II) in aqueous solutions. The presence of dewetted Au nanoparticles induces a strong enhancement of photocatalytic reduction and scavenging performances, with respect to naked TiO_2. In the presence of chlorides, a massive formation of Hg_2Cl_2 nanowires, produced from Au nanoparticles, was observed using highly Au loaded photocatalysts to treat a 10 ppm Hg(II) solution. EDS and XPS confirmed the nature of the photo-produced nanowires. In the absence of chlorides and/or at lower Hg(II) starting concentrations, the scavenging of mercury proceeds through the formation of Hg-Au amalgams. Solar light driven Hg(II) abatements up to 90% were observed after 24h. ICP-MS analysis revealed that the removed Hg(II) is accumulated on the photocatalyst surface. Regeneration of Hg-loaded exhaust photocatalysts was easily performed by anodic stripping of Hg(0) and Hg(I) to Hg(II). After four catalytic-regeneration cycles only a 10% decrease of activity was observed.

Introduction

Pollution of water with mercury and its compounds has received increasing attention due to its toxic and bioaccumulative properties.[189,287–290] High levels of Hg(II) can be found in industrial wastewaters coming from activities which extensively use mercury, such as

chlorine-alkali, petrochemical, metallurgical, paint and electrical industry.[287,291] Inorganic Hg(II) in water bodies can be transformed by a large number of anaerobic bacteria to methylmercury, which is a well-known neurotoxin. This compound is strongly held to fish protein when absorbed through the gills or when contaminated food sources are eaten. In some cases, methylmercury levels in carnivorous fishes can be biomagnified up to a million times higher concentration levels than in the surrounding water.[290,292,293] Thus, the alkylation process of Hg(II) poses a serious health risk to humans and fauna through the aquatic food chain: even if Hg(II) is present at very low concentration, few μg L^{-1} of Hg(II) could already lead to a significant mercury alkylation).

For these reasons, very restrictive worldwide regulations have been enacted with the goal of reducing mercury emissions into surface water bodies.[294] Nonetheless, the disposal of mercury currently represents a major environmental concern, and the development of new technologies for a green and efficient removal of Hg(II) from water is still a challenge.

Mercury can be successfully removed from highly concentrated aqueous solutions by membrane filtration, precipitation, ion exchange, adsorption and other methods.[195–197] However, these techniques become less efficient and more expensive with mercury concentration lower than 100 ppm.[194,195,198] This represents a great limitation because even in the presence of relatively low Hg concentrations high abatement rates are a fundamental prerequisite for a successful and viable removal technique.

A "green approach" that is emerging as one of the most promising method for mercury removal is the photocatalytic reduction of Hg(II), which combines simplicity of operation and high abatement performances even when treating feedstock with low mercury concentrations.[198,203–208]

Photocatalysis is based on the irradiation, with a proper light source, of a semiconductor, usually a metal oxide (e.g. TiO_2, Fe_2O_3, WO_3), which induces the promotion of electrons from the valence band (VB) to the conduction band (CB) leaving holes in the CB. The photo-generated holes and electrons can recombine (in the bulk or at the semiconductor surface) or, more preferably, can react with adsorbed species or with species in the environment to cause redox reactions.

Various metal oxide semiconductors have been explored as photocatalysts, and their field of application has been expanded in the recent years.[21,295,296]

Among these materials titanium dioxide (TiO_2) is undoubtedly considered one of the best photocatalytic material for a wide range of processes.[15,35,295,297] Several advantages of TiO_2 are its non-toxicity, low-cost, long-term stability, and corrosion and photo-corrosion stability.

In particular, nanostructured TiO_2, such as TiO_2 nanotubes (NTs),[35,258,298–300] having a one-dimensional (1D) morphology and a large specific surface area, exhibit a strongly enhanced photo(electro)chemical performance due to directional charge transport, together with a beneficial diffusion and adsorption geometry.[235,301,302]

TiO_2 is n-type semiconductor with a band gap of 3.00-3.20 eV, depending on its crystallographic structure. TiO_2 can be easily synthesized in two main crystalline forms: the most common ones are rutile (tetragonal, with a band gap of around 3.00 eV) and anatase (tetragonal, with a band gap of around 3.20 eV).[37,303]

In aqueous solution, the species that in principle can be oxidized by holes photo-generated in TiO_2 are water, hydroxyl ions, and, if present, organic compounds. Instead, promoted electrons can reduce oxygen (to produce superoxide radicals) or metallic ions – this given that the potential of the conduction band (CB) edge of the semiconductor is more negative than the reduction potential of the $M^{n+}/M^{(n-m)+}$ couple.[199] The knowledge of the reduction potential of the metal ions and the level of CB edge of the semiconductor is fundamental to predict the thermodynamic feasibility of the reduction: the higher the difference between these values, the higher the tendency towards reduction of metallic ions.[304] In the case of Hg(II)/Hg(0) and the CB edge of TiO_2, the potentials have been reported to "seat" at 0.851 V (vs NHE)[200] and ≈ - 0.50 V (at pH 7 vs NHE),[202] respectively – that is, it is thermodynamically possible to photo-reduce Hg(II) at the TiO_2 surface.

The photocatalytic reduction of Hg(II) over powdered TiO_2 has been previously reported in several works.[198,203–208] First attempts to photo-reduce Hg(II) on powdered TiO_2 photocatalysts were made by using commercial Degussa P25 and Hombikat UV100 (100% anatase) under UV light illumination.[204–206] Few years later Lenzi et al.[207] tried to improve the adsorption and photocatalytic performance by preparing via sol-gel and impregnation a Ag/TiO_2 powder with higher specific surface area.

To the best of our knowledge, the utilization of titania in a supported form (WO_3-decorated TiO_2 nanotubes) was reported only by Lee at al.,[198] who obtained promising mercury abatement results; ~ 76% of the initial Hg(II) content was removed in 2 hours, under illumination of a UV-B (280-315 nm, 96 W) germicidal lamp. However, the utilization of such a powerful light source, and the lack of data on the total irradiance that was used, makes it difficult to compare the results with previous and future photocatalysts.

In any case, no data about the exploitation of the potential beneficial effects of the presence of gold over TiO_2 are reported in the literature. In principle the presence of gold should enhance the photocatalytic performances of TiO_2 towards Hg(II) abatement by: i)

increasing the charge carriers separation and enhancing the electron transport to the TiO_2/electrolyte interface; ii) improving the Hg scavenging properties, through the in-situ formation of Hg-Au amalgams.

In this work we investigate for the first time, the performance of Au nanoparticles (NPs) modified TiO_2 nanotubes towards the solar light-driven Hg(II) photocatalytic reduction. More in detail, we found that the Hg accumulation capabilities of our Au/TiO_2 systems are unexpectedly high, with two main different mechanisms operating at higher or lower Hg concentrations. The influence of the presence of different amounts of gold and the regeneration/recycling ability of the photocatalysts were also explored.

Experimental

Preparation procedure of Au-TiO_2 NTs

Ti foils (Advent Research Materials, 0.125 mm thickness, 99.6+% purity) were degreased by sonicating in acetone, isopropanol, and deionized water and then were dried in a N_2 stream. The cleaned Ti foils were anodized to fabricate the highly ordered TiO_2 nanotube arrays at 100°C in a 3M HF solution in o-H_3PO_4 (Sigma- Aldrich). For this process, a two-electrode configuration was used, where the Ti foil (15 mm × 15 mm) was the working electrode and a Pt sheet was the counter electrode. The anodization was performed by applying a potential of 15 V (for 2 h) using a DC power supply (VLP 2403 Voltcraft). Subsequently, the TiO_2 nanotube arrays on Ti metal substrates were rinsed with ethanol and dried under N_2 stream.

After anodization and rinsing, an Au metal thin film was sputtered on the synthetized TiO_2 NTs layer by a plasma-sputtering machine (EM SCD 500, Leica) using a 99.999% pure Au target with an applied sputtering current of 16 mA and pressure of 10^{-2} mbar of Ar. The amount of sputtered material was in-situ determined by an automated quartz crystal monitor, and is reported in this work as nominal thickness of the sputtered film. After sputtering, the samples were annealed at 450°C in air to crystalize TiO_2 NTs and to induce dewetting (as described by Yoo et al.[305]). Although other deposition techniques can be used to obtain Au-decorated nanotubes (see ref.[306] as an example) we decided to use the templated-dewetting approach to obtain two morphologically different systems just changing the Au loading (i.e. just changing the sputtering time).

Characterization techniques

The morphology of photocatalytic material was studied using a XL30 Environmental Scanning Electron Microscopy (ESEM FEG Philips) at 20 kV under high and low vacuum conditions. Elemental analysis were performed with a silicon drifted EDS detector (EDAX element). High resolution SEM images where collected using a Hitachi S4800 FE-SEM.

XRD data were recorded on a Rigaku Miniflex system using Cu-Kα radiation, 30 kV, 10 mA with step of 0.02° (2θ) and a scanning speed of 2° min^{-1}.

XPS spectra were acquired using Al X-ray source. The XPS spectra were corrected in relation to the Ti2p signal at 458.5 eV. PHI MultiPak™ software and database were used for curve fitting analysis.

A Sun 2000 Solar Simulator (Abet Technologies, calibrated at 100 mW cm^{-2}) equipped with an AM 1.5 G filter was used as the vertical light source: a totally reflecting mirror has been used to deflect the light beam and to carry out the experiments in a side-illumination configuration.

A three-electrode system connected to an Amel 2551 potentiostat equipped with a silver chloride reference electrode (Ag/AgCl/saturated KCl), and a Pt wire as counter electrode was used for the photoelectrochemical (PEC) characterization (cyclic voltammetry and chrono-amperometry).

All measurements were performed using a 250 mL quartz beaker, placed over a magnetic stirrer: 135 g of solution were used in each test to obtain a good light focus and a total immersion of the electrodes.

Photocatalytic Hg(II) reduction tests

The same quartz cell and solar simulator described for the characterization techniques were used to carry out Hg(II) photo-reduction tests. Ultrapure water (MilliQ 18.2 MΩ cm, 3ppb TOC) was used for the preparation of all solutions. Abatement tests were conducted in solutions containing: i) 2 mM phosphate buffer (pH 7.0, 630 μS cm^{-1}) obtained by dilution of a concentrated 200 mM phosphate buffer, ii)100 mM of NaCl (prepared by dissolution of solid NaCl, Sigma-Aldrich, ≥ 98%).

The presence of Hg(II) in solution was ensured by the addition of a proper amount of a diluted solution obtained from the concentrated 1000 mg L^{-1} Hg(II) solution, that was prepared by dissolving 338.4 mg of $HgCl_2$ (Carlo Erba, ≥ 99.5%) in 250 mL ultrapure water. Total mercury concentration was determined on properly diluted samples that were collected

during the photocatalytic experiment with a Thermo Scientific ICAP Q inductively coupled plasma mass spectrometer (ICP-MS). The Hg concentration was determined by monitoring the 202-Hg channel and using a He-collision cell in kinetic energy discrimination (KED) mode, following the standard conditions indicated by the factory. Both external standards (prepared by dilution from a 10 mg L^{-1} Hg stock solution, Merck) and internal standards (10 ppb of Germanium added in each sample by dilution from a 1000 mg L^{-1} Ge stock solution, Fluka TraceSELECT®) were employed for Hg quantification. In addition, 0.2 mol L^{-1} of BrCl solution, prepared by dissolving 2.7 g of KBr (Sigma-Aldrich, ≥ 99.0%) in 250 mL HCl (Fluka, > 30%, TraceSELECT®) and adding 3.8 g of $KBrO_3$ (Sigma-Aldrich, ≥ 99.0%), were added to all analyzed solutions with a 1:100 dilution, in order to minimize mercury memory effects in ICP-MS analysis.[307]

Photoelectrochemical regeneration of Au-TiO_2 photocatalysts

The same quartz cell, three-electrode system and solar simulator described for the characterization techniques were used to carry out the PEC regeneration of Au-TiO_2 photocatalysts. After every Hg(II) abatement experiment, Au-TiO_2 NTs samples were dipped in a 100 mM KNO_3 (prepared by dissolving solid KNO_3, Sigma-Aldrich, ≥ 99.0%) solution and a positive +500 mV (vs. Ag/AgCl) potential was applied for 2 hours under stirring and front solar-irradiation. Cyclic voltammograms from -200 mV to +1000 mV (vs. Ag/AgCl) with a scan speed of 200 mV s^{-1} were recorded in this solution under permanent illumination conditions. The resulting solutions were analyzed in view of their composition with ICP-MS as described for the samples collected for photocatalytic reduction.

Results and discussion

Figure 35a shows the morphology of the top and cross-sectional view (see inset in Figure 35a) of the highly-ordered TiO_2 NTs employed in this work, which are anodically grown on Ti metal foils in a hot, concentrated H_3PO_4/HF electrolyte.[305] These well-defined nanostructures exhibit a nearly ideal hexagonal packing and each tube has an average internal diameter of ~ 90 nm and a length of ~ 200 nm.

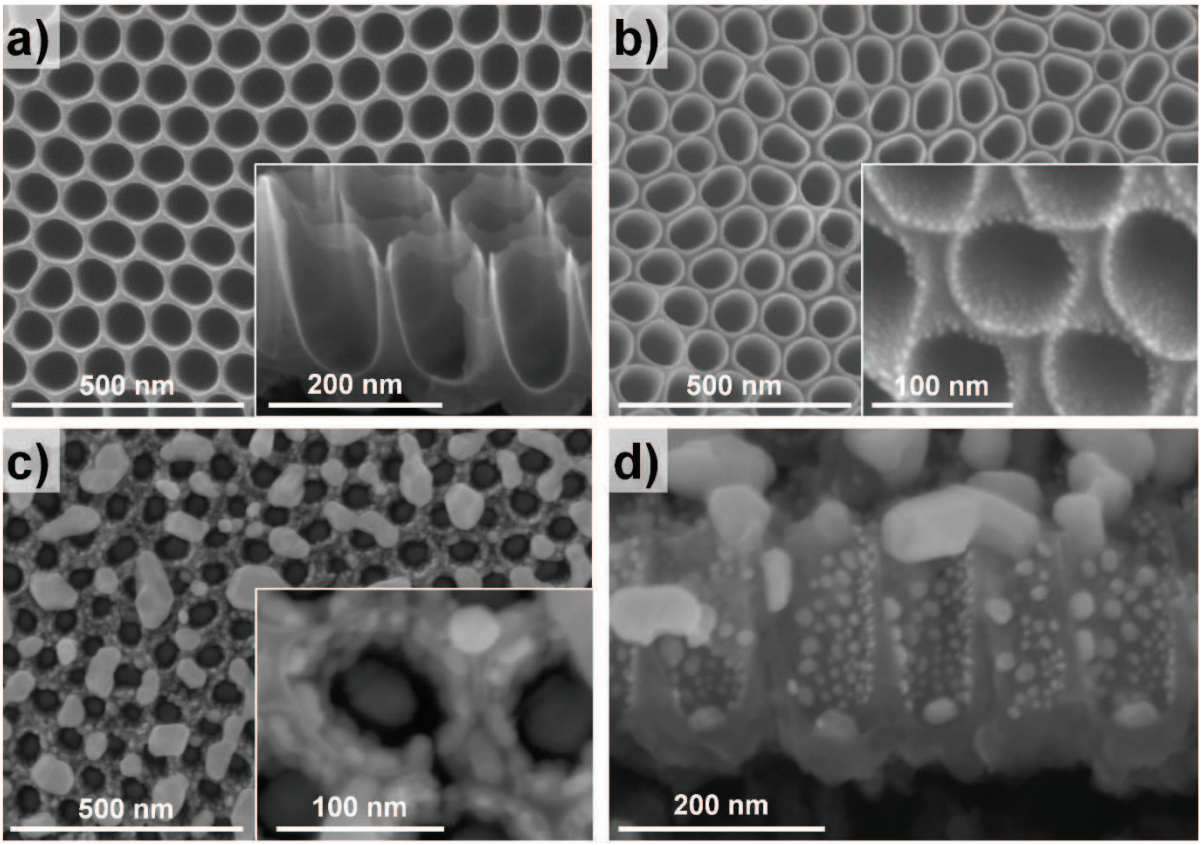

Figure 35. (a-d) SEM images of TiO_2 structures employed in this work: (a) top view of pristine TiO_2 nanotubes. Inset: cross-sectional view of pristine TiO_2; (b) TiO_2 NTs coated with a sputtered 1 nm-thick Au film after dewetting (1Au-TiO_2). Inset: magnified top view image of 1Au-TiO_2; (c) TiO_2 NTs coated with a sputtered 20 nm-thick Au film after dewetting (20Au-TiO_2). Inset: magnified top view image of 20Au-TiO_2; (d) cross-sectional view of 20Au-TiO_2

As reported in previous works these NT arrays can be decorated with nanoscopic precision by sputter-deposition of a thin metal film (Au in this work) followed by a proper thermal treatment that induces both the crystallization of TiO_2 and the solid-state templated-dewetting of the metal.[120,257,305,308–311] Images of TiO_2 NTs coated with a nominally 1 nm-thick (1Au-TiO_2) and 20 nm-thick (20Au-TiO_2) Au layers after a heat treatment (i.e. after dewetting) are reported in Figure 35b and 35c-d, respectively. Thermal dewetting of metal thin films occurs at the solid-state: the temperature of the thermal treatment is far below the melting point of

Au. Essentially, the driving force for dewetting is related to the minimization of: i) the free surface energy of the oxide surface (TiO_2), ii) the free surface energy of the metal layer (Au) and iii) the interfacial energy of the metal/substrate system (Au/TiO_2).[120,121]

For the sake of comparison, Figure 36 shows the SEM images recorded prior dewetting for 1Au-TiO_2 and 20Au-TiO_2, respectively: in the case of the 20 nm deposition a strong difference between pristine and dewetted samples can be observed, while for the 1 nm specimen no significant differences can be appreciated, as for this sample dewetting occurs at nearly room temperature (so thin layers require low energy input to dewet).[120]

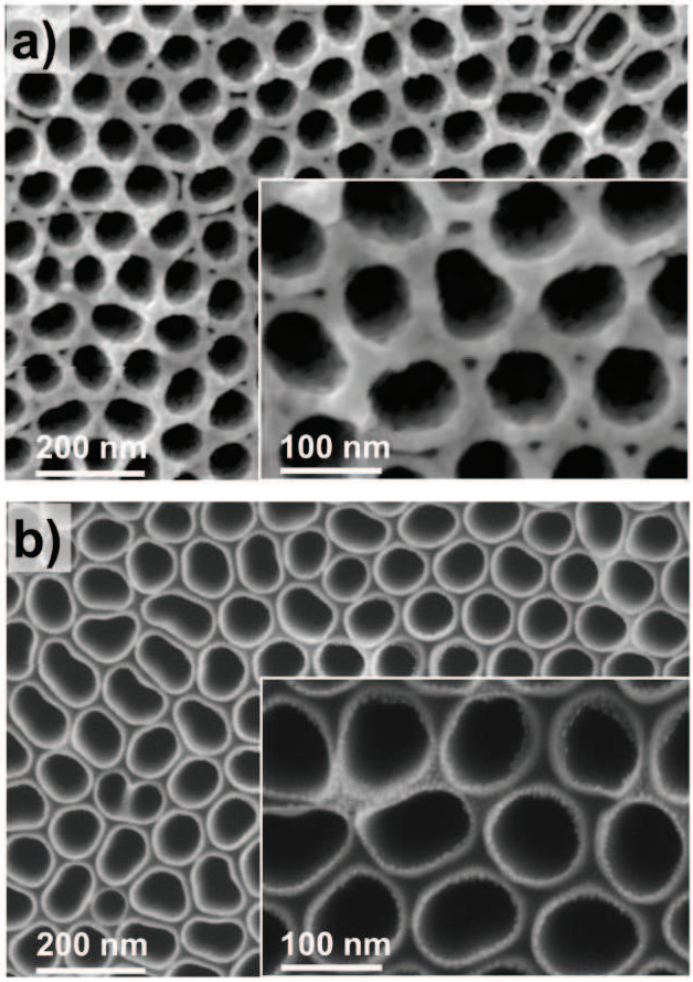

Figure 36. (a) SEM top view of 20Au-TiO_2 nanotubes before dewetting. Inset: magnified top view; (b) top view of 1Au-TiO_2 nanotubes before dewetting. Inset: magnified top view.

Analogous structures (same anodization conditions, thermal treatment and sputtered metal) were prepared and characterized (XRD, XPS and hydrogen evolution capability under UV irradiation) in a previous work.[305]

In this work, Au-TiO_2 systems were assessed in view of their photocatalytic Hg(II) reduction performance under solar light simulated irradiation. Both 1Au-TiO_2 and 20Au-TiO_2

were tested over solutions buffered at pH 7.0 (see experimental section), having two markedly different Hg starting concentrations.

Figure 37 shows the results of the photocatalytic abatement tests of both 1Au-TiO_2 and 20Au-TiO_2 systems, carried out with solutions having a starting Hg concentration of 10 ppm (Figure 37a) or 500 ppb (Figure 37b).

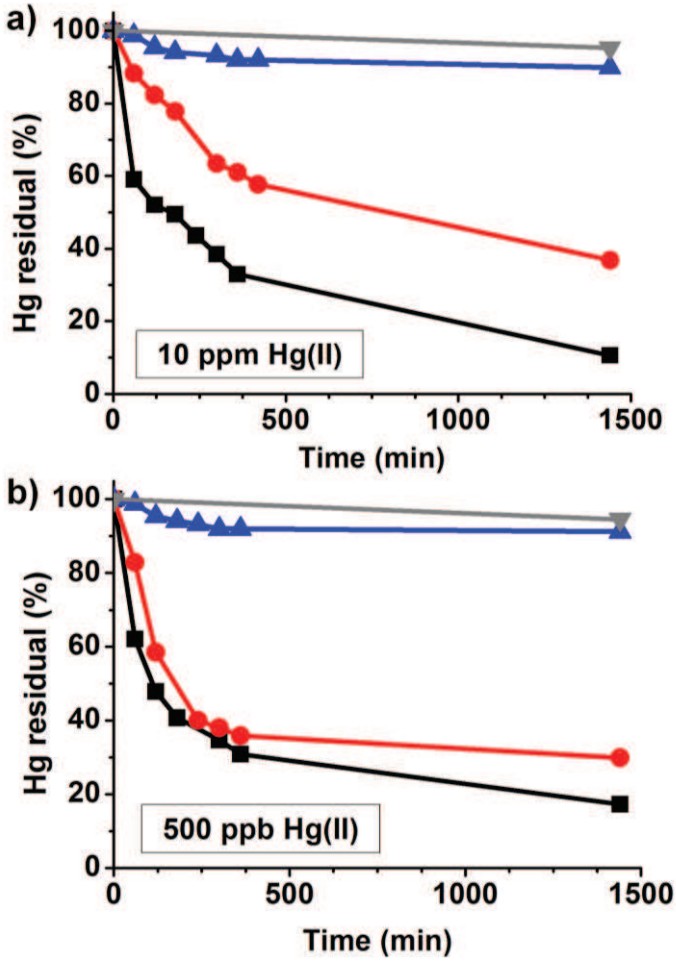

Figure 37. (a-b) Hg(II) concentration trends during photocatalytic reduction using 20Au-TiO_2 (black), 1Au-TiO_2 (red), TiO_2 (blue) and 20Au-TiO_2 in dark condition (grey) at pH 7.0 in presence of chloride with different starting Hg(II) concentrations: (a) 10 ppm and (b) 500 ppb.

The reported Hg reduction profiles are surely correlated to photo-activated processes, as no significant Hg abatement is observed in the dark. Moreover, a comparison of the abatement profiles obtained for naked TiO_2 and for both Au-TiO_2 systems strongly indicates that gold decoration is fundamental to obtain high photocatalytic Hg(II) reduction (removal) rates. As a preliminary consideration, the strong promotion effect caused by the presence of Au NPs might be ascribed to: i) the improvement of the electron transfer to reactants provided by Au NPs (localized Schottky-junctions);[258] ii) the strong interaction between Hg

and Au that can lead to the formation of nano-alloys ("nano-amalgams", if Hg(II) is completely reduced to Hg(0) and incorporated in the Au NPs). In particular, the best photocatalytic performance was obtained with the most Au-loaded photocatalyst (20Au-TiO_2), which is able to reduce up to ~ 90 % of Hg(II) after 24 hours, almost independently of the starting Hg(II) concentration. Instead, 1Au-TiO_2 exhibits a certain sensitivity to the mercury starting concentration: the higher the Hg(II) starting concentration, the lower the photocatalytic efficiency.

During the abatement of the 10ppm Hg solution the formation of a compact white-grayish layer was macroscopically observed on 20Au-TiO_2. Surprisingly, SEM images recorded on this specimen at the end of the abatement test revealed that the catalysts' surface is homogeneously covered by nano filaments, having a ~ 100 nm mean width and length of some tens of microns (Figure 38a).

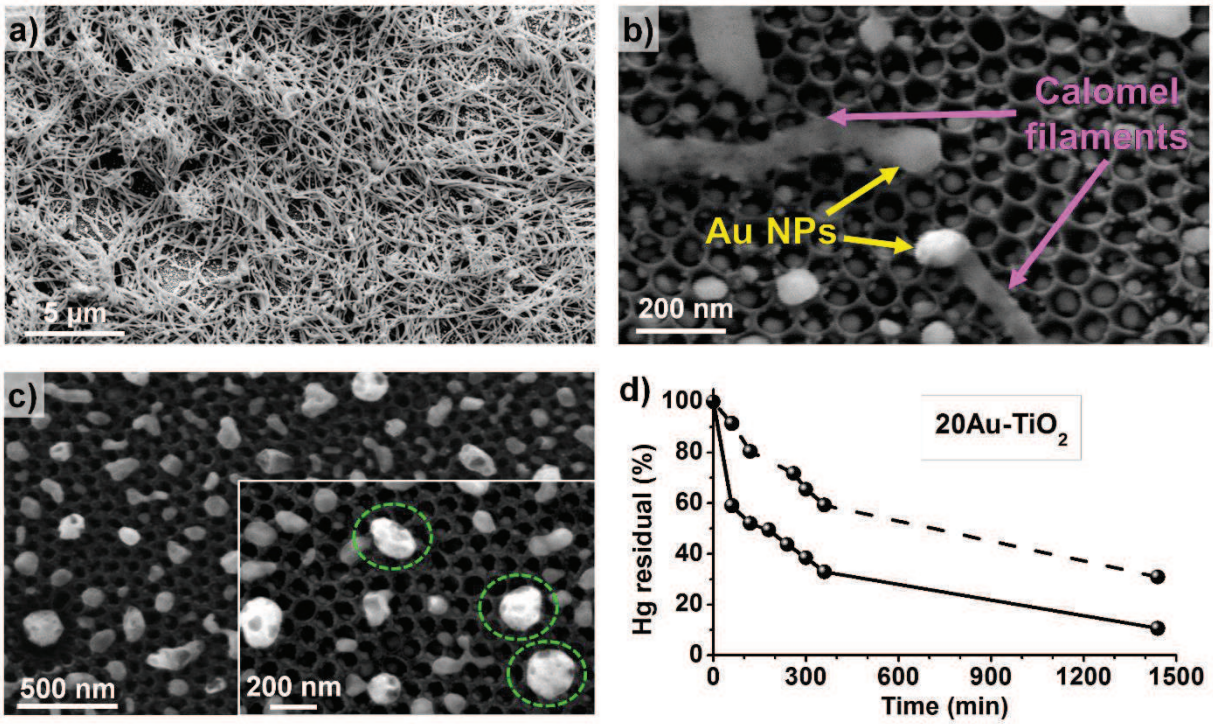

Figure 38. (a-b) SEM images of 20Au-TiO_2 recorded after (a) 24 hours and (b) 30 minutes long photocatalytic reduction of 10 ppm of Hg(II) in presence of chloride. (c) 20Au-TiO_2 after 24 hours long photocatalytic reduction of 10 ppm of Hg(II) in absence of chloride. Inset: magnified image in which larger and brighter Au NPs are circled in green. (d) Hg(II) concentration trends during photocatalytic reduction of 10 ppm of Hg(II) at pH 7.0 in presence (solid line) and absence (dashed line) of chlorides using 20Au-TiO_2.

The formation of such nanofibers is very reproducible, as it was always observed with different 20Au-TiO_2 specimens and even after each regeneration and recycling test (discussed below). No detachment of the compact layer of such nanowires from the catalyst surface was

observed even after 24h. EDS analysis carried out on several of these filaments revealed that they are mainly composed by Hg and Cl, with an approximate Hg/Cl atomic ratio of 1.1. It therefore reasonable to suggest the formation of insoluble Hg_2Cl_2 filaments, which is possible due to the presence of NaCl in the aqueous medium (additional characterization data to support the formation of Hg_2Cl_2 are shown below).

NaCl was intentionally introduced in solution for two main reasons: i) chlorides are always present in every Hg polluted aqueous medium (ranging from fresh to marine waters) ii) it was reported by Wang et al.[204] that with powdered TiO_2 photocatalysts the presence of Cl^- is detrimental in terms of Hg(II) reduction capability, due to the formation of a variety of complexes, including $HgCl^+$, $HgCl_3^-$ and $HgCl_4^{2-}$.

SEM images taken form a 20Au-TiO_2 specimen after an intentionally short reduction test (Figure 38b) clearly revealed that Au NPs act as nucleation sites for the directional growth of calomel nanowires. This evidence, together with the observation that the diameters of calomel nanowires (as measured from Figure 38a) are slightly lower than the diameters of Au NPs, would indicate that these wires exclusively grow starting from Au NPs.

It should be underlined that the formation of calomel nanowires is relevant as such because it strongly enhances the scavenging properties of the Au-TiO_2 photocatalyst (this is key especially when highly concentrated Hg solutions have to be treated). In the absence of NaCl, the formation of Hg_2Cl_2 filaments was not observed (Figure 38c), and in these conditions the photocatalytic Hg reduction is significantly slower (Figure 38d). We report in Figure 38c the SEM image of sample 20Au-TiO_2 after the reduction tests carried out in the absence of chlorides: the presence of some larger and brighter metallic NPs, which were not present before the photocatalytic experiment (Figure 35c), is clearly visible. EDS analysis revealed that these larger NPs are composed of Au and Hg with a variable atomic Hg-Au ratio, which ranges from ~ 0.8 to 1.8. These results are consistent with the formation of an amalgam between Hg(0) and Au, and in this case the mechanism would probably involve the complete reduction of Hg(II) to Hg(0).

XRD patterns recorded prior and after the photocatalytic test carried out without chlorides (compare patterns a-d in Figure 39) show a substantial loss of crystallinity of the Au NPs: the decrease in intensity of Au (200) reflection at ~ 44.6° is consistent with the suggested formation of Au-Hg alloy.[312,313] As we will show later, this is also confirmed by XPS analysis. A partial loss of crystallinity was observed also in the XRD spectrum (Figure 39b) recorded after the photoreduction test carried out in the presence of chlorides (i.e. with the formation of Hg_2Cl_2 filaments): therefore, the partial formation of Hg-Au amalgams may not

be excluded even in this case; however, owing to the structure coverage caused by the calomel nanowires, we could not observe by SEM the formation of structures comparable to those in Figure 38c (Hg-Au NPs).

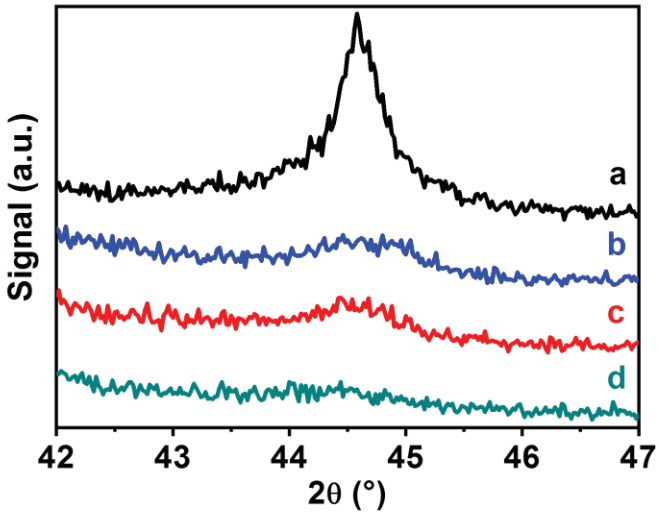

Figure 39. Detail of Au (200) reflection in XRD spectra for 4 differently treated samples: (a) as-prepared 20Au-TiO_2; (b) 20Au-TiO_2 after photocatalytic reduction of 10 ppm of Hg(II) in presence of chloride; (c) the same material reported in (b) after PEC regeneration in KNO_3; (d) 20Au-TiO_2 after photocatalytic reduction of 10 ppm of Hg(II) in absence of chloride. Full XRD spectra are provided in Figure 40.

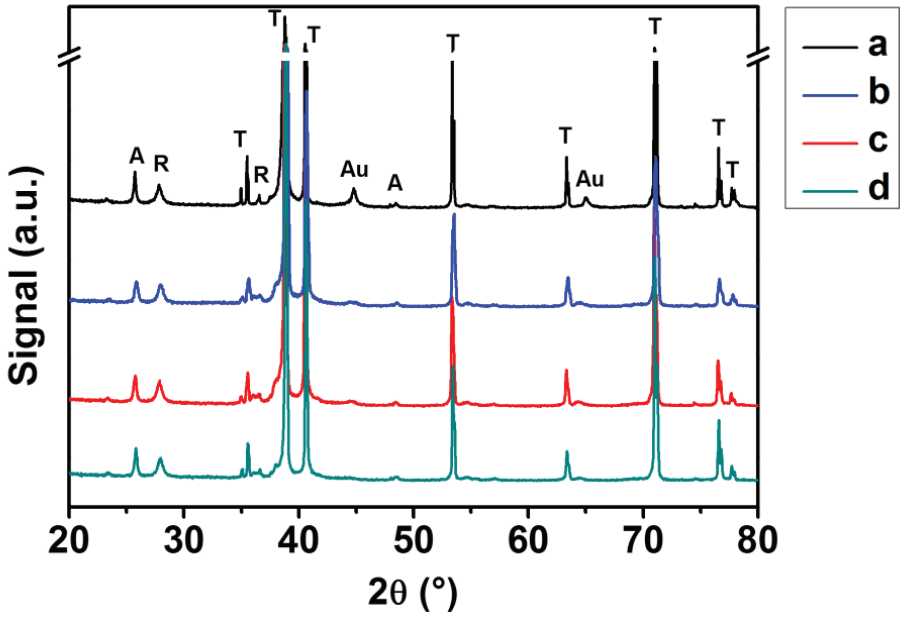

Figure 40. XRD spectra of 20Au-TiO_2 (a) as prepared, (b) after photocatalytic reduction of 10 ppm of Hg(II) in the presence of chlorides, (c) the same material reported in (b) after PEC regeneration in KNO_3 and (d) after photocatalytic reduction of 10 ppm of Hg(II) in the absence of chlorides. The reflections in XRD spectra are assigned to anatase (A), rutile (R), gold (Au) and titanium (T).

The XPS spectra reported in Figures 41a-d and Figure 42 further confirm the formation of calomel nanowires in the presence of chlorides, and the formation of Hg-Au alloy in the absence of chloride. The XPS analysis of 20Au-TiO_2 after photoreduction of Hg(II) in the presence of chlorides revealed two peaks at 101.05 eV and 105.10 eV which can be attributed to the $Hg4f_{7/2}$ and $Hg4f_{5/2}$ signals of Hg_2Cl_2.[314,315] Instead, the formation of Hg-Au alloy (i.e. Hg(0)) in the absence of chlorides is supported by a shift and be the broadening of the Hg signals, which can fitted according to two doublets peaking at 98.90 and 102.79 eV, and 99.99 and 103.92 eV ($Hg4f_{7/2}$ and $Hg4f_{5/2}$, respectively).[315,316] The doublet nature and broadening of the Hg XPS signal reflects that Hg(0) is present with different chemical surroundings; such signal can e.g. be ascribed to the formation of Hg-Au alloy with various stoichiometric composition,[317] and to the presence of "free" Hg(0) adsorbed on TiO_2 NTs or at the Au NP surface.[316] As shown in Figure 42, the Au4f XPS doublet for as-prepared 20Au-TiO_2 peaks at 83.10 eV and 86.70 eV, which corresponds well to data in the literature on Au deposited on TiO_2.[305] These signals however seem not to shift with the formation of calomel or Hg-Au alloy; this results is also in line with data in the literature.[316]

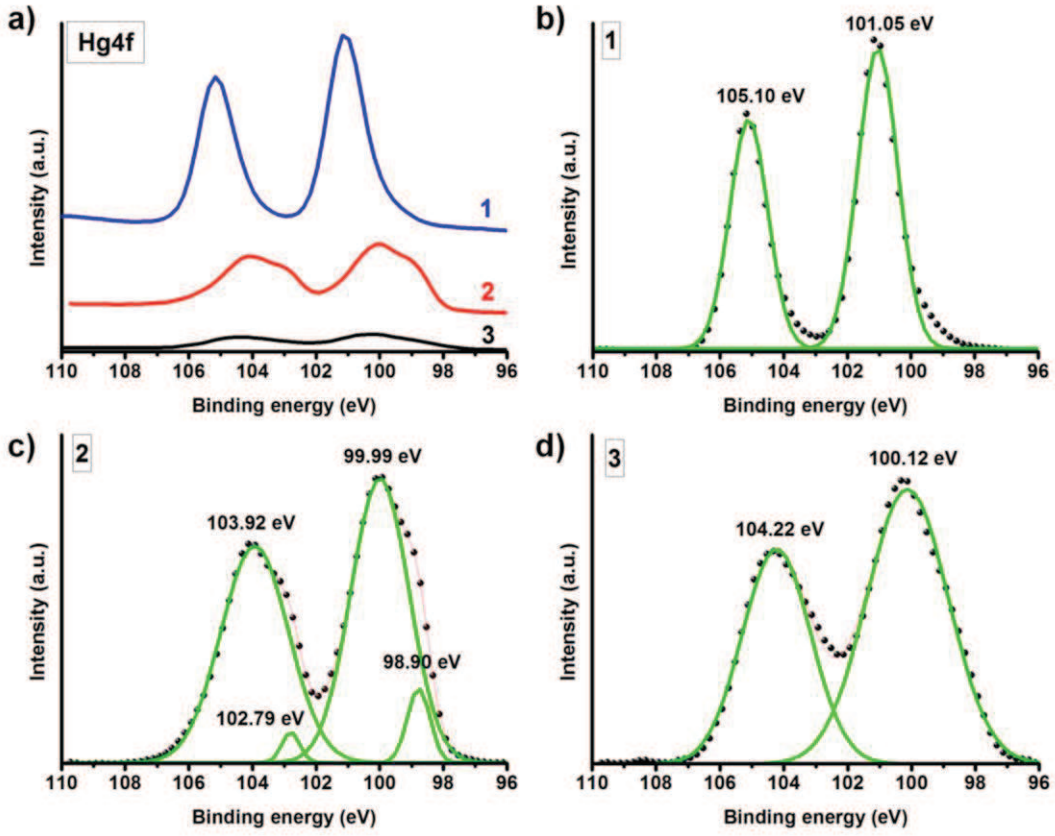

Figure 41. (a) Comparison between Hg4f XPS spectra of (1) 20Au-TiO_2 after photocatalytic reduction of 10 ppm of Hg(II) in presence of chlorides, (2) 20Au-TiO_2 after photocatalytic reduction of 10 ppm of Hg(II) in absence of chlorides, (3) 20Au-TiO_2 after PEC regeneration. (b-d) Deconvolution of Hg4f signals for samples 1-3.

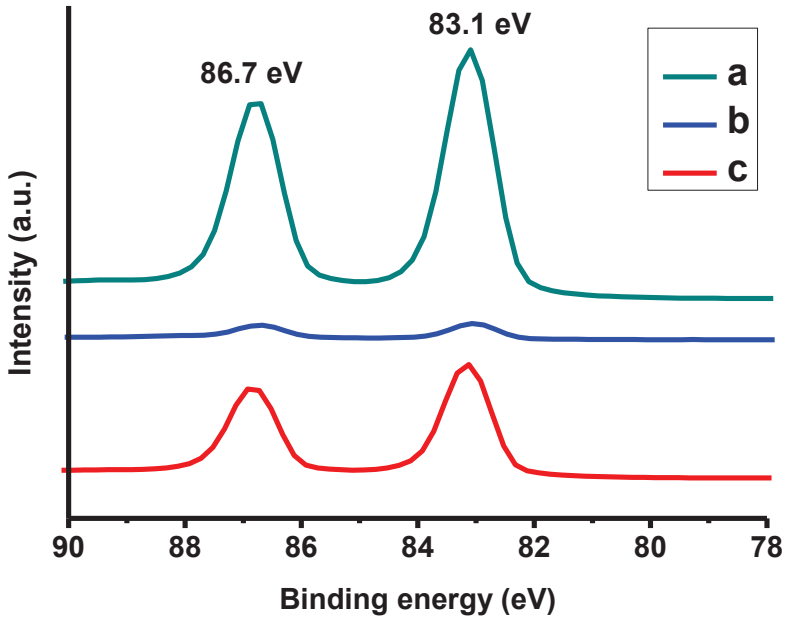

Figure 42. Au4f XPS spectra of (a) 20Au-TiO_2 as prepared, (b) 20Au-TiO_2 after photocatalytic reduction of 10 ppm of Hg(II) in the presence of chlorides, (c) 20Au-TiO_2 after photocatalytic reduction of 10 ppm of Hg(II) in the absence of chlorides.

All the results so far reported can be rationalized as follows: i) Hg(II) → Hg(0) proceeds stepwise with the intermediate formation of Hg(I); ii) in the presence of Cl^- the concentration of Hg(I) produced by photoreduction in close proximity of Au NPs is sufficiently high to grow Hg_2Cl_2 nanowires starting from such NPs; iii) in the absence of Cl^-, the reduction further proceeds to Hg(0), i.e. with the formation of Hg-Au nano-amalgam; iv) a partial formation of Hg-Au amalgams cannot be excluded even in the presence of chlorides.

Apart from the presence of chlorides, the formation of calomel nanowires strongly depends on the amount of gold deposited on TiO_2 NTs and on the initial Hg concentration. In fact, the formation of such nanowires was neither observed on 1Au-TiO_2 (independently of the initial Hg concentration), nor on 20Au-TiO_2 for Hg concentration > 500 ppb (see Figure 43a and 43b, respectively). Based on these results, we can infer that sufficiently big Au NPs, together with high Hg(II) concentrations, are fundamental to generate a sufficiently high Hg(I) local concentration to produce calomel nanowires. Apparently, the mechanism for such a directional and anisotropic growth of calomel nanowires roughly resembles the growth of carbon nanotubes starting from metal NPs,[318,319] with the obvious difference that here we are working in the liquid phase rather than in the gas phase.

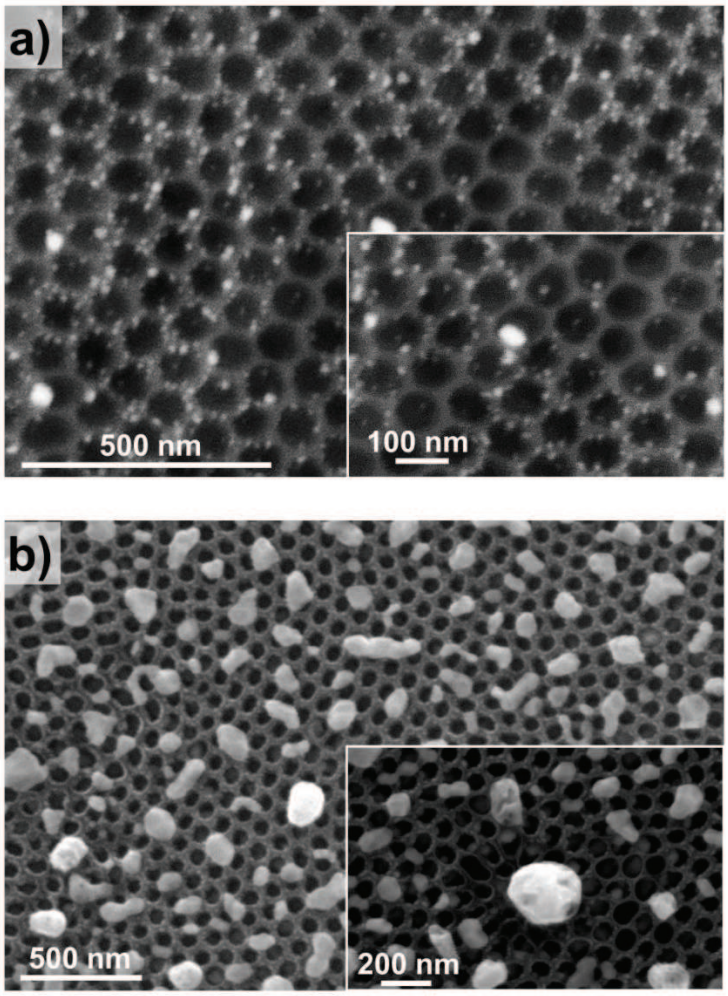

Figure 43. (a) Backscattering SEM image of 1Au-TiO_2 after photocatalytic reduction of 10 ppm of Hg(II) in the presence of chlorides. Inset: magnified image. (b) SEM top view of 20Au-TiO_2 nanotubes after photocatalytic reduction of 500 ppb of Hg(II) in the presence of chlorides. Inset: magnified image.

In any case, when the conditions are suitable for the growth of calomel nanowires, no Hg_2Cl_2 filaments produced from Au NPs inside TiO_2 nanotubes were observed, as well as from TiO_2. Additionally, when the conditions are not suitable for the growth of calomel nanowires, adsorption of Hg over TiO_2 surely occurs, as already reported in the literature.[198,320,321] This evidence is only indirect (EDS resolution is not sufficient to locate Hg on TiO_2 rather than on Au), since the Au loading on TiO_2, cannot account for the scavenged Hg amounts.

Another investigated aspect was the possibility of reusing the Au-TiO_2 photocatalysts after a proper regeneration process. This investigation was conducted on 20Au-TiO_2 only, due to its superior performances at high Hg concentrations.

Since photo-reduced Hg is mainly loaded on Au NPs and on calomel nanowires bound to the Au NPs, the most rational way to efficiently reuse the photocatalyst is to selectively

dissolve mercury, leaving behind Au NPs on TiO_2 NTs, that is, regenerating the original photocatalyst morphology and composition. In principle this process can be performed trough an electrochemical oxidation of the Hg-loaded photocatalyst, in a similar way to the anodic stripping determination of Hg on gold electrodes. This process would allow i) the regeneration of the photocatalyst (Hg-free Au NPs), and ii) the recovery of mercury in a small concentrated waste volume.

Therefore, we investigated the feasibility of using an electrochemical dissolution in a KNO_3 100 mM media to regenerate the electrode. KNO_3 was chosen because of the high solubility of both mercuric and mercurous nitrates.[322] It should be underlined that, since TiO_2 is a semiconductor, it is mandatory to perform electrochemical dissolution under light illumination to produce the necessary charge carriers (as a matter of fact, any attempt to regenerate Au-TiO_2 catalysts applying up to 800 mV in the dark failed). In order to establish the regeneration potential to be applied to the Hg-loaded photocatalyst, cyclic voltammograms (CVs) were recorded in KNO_3 under illumination (Figure 44a). One can observe the anodic region to start slightly above 0 mV (vs. Ag/AgCl). Moreover, as the stripping potential of Hg over gold electrodes is reported to fall on around 350-450 mV[323,324] we decided to use 500 mV (a slightly more positive potential) as the regeneration potential.

From the current vs. time plot (Figure 44b) recorded during the PEC regeneration it is possible to observe that a constant current value is reached after 120 min. The regeneration time was accordingly set to 120 min.

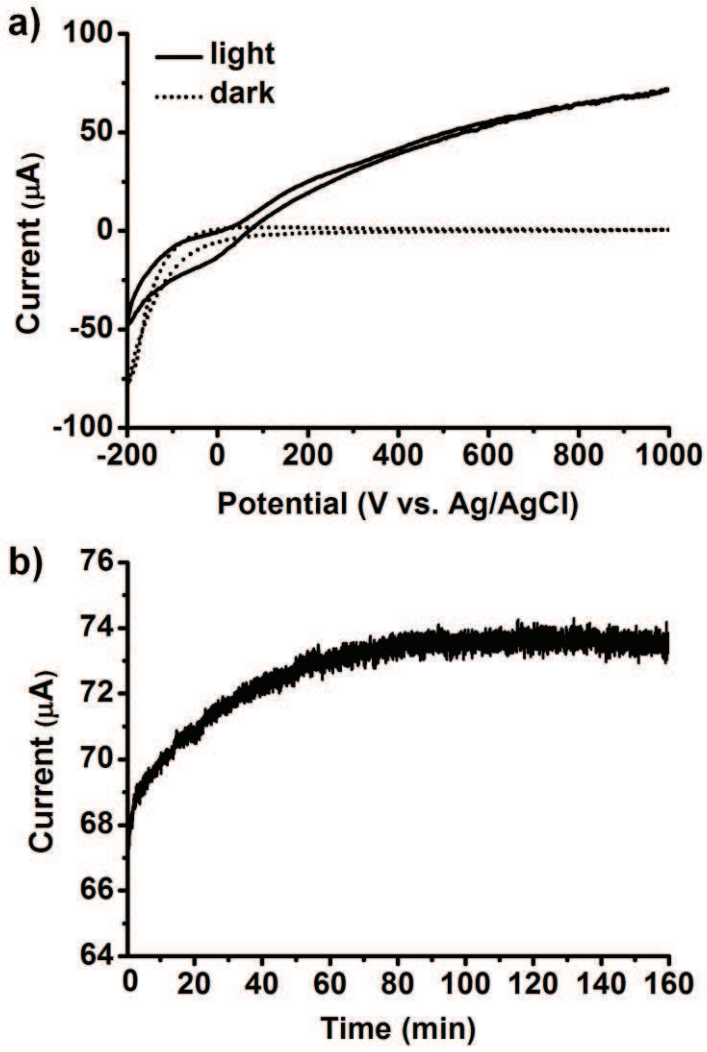

Figure 44. (a) Cyclic voltammograms recorded using 20Au-TiO_2 in KNO_3 100 mM with and without solar light irradiation; (b) chronoamperometric measurements recorded during 20Au-TiO_2 regeneration in 100mM KNO_3 solution applying 500 mV (vs. Ag/AgCl).

EDS analysis performed after PEC regeneration on different 20Au-TiO_2 samples revealed that the treatment was very successful: in the worst case only a ~ 0.14 Hg/Au atomic ratio was determined (please note that the Hg/Au ratios after Hg abatement were ~ 0.8-1.8). Furthermore, ICP-MS analysis of the KNO_3 solution after regeneration revealed the presence of more than 80 % of the previously photocatalytically removed Hg(II). These results fit very well with the XPS analysis of 20Au-TiO_2 after PEC regeneration (Figure 41d): it is possible to observe a strong decrease of the XPS signals at 100.12 eV and 104.22 eV, which, as outlined above, is attributed to Hg(0).[315,316]

As shown in Figure 45, the regeneration process does not cause any modification of the Au NPs shape, and leads to a complete cleaning of the Au-TiO_2 structures from calomel nanowires. The only relevant difference between fresh and regenerated photocatalysts is

reported in Figure 39c, where it can be seen that the loss of crystallinity of Au NPs observed during the catalytic test is not recovered after regeneration.

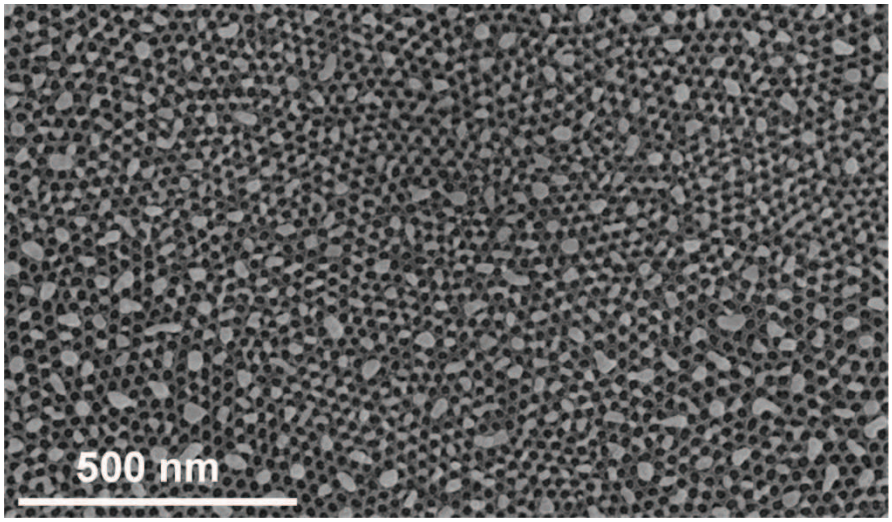

Figure 45. SEM image of 20Au-TiO_2 after PEC regeneration procedure.

The abatement performances obtained for a freshly prepared 20Au-TiO_2 photocatalyst and for three subsequent recycling tests (a regeneration cycle was applied between each test) are schematically reported in Figure 46. As it can be seen, the loss of activity is quite low even after 4 catalytic runs, indicating thus the effectiveness of the applied regeneration approach. These results are even more attractive if we consider that regeneration parameters were not optimized (this will be subject to further work).

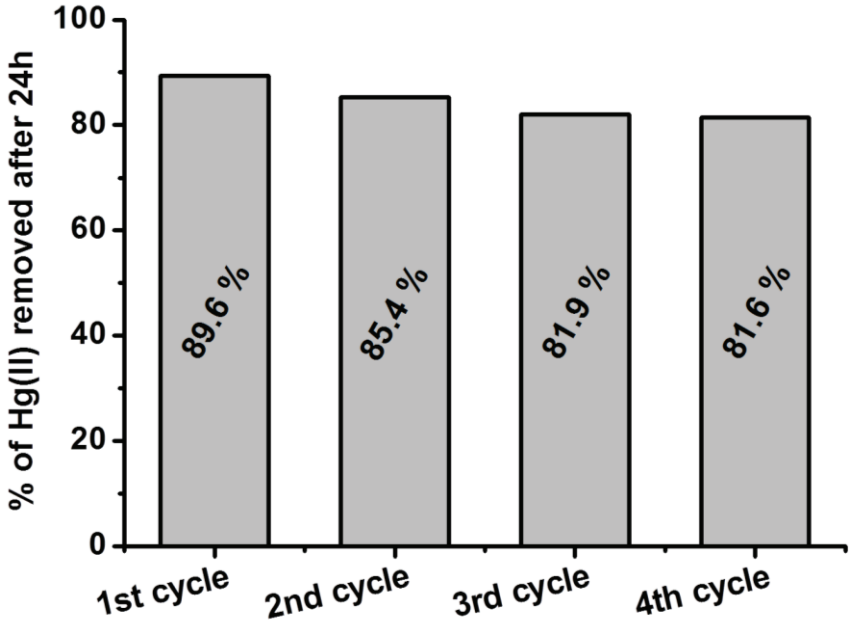

Figure 46. Percentage of Hg(II) removed from 10 ppm Hg(II) chlorides-containing solutions after 24 hours long photocatalytic experiments carried out using 20Au-TiO_2 re-cycled up to 4 times

Conclusions

In this paper we have shown that Au-TiO_2 photocatalysts are able under sun light irradiation to efficiently photo-reduce Hg(II) to Hg(I) or Hg(0) and to accumulate these species. This functionality is enabled by the Au NPs at TiO_2 NT surface.

Two different mechanisms can be identified depending on the chloride concentration, Hg(II) concentration and Au NPs size. The first involves the partial reduction of Hg(II) to Hg(I) and, as a result, produce the massive formation of insoluble calomel nanowires that occurs when 20Au-TiO_2 is used to treat solution of quite high Hg(II) concentration levels and containing chlorides. A second mechanism involves the complete reduction of Hg(II) to Hg(0) and the formation of Hg-Au amalgam; this seems to occur whenever it is not possible to form insoluble Hg_2Cl_2.

Best results, in terms of Hg abatement, were obtained with the most Au-loaded photocatalyst (20Au-TiO_2). It is noteworthy that this photocatalyst has an intrinsic bimodal abatement behavior: at higher Hg concentrations the abatement proceeds through the formation of calomel wire (with attracting scavenging features), while the formation of Hg-Au amalgam is preferred at low Hg concentrations.

We also demonstrated the feasibility of an efficient regeneration of the photocatalyst by PEC anodic stripping, which additionally allows to recover the previously removed Hg(II) in a concentrated waste.

2.4. Photoelectrocatalytic oxidation of As(III) over hematite photoanodes: a sensible indicator of the presence of highly reactive surface sites

Reproduced and adapted with permission from *Electrochimica Acta,* In press (**2018)**, **DOI**: 10.1016/j.electacta.2018.10.003, **Copyright © 2018 Elsevier B.V.**.

The original idea of using hematite for photoelectrochemical As(III) oxidation was conceived in a joint research group formed by Politecnico of Milan, ISTM-CNR and University of Insubria. The results reported in this chapter were mainly obtained at the University of Insubria. More in detail, my contribution has concerned the fabrication of all the photoelectrodes (in ISTM-CNR and University of Insubria), their complete characterization and the evaluation of their performances towards photoelectrocatalytic As(III) oxidation (in University of Insubria). XPS analysis, instead, were performed in FAU. Finally, I contributed extensively in the drafting and finalization of the published article. This article is considered the preliminary step and the base for future works using hematite for As(III) abatement in a flowing system (already designed and realized by the research group of Politecnico of Milan).

Abstract

Hematite-based photoanodes were used for the photoelectrocatalyzed batch oxidation of As(III) in water at pH 7 and 10. Tests were carried out at different As(III) initial concentrations, ranging from 150 μg/L to 30 mg/L. With no pre-treatments, an initial inactive period of 40-50 minutes was always observed at the beginning of every test. This initial inactive period is completely removed by a surface modification of surface active sites induced by a pre-polarization at 800 mV (vs. Ag/AgCl).

The water splitting active sites related to the Fe(III)-Fe(IV) redox couple were proved to be not active towards As(III) oxidation. The modifications induced by the anodic prepolarization were deeply studied: no evidence of the formation of surface highly oxidized iron sites (Fe(V) or Fe(VI)) and/or of highly reactive oxygen vacant sites emerges from XPS analysis. Rather, all collected characterization data support the conclusion that more reactive terminal oxygen species are necessary for As(III) oxidation. The As(III) abatement reaction was modelled by two subsequent first order kinetics in As(III), independently from the initial As(III) concentration: this behavior was explained suggesting that the highly reactive sites, being formed after prepolarization, are gradually depleted during the reaction. As this

reaction was proved to be very sensitive to the presence of highly reactive iron sites, its utilization as a probe reaction to study hematite photoanodes is suggested.

Introduction

Arsenic has long been known as a toxin and extended term exposure to inorganic arsenic, mainly through consumption of contaminated waters or eating of food prepared with contaminated waters, can lead to cancer, skin lesions and other diseases.[210–212] Since the presence of arsenic in the environment is due mostly to natural sources and, to a minor extent, to industrial wastes, its compounds can be found soil, water, air as well as in plant and animal tissues.[212] Naturally occurring arsenic in drinking water represents a major source of chronic arsenic exposure, and this is the reason why accepted limits in drinking water are as low as 10 μg/L, according to EU regulations.[214]

Given their toxicity and their abundance, arsenate ions (AsO_4^{3-}, $HAsO_4^{2-}$, $H_2AsO_4^{-}$) and arsenous acid ($As(OH)_3$) are the species of major concern in the typical pH range of natural waters (6.5 - 8.5).

Traditional physico-chemical removal processes of arsenic include: oxidation, coagulation/filtration, adsorptive media, ion exchange and reverse osmosis.[219]

The adsorption on iron oxide minerals (including amorphous iron oxide, goethite, magnetite and hematite) is one of the most used techniques and several studies about this As/iron oxides interaction were reported in the literature.[178–184]

In case of removal by adsorption on iron oxide materials a preliminary oxidation of As(III) to arsenate anions is desirable since: i) As(III) species are more toxic as compared to the oxidized forms [221]; ii) As(III) is less strongly retained than As(V) by iron oxide surfaces, mainly due to its neutral charge occurring at pH values of natural waters.[179,220]

Different stoichiometric oxidants have been used to convert As(III) species to As(V), among which there are oxygen, ozone, chlorine dioxide, chlorine, dichloroamine, hydrogen peroxide, permanganate and ferrate.[215] The common drawbacks of these oxidants, such as limited efficiency, expensive reagents and disposal of potential dangerous wastes, are obviously related to the massive usage of chemicals.[222]

To solve some of these drawbacks, photocatalysis was recently proposed as an alternative technique to oxidize As(III) through the use of semiconductor photocatalysts, such as TiO_2,[224–227] Fe_2O_3/TiO_2,[228] and WO_3.[229] However, these processes show low quantum

efficiency due to high charge recombination along with drawbacks related to the disposal and regeneration of exhausted powdered photocatalysts.

In principle, all these problems may be overcome by using a photoelectrochemical (PEC) oxidation approach. The application of an external bias potential increases the band banding at the solid-liquid interface and draws the photo-generated electrons away via the external circuit, leaving surface holes available for oxidation reaction. Therefore, the probability of the rapid recombination of electron-hole pairs is largely reduced.[325] The application of a bias positive potential allows to tune the activity of the PEC system mainly shifting the energy band level of the photoactive anode with respect to the redox potentials of the investigated reactions. Moreover, in the case of photoelectrodes for pollutants abatement the issue related to disposal and regeneration of materials is alleviated thus representing a suitable technology for large scale plants. Finally, the simultaneous occurrence of PEC water splitting would allow the parallel cathodic production of suitable amounts of hydrogen, which can be efficiently used as the plant power source.

Hematite (α-Fe_2O_3)-based photoelectrodes have recently attracted considerable attention in PEC water splitting reaction due to their promising properties. Hematite is an earth abundant, non-toxic, photoelectrochemically stable material with a suitable valence band position for the water oxidation[142] and a narrow bandgap (1.9–2.2 eV) [140] that allows 15.3% of theoretical solar-to-hydrogen (STH) efficiency,[135] thus matching the requirements for practical applications.[138]

Taking into account the PEC and the arsenic adsorption properties of α-Fe_2O_3, we decided to explore the idea to test hematite for As(III) PEC oxidation, using either the reactive oxygen species (ROS) generated during water splitting or by a direct interaction between As(III) and α-Fe_2O_3 surface. Although different types of α-Fe_2O_3-based systems, optimised for water splitting (doped, multi-layered, etc.[173] (and references contained therein), are reported in the literature, we decided to work on pure α-Fe_2O_3/FTO photoanodes. This decision was taken considering that, to the best of our knowledge, α-Fe_2O_3 photoanodes have never been used for this application. Therefore, this work should be regarded as a proof of concept and/or as starting point of knowledges to develop more efficient systems. To obtain high surface area pure α-Fe_2O_3 photoanodes with quite good PEC properties under visible light, a modified thermal-solution method was used.[157]

As we will show later, the catalytic performances obtained with pure hematite photoanodes are not as good as the ones reported for other systems working under a photocatalytic approach (i.e. without any polarising circuit).[224–229] Anyway, we must

underline that the aim of this work is not to optimises the PEC performances, but rather to study the mechanism of action of hematite-based photoanodes towards As(III) oxidation, as we think that a starting basis of knowledges is fundamental to drive the research towards improvements of catalytic performances. Interestingly, this study revealed that highly oxidised iron active sites are necessary to oxidise As(III) which, in turns, means that As(III) oxidation can also be proposed as a model reaction to detect the presence of such sites.

Experimental

Preparation procedure of α-Fe_2O_3 photoanodes

$FeCl_3 \cdot 6H_2O$ (Sigma-Aldrich, 97%) and $NaNO_3$ (Sigma-Aldrich, ≥ 99.0%) were used as precursors in the thermal-solution deposition of α-Fe_2O_3on fluorine-doped tin oxide (FTO) coated glass substrates (Sigma-Aldrich, 7 Ω/sq).

Prior to the thin α-Fe_2O_3 film growth, the FTO substrates (2 x 1 cm^2) were cleaned by sonication with acetone, ethanol, and ultrapure water, separately for 15 min, and then dried. The synthesis of the α-Fe_2O_3 layer was carried out as described in the literature [135,157]. Briefly, FTO substrates were immersed for 3h at 70°C in a water solution of $FeCl_3 \cdot 6H_2O$ (0.15M) and $NaNO_3$ (1M), at pH 1.5, in case adjusted with HCl; a calcination at 550°C for 1 h, followed by 20 min at 800 °C was then performed to obtain the crystalline worm-like α-Fe_2O_3.

Characterization techniques

The morphology of photoelectrodes was studied with the use of a XL30 Environmental Scanning Electron Microscopy (ESEM FEG Philips) at 10 kV under high vacuum conditions. Elemental analysis and mapping were performed with a silicon drifted EDS detector (EDAX element).

Transmission electron microscopy (TEM) and high-resolution TEM (HR-TEM) analysis were performed by a ZEISS LIBRA200FE microscope. The sample was prepared gentle scratching the electrode surface with a scalpel and collecting it by simple adherence onto an holey-carbon supported film TEM grid [158].

The analysis of optical absorption properties was performed on a UV-Vis Thermo Scientific Evolution 220 UV-Vis spectrophotometer in the region of 200-800 nm by transmission absorption measurements.

X-ray diffraction (XRD) data were recorded on a Rigaku Miniflex system using Cu-Kα radiation. The measurement was performed at room temperature in the $20° \leq 2\theta \leq 70°$ range by placing the FTO films directly within the sample holder of the diffractometer.

XPS spectra were acquired using Al X-ray source equipped on a Physical Electronics 5600 instrumentation. The XPS spectra were corrected in relation to the C1s signal. The spectra were curve-fitted using OriginPro 2018 (Originlab corporation, USA) software application.

Cyclic voltammetry (CV), open circuit voltage (OCV) and photocurrent measurements (J-V) were carried out with a three-electrode system connected to an Amel 2551 potentiostat equipped with a silver chloride electrode (Ag/AgCl/saturated KCl) as reference electrode, and a Pt wire as counter electrode.

CV measurements reported in Figure 51 were carried out at pH 13.6 (NaOH 1M) with a voltage scan speed of 0.01 V/s in the range from -0.7 V to 0.50 V vs. Ag/AgCl. All other experiments were carried out at pH 10.0 or pH 7.0, using diluted NaOH or a phosphate buffer, respectively (see section 2.4).

A Sun 2000 Solar Simulator (Abet Technologies, calibrated at 100 mW/cm^2) coupled to an AM 1.5 G filter was used as the vertical light source: a totally reflecting mirror has been used to deflect the light beam in the horizontal direction to carry out the measurements in light conditions.

All measurements were performed using a 250 mL quartz beaker, placed over a magnetic stirrer: to obtain a good light focus and a total immersion of the electrodes it was necessary to use 135 mL of solution in each test.

Arsenic determination

A potentiostat/galvanostat μAUTOLAB type III interfaced with the multi-mode electrode stand model 663 VA (Metrohm) was used for the voltammetric determination of As(III).

Hydrochloric acid (Fluka, TraceSELECTultra) and ultrapure water (MilliQ 18.2 MΩ cm, 3ppb TOC) were employed.

A standard solution of 1000 ppm As (III) was prepared by dissolving 0.1320 g As_2O_3 (Carlo Erba, 99.997% purity) in 2 mL of 1M NaOH, subsequently acidified with 2 mL of concentrated ultrapure HCl and diluted to 100 g with ultrapure water. The solution stored at room temperature was stable for at least 4 months. A 1 ppm work solution of As (III) was prepared weekly by diluting the concentrated standard solution. A 5000 ppm Cu(II) solution

was prepared by dissolving 0.7920 g $CuCl_2 \cdot 2H_2O$ (Sigma-Aldirch, 99.999%) in 125 g of a 0.5% HCl solution.

A modified cathodic stripping voltammetry (CSV) [326] was used for As(III) determination. Briefly, a 10 mL blank solution composed by 1M HCl and 45 ppm of Cu(II) was purged for 5 min with N_2: the HMDE was scanned from −0.40 V to −1.00 V according to the parameters reported in Table 4. Subsequent additions of the sample and of the diluted As standard solutions were performed and after each addition four replicated scans were recorded (a purge of 15 s was used after each addition).

Total Arsenic concentration was determined with a Thermo Scientific ICAP Q inductively coupled plasma mass spectrometer (ICP-MS) using a He-collision cell in kinetic energy discrimination (KEDS) mode with the standard conditions indicated by the factory.

Table 4. CSV instrumental parameters used for the quantitative determination of As(III).

Parameter	Value
Deposition potential	- 400mV
Deposition time	10 s
Equilibration time	2 s
Modulation time	60 ms
Interval time	100 ms
Step potential	10 mV
Modulation amplitude	80 mV

PEC oxidation tests

The same three-electrode PEC cell and solar simulator described in paragraph 2.2 were used to perform the As(III) photoelectro-oxidation tests. A front illumination set-up was used for all the reported tests.

Preliminary tests were carried out at pH 10.0 (adjusting the pH of MilliQ water with concentrated NaOH). All the other tests were conducted in 2 mM pH 7.0 phosphate buffer solution (with a 630 μS/cm conductivity) obtained by dilution of a concentrated 200 mM phosphate buffer.

The presence of As(III) in solution was ensured by the addition of a proper amount of a diluted solution obtained from the concentrated 1000ppm As(III) solution above reported. In order to avoid the influence of pH and conductivity variations during additions, the diluted

solution was adjusted to pH 7.0 and to 630 μS/cm. Every test was carried out by using a solution volume of 135 mL.

The constant applied bias potential was chosen (after CV measurements) as the voltage which ensured high recorded photocurrents avoiding contribution from electrochemical water splitting. As the result, a 660 mV potential (vs. Ag/AgCl) was used for all tests carried out at pH 10.0, while a 800mV potential was used for all test at pH 7.0.

Results and discussion

Characterizations of α-Fe_2O_3 photoelectrodes

The synthesised α-Fe_2O_3 photoanodes show the worm-like morphology (Figure 47a-c) typical for nanostructured films grown by the solution method [157]. The cross sectional view of the photoanode (Figure 47c) and the relative EDS analysis (Figure 47d) allow to distinguish the three expected different layers: α-Fe_2O_3, FTO, and glass substrate.

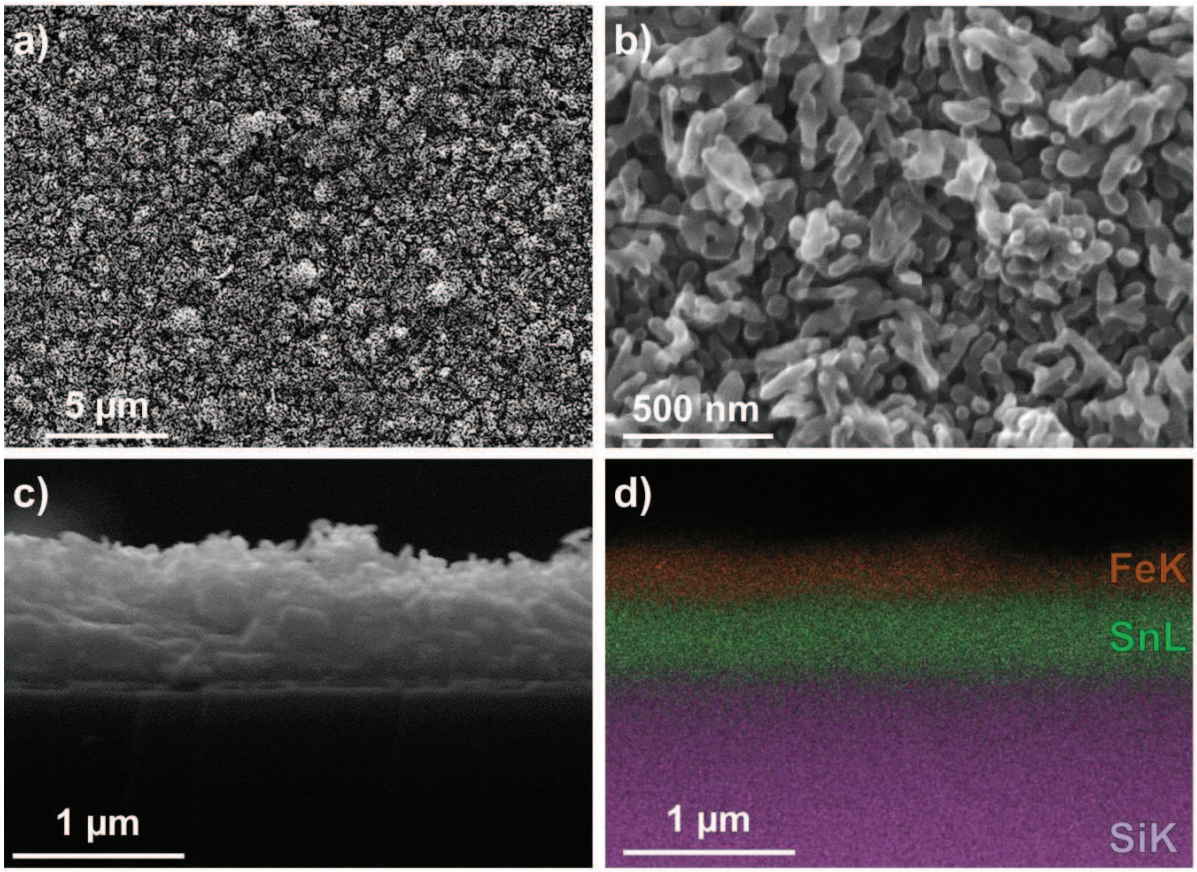

Figure 47. (a-b) SEM top view of nanostructured worm-like α-Fe_2O_3 deposited over an FTO electrode. (c) Cross-sectional view and (d) relative EDS map, in which are reported the signals of SiK (purple), SnL (green) and FeK (orange).

UV-vis spectrum of synthesized α-Fe_2O_3 nanostructures (Figure 48) shows that the threshold absorption is located around 600 nm. Hematite absorption is dominated by a strong transition in the region 400–600 nm, which is assigned to the pair excitation processes $^6A_1(^6S) + {}^6A_1(^6S)$ to $^4T_1(^4G) + {}^4T_1(^4G)$ at 485–550 nm, and is overlapped by the contributions of $^6A_1(^6S)$ to ^4E, $^4A_1(4G)$ ligand field transitions at 430 nm and the ligand to metal charge transfer transition band tail [327]. The double exciton process $^6A_1(^6S) + {}^6A_1(^6S)$ to $^4T_1(^4G) + {}^4T_1(^4G)$ yields the strongest absorption band at around 535 nm and it is primarily responsible for the red color of α-Fe_2O_3.

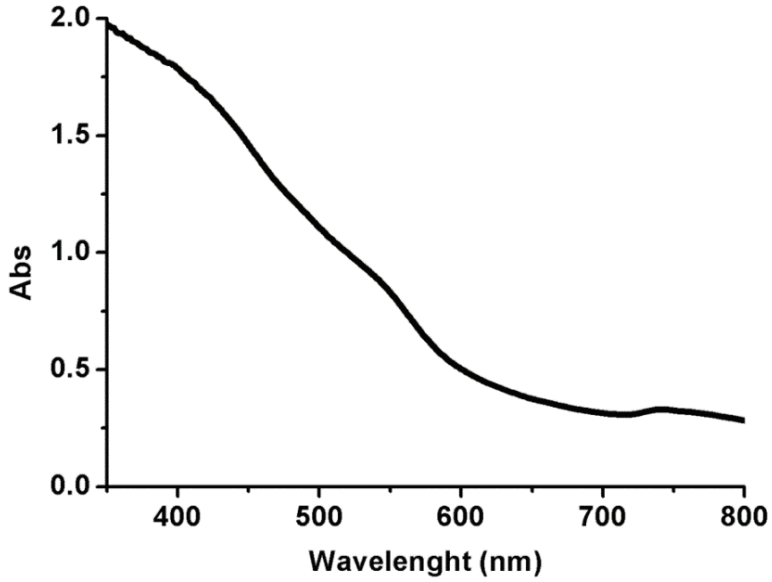

Figure 48. Transmission UV-Vis spectrum of hematite/FTO.

The presence of crystalline hematite is proven by the XRD spectrum shown in Figure 49. Besides the strong diffraction peaks of SnO_2 (present in the FTO coating), it is possible to identify two characteristics reflections of crystalline hematite: (110) and (300) reflections of α-Fe_2O_3 are clearly visible at 35.8° and 64.2°, respectively. This assignment is in agreement with the standard data provided in α-Fe_2O_3 JCPDS card (33-0664) [328].

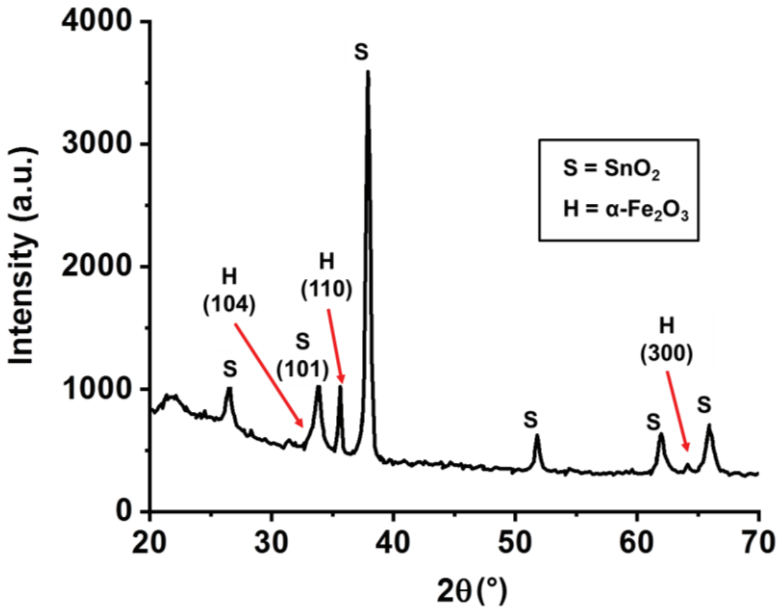

Figure 49. XRD pattern of a α-Fe_2O_3 photoanode. The reflections labeled with "S" belong to the SnO_2 (cassiterite) associated to the FTO coating of the glass substrate. The diffraction peaks labeled with "H" and indexed as (110) and (300) belong to α-Fe_2O_3.

TEM micrograph (Figure 50) further confirms the expected morphology as globular, coral-like nanostructure. Additionally, HR-TEM analysis showed the nanocrystalline α-Fe_2O_3 structure, in accord with the reported XRD data (Figure 49). The (104) reflection of hematite, which is hindered in the XRD spectrum by the (101) reflection of SnO_2 [329], is instead clearly visible from the FFT analysis of HR-TEM images (Figure 50c).

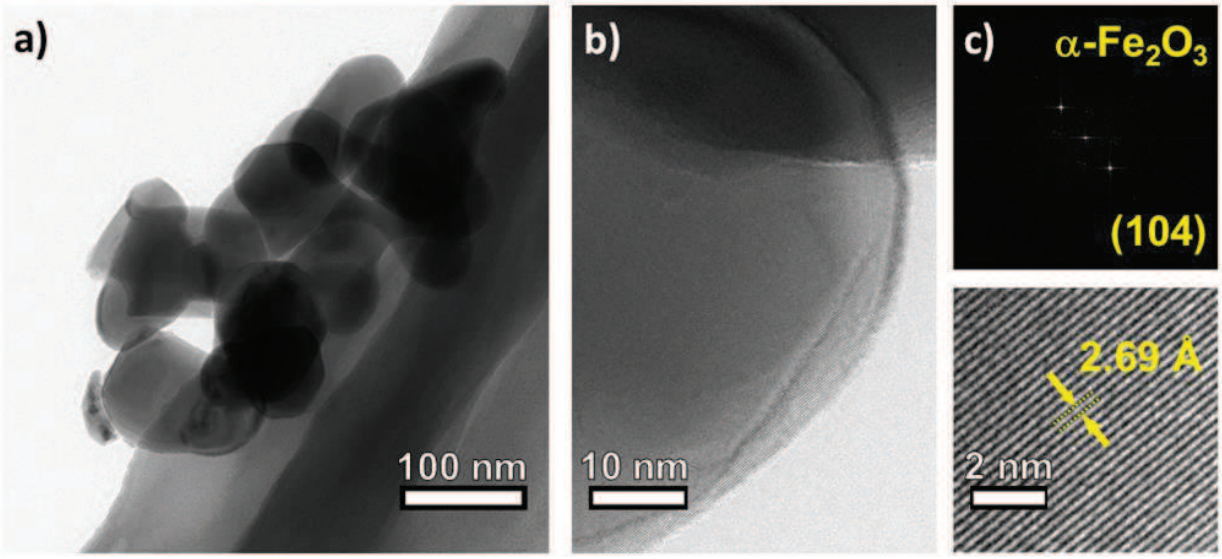

Figure 50. Sample morphological overview: (a) TEM micrograph, (b) HRTEM micrograph and (c) related FFT analysis along with crystalline phase identification.

The PEC characterization shows a good activity towards the water splitting reaction at pH 13.6, even though we used a large area photoanode (2 cm^2), which shows an onset potential for PEC water splitting of -0.25 V vs Ag/AgCl and generates a stable photocurrent density (J) of about 100 $\mu A/cm^2$ at 0.23 V) (Figure 51).

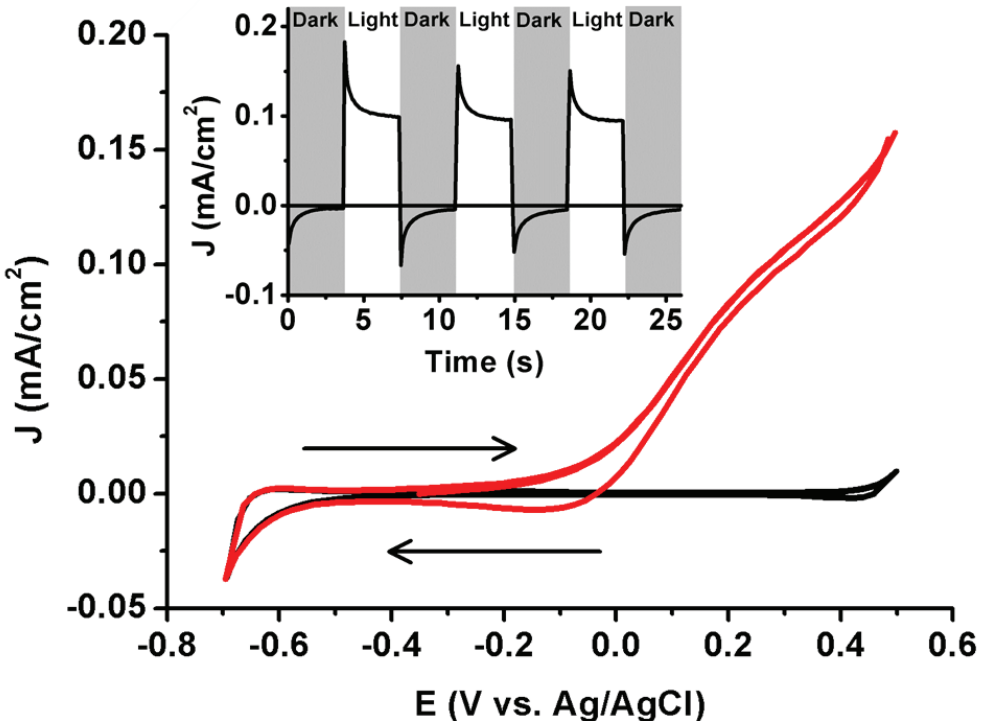

Figure 51. Current density (J)-potential (V) characterization of α-Fe_2O_3/FTO at pH 13.6 (NaOH 1 M) and 1 sun illumination. Main graph: CV curves in dark (black) and light (red) conditions; both CVs started from OCV values in the anodic direction. Inset: chronoamperometry at 0.23 V (vs Ag/AgCl) under chopped light irradiation.

As(III) abatement tests

The very first PEC experiments were conducted in mild basic conditions at pH 10.0 to favour the reaction of water splitting [39], as the formation of ROS (representing important intermediates of this reaction), may play also a significant role in As(III) oxidation.

Figure 52 displays plots of the relative As(III) residual concentration vs. reaction time using different initial As(III) concentrations: a 40-45% As(III) abatement is observed after 450 minutes, independently from the initial concentration. These tests suggest that the abatement reaction proceeds, after an initial induction time, via a first order kinetics with respect to the As(III) concentration. The presence of an initial induction time that delays the beginning of the reaction of about 30-45 minutes (see the inset of Figure 52) was observed in

all experiments carried out in these conditions: during this period only a slight decrease of the As(III) concentration is observed.

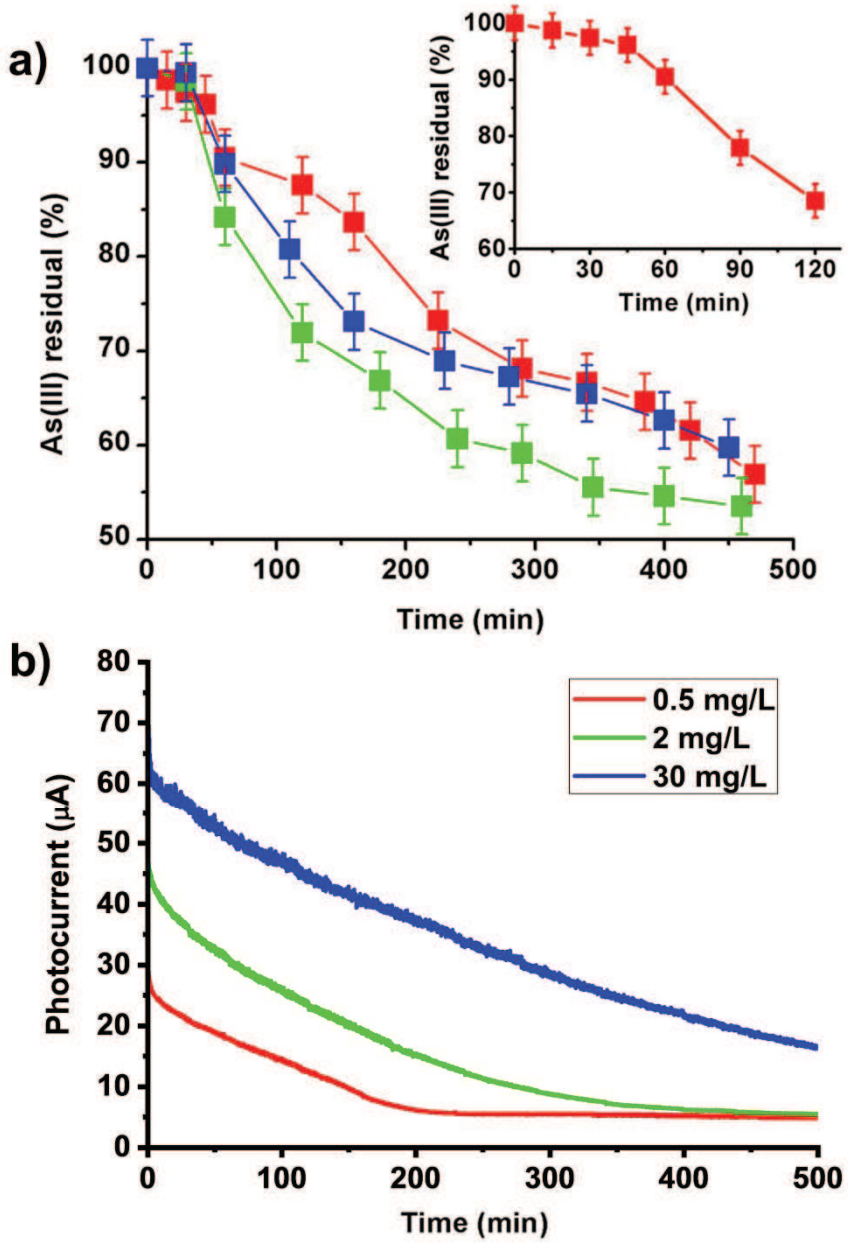

Figure 52. (a) As(III) concentration trends during PEC oxidation at pH 10.0 with different starting As concentrations: 0.5 mg/L (red), 2 mg/L (green), 30 mg/L (blue). Inset: initial part of the test over the 0.5 mg/L As(III) solution. (b) Photocurrent vs. time plots recorded during PEC oxidation tests shown in (a). This experiments were carried using a solar simulator as light source (described in the experimental section) and applying a potential of 660 mV.

This induction period could be ascribed to the establishment of the electrode/As(III) adsorption-desorption equilibrium[330,331]. To verify this hypothesis, and to try to avoid the initial non-reactive step, an abatement test was performed keeping in contact for 30 min in

darkness the α-Fe_2O_3 photoelectrode with the electrolyte in the presence of As(III), before polarisation and illumination. As the result, the inactive induction period is still present to the same extent: this evidence clearly indicates that the establishment of the As(III) pre-adsorption equilibrium is not the cause of the presence of the initial inactive period.

After these initial tests we moved to conditions that closely resemble natural waters-like condition, working thus with a buffered solution at pH 7.0 (2 mM phosphate buffer, 630 μS/cm).

Green and red lines reported in Figure 53a show the trends of the As(III) concentration versus time obtained by using in every experiments a 500 μg/L As(III) solution, with and without As(III) pre-adsorption, respectively. As can be seen, at pH 7.0 the photoanode shows activities which are similar (or even better) to the ones recorded at pH 10.0 with a 20% abatement observed after about 100 minutes. Even at pH 7.0 the initial non-active phase (either with or without a pre-adsorption step in dark condition) is still present.

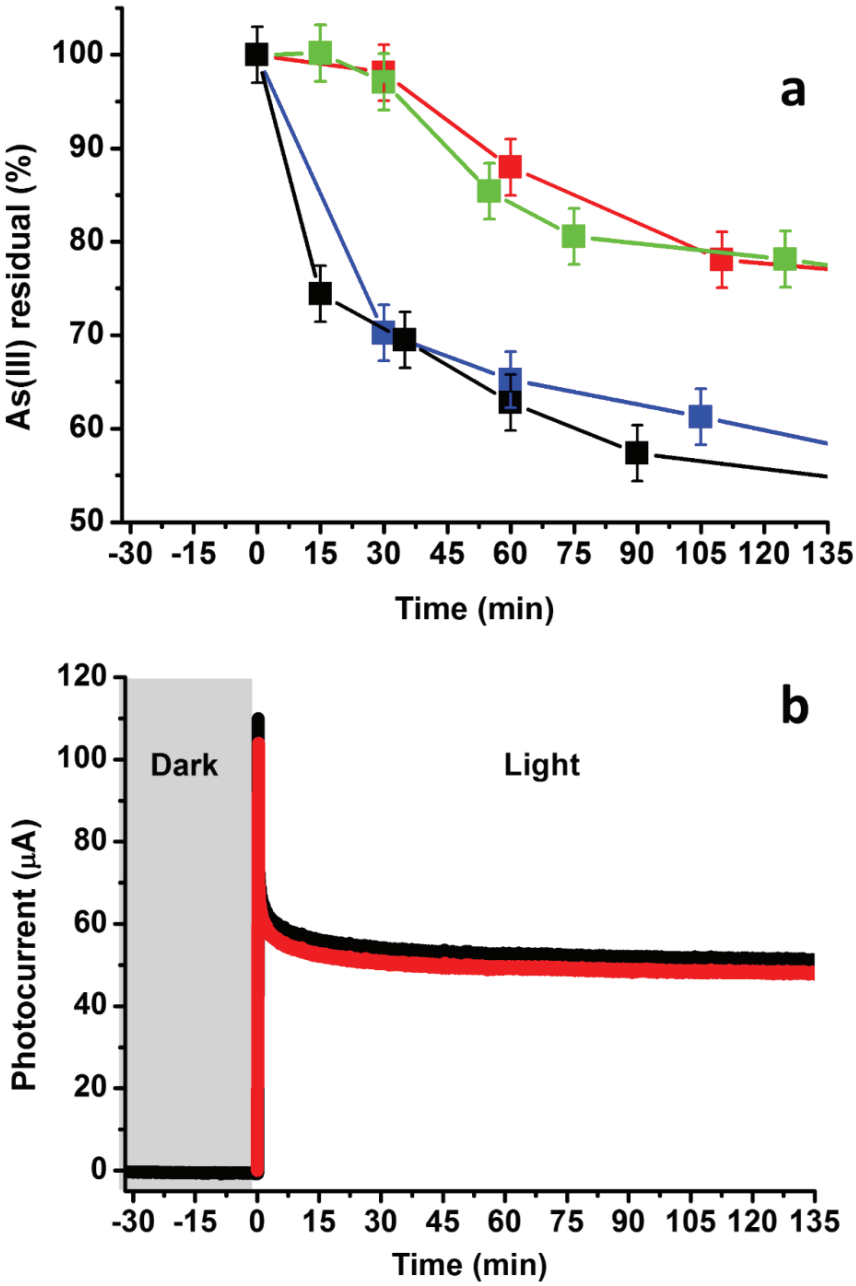

Figure 53. (a) PEC oxidation tests over 500 μg L^{-1} of As(III) at pH 7.0 with different pre-test treatments: red line -without pretreatment; green line -with 30 minutes As(III) pre-adsorption in open-circuit conditions; blue line -with the application of a 800 mV potential (vs. Ag/AgCl) in dark for 30 minutes in the presence of 500 μg L^{-1} of As(III); black line -with the application of a 800 mV potential (vs. Ag/AgCl) in dark for 30 minutes in the absence of As(III). (b) Photocurrents recorded during the red line and the black line experiments.

It is interesting to note that these preliminary data rule out any role of ROS produced by water splitting reaction in the oxidative mechanism of As(III), as these species are quickly formed from the very beginning of the test (as evidenced by the photocurrents shown in Figure 53b), i.e. during the inactive induction period.

Concerning the potential capability of α-Fe_2O_3 to adsorb the As(V) species being formed, we didn't observed (as detected by ICP-MS analysis) a significant decrease of the total As

concentration during PEC oxidations, both at pH 10.0 and 7.0. This can be explained considering that the total amount of hematite deposited onto the FTO substrate is only about 850 μg, and that the superficial amount of α-Fe_2O_3 available for adsorption phenomena represents only a small fraction in weight of the total deposited α-Fe_2O_3.

As a final consideration, since the As(III) oxidation performances of photoanodes at pH 7.0 are similar (or even better) to the ones at pH 10.0, after these preliminary experiments we decided to work only at pH 7.0, as this condition is closer to a possible application of this process.

On the nature of the induction period

After having ruled out any possible influence of As(III) pre-adsorption phenomena, we decided to study if a pre-polarisation step at 800 mV (the same potential applied during the PEC abatement) in dark condition, applied before starting the abatement of As(III), could play a beneficial effect.

Figure 53a (blue and black lines) clearly show that the initial unreactive induction period is completely deleted if such a pre-polarisation is applied. Moreover, the initial reaction rate is significantly fastened as it is possible to remove up to 40% of As(III) in the first 60 minutes.

Apparently, the presence or the absence of As(III) during the pre-polarisation step in dark conditions (compare blue and black lines of Figure 53a) does not cause relevant differences in the abatement performances of the pre-activated photoanodes. As a result, all the data reported in Figure 53a rule out any possible role of As(III) in the transformations occurring during the pre-activation step, thus suggesting that a modification of the α-Fe_2O_3 surface active sites could be the main process involved.

To get insights about the modifications occurring at the α-Fe_2O_3 surface through the pre-polarisation step, additional experiments were carried out.

Figure 54 shows CV plots obtained for the α-Fe_2O_3 photoanodes in dark conditions prior and after the 30 min of polarization at 800 mV. In the negative voltage region of the scan the two voltammograms show the reversible Fe(II)/Fe(III) surface redox process [332]: the photoanode after polarisation shows less pronounced Fe(II)/Fe(III) redox peaks, which would indicate a lower surface availability of Fe(III) sites belonging to this reversible redox pathway. Both CVs show a slightly visible quasi-reversible redox process (~ 120 mV peak separation) in the 300-420 mV region: this quasi-reversible process was always observed to

the same extent before and after polarisation. More interestingly, both CVs show a non-reversible (with respect to the CV time scale) reduction peak in the cathodic return scan at about 1.05 V vs. Ag/AgCl, which is markedly more pronounced for the pre-polarised electrode.

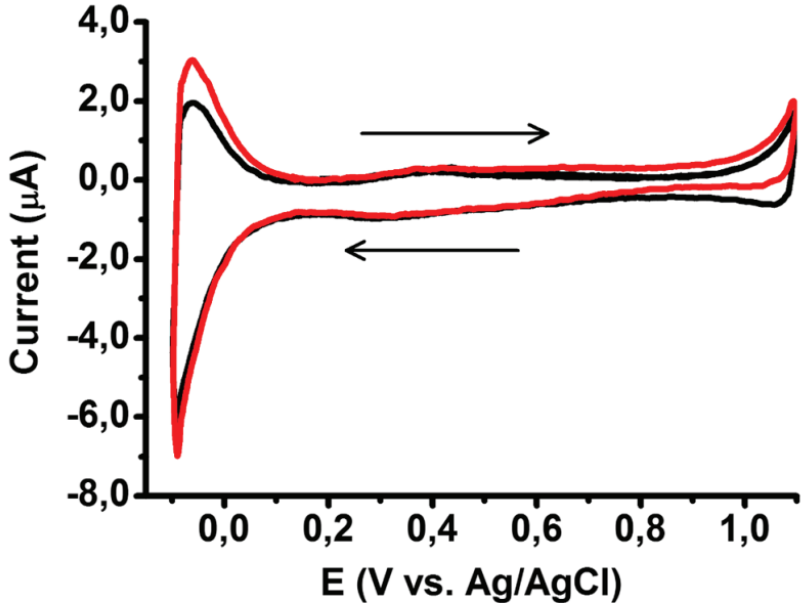

Figure 54. CV curves recorded prior (red) and after a 30 minutes polarization at 800 mV (black): both CVs started from OCV values in the anodic direction.

We may tentatively assign the first quasi-reversible redox feature at 300-420 mV to the Fe(III)/Fe(IV) coupled. This assignment is based on the consideration that it is now well established that PEC water splitting on hematite involves Fe(IV) sites [333–335] and that these sites must be immediately formed at the beginning of the test. Anyway, we cannot rule out mechanisms involving other iron oxidation states, as it was very recently claimed that a similar peak on hematite nanorods has to be ascribed to a Fe(III)-Fe(III)/Fe(IV)-Fe(V) transition [336]. Independently from an unambiguous assignment, it should be underlined that these sites are not active for As(III) PEC oxidation, as As(III) is not depleted during the first 30-45 min of the reaction. The formation of the As(III) oxidation active sites must be then related to the other non-reversible signal observed in the positive voltage region. According to the literature, we were initially tempted to assign the signal at 1.05 V to the reduction of previously formed Fe(VI) sites, as the 800mV pre-polarisation potential could be sufficient to reach such an high iron oxidation state (see [336] and references contained therein). This assignment is not correct since, as we will show later, XPS data rule out the formation of Fe(VI) sites after pre-polarisation. In any case, we have also to rule out that the enhanced

reactivity obtained with the pre-polarisation step is related to the increase of the surface hole density (as reported for water splitting [333]), as the pre-polarisation step is done in dark conditions.

With the purpose of monitoring the durability of the induced surface modifications, open circuit voltage (OCV) values were measured at increasing times after the pre-polarization step.

As shown in Figure 55, the pre-polarisation of α-Fe_2O_3 causes an increase of OCV values (both under dark and light conditions): from this point OCVs decrease very slowly reaching the original values only after about one day.

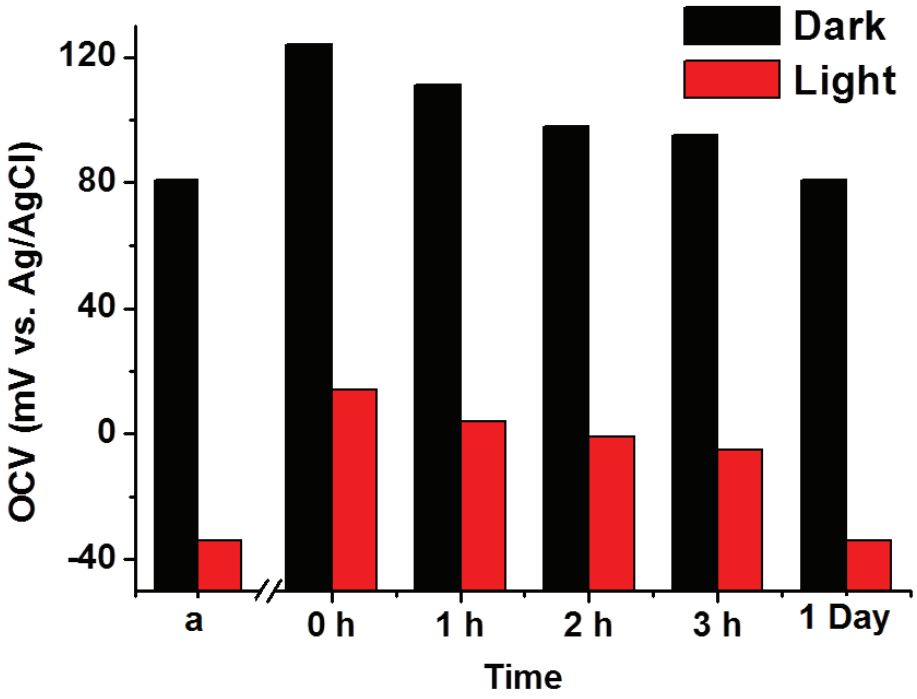

Figure 55. OCV values both in dark (black) and light (red) condition (a) before a 30 minutes polarization at 800 mV and after 0h, 1h, 2h, 3h and 1 day from the end of polarization.

These data, along with the data reported in Figure 54, clearly indicate that the modification of the electrode surface is not a fast and reversible process, with respect to the CV time scale, while it appears to be reversible for longer times. The one-day reversibility of the modifications induced by the pre-polarisation step was confirmed by three As(III) PEC oxidation tests carried out introducing an open circuit delay of 1h, 3h and 24h between the pre-polarisation and the beginning of the tests (Figure 56a, b and c, respectively). As the result, after a 1h delay, the observed performances are close to the ones without any delay, with about 35% As(III) removed in 70 minutes (compare Figure 56a with Figure 53a - blue

and black lines). After a 3h delay (Figure 56b) an induction period starts to reappear and the reaction rate decreases (~25% As(III) removed in 180 minutes). After 24h, the behaviour of the unpolarised electrode was completely restored (compare Figure 56c with Figure 53a – green and red lines).

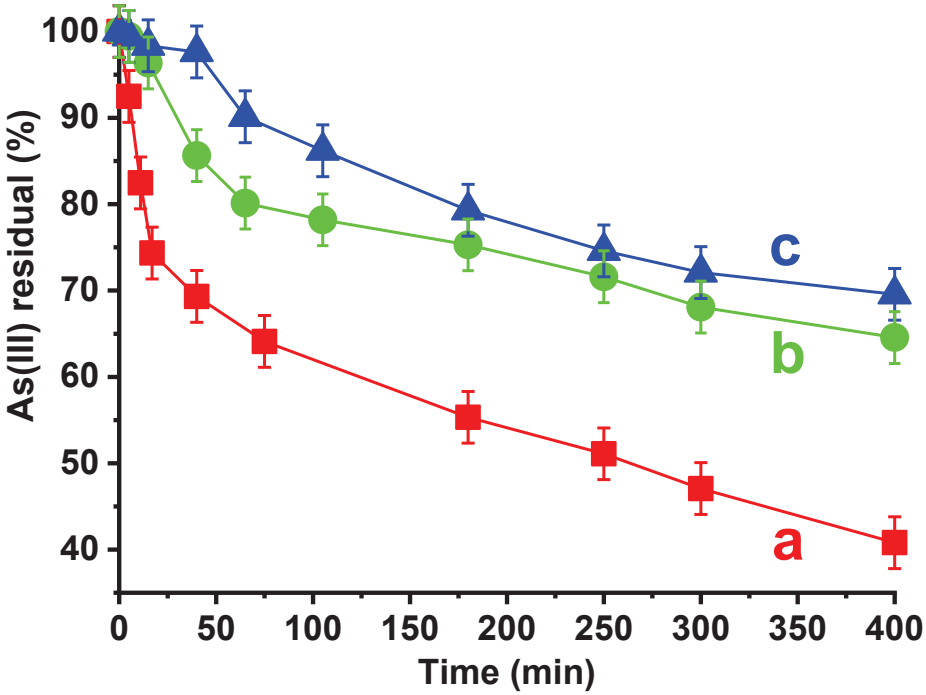

Figure 56. PEC As(III) oxidation tests carried out after different pre-starting conditions: (a) after 1h, (b) after 3h and (c) after 24h from the end of polarization at 800 mV for 30 minutes in dark.

From another point of view, the strong correlation that emerges between OCV values and catalytic data, indicates that OCV can be tentatively used as a convenient tool to predict the catalysts' performances towards As(III) oxidation.

The competition between water splitting and As(III) oxidation is confirmed by the data shown in Figure 57, where it can be seen that the photocurrent (that at the beginning of the test is only due to water splitting) decreases after every 100 μg/L addition of As(III): these data suggest that at least a part of the active water splitting sites interacts with As(III), thus reducing the oxidation of water in favour of the slower oxidation of As(III). The data reported in Figure 57 also indicate that the photocurrent lowering caused by subsequent additions of As(III) gradually decreases, with no more photocurrent changes after 500 μg/L of added As(III). This evidence suggests that: i) a saturation of the active sites for As(III) oxidation is reached; ii) only a fraction of the PEC oxidation active sites are active for As(III) oxidation,

as a quite high photocurrent due to water splitting is still recorded after a 500µg/L As(III) addition.

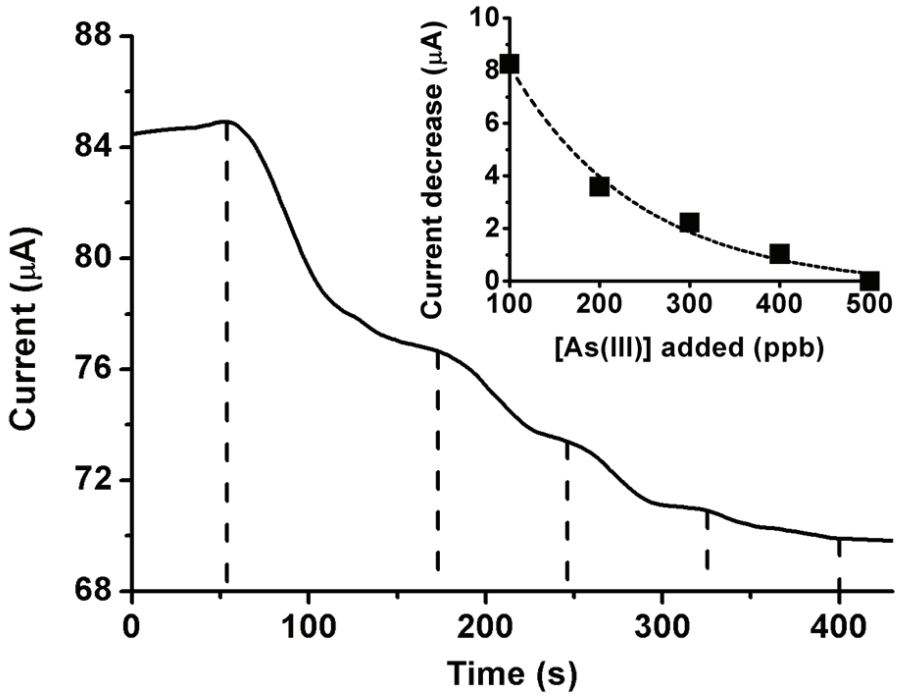

Figure 57. Effect of the subsequent additions of 100 µg/L of As(III) on the photocurrent recorded at 800 mV at pH 7.0

Diffuse reflectance UV-Vis and ATR spectroscopies were initially employed to study the nature of the active sites formed during the pre-polarisation: no appreciable differences were observed in the spectra (not shown) recorded with both techniques prior and after polarisation. These evidences indicate that no bulk hematite changes occur, and that modifications are only happening at the α-Fe_2O_3 surface.

XPS characterisation was then carried out in order to better emphasise modifications eventually occurring over the hematite surface. These measurements were carried out on untreated hematite and after fixed times from polarization (0h, 3h and 24h of air exposure).

It should be noted that prior and after any XPS analysis, the stability of OCV values was checked in order to exclude the occurrence of vacuum- or X-Ray-induced surface modifications on hematite: as a matter of fact OCV values didn't change significantly during every measurement.

In Figure 58, are reported the Fe2p signals of not treated and pre-polarised samples. The presence of α-Fe_2O_3 is confirmed in all samples, with peaks at 711.2, 724.9 and 719.3 eV corresponding to the binding energies of $Fe2p_{3/2}$, $Fe2p_{1/2}$ and the satellite peak of $Fe2p_{3/2}$,

respectively [337,338]. However, none of these spectra significantly differ from each other, neither in peak intensities, nor in peak positions. Therefore, no evidences of surface modification related to an alteration of the iron oxidation state could be inferred.

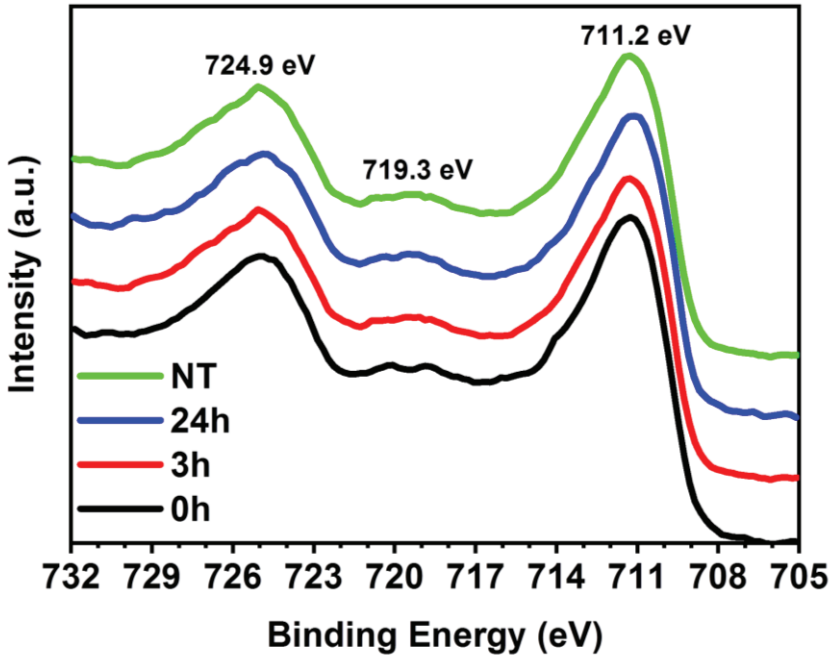

Figure 58. Comparison of XPS Fe2p signals of not treated and polarized hematite.

A noticeable effect of the polarization on the hematite surface was instead observed on O1s signals (Figure 59). Thanks to the deconvolution of O1s peaks, 3 characteristic peaks can be identified for all the samples (any attempt to fit these signals with more or less than 3 peaks failed). The relative intensities of these signals are strongly modified by the electrochemical history of the material.

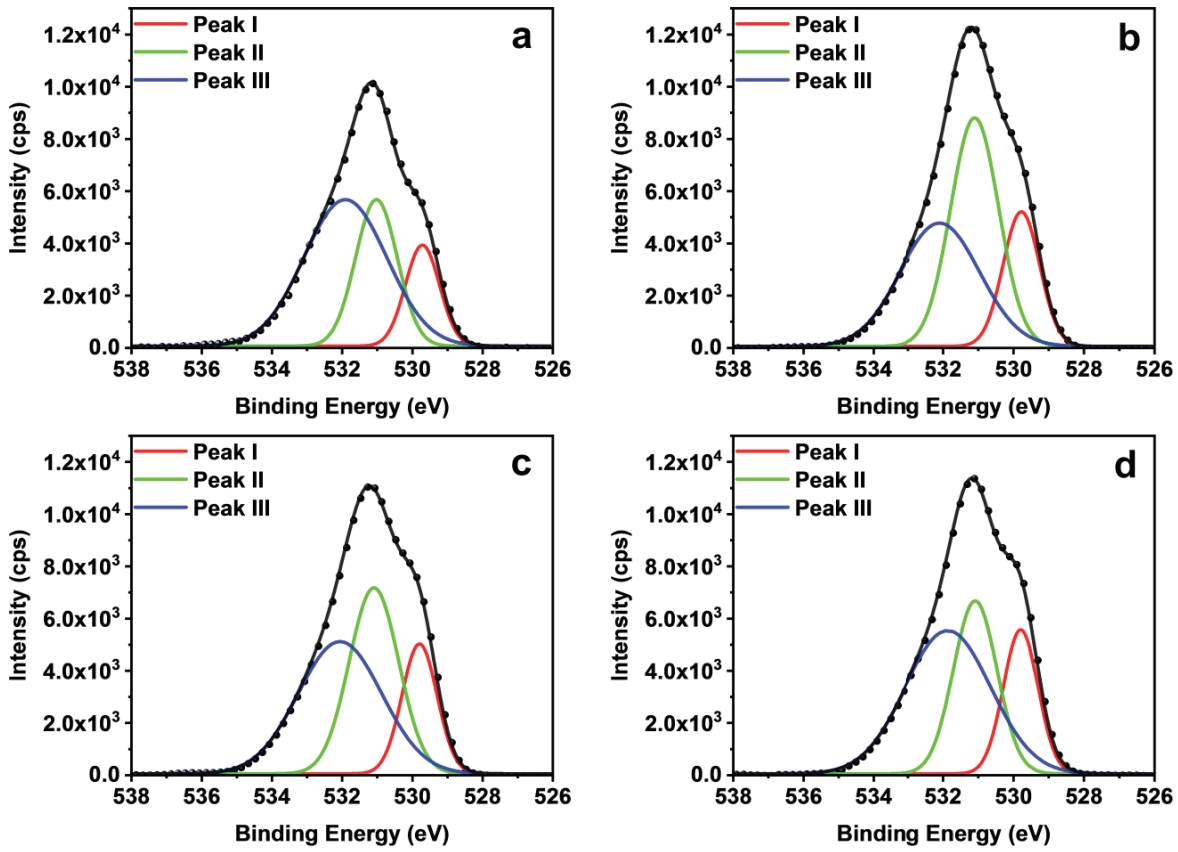

Figure 59. (a-d) XPS O1s deconvoluted signals of hematite (a) not treated, (b) right after polarization and after (c) 3 and (d) 24 hours from the polarization.

Any role of phosphate adsorption on such modifications can be ruled out since no differences in P2p signals after air exposure (see Figure 60) are observed.

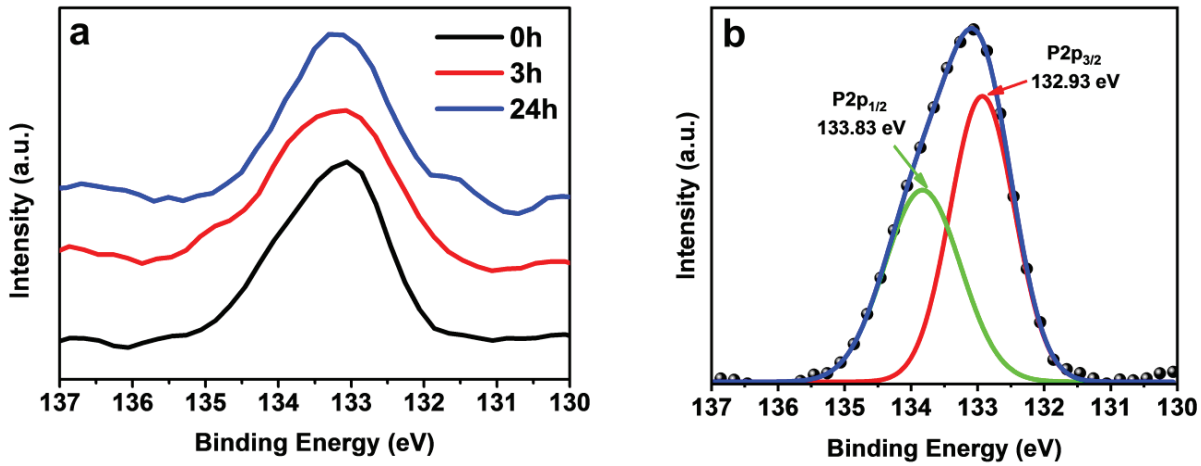

Figure 60. (a) Comparison of XPS P2p signals of polarized hematite after 0, 3 and 24 hours from the application of the bias potential. (b) Deconvolution of P2p peak obtained for 0h sample.

The peak located at 529.7 eV (Peak I) correspond to the lattice oxygen (O^{2-}) binding energy [285,337,339] and, as reported in Figure 61, its intensity is not significantly affected by the application of a positive voltage.

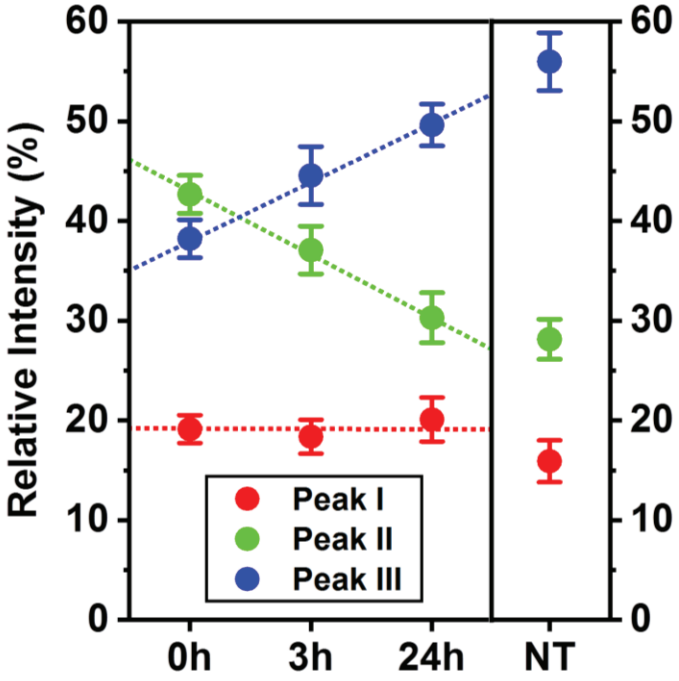

Figure 61. Trend of the relative intensity of Peak I, II and III after polarization (0h, 3h and 24h) and comparison with not treated hematite (NT)

Instead, a clear trend, after polarization and exposure to air, was observed for Peak II (at 531.0 eV) and Peak III (at 532.0 eV). The intensity of Peak II increases considerably right after the application of 800 mV, while Peak III becomes less intense (see Figure 61): starting from this point Peak II gradually decreases its intensity after subsequent air exposures, while Peak III becomes more intense.

Although the interpretation of Peak II and Peak III is a controversial matter, it is undoubtedly clarified that signals at higher binding energies are related to less electron-rich oxygen species [339]. Among the different possible assignment of Peak II, the formation of oxygen vacancies [340,341], must be ruled out since: i) oxygen vacancies are normally formed in quite hard conditions such as annealing in oxygen deficient environments; ii) the constant relative intensity of lattice oxygen signal (Peak I) does not fit with an oxygen depletion mechanism. Considering also that the signal due to the presence of adsorbed water (or organic O) on hematite surface is reported to be at ~533 eV [285,342], the strong correlation between Peak II and III can be reasonably attributed to a modification of hematite surface terminations. Therefore we are inclined to assign Peak II and Peak III to the presence of

O_2^{2-}/O^- and hydroxyl groups (-OH) on the surface, respectively [339]. The increase of the amount of high oxidative surface species (O_2^{2-}/O^-) can surely account for the enhancement in PEC oxidation performances. Finally, this interpretation can find further justification in light of the fact that the existence of an effect on the nature of hematite surface terminations due to the application of a bias voltage was already mentioned in the literature [343,344].

The restoration to starting hematite surface states is quite slow and only after 24 hours the situation returns to be almost like in the untreated sample (Figure 61). This final evidence, together with all XPS findings so far reported, matches perfectly with OCV measurements and As(III) abatement results.

Kinetics of As(III) oxidation

Two abatement tests over 150 and 500 μg/L As(III) solutions were conducted under revised conditions, i.e. after a 30 min pre-polarisation at 800 mV. The processed results of these two tests are reported in Figure 62a and 61b, respectively. In both cases, the overall reaction does not fit with any univariate scheme. Rather, these data could be tentatively modelled with two different and subsequent first order kinetics in As(III) concentration (see kinetic constants - *k* - in Table 5). In both cases the calculated *k* values indicate that the reaction is initially fast and becomes slower after about 45 min.

The results would indicate the initial surface concentration of the highly oxidative reactive sites (being formed during the pre-polarisation step) are gradually depleted within the first 45 min of reaction. After this initial highly active period, a steady state is reached and the catalysts' performances are constant for the whole duration of the PEC As(III) abatement.

Table 5. Kinetic constants and residual As(III) concentrations determined for the PEC oxidation tests shown in Figure 62.

As (III) conc. (μg/L)	k_1 (min^{-1})	k_2 (min^{-1})	% residual As (III) after 24h
150	0.0143	0.00262	7.50
500	0.0176	0.00143	17.15

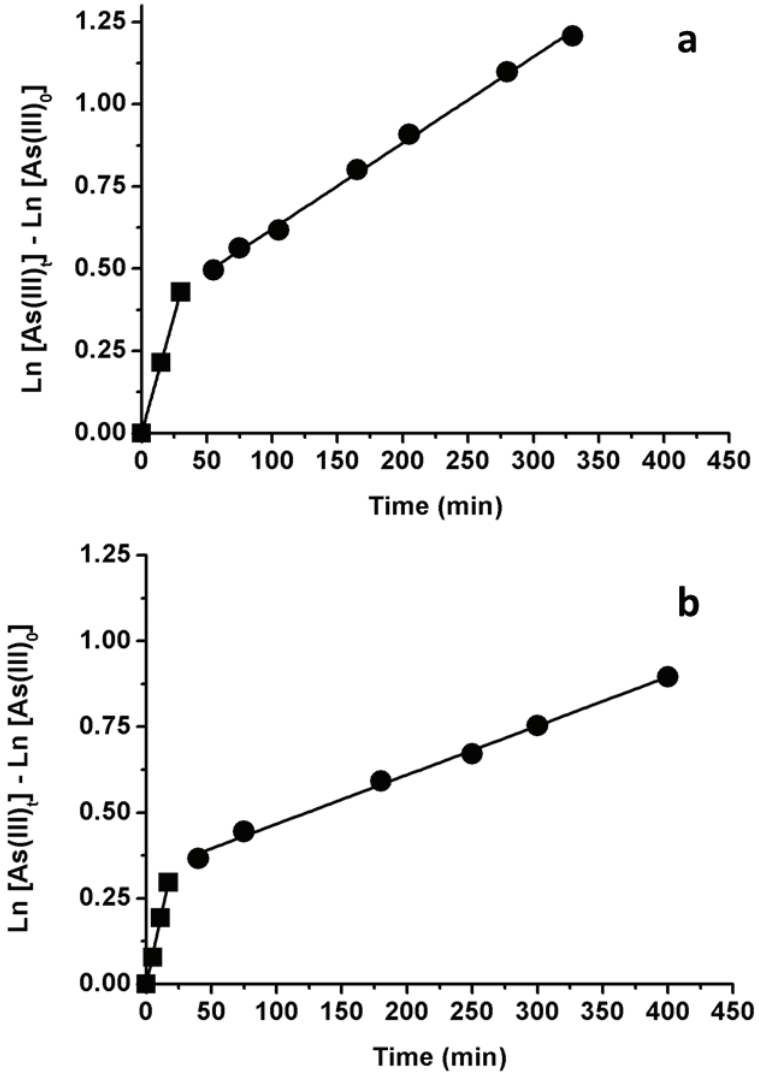

Figure 62. Kinetic linearizations of the PEC oxidation of a 150 µg/L (a) and a 500 µg/L (b) of As(III) at pH 7.0.

Finally, an As(III) PEC oxidation test using alternatively 30 minutes of darkness and 30 minutes of light has been performed. This experiment was necessary to verify that the As(III) oxidation takes place at the electrode surface. As shown in Figure 63 during every 30 minutes of dark, the oxidation of As(III) stops, meaning that the oxidation happens by the direct interaction of As(III) with the active surface and that the highly oxidised iron sites are unambiguously surface sites.

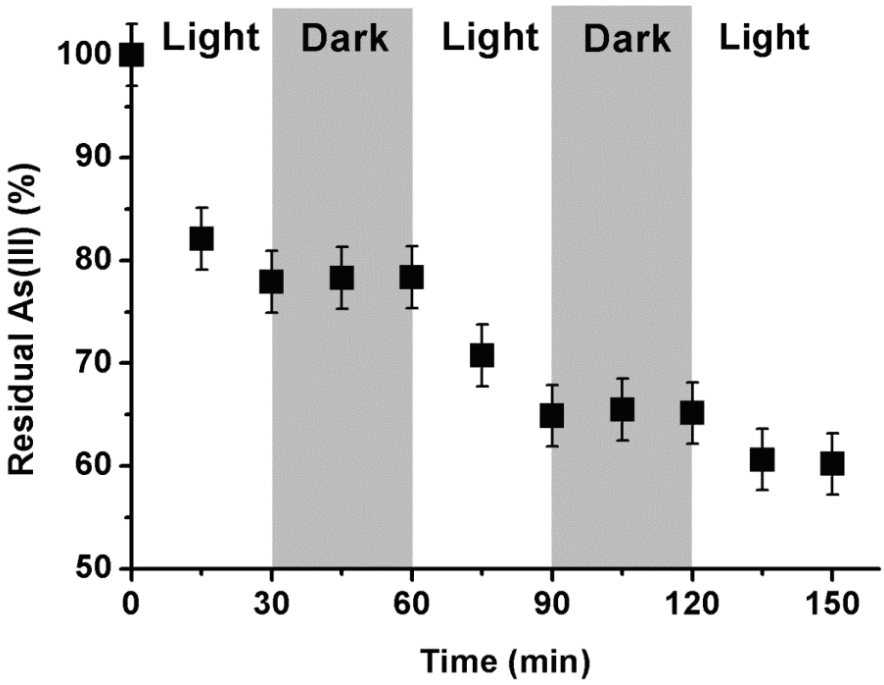

Figure 63. Abatement test at pH 7.0 over a 500 µg/L As(III) solution (after an initial 30 min pretreatment at 800 mV in dark condition) using alternatively 30 minutes of darkness and 30 minutes of illumination applying continuously 800 mV (i.e. both in dark and light conditions).

Conclusions

In this paper we have shown that α-Fe_2O_3 photoanodes are active toward the PEC oxidation of As(III). It was also shown that such an oxidation reaction happens at the electrode surface and that it is not significantly related to the presence of ROS. Although an optimisation of catalytic performances is out of the goals of this paper, the reported data are promising as modifications to the anode, like the ones reported to improve water splitting performances, may also apply to As(III) oxidation.

Even though it cannot be excluded that a photocatalytic tandem configuration could be also active toward As(III) oxidation, photoelectrocatalysis should be preferred, as the presence of a bias potential was shown to be fundamental for the formation of highly reactive sites on the α-Fe_2O_3 surface. In particular, the 800 mV pre-polarisation of photoanodes leads to the formation of modified hematite surface oxygen terminations which are able to oxidise up to 30% of the initial As(III) concentration within the first 30 min. However, these highly reactive sites are not stable for the whole duration of As(III) abatement tests. Future work will be focused in trying to stabilise these highly reactive sites by the utilisation of dopants and/or by the utilisation of a pulsed light strategy.

It is very interesting to notice that As(III) PEC oxidation tests have shown to be highly selective for the discrimination of these high oxidative surface sites, while water splitting is not. From another point of view, this final evidence prompts us to propose the utilisation of the As(III) PEC oxidation as an additional tool to study the surface reactivity of hematite-based photoanodes.

3. Conclusions

Differently decorated-TiO_2 nanotubes photocatalysts and nanostructured α-Fe_2O_3 photoanodes were investigated in view of their photocatalytic performances towards 3 topical environmental applications: i) photocatalytic hydrogen evolution, ii) photocatalytic reduction/scavenging of inorganic Hg(II), and iii) photoelectrocatalytic oxidation of inorganic As(III).

Concerning TiO_2-based photocatalysts, the site-selective decoration with nanoscopic precision of highly-ordered TiO_2 nanotubes, made possible by the employment of sputtering/dewetting approach, allowed to fabricate highly efficient photocatalytic systems which were used for photocatalytic hydrogen evolution and inorganic Hg(II) abatement. The enhancement of the photocatalytic performances obtained with these systems can be ascribed to several beneficial features which are enabled by this decoration technique.

First of all, as reported in Chapter 2.1, a well-defined WO_3-Pt co-catalyst stack deposited over the top of TiO_2 NTs enables an efficient electron transfer cascade mechanism which leads to strongly improved photocatalytic performances towards hydrogen evolution. These stacked structures, in fact, were able to produce a noticeably higher amount of H_2 than the one generated by any other single co-catalyst decorated (and non-decorated) TiO_2 nanotubes. The key to this enhancement is the high morphological control over the co-catalyst/photocatalyst structure which not only allows for improved performances, but it makes possible a detailed evaluation of the charge carrier dynamics.

This strategy was also used to form metal alloy co-catalyst nanoparticles at the photocatalyst surface starting from two sputtered metal layers. As reported in Chapter 2.2, it was investigated in detail the dewetting-induced formation of Ni/Cu nanoalloys at the TiO_2 NTs surface to fabricate an efficient noble metal-free photocatalyst for H_2 evolution from water-ethanol mixtures. A complete control over the alloyed nanoparticles composition allows for a fine tuning of the properties of the material. The performances obtained using NiCu-decorated TiO_2 systems are much higher than the ones achieved by any single metal-loaded (i.e. pure Ni or pure Cu) photocatalyst and, surprisingly, they are comparable to those obtained by Pt-decorated of TiO_2.

The same sputtering/dewetting approach was also employed to fabricate TiO_2-Au systems for photocatalytic inorganic Hg(II) abatement from aqueous solutions under solar light irradiation. Although in this case the employed decoration technique did not play a key role

in achieving high photocatalytic performances, the scavenging properties enabled by the presence of Au NPs make this material fascinating for the simultaneous reduction and accumulation of inorganic Hg species. Different reaction pathways were recognized for the photocatalytic reduction/scavenging of Hg(II) depending on several parameters (e.g. Cl^- and Hg(II) concentration and Au NPs size). More in detail, if the Au NPs size and the Hg(II) and Cl^- concentrations are sufficiently high, the photocatalytic abatement leads to the massive growth of calomel nanowires, while at low Hg(II) the formation of Au-Hg nanoalloys (amalgam) occurs. In any case, both the mechanisms lead to noticeable abatement results. Additionally, the feasibility of a photoelectrochemical regeneration of the exhausted material makes more fascinating this system and allows to i) recycle the photocatalyst for subsequent Hg(II) abatement and ii) recover re-dissolved Hg(II) in a small concentrated waste volume.

Finally, nanostructured worm-like hematite (deposited on FTO glass substrates) was employed for the first time to photoelectrochemically oxidize As(III) to As(V) under solar light illumination. Although the PEC performances reported in Chapter 2.4 are not better than the ones obtained in previous works, some interesting findings regarding the mechanism of action were obtained. The application of a positive bias voltage, in fact, was revealed to be fundamental for the in-situ generation of temporarily stable highly oxidative sites on the photoanode surface which are necessary for an efficient As(III) oxidation. The surprisingly high selectivity exhibited by As(III) to detect such modified oxygen terminations suggests the potential utilization of PEC As(III) oxidation as a supplementary method to explore the nature of the hematite-based photoanodes surface.

4. References

1 J. J. Berzelius, *Ann. Chim. Phys.*, 1836, **61**, 146.
2 A. J. B. Robertson, *Platin. Met. Rev.*, 1975, **19**, 175.
3 W. Ostwald, *Z. Phys. Chem.*, 1894, **15**, 705–706.
4 F. Haber, *Z. Elektrochem.*, 1910, **16**, 244.
5 G. Ertl, *Surf. Sci.*, 1967, **6**, 208–232.
6 W. T. Grubb, *Nature*, 1964, **201**, 699–700.
7 A. P. van Troostwijk and J. R. Deimann, *J. Phys.*, 1790, **2**, 130.
8 A. Fujishima and K. Honda, *Nature*, 1972, **238**, 37–38.
9 F. di Quarto, K. Doblhofer and H. Gerischer, *Electrochim. Acta*, 1978, **23**, 195–201.
10 A. Heller and R. G. Vadimsky, *Phys. Rev. Lett.*, 1981, **46**, 1153–1156.
11 S. Menezes, H.-J. Lewerenz and K. J. Bachmann, *Nature*, 1983, **305**, 615–616.
12 B. O'Regan and M. Grätzel, *Nature*, 1991, **353**, 737–740.
13 I. K. Konstantinou and T. A. Albanis, *Appl. Catal. B Environ.*, 2004, **49**, 1–14.
14 S. Rehman, R. Ullah, A. M. Butt and N. D. Gohar, *J. Hazard. Mater.*, 2009, **170**, 560–569.
15 A. Fujishima, T. N. Rao and D. A. Tryk, *J. Photochem. Photobiol. C Photochem. Rev.*, 2000, **1**, 1–21.
16 K. Rajeshwar, M. E. Osugi, W. Chanmanee, C. R. Chenthamarakshan, M. V. B. Zanoni, P. Kajitvichyanukul and R. Krishnan-Ayer, *J. Photochem. Photobiol. C Photochem. Rev.*, 2008, **9**, 171–192.
17 A. L. Linsebigler, G. Lu and J. T. Yates, *Chem. Rev.*, 1995, **95**, 735–758.
18 Z. Zhang and J. T. Yates, *Chem. Rev.*, 2012, **112**, 5520–5551.
19 R. Beranek, *Adv. Phys. Chem.*, 2011, **2011**, 1–20.
20 M. R. Hoffmann, S. T. Martin, W. Choi and D. W. Bahnemann, *Chem. Rev.*, 1995, **95**, 69–96.
21 X. Chen, S. Shen, L. Guo and S. S. Mao, *Chem. Rev.*, 2010, **110**, 6503–6570.
22 U. I. Gaya and A. H. Abdullah, *J. Photochem. Photobiol. C Photochem. Rev.*, 2008, **9**, 1–12.
23 J. L. Guzmán-Mar, M. Villanueva-Rodríguez and L. Hinojosa-Reyes, eds. A. Hernández-Ramírez and I. Medina-Ramírez, Springer International Publishing, Cham, 2015, pp. 229–254.
24 J. Zhao and X. Yang, *Build. Environ.*, 2003, **38**, 645–654.
25 J. C. Yu, W. Ho, J. Lin, H. Yip and P. K. Wong, *Environ. Sci. Technol.*, 2003, **37**, 2296–2301.
26 D. Sudha and P. Sivakumar, *Chem. Eng. Process. Process Intensif.*, 2015, **97**, 112–133.
27 M. Ni, M. K. H. Leung, D. Y. C. Leung and K. Sumathy, *Renew. Sustain. Energy Rev.*, 2007, **11**, 401–425.
28 R. Daghrir, P. Drogui and D. Robert, *Ind. Eng. Chem. Res.*, 2013, **52**, 3581–3599.
29 A. Kudo and Y. Miseki, *Chem. Soc. Rev.*, 2009, **38**, 253–278.
30 J. Zaanen, G. A. Sawatzky and J. W. Allen, *Phys. Rev. Lett.*, 1985, **55**, 418–421.
31 C. Han, M.-Q. Yang, B. Weng and Y.-J. Xu, *Phys. Chem. Chem. Phys.*, 2014, **16**, 16891–16903.
32 D. Cahen, J. Manassen and G. Hodes, *Sol. Energy Mater.*, 1979, **1**, 343–355.
33 Y.-K. Peng and S. C. E. Tsang, *Nano Today*, 2018, **18**, 15–34.
34 A. Fujishima and K. Honda, *Nature*, 1972, **238**, 37–38.
35 P. Roy, S. Berger and P. Schmuki, *Angew. Chemie Int. Ed.*, 2011, **50**, 2904–2939.

36 K. Lee, A. Mazare and P. Schmuki, *Chem. Rev.*, 2014, **114**, 9385–9454.
37 T. Luttrell, S. Halpegamage, J. Tao, A. Kramer, E. Sutter and M. Batzill, *Sci. Rep.*, 2014, **4**, 4043.
38 H. Tang, K. Prasad, R. Sanjinès, P. E. Schmid and F. Lévy, *J. Appl. Phys.*, 1994, **75**, 2042–2047.
39 L. Thulin and J. Guerra, *Phys. Rev. B*, 2008, **77**, 195112.
40 W. R. Siah, H. O. Lintang, M. Shamsuddin and L. Yuliati, *IOP Conf. Ser. Mater. Sci. Eng.*, 2016, **107**, 12005.
41 A. Bojinova, R. Kralchevska, I. Poulios and C. Dushkin, *Mater. Chem. Phys.*, 2007, **106**, 187–192.
42 B. Ohtani, O. O. Prieto-Mahaney, D. Li and R. Abe, *J. Photochem. Photobiol. A Chem.*, 2010, **216**, 179–182.
43 P. Roy, S. Berger and P. Schmuki, *Angew. Chemie Int. Ed.*, 2011, **50**, 2904–2939.
44 Y. Xia, P. Yang, Y. Sun, Y. Wu, B. Mayers, B. Gates, Y. Yin, F. Kim and H. Yan, *Adv. Mater.*, 2003, **15**, 353–389.
45 T. M. and R. A. and T. O. and K. A. and Y. Taga, *Jpn. J. Appl. Phys.*, 2001, **40**, L561.
46 J. Choi, H. Park and M. R. Hoffmann, *J. Mater. Res.*, 2010, **25**, 149–158.
47 L. Jingxiang, Y. Jiaguo, J. Mietek, W. Swelm and A. A. A., *Adv. Mater.*, 2017, **29**, 1601694.
48 A. Bumajdad and M. Madkour, *Phys. Chem. Chem. Phys.*, 2014, **16**, 7146–7158.
49 V. Zwilling, M. Aucouturier and E. Darque-Ceretti, *Electrochim. Acta*, 1999, **45**, 921–929.
50 C. M. Lieber, *Solid State Commun.*, 1998, **107**, 607–616.
51 T. Kasuga, M. Hiramatsu, A. Hoson, T. Sekino and K. Niihara, *Langmuir*, 1998, **14**, 3160–3163.
52 P. Hoyer, *Langmuir*, 1996, **12**, 1411–1413.
53 A. Ghicov and P. Schmuki, *Chem. Commun.*, 2009, 2791.
54 K. Doohun, L. Kiyoung, R. Poulomi, B. Balaji I., S. Erdmann and S. Patrik, *Angew. Chemie*, 2009, **121**, 9490–9493.
55 K. Lee, D. Kim, P. Roy, I. Paramasivam, B. I. Birajdar, E. Spiecker and P. Schmuki, *J. Am. Chem. Soc.*, 2010, **132**, 1478–1479.
56 J. J. Kelly, *Electrochim. Acta*, 1979, **24**, 1273–1282.
57 D. Gong, C. A. Grimes, O. K. Varghese, W. Hu, R. S. Singh, Z. Chen and E. C. Dickey, *J. Mater. Res.*, 2001, **16**, 3331–3334.
58 R. Beranek, H. Hildebrand and P. Schmuki, *Electrochem. Solid-State Lett.* , 2003, **6**, B12–B14.
59 K. Yasuda and P. Schmuki, *Electrochim. Acta*, 2007, **52**, 4053–4061.
60 K. Yasuda, J. M. Macak, S. Berger, A. Ghicov and P. Schmuki, *J. Electrochem. Soc.*, 2007, **154**, C472–C478.
61 J. M. Macak, H. Hildebrand, U. Marten-Jahns and P. Schmuki, *J. Electroanal. Chem.*, 2008, **621**, 254–266.
62 J. M. Macak and P. Schmuki, *Electrochim. Acta*, 2006, **52**, 1258–1264.
63 A. V. and D. J. L. and T. H. and P. S. and G. E. T. and S. B. and J. K. and P. Schmuki, *Nanotechnology*, 2008, **19**, 355701.
64 P. Indhumati, J. Himendra, L. Ning and S. Patrik, *Small*, 2012, **8**, 3073–3103.
65 K. Lee, A. Mazare and P. Schmuki, *Chem. Rev.*, 2014, **114**, 9385–9454.
66 J. M. Macak, K. Sirotna and P. Schmuki, *Electrochim. Acta*, 2005, **50**, 3679–3684.
67 A. Tighineanu, T. Ruff, S. Albu, R. Hahn and P. Schmuki, *Chem. Phys. Lett.*, 2010, **494**, 260–263.
68 G. Andrei, A. Sergiu P., H. Robert, K. Doohun, S. Thomas, K. Julia, S. Carl-

Albrecht, F. Polycarpos and S. Patrik, *Chem. – An Asian J.*, 2009, **4**, 520–525.
69 V. Guidi, M. C. Carotta, M. Ferroni, G. Martinelli and M. Sacerdoti, *J. Phys. Chem. B*, 2003, **107**, 120–124.
70 L. E. Depero, L. Sangaletti, B. Allieri, E. Bontempi, A. Marino and M. Zocchi, *J. Cryst. Growth*, 1999, **198**–**199**, 516–520.
71 R. Asahi, T. Morikawa, T. Ohwaki, K. Aoki and Y. Taga, *Science*, 2001, **293**, 269-271.
72 M. Anpo, *Pure Appl. Chem.*, 2000, **72**, 1787–1792.
73 A. K. Ghosh and H. P. Maruska, *J. Electrochem. Soc.*, 1977, **124**, 1516–1522.
74 S. Shanmugasundaram and K. Horst, *Angew. Chemie Int. Ed.*, 2003, **42**, 4908–4911.
75 J. C. Yu, W. Ho, J. Yu, H. Yip, P. K. Wong and J. Zhao, *Environ. Sci. Technol.*, 2005, **39**, 1175–1179.
76 T. Umebayashi, T. Yamaki, H. Itoh and K. Asai, *Appl. Phys. Lett.*, 2002, **81**, 454–456.
77 X. Qiu and C. Burda, *Chem. Phys.*, 2007, **339**, 1–10.
78 X. Chen and C. Burda, *J. Phys. Chem. B*, 2004, **108**, 15446–15449.
79 J. H. Park, S. Kim and A. J. Bard, *Nano Lett.*, 2006, **6**, 24–28.
80 E. Barborini, A. M. Conti, I. Kholmanov, P. Piseri, A. Podestà, P. Milani, C. Cepek, O. Sakho, R. Macovez and M. Sancrotti, *Adv. Mater.*, 2005, **17**, 1842–1846.
81 A. Ghicov, J. M. Macak, H. Tsuchiya, J. Kunze, V. Haeublein, L. Frey and P. Schmuki, *Nano Lett.*, 2006, **6**, 1080–1082.
82 A. Benoit, I. Paramasivam, Y.-C. Nah, P. Roy and P. Schmuki, *Electrochem. commun.*, 2009, **11**, 728–732.
83 J. Papp, S. Soled, K. Dwight and A. Wold, *Chem. Mater.*, 1994, **6**, 496–500.
84 M. Altomare, N. T. Nguyen, S. Hejazi and P. Schmuki, *Adv. Funct. Mater.*, 2018, **28**, 1–9.
85 M. A. Butler, *J. Appl. Phys.*, 1977, **48**, 1914–1920.
86 W. Gissler, *J. Electrochem. Soc.*, 1977, **124**, 1710.
87 A. O. T. Patrocinio, L. F. Paula, R. M. Paniago, J. Freitag and D. W. Bahnemann, *ACS Appl. Mater. Interfaces*, 2014, **6**, 16859–16866.
88 F. Riboni, L. G. Bettini, D. W. Bahnemann and E. Selli, *Catal. Today*, 2013, **209**, 28–34.
89 F. Riboni, M. V. Dozzi, M. C. Paganini, E. Giamello and E. Selli, *Catal. Today*, 2017, **287**, 176–181.
90 A. Fuerte, M. D. Hernández-Alonso, A. J. Maira, A. Martínez-Arias, M. Fernández-García, J. C. Conesa, J. Soria and G. Munuera, *J. Catal.*, 2002, **212**, 1–9.
91 M. M. Momeni and Y. Ghayeb, *J. Mol. Catal. A Chem.*, 2016, **417**, 107–115.
92 Y. Tae Kwon, K. Yong Song, W. In Lee, G. Jin Choi and Y. Rag Do, *J. Catal.*, 2000, **191**, 192–199.
93 V. Keller, *J. Catal.*, 2003, **215**, 129–138.
94 J. H. Pan and W. I. Lee, *Chem. Mater.*, 2006, **18**, 847–853.
95 K. K. Akurati, A. Vital, J. Dellemann, K. Michalow, T. Graule, D. Ferri and A. Baiker, *Appl. Catal. B Environ.*, 2008, **79**, 53–62.
96 M. Carrus, M. Fantauzzi, F. Riboni, M. Makosch, A. Rossi, E. Selli and J. A. van Bokhoven, *Appl. Catal. A Gen.*, 2016, **519**, 130–138.
97 K. Y. Song, M. K. Park, Y. T. Kwon, H. W. Lee, W. J. Chung and W. I. Lee, *Chem. Mater.*, 2001, **13**, 2349–2355.
98 I. Paramasivam, J. M. Macak, A. Ghicov and P. Schmuki, *Chem. Phys. Lett.*, 2007, **445**, 233–237.
99 J. M. Macak, P. J. Barczuk, H. Tsuchiya, M. Z. Nowakowska, A. Ghicov, M. Chojak, S. Bauer, S. Virtanen, P. J. Kulesza and P. Schmuki, *Electrochem. commun.*, 2005, **7**,

1417–1422.
100 Z. Jiang, J. Li, W. Liao, G. Fan, H. Yu, L. Chen and Z. Su, *J. Nanomater.*, 2017, **2017**, 1–9.
101 N. T. Nguyen, M. Altomare, J. E. Yoo, N. Taccardi and P. Schmuki, *Adv. Energy Mater.*, 2016, **6**, 1501926.
102 J. Yoo, M. Altomare, M. Mokhtar, A. Alshehri, S. A. Al-Thabaiti, A. Mazare and P. Schmuki, *J. Phys. Chem. C*, 2016, **120**, 15884–15892.
103 N. T. Nguyen, J. Yoo, M. Altomare and P. Schmuki, *Chem. Commun.*, 2014, **50**, 9653–9656.
104 G. R. Bamwenda, S. Tsubota, T. Nakamura and M. Haruta, *J. Photochem. Photobiol. A Chem.*, 1995, **89**, 177–189.
105 A. Naldoni, M. D'Arienzo, M. Altomare, M. Marelli, R. Scotti, F. Morazzoni, E. Selli and V. Dal Santo, *Appl. Catal. B Environ.*, 2013, **130–131**, 239–248.
106 G. L. Chiarello, M. H. Aguirre and E. Selli, *J. Catal.*, 2010, **273**, 182–190.
107 L. S. Yoong, F. K. Chong and B. K. Dutta, *Energy*, 2009, **34**, 1652–1661.
108 H. Choi and M. Kang, *Int. J. Hydrogen Energy*, 2007, **32**, 3841–3848.
109 M. Jung, J. N. Hart, J. Scott, Y. H. Ng, Y. Jiang and R. Amal, *Appl. Catal. A Gen.*, 2016, **521**, 190–201.
110 S. Xu, J. Ng, X. Zhang, H. Bai and D. D. Sun, *Int. J. Hydrogen Energy*, 2010, **35**, 5254–5261.
111 T. Sreethawong, Y. Suzuki and S. Yoshikawa, *Int. J. Hydrogen Energy*, 2005, **30**, 1053–1062.
112 R. Ishii, K. Matsumura, A. Sakai and T. Sakata, *Appl. Surf. Sci.*, 2001, **169–170**, 658–661.
113 I. Pašti and S. Mentus, *Mater. Chem. Phys.*, 2009, **116**, 94–101.
114 Y. Shiraishi, H. Sakamoto, Y. Sugano, S. Ichikawa and T. Hirai, *ACS Nano*, 2013, **7**, 9287–9297.
115 É. Karácsonyi, L. Baia, A. Dombi, V. Danciu, K. Mogyorósi, L. C. Pop, G. Kovács, V. Coşoveanu, A. Vulpoi, S. Simon and Z. Pap, *Catal. Today*, 2013, **208**, 19–27.
116 G. Kovács, L. Baia, A. Vulpoi, T. Radu, É. Karácsonyi, A. Dombi, K. Hernádi, V. Danciu, S. Simon and Z. Pap, *"Applied Catal. B, Environ.*, 2014, **147**, 508–517.
117 M. Rusu, M. Baia, Z. Pap, V. Danciu and L. Baia, *J. Mol. Struct.*, 2014, **1073**, 150–156.
118 L. Baia, A. Vulpoi, T. Radu, É. Karácsonyi, A. Dombi, K. Hernádi, V. Danciu, S. Simon, K. Norén, S. E. Canton, G. Kovács and Z. Pap, *Appl. Catal. B Environ.*, 2014, **148–149**, 589–600.
119 I. Paramasivam, H. Jha, N. Liu and P. Schmuki, *Small*, 2012, **8**, 3073–3103.
120 M. Altomare, N. T. Nguyen and P. Schmuki, *Chem. Sci.*, 2016, **7**, 6865–6886.
121 C. V Thompson, *Annu. Rev. Mater. Res.*, 2012, **42**, 399–434.
122 S. Yang, F. Xu, S. Ostendorp, G. Wilde, H. Zhao and Y. Lei, *Adv. Funct. Mater.*, 2011, **21**, 2446–2455.
123 J. Mizsei, *Sensors Actuators B Chem.*, 1993, **16**, 328–333.
124 S. S. and C. K. and J.-B. C. and K. K. Berggren, *Nanotechnology*, 2010, **21**, 505301.
125 H. L. Caswell and Y. Budo, *J. Appl. Phys.*, 1964, **35**, 644–647.
126 A. E. B. Presland, G. L. Price and D. L. Trimm, *Prog. Surf. Sci.*, 1972, **3**, 63–96.
127 J. R. Levine, J. B. Cohen and Y. W. Chung, *Surf. Sci.*, 1991, **248**, 215–224.
128 A. I. Galuza, A. B. Beznosov and V. V Eremenko, *Low Temp. Phys.*, 1998, **24**, 726–729.
129 M. Mishra and D.-M. Chun, *Appl. Catal. A Gen.*, 2015, **498**, 126–141.
130 J. Yu, X. Yu, B. Huang, X. Zhang and Y. Dai, *Cryst. Growth Des.*, 2009, **9**, 1474–

1480.
131 J. Chen, L. Xu, W. Li and X. Gou, *Adv. Mater.*, 2005, **17**, 582–586.
132 X. Hu, J. C. Yu, J. Gong, Q. Li and G. Li, *Adv. Mater.*, 2007, **19**, 2324–2329.
133 B. Wang, J. S. Chen, H. Bin Wu, Z. Wang and X. W. (David) Lou, *J. Am. Chem. Soc.*, 2011, **133**, 17146–17148.
134 C.-Y. Cao, J. Qu, W.-S. Yan, J.-F. Zhu, Z.-Y. Wu and W.-G. Song, *Langmuir*, 2012, **28**, 4573–4579.
135 J. Y. Kim, G. Magesh, D. H. Youn, J.-W. Jang, J. Kubota, K. Domen and J. S. Lee, *Sci. Rep.*, 2013, **3**, 2681.
136 J. Brillet, M. Cornuz, F. Le Formal, J.-H. Yum, M. Grätzel and K. Sivula, *J. Mater. Res.*, 2010, **25**, 17–24.
137 Z. Chen, T. F. Jaramillo, T. G. Deutsch, A. Kleiman-Shwarsctein, A. J. Forman, N. Gaillard, R. Garland, K. Takanabe, C. Heske, M. Sunkara, E. W. McFarland, K. Domen, E. L. Miller, J. A. Turner and H. N. Dinh, *J. Mater. Res.*, 2010, **25**, 3–16.
138 L. Fu, H. Yu, Y. Li, C. Zhang, X. Wang, Z. Shao and B. Yi, *Phys. Chem. Chem. Phys.*, 2014, **16**, 4284.
139 M. G. Walter, E. L. Warren, J. R. McKone, S. W. Boettcher, Q. Mi, E. A. Santori and N. S. Lewis, *Chem. Rev.*, 2010, **110**, 6446–6473.
140 J. H. Kennedy, *J. Electrochem. Soc.*, 1978, **125**, 709.
141 C. Jorand Sartoretti, B. D. Alexander, R. Solarska, I. A. Rutkowska, J. Augustynski and R. Cerny, *J. Phys. Chem. B*, 2005, **109**, 13685–13692.
142 K. Sivula, F. Le Formal and M. Grätzel, *ChemSusChem*, 2011, **4**, 432–449.
143 J. Sundaramurthy, P. S. Kumar, M. Kalaivani, V. Thavasi, S. G. Mhaisalkar and S. Ramakrishna, *RSC Adv.*, 2012, **2**, 8201–8208.
144 G.-Y. Zhang, Y. Feng, Y.-Y. Xu, D.-Z. Gao and Y.-Q. Sun, *Mater. Res. Bull.*, 2012, **47**, 625–630.
145 L. Li, Y. Chu, Y. Liu and L. Dong, *J. Phys. Chem. C*, 2007, **111**, 2123–2127.
146 J.-S. Xu and Y.-J. Zhu, *CrystEngComm*, 2011, **13**, 5162–5169.
147 M. A. Valenzuela, P. Bosch, J. Jiménez-Becerrill, O. Quiroz and A. I. Páez, *J. Photochem. Photobiol. A Chem.*, 2002, **148**, 177–182.
148 T. K. Townsend, E. M. Sabio, N. D. Browning and F. E. Osterloh, *Energy Environ. Sci.*, 2011, **4**, 4270–4275.
149 L. Xu, J. Xia, K. Wang, L. Wang, H. Li, H. Xu, L. Huang and M. He, *Dalt. Trans.*, 2013, **42**, 6468–6477.
150 S. K. Maji, N. Mukherjee, A. Mondal and B. Adhikary, *Polyhedron*, 2012, **33**, 145–149.
151 S. K. Apte, S. D. Naik, R. S. Sonawane, B. B. Kale and J. O. Baeg, *J. Am. Ceram. Soc.*, 2007, **90**, 412–414.
152 S. Saremi-Yarahmadi, K. G. U. Wijayantha, A. A. Tahir and B. Vaidhyanathan, *J. Phys. Chem. C*, 2009, **113**, 4768–4778.
153 O. Akhavan, *Appl. Surf. Sci.*, 2010, **257**, 1724–1728.
154 A. Qurashi, Z. Zhong and M. W. Alam, *Solid State Sci.*, 2010, **12**, 1516–1519.
155 Z. Zhang, M. F. Hossain, T. Miyazaki and T. Takahashi, *Environ. Sci. Technol.*, 2010, **44**, 4741–4746.
156 P. Sharma, P. Kumar, D. Deva, R. Shrivastav, S. Dass and V. R. Satsangi, *Int. J. Hydrogen Energy*, 2010, **35**, 10883–10889.
157 F. Malara, F. Fabbri, M. Marelli and A. Naldoni, *ACS Catal.*, 2016, **6**, 3619–3628.
158 M. Marelli, A. Naldoni, A. Minguzzi, M. Allieta, T. Virgili, G. Scavia, S. Recchia, R. Psaro and V. Dal Santo, *ACS Appl. Mater. Interfaces*, 2014, **6**, 11997–12004.
159 S. Bharathi, D. Nataraj, K. Senthil and Yoshitake Masuda, *J. Nanoparticle Res.*, 2013,

15, 1346.
160 H. Zhou and S. S. Wong, *ACS Nano*, 2008, **2**, 944–958.
161 S.-W. Cao, Y.-J. Zhu, G.-F. Cheng and Y.-H. Huang, *J. Phys. Chem. Solids*, 2010, **71**, 1680–1683.
162 A. Mao, N.-G. Park, G. Y. Han and J. H. Park, *Nanotechnology*, 2011, **22**, 175703.
163 B. Weng, S. Liu, Z.-R. Tang and Y.-J. Xu, *RSC Adv.*, 2014, **4**, 12685–12700.
164 H. G. Cha, J. Song, H. S. Kim, W. Shin, K. B. Yoon and Y. S. Kang, *Chem. Commun.*, 2011, **47**, 2441–2443.
165 J. He and B. A. Parkinson, *ACS Comb. Sci.*, 2011, **13**, 399–404.
166 S.-W. Cao, J. Fang, M. M. Shahjamali, Z. Wang, Z. Yin, Y. Yang, F. Y. C. Boey, J. Barber, S. C. J. Loo and C. Xue, *CrystEngComm*, 2012, **14**, 7229–7235.
167 C. Miao, T. Shi, G. Xu, S. Ji and C. Ye, *ACS Appl. Mater. Interfaces*, 2013, **5**, 1310–1316.
168 X. H. Wen and H. J. Pan, *Adv. Mater. Res.*, 2012, **562**–**564**, 298–301.
169 D. K. Zhong, M. Cornuz, K. Sivula, M. Gratzel and D. R. Gamelin, *Energy Environ. Sci.*, 2011, **4**, 1759–1764.
170 S. J. Hong, S. Lee, J. S. Jang and J. S. Lee, *Energy Environ. Sci.*, 2011, **4**, 1781–1787.
171 F. Lin, D. Wang, Z. Jiang, Y. Ma, J. Li, R. Li and C. Li, *Energy Environ. Sci.*, 2012, **5**, 6400–6406.
172 L. Badia-Bou, E. Mas-Marza, P. Rodenas, E. M. Barea, F. Fabregat-Santiago, S. Gimenez, E. Peris and J. Bisquert, *J. Phys. Chem. C*, 2013, **117**, 3826–3833.
173 A. G. Tamirat, J. Rick, A. A. Dubale, W.-N. Su and B.-J. Hwang, *Nanoscale Horiz.*, 2016, **1**, 243–267.
174 H. Wender, R. V Goncalves, C. S. B. Dias, M. J. M. Zapata, L. F. Zagonel, E. C. Mendonca, S. R. Teixeira and F. Garcia, *Nanoscale*, 2013, **5**, 9310–9316.
175 M. Barroso, C. A. Mesa, S. R. Pendlebury, A. J. Cowan, T. Hisatomi, K. Sivula, M. Grätzel, D. R. Klug and J. R. Durrant, *Proc. Natl. Acad. Sci. U. S. A.*, 2012, **109**, 15640–15645.
176 K. M. H. Young and T. W. Hamann, *Chem. Commun.*, 2014, **50**, 8727–8730.
177 T. Hisatomi, F. Le Formal, M. Cornuz, J. Brillet, N. Tetreault, K. Sivula and M. Gratzel, *Energy Environ. Sci.*, 2011, **4**, 2512–2515.
178 S. Aredes, B. Klein and M. Pawlik, *J. Clean. Prod.*, 2012, **29**–**30**, 208–213.
179 S. Dixit and J. G. Hering, *Environ. Sci. Technol.*, 2003, **37**, 4182–4189.
180 Y. Mamindy-Pajany, C. Hurel, N. Marmier and M. Roméo, *Desalination*, 2011, **281**, 93–99.
181 S. Goldberg and C. T. Johnston, *J. Colloid Interface Sci.*, 2001, **234**, 204–216.
182 V. Lenoble, O. Bouras, V. Deluchat, B. Serpaud and J.-C. Bollinger, *J. Colloid Interface Sci.*, 2002, **255**, 52–58.
183 R. Prucek, J. Tuček, J. Kolařík, J. Filip, Z. Marušák, V. K. Sharma and R. Zbořil, *Environ. Sci. Technol.*, 2013, **47**, 130315062542003.
184 V. Chandra, J. Park, Y. Chun, J. W. Lee, I.-C. Hwang and K. S. Kim, *ACS Nano*, 2010, **4**, 3979–3986.
185 M. Smerlak, *Eur. J. Phys.*, 2011, **32**, 1143–1153.
186 Z. Chen, H. N. Dinh and E. Miller, *Photoelectrochemical Water Splitting*, 2013.
187 O. Khaselev and J. A. Turner, *Science (80-.).*, 1998, **280**, 425–427.
188 H. M. Boylan, R. D. Cain and H. M. 'Skip' Kingston, *J. Air Waste Manage. Assoc.*, 2003, **53**, 1318–1325.
189 R. A. Bernhoft, *J. Environ. Public Health*, 2012, **2012**, 1–10.
190 M. Harada, in *Adverse Effects of Foods*, Springer US, Boston, MA, 1982, pp. 135–148.
191 M. R. Greenwood, *J. Appl. Toxicol.*, 1985, **5**, 148–159.

192 S. Wolff, G. Brown, J. Chen, K. Meals, C. Thornton, S. Brewer, J. V Cizdziel and K. L. Willett, *J. Toxicol. Environ. Heal. Part A*, 2016, **79**, 894–904.
193 J. Burger, C. Jeitner and M. Gochfeld, *J. Toxicol. Environ. Heal. Part A*, 2011, **74**, 863–874.
194 M. A. Barakat, *Arab. J. Chem.*, 2011, **4**, 361–377.
195 A. Sharma, A. Sharma and R. K. Arya, *Sep. Sci. Technol.*, 2015, **50**, 1310–1320.
196 F. Fu and Q. Wang, *J. Environ. Manage.*, 2011, **92**, 407–418.
197 J. G. Yu, B. Y. Yue, X. W. Wu, Q. Liu, F. P. Jiao, X. Y. Jiang and X. Q. Chen, *Environ. Sci. Pollut. Res.*, 2016, **23**, 5056–5076.
198 W. H. Lee, C. W. Lai and S. B. Abd Hamid, *Materials (Basel).*, 2015, **8**, 5702–5714.
199 F. Forouzan, T. C. Richards and A. J. Bard, *J. Phys. Chem.*, 1996, **100**, 18123–18127.
200 C. Schopf, A. Martín and D. Iacopino, *Sci. Technol. Adv. Mater.*, 2017, **18**, 60–67.
201 S. G. Bratsch, *J. Phys. Chem. Ref. Data*, 1989, **18**, 1–21.
202 M. Gärtner, V. Dremov, P. Müller and H. Kisch, *ChemPhysChem*, 2005, **6**, 714–718.
203 M. A. Aguado, S. Cervera-March and J. Giménez, *Chem. Eng. Sci.*, 1995, **50**, 1561–1569.
204 X. Wang, S. O. Pehkonen and A. K. Ray, *Electrochim. Acta*, 2004, **49**, 1435–1444.
205 L. B. Khalil, M. W. Rophael and W. E. Mourad, *Appl. Catal. B Environ.*, 2002, **36**, 125–130.
206 M. J. López-Muñoz, J. Aguado, A. Arencibia and R. Pascual, *Appl. Catal. B Environ.*, 2011, **104**, 220–228.
207 G. G. Lenzi, C. V. B. Fávero, L. M. S. Colpini, H. Bernabe, M. L. Baesso, S. Specchia and O. A. A. Santos, *Desalination*, 2011, **270**, 241–247.
208 H. E. Byrne and D. W. Mazyck, *J. Hazard. Mater.*, 2009, **170**, 915–919.
209 J. C. Ng, *Environ. Chem.*, 2005, **2**, 146–160.
210 B. Mandal, *Talanta*, 2002, **58**, 201–235.
211 C. . Jain and I. Ali, *Water Res.*, 2000, **34**, 4304–4312.
212 World Health Organization, *Guidel. Drink. Qual.*
213 A. H. Smith, C. Hopenhayn-Rich, M. N. Bates, H. M. Goeden, I. Hertz-Picciotto, H. M. Duggan, R. Wood, M. J. Kosnett and M. T. Smith, *Environ. Health Perspect.*, 1992, **97**, 259–267.
214 European Union (Drinking water) Regulations, *S.I. No. 122*.
215 V. K. Sharma and M. Sohn, *Environ. Int.*, 2009, **35**, 743–759.
216 A. A. Meharg and J. Hartley-Whitaker, *New Phytol.*, 2002, **154**, 29–43.
217 B. L. Vallee, D. D. Ulmer and W. E. C. Wacker, *J. Occup. Environ. Med.*
218 M. L. Pierce and C. B. Moore, *Water Res.*, 1982, **16**, 1247–1253.
219 D. Mohan and C. U. Pittman, *J. Hazard. Mater.*, 2007, **142**, 1–53.
220 A. Jain, K. P. Raven and R. H. Loeppert, *Environ. Sci. Technol.*, 1999, **33**, 1179–1184.
221 P. H. Masscheleyn, R. D. Delaune and W. H. Patrick, *Environ. Sci. Technol.*, 1991, **25**, 1414–1419.
222 G. Iervolino, V. Vaiano, L. Rizzo, G. Sarno, A. Farina and D. Sannino, *J. Chem. Technol. Biotechnol.*, 2016, **91**, 88–95.
223 M. Bissen, M.-M. Vieillard-Baron, A. J. Schindelin and F. H. Frimmel, *Chemosphere*, 2001, **44**, 751–757.
224 H. Lee and W. Choi, *Environ. Sci. Technol.*, 2002, **36**, 3872–3878.
225 J. I. Garza-Arévalo, I. García-Montes, M. H. Reyes, J. L. Guzmán-Mar, V. Rodríguez-González and L. H. Reyes, *Mater. Res. Bull.*, 2016, **73**, 145–152.
226 Y. Wang, J. Duan, W. Li, S. Beecham and D. Mulcahy, *J. Hazard. Mater.*, 2016, **303**, 162–170.
227 W. Zhou, H. Fu, K. Pan, C. Tian, Y. Qu, P. Lu and C.-C. Sun, *J. Phys. Chem. C*, 2008,

112, 19584–19589.
228 H. Su, X. Lv, Z. Zhang, J. Yu and T. Wang, *J. Porous Mater.*, , DOI:10.1007/s10934-017-0362-9.
229 J. Kim, G. Moon, S. Kim and J. Kim, *J. Photochem. Photobiol. A Chem.*, 2015, **311**, 35–40.
230 P. K. Dutta, S. O. Pehkonen, V. K. Sharma and A. K. Ray, *Environ. Sci. Technol.*, 2005, **39**, 1827–1834.
231 P. K. Dutta, A. K. Ray, V. K. Sharma and F. J. Millero, *J. Colloid Interface Sci.*, 2004, **278**, 270–275.
232 F.-S. Zhang and H. Itoh, *Chemosphere*, 2006, **65**, 125–131.
233 M. Assefpour-Dezfuly, C. Vlachos and E. H. Andrews, *J. Mater. Sci.*, 1984, **19**, 3626–3639.
234 M. Ge, C. Cao, J. Huang, S. Li, Z. Chen, K.-Q. Zhang, S. S. Al-Deyab and Y. Lai, *J. Mater. Chem. A*, 2016, **4**, 6772–6801.
235 F. Riboni, N. T. Nguyen, S. So and P. Schmuki, *Nanoscale Horiz.*, 2016, **1**, 445–466.
236 D. Kowalski, D. Kim and P. Schmuki, *Nano Today*, 2013, **8**, 235–264.
237 X. Feng, K. Shankar, O. K. Varghese, M. Paulose, T. J. Latempa and C. A. Grimes, *Nano Lett.*, 2008, **8**, 3781–3786.
238 H. Gao, P. Zhang, J. Hu, J. Pan and J. Fan, *Appl. Surf. Sci.*, 2017, **391**, 211–217.
239 Z. Liu, Y. Lu, L. Yuan, L. Ma, L. Zheng, J. Zhang and T. Hu, *Appl. Catal. B Environ.*, 2016, **188**, 189–197.
240 J. E. Yoo, K. Lee, M. Altomare, E. Selli and P. Schmuki, *Angew. Chemie Int. Ed.*, 2013, **52**, 7514–7517.
241 G. Cha, M. Altomare, N. Truong Nguyen, N. Taccardi, K. Lee and P. Schmuki, *Chem. - An Asian J.*, 2017, **12**, 314–323.
242 M. Liu, L. Piao, L. Zhao, S. Ju, Z. Yan, T. He, C. Zhou and W. Wang, *Chem. Commun.*, 2010, **46**, 1664.
243 B. Liu and E. S. Aydil, *J. Am. Chem. Soc.*, 2009, **131**, 3985–3990.
244 M. Righettoni and S. E. Pratsinis, *Mater. Res. Bull.*, 2014, **59**, 199–204.
245 K. S. Kim, N. Winograd and R. E. Davis, *J. Am. Chem. Soc.*, 1971, **93**, 6296–6297.
246 B. O. Loopstra and H. M. Rietveld, *Acta Crystallogr. Sect. B Struct. Crystallogr. Cryst. Chem.*, 1969, **25**, 1420–1421.
247 M. Altomare, O. Pfoch, A. Tighineanu, R. Kirchgeorg, K. Lee, E. Selli and P. Schmuki, *J. Am. Chem. Soc.*, 2015, **137**, 5646–5649.
248 A. Herz, A. Franz, F. Theska, M. Hentschel, T. Kups, D. Wang and P. Schaaf, *AIP Adv.*, 2016, **6**, 35109.
249 H. Han, F. Riboni, F. Karlicky, S. Kment, A. Goswami, P. Sudhagar, J. Yoo, L. Wang, O. Tomanec, M. Petr, O. Haderka, C. Terashima, A. Fujishima, P. Schmuki and R. Zboril, *Nanoscale*, 2017, **9**, 134–142.
250 D. S. Ginley and M. A. Butler, *J. Appl. Phys.*, 1977, **48**, 2019–2021.
251 L. Weinhardt, M. Blum, M. Bär, C. Heske, B. Cole, B. Marsen and E. L. Miller, *J. Phys. Chem. C*, 2008, **112**, 3078–3082.
252 D. Tsukamoto, M. Ikeda, Y. Shiraishi, T. Hara, N. Ichikuni, S. Tanaka and T. Hirai, *Chem. - A Eur. J.*, 2011, **17**, 9816–9824.
253 G. Palmisano, V. Augugliaro, M. Pagliaro and L. Palmisano, *Chem. Commun.*, 2007, 3425.
254 R. van de Krol, Y. Liang and J. Schoonman, *J. Mater. Chem.*, 2008, **18**, 2311.
255 D. Barreca, G. Carraro, A. Gasparotto, C. Maccato, M. E. A. Warwick, E. Toniato, V. Gombac, C. Sada, S. Turner, G. Van Tendeloo and P. Fornasiero, *Adv. Mater. Interfaces*, 2016, **3**, 1600348.

256 M. C. Toroker, D. K. Kanan, N. Alidoust, L. Y. Isseroff, P. Liao and E. A. Carter, *Phys. Chem. Chem. Phys.*, 2011, **13**, 16644–16654.
257 M. Altomare, N. T. Nguyen, S. Hejazi and P. Schmuki, *Adv. Funct. Mater.*, 2018, **28**, 1704259.
258 I. Paramasivam, H. Jha, N. Liu and P. Schmuki, *Small*, 2012, **8**, 3073–3103.
259 J. R. Jennings, A. Ghicov, L. M. Peter, P. Schmuki and A. B. Walker, 2008, 13364–13372.
260 D. Wang, Z. P. Liu and W. M. Yang, *ACS Catal.*, 2017, **7**, 2744–2752.
261 Z. Lin, J. Li, L. Li, L. Yu, W. Li and G. Yang, *J. Mater. Chem. A*, 2017, **5**, 773–781.
262 H. Tian, S.-Z. Kang, X. Li, L. Qin, M. Ji and J. Mu, *Sol. Energy Mater. Sol. Cells*, 2015, **134**, 309–317.
263 Y. Yamada, S. Shikano and S. Fukuzumi, *RSC Adv.*, 2015, **5**, 47997.
264 S. Zhang, B. Peng, S. Yang, H. Wang, H. Yu, Y. Fang and F. Peng, *Int. J. Hydrogen Energy*, 2015, **40**, 303–310.
265 X. Li, J. Yao, F. Liu, H. He, M. Zhou, N. Mao, P. Xiao and Y. Zhang, *Sensors Actuators B Chem.*, 2013, **181**, 501–508.
266 Y. Su, S. Yang, W. Liu, L. Qiao, J. Yan, Y. Liu, S. Zhang and Y. Fang, *Microchim. Acta*, 2017, **184**, 4065–4072.
267 N. Riaz, F. K. Chong, Z. B. Man, R. Sarwar, U. Farooq, A. Khan and M. S. Khan, *RSC Adv.*, 2016, **6**, 55650–55665.
268 M. G. Prakash, R. Mahalakshmy, K. R. Krishnamurthy and B. Viswanathan, *Catal. Today*, 2016, **263**, 105–111.
269 M. M. Ambursa, T. H. Ali, H. V. Lee, P. Sudarsanam, S. K. Bhargava and S. B. A. Hamid, *Fuel*, 2016, **180**, 767–776.
270 B. Seemala, C. M. Cai, C. E. Wyman and P. Christopher, *ACS Catal.*, 2017, **7**, 4070–4082.
271 J. E. Yoo, K. Lee, M. Altomare, E. Selli and P. Schmuki, 2013, 7514–7517.
272 A. B. Tesler, B. M. Maoz, Y. Feldman, A. Vaskevich and I. Rubinstein, *J. Phys. Chem. C*, 2013, **117**, 11337–11346.
273 F. Niekiel, P. Schweizer, S. M. Kraschewski, B. Butz and E. Spiecker, *Acta Mater.*, 2015, **90**, 118–132.
274 P. Jacquet, R. Podor, J. Ravaux, J. Teisseire, I. Gozhyk, J. Jupille and R. Lazzari, *Scr. Mater.*, 2016, **115**, 128–132.
275 J. Yoo, M. Altomare, M. Mokhtar, A. Alshehri, S. A. Al-thabaiti, A. Mazare and P. Schmuki, *J. Phys. Chem. C*, 2016, **120**, 15884–15892.
276 N. T. Nguyen, M. Altomare, J. Yoo and P. Schmuki, *Adv. Mater.*, 2015, **27**, 3208–3215.
277 S.-H. Wu and D.-H. Chen, *J. Colloid Interface Sci.*, 2004, **273**, 165–169.
278 F. Davar, Z. Fereshteh and M. Salavati-Niasari, *J. Alloys Compd.*, 2009, **476**, 797–801.
279 L. De Rogatis, T. Montini, B. Lorenzut and P. Fornasiero, *Energy Environ. Sci.*, 2008, **1**, 501–509.
280 Q. Wu, L. D. L. Duchstein, G. L. Chiarello, J. M. Christensen, C. D. Damsgaard, C. F. Elkjaer, J. B. Wagner, B. Temel, J.-D. Grunwaldt and A. D. Jensen, *ChemCatChem*, 2014, **6**, 301–310.
281 D. A. Cadenhead and N. J. Wagner, *J. Phys. Chem.*, 1968, **72**, 2775–2781.
282 J. Sinfelt, *J. Catal.*, 1972, **24**, 283–296.
283 D. E. Eastman, *Phys. Rev. B*, 1970, **2**, 1–2.
284 P. O. Larsson and A. Andersson, *J. Catal.*, 1998, **179**, 72–89.
285 M. C. Biesinger, B. P. Payne, L. W. M. Lau, A. Gerson and R. S. C. Smart, *Surf. Interface Anal.*, 2009, **41**, 324–332.

286 A. Wolfbeisser, G. Kovács, S. M. Kozlov, K. Föttinger, J. Bernardi, B. Klötzer, K. M. Neyman and G. Rupprechter, *Catal. Today*, 2017, **283**, 134–143.
287 W. H. Schroeder and J. Munthe, *Atmos. Environ.*, 1998, **32**, 809–822.
288 M. Jaishankar, T. Tseten, N. Anbalagan, B. B. Mathew and K. N. Beeregowda, *Interdiscip. Toxicol.*, 2014, **7**, 60–72.
289 K. M. Rice, E. M. Walker, M. Wu, C. Gillette and E. R. Blough, *J. Prev. Med. Public Heal.*, 2014, **47**, 74–83.
290 R. P. Mason, J. R. Reinfelder and F. M. M. Morel, *Water, Air, Soil Pollut.*, 1995, **80**, 915–921.
291 Q. Wang, D. Kim, D. D. Dionysiou, G. A. Sorial and D. Timberlake, *Environ. Pollut.*, 2004, **131**, 323–336.
292 R. A. Lavoie, T. D. Jardine, M. M. Chumchal, K. A. Kidd and L. M. Campbell, *Environ. Sci. Technol.*, 2013, **47**, 13385–13394.
293 A. E. Poste, D. C. G. Muir, S. J. Guildford and R. E. Hecky, *Sci. Total Environ.*, 2015, **506–507**, 126–136.
294 EU, *Regulation (EU) 2017/852 of the European Parliament and of the Council of 17 May 2017 on mercury, and repealing Regulation (EC) No 1102/2008*, 2017.
295 D. Sudha and P. Sivakumar, *Chem. Eng. Process. Process Intensif.*, 2015, **97**, 112–133.
296 F. Opoku, K. K. Govender, C. G. C. E. van Sittert and P. P. Govender, *Adv. Sustain. Syst.*, 2017, **1**, 1700006.
297 J. Schneider, M. Matsuoka, M. Takeuchi, J. Zhang, Y. Horiuchi, M. Anpo and D. W. Bahnemann, *Chem. Rev.*, 2014, **114**, 9919–9986.
298 J. M. Macak, H. Tsuchiya, A. Ghicov, K. Yasuda, R. Hahn, S. Bauer and P. Schmuki, *Curr. Opin. Solid State Mater. Sci.*, 2007, **11**, 3–18.
299 M. Altomare, K. Lee, M. S. Killian, E. Selli and P. Schmuki, *Chem. - A Eur. J.*, 2013, **19**, 5841–5844.
300 M. Altomare, M. Pozzi, M. Allieta, L. G. Bettini and E. Selli, *Appl. Catal. B Environ.*, 2013, **136–137**, 81–88.
301 C. Adán, J. Marugán, E. Sánchez, C. Pablos and R. van Grieken, *Electrochim. Acta*, 2016, **191**, 521–529.
302 M. Ge, C. Cao, J. Huang, S. Li, Z. Chen, K.-Q. Zhang, S. S. Al-Deyab and Y. Lai, *J. Mater. Chem. A*, 2016, **4**, 6772–6801.
303 M. Landmann, E. Rauls and W. G. Schmidt, *J. Phys. Condens. Matter*, 2012, **24**, 195503.
304 S. Chen and L. W. Wang, *Chem. Mater.*, 2012, **24**, 3659–3666.
305 J. E. Yoo, K. Lee, M. Altomare, E. Selli and P. Schmuki, *Angew. Chemie Int. Ed.*, 2013, **52**, 7514–7517.
306 Y. X. Zhang, B. Gao, G. Li Puma, A. K. Ray and H. C. Zeng, *Sci. Adv. Mater.*, 2010, **2**, 503–513.
307 E. Ciceri, S. Recchia, C. Dossi, L. Yang and R. E. Sturgeon, *Talanta*, 2008, **74**, 642–647.
308 D. Spanu, S. Recchia, S. Mohajernia, O. Tomanec, Š. Kment, R. Zboril, P. Schmuki and M. Altomare, *ACS Catal.*, 2018, **8**, 5298–5305.
309 D. Spanu, S. Recchia, S. Mohajernia, P. Schmuki and M. Altomare, *Appl. Catal. B Environ.*, 2018, **237**, 198–205.
310 J. Yoo, M. Altomare, M. Mokhtar, A. Alshehri, S. A. Al-Thabaiti, A. Mazare and P. Schmuki, *J. Phys. Chem. C*, 2016, **120**, 15884–15892.
311 G. Cha, P. Schmuki and M. Altomare, *Electrochim. Acta*, 2017, **258**, 302–310.
312 S. F. L. Mertens, M. Gara, A. S. Sologubenko, J. Mayer, S. Szidat, K. W. Krämer, T.

Jacob, D. J. Schiffrin and T. Wandlowski, *Adv. Funct. Mater.*, 2011, **21**, 3259–3267.
313 T. Kobiela, B. Nowakowski and R. Dus, *Appl. Surf. Sci. Appl. Surf. Sci.*, 2003, **206**, 78–89.
314 Y. V. Fedoseeva, A. S. Orekhov, G. N. Chekhova, V. O. Koroteev, M. A. Kanygin, B. V. Senkovskiy, A. Chuvilin, D. Pontiroli, M. Riccò, L. G. Bulusheva and A. V. Okotrub, *ACS Nano*, 2017, **11**, 8643–8649.
315 P. Bonnissel-Gissinger, M. Alnot, J.-P. Lickes, J.-J. Ehrhardt and P. Behra, *J. Colloid Interface Sci.*, 1999, **215**, 313–322.
316 T. Morris and G. Szulczewski, *Langmuir*, 2002, **18**, 2260–2264.
317 C. Ramasindarum, V. Balakrishnan, N. H. Abu Kasim and M. A. Yarmo, in *Characterization and Development of Biosystems and Biomaterials*, 2013, pp. 153–166.
318 J.-Y. Raty, F. Gygi and G. Galli, *Phys. Rev. Lett.*, 2005, **95**, 96103.
319 G. Hong, Y. Chen, P. Li and J. Zhang, *Carbon N. Y.*, 2012, **50**, 2067–2082.
320 B. Dou, V. Dupont, W. Pan and B. Chen, *Chem. Eng. J.*, 2011, **166**, 631–638.
321 Y. Li and C. Y. Wu, *Environ. Sci. Technol.*, 2006, **40**, 6444–6448.
322 H. L. Clever, S. A. Johnson and M. E. Derrick, *J. Phys. Chem. Ref. Data*, 1985, **14**, 631–680.
323 P. Salaün and C. M. G. Van Den Berg, *Anal. Chem.*, 2006, **78**, 5052–5060.
324 I. T. Somé, A. K. Sakira, D. Mertens, S. N. Ronkart and J.-M. Kauffmann, *Talanta*, 2016, **152**, 335–340.
325 H. Fei, W. Leng, X. Li, X. Cheng, Y. Xu, J. Zhang and C. Cao, *Environ. Sci. Technol.*, 2011, **45**, 4532–4539.
326 M. A. Ferreira and A. A. Barros, *Anal. Chim. Acta*, 2002, **459**, 151–159.
327 D. A. Wheeler, G. Wang, Y. Ling, Y. Li and J. Z. Zhang, *Energy Environ. Sci.*, 2012, **5**, 6682.
328 Y. Jin, C. Zhao, Y. Lin, D. Wang, L. Chen and C. Shen, *J. Mater. Sci. Technol.*, 2017, **33**, 768–774.
329 W. Chen, Q. Zhou, F. Wan and T. Gao, *J. Nanomater.*, 2012, **2012**, 1–9.
330 C. S. Turchi and D. F. Ollis, *J. Catal.*, 1990, **122**, 178–192.
331 K. S. Ochoa-Gutierrez and M. A. Mueses, *Ing. y Compet.*, 2014, **16**, 309–320.
332 C. Y. Cummings, M. J. Bonné, K. J. Edler, M. Helton, A. McKee and F. Marken, *Electrochem. commun.*, 2008, **10**, 1773–1776.
333 F. Le Formal, E. Pastor, S. D. Tilley, C. A. Mesa, S. R. Pendlebury, M. Grätzel and J. R. Durrant, *J. Am. Chem. Soc.*, 2015, **137**, 6629–6637.
334 B. Klahr, S. Gimenez, F. Fabregat-Santiago, J. Bisquert and T. W. Hamann, *Energy Environ. Sci.*, 2012, **5**, 7626.
335 O. Zandi and T. W. Hamann, *Nat. Chem.*, 2016, **8**, 778–783.
336 H. Bülter, G. Denuault, S. Mátéfi-Tempfli, M. Mátéfi-Tempfli, C. Dosche and G. Wittstock, *Electrochim. Acta*, 2016, **222**, 1326–1334.
337 N. S. McIntyre and D. G. Zetaruk, *Anal. Chem.*, 1977, **49**, 1521–1529.
338 T. Yamashita and P. Hayes, *Appl. Surf. Sci.*, 2008, **254**, 2441–2449.
339 F. Liang, Y. Yu, W. Zhou, X. Xu and Z. Zhu, *J. Mater. Chem. A*, 2015, **3**, 634–640.
340 X. Lu, Y. Zeng, M. Yu, T. Zhai, C. Liang, S. Xie, M.-S. Balogun and Y. Tong, *Adv. Mater.*, 2014, **26**, 3148–3155.
341 J. Socratous, K. K. Banger, Y. Vaynzof, A. Sadhanala, A. D. Brown, A. Sepe, U. Steiner and H. Sirringhaus, *Adv. Funct. Mater.*, 2015, **25**, 1873–1885.
342 A. P. Grosvenor, B. A. Kobe and N. S. McIntyre, *Surf. Sci.*, 2004, **572**, 217–227.
343 M.-T. Nguyen, N. Seriani, S. Piccinin and R. Gebauer, *J. Chem. Phys.*, 2014, **140**, 64703.

344 A. Hellman, B. Iandolo, B. Wickman, H. Grönbeck and J. Baltrusaitis, *Surf. Sci.*, 2015, **640**, 45–49.

5. List of publications

1. “Photocatalytic reduction and scavenging of Hg(II) over templated-dewetted Au on TiO_2 nanotubes”, D. Spanu, A. Bestetti, H. Hildebrand, P. Schmuki, M. Altomare, S. Recchia, Photochemical & Photobiological Sciences, (2019). DOI: 10.1039/C8PP00424B.

2. “Photoelectrocatalytic oxidation of As(III) over hematite photoanodes: A sensible indicator of the presence of highly reactive surface sites”, D. Spanu, V. Dal Santo, F. Malara, A. Naldoni, A. Turolla, M. Antonelli, C. Dossi, M. Marelli, M. Altomare, P. Schmuki, S. Recchia, Electrochimica Acta (2018). DOI: 10.1016/j.electacta.2018.10.003.

3. “Templated Dewetting-Alloying of NiCu Bilayers on TiO_2 Nanotubes Enables Efficient Noble Metal-Free Photocatalytic H_2 Evolution”, D. Spanu, S. Recchia, S. Mohajernia, O. Tomanec, S. Kment, R. Zbořil, P. Schmuki, and M. Altomare, ACS Catalysis, 8 (2018) 5298-5305. DOI: 10.1021/acscatal.8b01190.

4. “Site-Selective Pt Dewetting on WO_3-Coated TiO_2 Nanotube Arrays: an Electron Transfer Cascade-Based H_2 Evolution Photocatalyst”, D. Spanu, S. Recchia, S. Mohajernia, M. Altomare, P. Schmuki, Applied Catalysis B: Environmental, 237 (2018) 198-205. DOI: 10.1016/j.apcatb.2018.05.061.

5. “A viscous film sample chamber for Laser Ablation Inductively Coupled Plasma – Mass Spectrometry”, D. Monticelli, D. Civati, B. Giussani, C. Dossi, D. Spanu, S. Recchia, Talanta, 179 (2018) 100-106. DOI: 10.1016/j.talanta.2017.10.060.

6. “Understanding microwave vessel contamination by chloride species"; S. Recchia, D. Spanu, D. Bianchi, A. Pozzi, C. Dossi, D. Monticelli, Talanta, 159 (2016) 29-33. DOI: 10.1016/j.talanta.2016.05.073.